NASA Contractor Report 3773

An Assessment of the Accuracy of Orthotropic Photoelasticity

M. W. Hyer and D. H. Liu

19960229 138

NASA

NASA Contractor Report 3773

An Assessment of the Accuracy of Orthotropic Photoelasticity

M. W. Hyer and D. H. Liu

Virginia Polytechnic Institute and State University
Blacksburg, Virginia

NASA

National Aeronautics
and Space Administration

**Scientific and Technical
Information Office**

1984

DISCLAIMER NOTICE

UNCLASSIFIED
Technical
Report

DEFENSE
TECHNICAL
INFORMATION
CENTER

DTIC Acquiring Information
Imparting Knowledge

DEFENSE LOGISTICS
AGENCY
Cameron Station, Virginia 22304-6145

UNCLASSIFIED
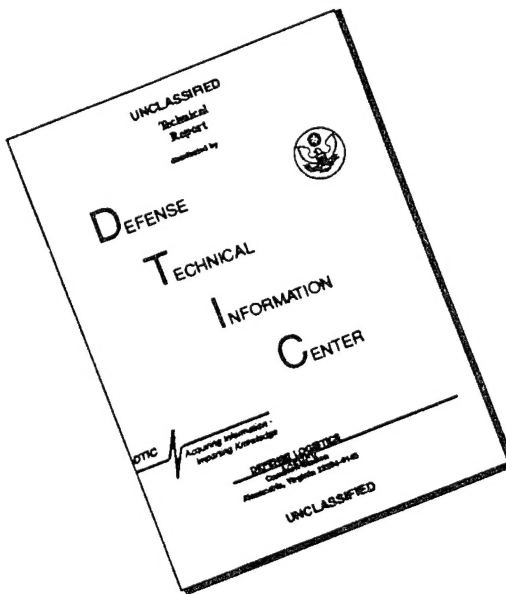
THIS DOCUMENT IS BEST
QUALITY AVAILABLE. THE COPY
FURNISHED TO DTIC CONTAINED
A SIGNIFICANT NUMBER OF
PAGES WHICH DO NOT
REPRODUCE LEGIBLY.

Table of Contents

List of Figures

viii

List of Tables

Acknowledgements

List of Symbols

a_{ij}	stress-birefringent coefficients.
A, B, C	constants related to calibration of 45° four-point bending specimen.
C	isotropic material stress-optic coefficient.
c	speed of light in a medium.
c_0	speed of light in a free space.
c_1, c_2	speed of light in slow and fast direction.
$C_1 - C_5$	stress-optic coefficients.
$\bar{C}_1 - \bar{C}_5$	stress-optic coefficients $(\bar{C}_i = 1/C_i)$.
D	disk diameter.
e	dielectric constant in isotropic material.
e_0	dielectric constant of free space.
e_x, e_y, e_{xy}	components of dielectric tensor referred to xy system.
$\hat{e}_1, \hat{e}_2$	principal values of dielectric tensor.
e_{ave}, e_{ave}^T	averages related to a general dielectric tensor and the total dielectric tensor, respectively.
e_{1M}, e_{2M}, e_{12M}	components of dielectric tensor referred to material system.
$e_{1M}^R, e_{2M}^R, e_{12M}^R$	components of residual dielectric tensor referred to material system.
$\hat{e}_{1R}, \hat{e}_{2R}$	principal values of residual dielectric tensor.
$e_{1M}^T, e_{2M}^T, e_{12M}^T$	components of total dielectric tensor referred to material system.
$\hat{e}_{1T}, \hat{e}_{2T}$	principal values of total dielectric tensor.
$e_{1M}^\sigma, e_{2M}^\sigma, e_{12M}^\sigma$	components of dielectric tensor associated with the application of mechanical loads, referred to material system.

$\hat{e}_{1\sigma}, \hat{e}_{2\sigma}$ principal values of dielectric tensor associated with the application of mechanical loads.

E_1, E_2 Young's modulii of material in fiber and matrix directions, respectively.

f_1, f_2, f_{12} stress optic coefficients, related to a_{ij}.

G_{12} shear modulus in material coordinate system.

h thickness of birefringent material.

I moment of inertia of four-point bend specimen.

M moment applied to four-point bend specimen.

n index of refraction, c_0/c.

n_{ave}, n_{ave}^T averages of indices of refraction, general and total, respectively.

$\hat{n}_1, \hat{n}_2$ slow and fast indices of refraction, respectively.

N isochromatic fringe order, associated with situations where there is no residual birefringence.

N_R residual isochromatic fringe order.

N_T total isochromatic fringe order, associated with situations where there is residual birefringence.

$N_{1M}^T, N_{2M}^T, N_{12M}^T$ components of total birefringence tensor referred to material system.

$\hat{N}_{1M}, \hat{N}_{2T}$ principal values of total birefringence tensor.

$N_{1M}^\sigma, N_{2M}^\sigma, N_{12M}^\sigma$ components of birefringence tensor associated with the application of mechanical loads, referred to material system.

$\hat{N}_{1R}, \hat{N}_{2R}$ principal values of residual birefringence tensor.

P diametral load, compression is negative.

q_{ij} stress-dielectric constants.

t disk thickness.

t_0 travel time for light in a vacuum.

t_1, t_2 travel times for light in birefringent material.

x,y	global coordinates, x and y in plane of material.
z	used to denote distance from neutral axis in four-point bending specimen.
α,β,γ	least-squares coefficients related to calibration of 45° specimens.
Δ	relative retardation.
$\Delta e, \Delta e^T$	increment in dielectric quantities.
Δt	time interval.
λ	light wavelength.
μ	magnetic permeability.
μ_o	magnet permeability of free space.
θ	isocline angle, associated with isotropic photoelasticity.
θ_R	orientation of residual dielectric tensor principal coordinate system, relative to material system.
θ_T	orientation of total dielectric tensor principal coordinate system, relative to material system.
θ_σ	orientation of principal coordinate system of dielectric tensor associated with the application of mechanical loads, relative to material system.
ϕ	orientation of material system relative to the global system.
ν	Poisson's ratio.
$\sigma_x, \sigma_y, \tau_{xy}$	stresses referred to global system.
$\sigma_1, \sigma_2, \tau_{12}$	stresses referred to material system.
1M,2M	material coordinate system.
1T,2T	principal total dielectric tensor coordinate system.
1R,2R	principal residual dielectric tensor coordinate system.
$1\sigma,2\sigma$	principal coordinate system of dielectric tensor associated with the application of mechanical loads.

INTRODUCTION

Considerable work has been performed over the past 15 years on the development of orthotropic photoelastic material and the development of stress-optic laws which characterize the relations between the optical and mechanical responses of the material. Some plane stress elasticity problems have been solved with the material but these problems have been more or less of a demonstration nature, designed to show the extent to which orthotropic photoelasticity works. In many cases the problems solved were such that the load was applied parallel to or perpendicular to the fiber direction, the principal stress system coincided with the principal material system, the principal stress directions were known, the stresses were computed along paths parallel or perpendicular to the fiber direction, or the vast majority of the boundaries were traction free so that 2 out of the 3 stresses were known with certainty over much of the boundary. Oftentimes the problems were chosen because there existed known solutions, or good first approximations, to the state of stress in the body. The stresses calculated using orthotropic photoelasticity were compared to the known solution. These types of exercises were necessary in the development stages of this new technology. However, to have the same utility as classical isotropic photoelasticity, orthotropic photoelasticity must be applicable to a wide variety of situations. Ultimately, orthotropic photoelasticity must be able to predict the state of stress when the applied load is at an arbitrary angle relative to the fibers, when the principal stress directions are variable from point to point and are unknown, and when the stresses along arbitrary paths are required. In addition, if residual birefringence

1

exists in the material due to the manufacturing process, its effect on interpreting photoelastic data must be taken into account.

This study was initiated to assess the ability of currently accepted orthotropic stress-optic laws to accurately predict the state of plane stress in currently available orthotropic photoelastic material. The ability to be able to examine a variety of loading directions, relative to the axes of orthotropicity, was of prime concern. In addition, it was important to be able to compute the stresses at more or less arbitrary locations in the interior of the body. In classical isotropic photoelasticity, if one of the principal stresses is known, the other principal stress can be computed directly from the isochromatic fringe pattern. This is always the case when examining the stresses at a traction-free boundary. For this case the shear and normal stresses are zero. With the shear stress zero, the principal stress directions are tangent and normal to the traction-free edge. With the normal stress zero, the only unknown is the principal stress tangent to the free edge. Using the stress-optic coefficient of the material and the isochromatic fringe count, this non-zero principal stress can be computed. In the interior of a body, both the isochromatic and isoclinic fringe patterns are used to compute stresses. Unless a third point-by-point experimental measurement is used in conjunction with the two photoelastic fringe measurements, an auxiliary numerical scheme is generally used to compute the complete state of stress in the interior of the body. This auxiliary numerical scheme is usually in the form of the numerical integration of the plane-stress equilibrium equations or the compatibility equations along a path from a boundary, or other region of known conditions, to

2

the interior point of interest. For simplicity, this path is usually a straight line.

This report begins by developing the stress-optic law for orthotropic materials. The laws are developed on a physical basis. Some of the development draws from the past work in orthotropic photoelasticity and can be considered as a summary and/or a reformating of results. However, early in this study it became obvious that the techniques used to fabricate the photoelastic material could produce a residual birefringence. With no applied loads, there could be an isochromatic fringe count of, say, 0.1. There would, of course, be an isoclinic associated with this value. The development which follows includes the effect of residual birefringence in the stress-optic law. Conceptually, accounting for residual birefringence effects is simple. Accounting for residual effects operationally is also quite simple. Since birefringence is associated with tensor quantities, keeping track of residual effects is bookkeeping.

To have the ability to generate a wide variety of stress states experimentally and at the same time to have a good approximation to the state of stress, an unidirectional disk in diametral compression was chosen as the study specimen. With such a specimen the fibers could be oriented at arbitrary directions relative to the applied diametral load and a wide variety of stress states could be produced. In addition, the stress state along arbitrary diameters or chords could be computed using the photoelastic data and an auxiliary numerical scheme. It was decided to refrain from using a third point-by-point experimental measure to compute the stresses. The most accurate point-by-point measure is to use interferometry to measure the thickness change of the material.

This requires optical equipment beyond the standard polariscope set-up. It was a goal to keep this study within the context of common polariscopes. Oblique incidence techniques were not considered because of the poor fringe resolution associated with orthotropic photoelastic materials.

The disk geometry was chosen for several other reasons. First, it was an easy specimen geometry to make. Second, and more importantly, it did not use much of the valuable photoelastic material that was available. One specimen could be used for all load orientations. Finally, the disk geometry is an ideal specimen for calibration of orthotropic photoelastic material. In theory, according to the state-of-the-art stress-optic laws, three tests must be made on an orthotropic photoelastic material to completly characterize its stress-optic relations. In the past, three tensile tests have been conducted. One tensile test is conducted on a 0° specimen, one test on a 90° specimen, and one test on a 45° specimen. The experimenter can judiciously choose the length and width of the tensile specimens but the specimens do tend to consume the valuable photoelastic material. Since the material has some variability in its mechanical and optical properties, it is a good idea to calibrate the actual panel from which experimental models are to be made. Although three is a minimum, conceivably more tensile specimens, say at 30°, 60°, and 75°, could be tested and the calibration could be done with some form of least-squares approach to the data reduction. This would be done, of course, at the expense of valuable photoelastic material. This has not been done, rather, the minimum three tests have generally been the standard. With a single disk, theoretically, an infinite number of stress states is possible. Practically speaking, with

various disk orientations relative to the load direction, and with photoelastic data taken at several points on the disk, 15-20 sets of stress and corresponding photoelastic fringe information could be readily obtained and a least-squares calibration could be conducted to determine the stress-optic characterization of the material.

Experimentally there were many compelling reasons for choosing the disk geometry. In addition, the theoretical elasticity solution to the disk in diametral compression could be derived from the complex variable approach. The complex variable solution is presented in an appendix and will not be discussed further except as to quote stress predictions from the solution.

This report summarizes the work performed using the disk as a study specimen. The work followed the basic line of reasoning: If a particular stress-optic law for the orthotropic photoelastic material is true, and if the calibration of the material is done using three tensile tests, then two types of experiments can be done to test the validity of the stress-optic law. Using the calibration information, the stress-optic law, and the theoretical elasticity solution, the isochromatic and isoclinic fringe patterns in the disk can be predicted. By examining different load orientations, relative to the fiber directions, a wide variety of spatial variations of fringe patterns can be generated. This wide variety of predicted fringe patterns can then be compared to the experimentally observed fringe patterns. This is a legitimate test of the assumed stress-optic behavior and the calibration. These so-called "forward tests" were conducted and are reported. Real interest, of course, is in starting with a specific fringe pattern and working backwards to obtain the stress state. This is the essence of photoelastici-

ty. A numerical scheme was previously developed for studying the stresses in the inner laps of double-lapped, double-pin connector models constructed from acrylic and isotropic photoelastic material. This scheme was based on the stress-optic law for classic isotropic materials and a finite-difference form of the plane-stress equilibrium equations. The equilibrium equations were chosen as the auxiliary conditions to obtain the three components of stress at interior points in the model. This scheme was modified to accomodate an orthotropic stress-optic law. The stress-optic calibration information from auxiliary calibration tests, the isochromatic and isoclinic fringe count at the various mesh points of the finite-difference grid, and the finite-difference equilibrium equations were used to experimentally determine the stresses in the disk. These stresses were compared with the stresses computed from the complex variable elasticity solution. These stress prediction tests could be considered as "backwards tests." To put the results into context, numerical and experimental results for disks made from isotropic photoelastic material are compared. Also numerical studies were conducted to determine the effect of isocline measurement error on the experimental results.

Throughout the report specific references to previous investigations are made. These are noted in a list of references. However, for completeness, a bibliography is included at the end of this report to mention those investigations not specifically cited.

Birefringence

In many transparent solids, the index of refraction* can be considered as a quantity which is independent of the direction of propagation and the plane of polarization of the transmitted light. However, in some transparent solids the speed of propagation of light depends both on the direction of propagation and the plane of polarization of the light. Within such a solid there will be a direction of propagation and a plane of polarization for which the light travels the fastest. There is also a direction of propagation and plane of polarization for which light travels the slowest. Because of the orthogonality and symmetry of the molecular structure and crystals making up these solids, many of these directions and planes are perpendicular to each other. This idea of multiple propagation speeds and directional-dependence of the speed of propagation is termed birefringence. In the discussions here, the birefringence phenomenon will be considered something that can occur in an unstressed material and also something that can be induced in a material by application of loads. Because of the orthogonality of the directions associated with the different propagation speeds, the indices of refraction can be associated with quantities which can be regarded as tensors. Tensor quantities have principal values and the directions associated with these values are quite often perpendicular to each other. The ideas of extremums in the propagation speeds, tensors, planes of polarization, etc., can all be used to put the ideas of classical

---

*index of refraction of a medium, n, is defined as the speed of light in a vacuum, c_o, divided by the speed of light in the medium, c.

7

isotropic photoelasticity on a formal and rigorous foundation. This has been done in various texts and papers. However, if one is trying to determine, for example, the stress concentration factor at the base of a fillet in a model representing a metal component, the formalism is not required. All that is required is to know that the isochromatic fringe number times some a priori determined numerical factor gives the value of the stress at the base of the fillet. However, if one is dealing with a new photoelastic phenomenon such as orthotropic photoelasticity, the formalism helps guide the interpretation of the photoelastic data. The formalism also provides insight into the potential of the new phenomenon. In this report, some of the formalism will be used to establish ideas regarding orthotropic photoelasticity. The dielectric tensor and its relation to the indices of refraction will be introduced. Then the notion of the birefringence tensor will be discussed. The introduction of the birefringence tensor is a convenient abstraction and is not at all necessary in order to understand the implications of orthotropic photoelasticity. However, many past investigators have used the idea of a birefringence tensor and so it will be used here to illustrate how it fits into the nomenclature and mechanics of orthotropic photoelasticity. These ideas will be used to derive relations between the applied stress and the observed optical response. These relations will be such that they can be used in a numerical scheme to compute the stresses in a loaded photoelastic model. To begin, however, the approach used by many texts to start the discussion of isotropic photoelasticity will be reproduced. The expression for the relative retardation will be derived. This approach will introduce the relations between the wavelength of light, the model thickness, the indices of refraction, and the slowing

8

of the light passing through photoelastic material. For those not familiar with even isotropic photoelasticity, this approach will be quite palatable because it is based on the ideas of travel times of a light wave, optical path lengths, etc. Also, since many texts use this idea, it will be a point of reference if one is consulting these texts. For those familiar with isotropic photoelasticity, the derivation will be a review and it will provide some commonality between isotropic and orthotropic photoelasticity. The relative retardation is introduced because it is one of the two basic quantities measured directly by a standard polariscope. The other quantity, which will be introduced after the relative retardation is discussed, is the isocline.

Relative Retardation

Consider a transparent solid in the form of a thin plate, of thickness h, oriented perpendicular to the direction of propagation of a light vector. As shown in fig. 1, a light vector is impinging on or incident to the plate. If the light vector is polarized, it can be thought of as oscillating harmonically in a single plane as it propagates toward the plate, as shown in fig. 2. If the plate is made of a material with indices of refraction which are dependent on the plane of polarization of the incident light, then it is possible to identify a plane of polarization in which the light travels through the plate with the fastest propagation velocity. It is also possible to identify a plane of polarization in which the light passes through the plate with the slowest propagation velocity. These directions, as shown in fig. 3, are referred to as fast and slow directions, respectively. The descriptions fast and slow can be misleading. In a transparent solid light

9

thin plate

h

direction of incident light
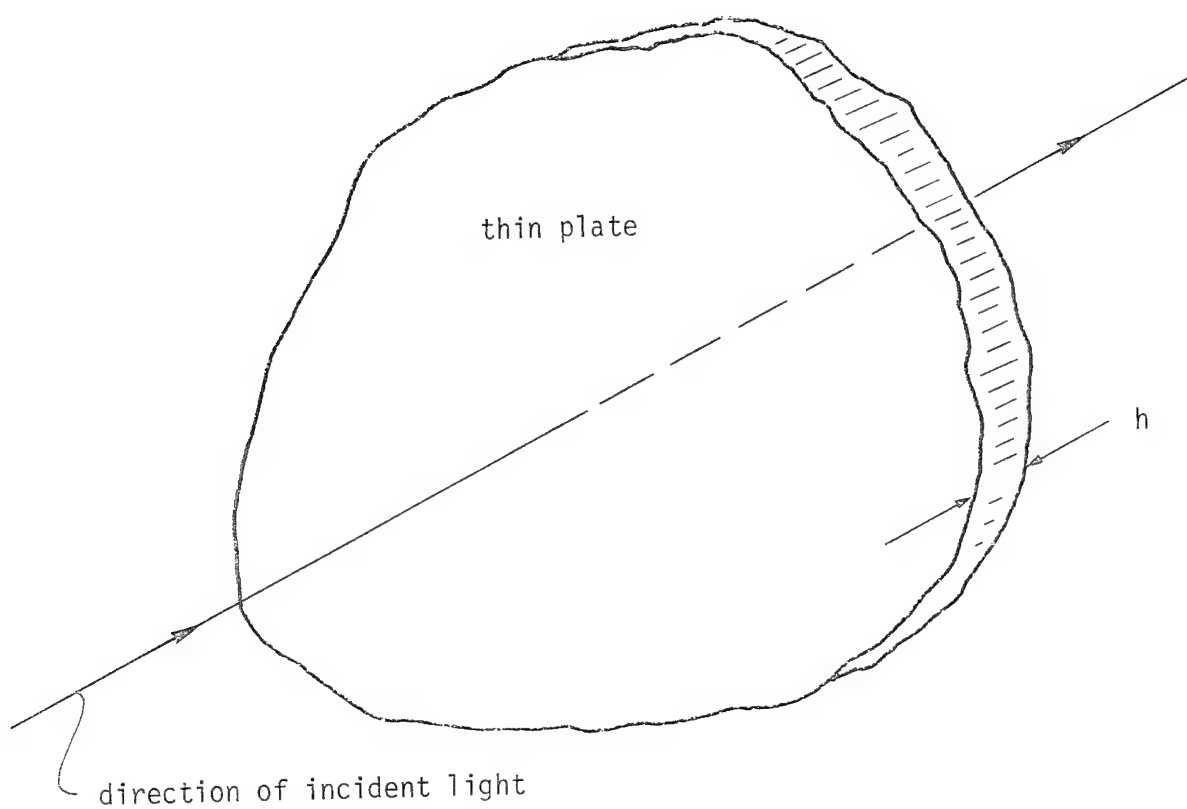
Fig. 1 Light incident perpendicular to thin plate.
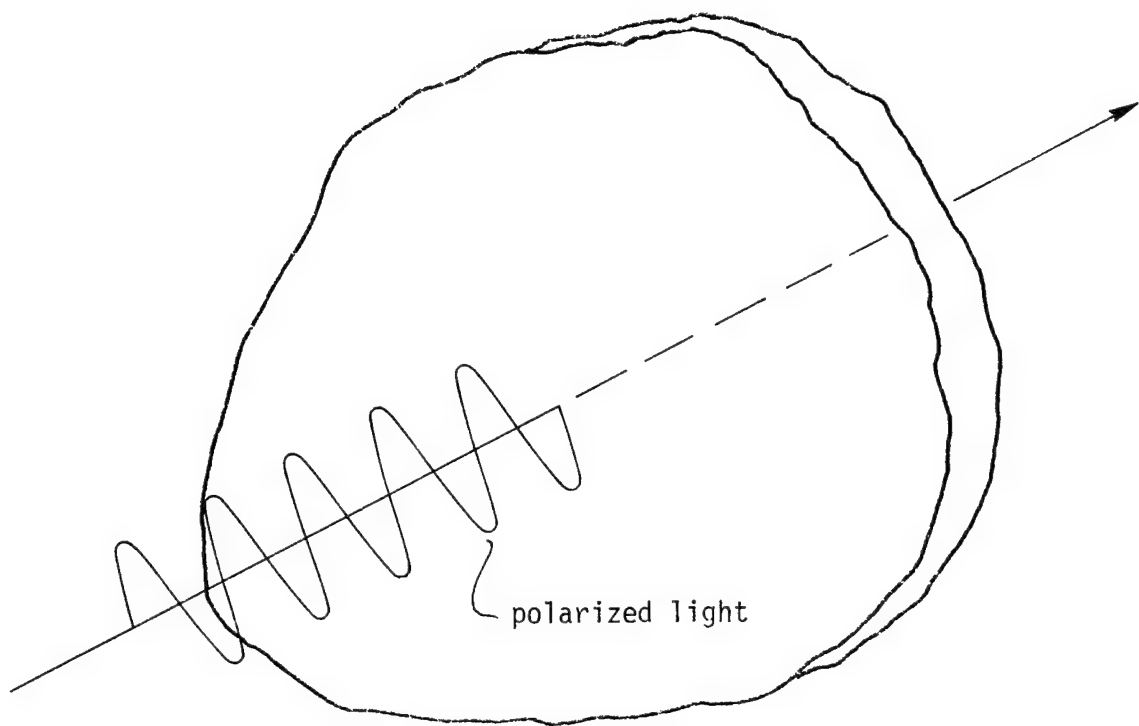
Fig. 2 Orientation of polarized light.

11

fast
direction

slow
direction

direction of incident light
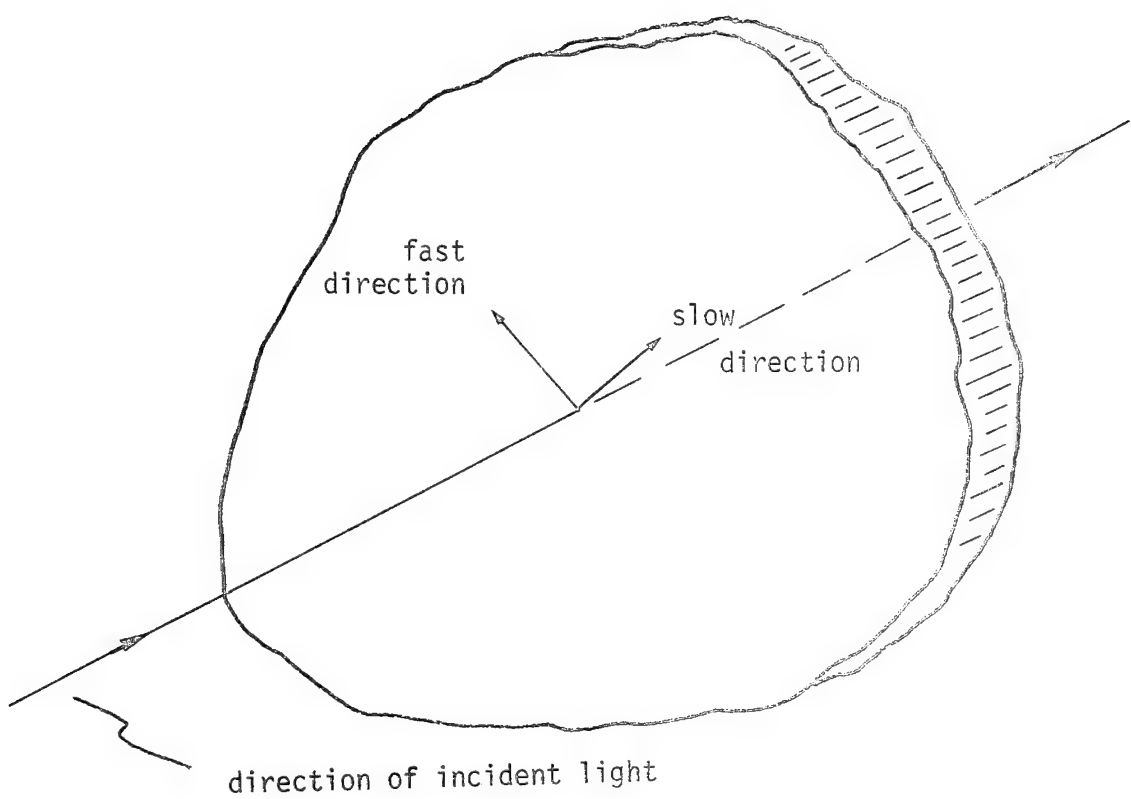
Fig. 3 Fast and slow directions through thickness.

12

actually slows, when compared to its speed in air, independent of the plane of polarization. However, in the so-called fast direction the light slows the least.

The polarized light that is impingent on the plate in some direction other than the fast or slow direction, as shown in figure 4, can be decomposed into vector components in the fast direction and slow direction, respectively. Referring to in fig. 5, due to differences in the speed of propagation in the two directions, these two components are out-of-phase with each other when they emerge from the plate. Since the components are out of phase they can be made to interfere constructively and destructively. The specific conditions required to obtain interference is a function of the optical apparatus used for viewing the phenomenon. The various optical devices, or polariscope arrangements, and the specific relations for interference of these out-of-phase components are discussed in [1]. It is this phase difference which is the basis for using the birefringent phenomenon to an advantage. An expression for this phase difference is developed in the next section.

Phase Difference

If the index of refraction in the fast direction is denoted as $\hat{n}_2$, then

$$\hat{n}_2 = \frac{c_0}{c_2} , \tag{1}$$

where c_0 is the speed of light in a vacuum and c_2 is the speed of light in the plate if the polarized light vector is aligned with the fast, 2, direction. The index of refraction in the slow, 1, direction is similarly defined, i.e.

13

component in
fast direction

component in
slow direction
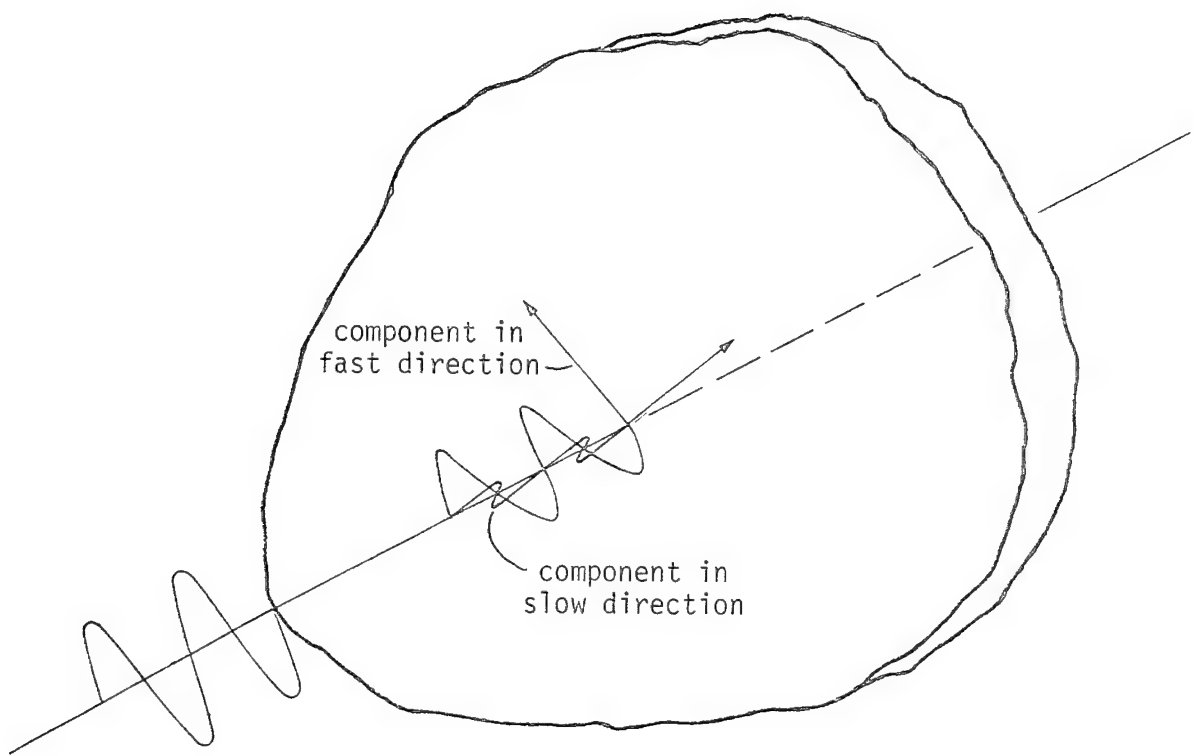
Fig. 4   Decomposition of polarized light.
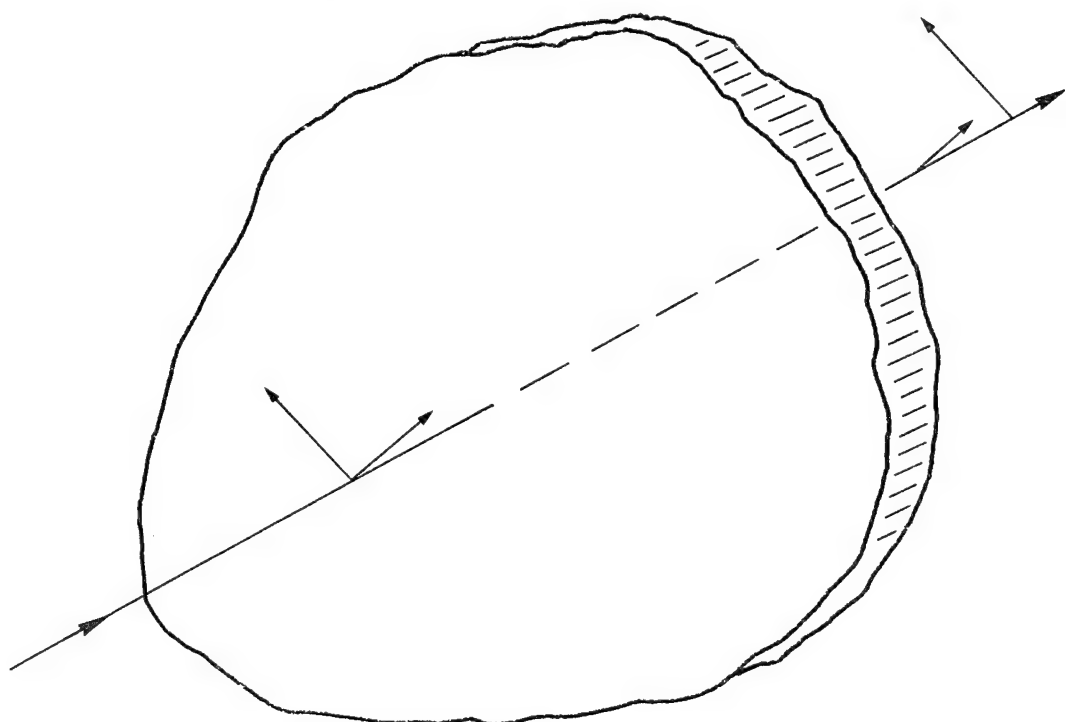
Fig. 5 Effect of speed differences on emerging light.

$$\hat{n}_1 = \frac{c_0}{c_1} \, . \tag{2}$$

The hat, ^, over the indices of refraction signifies that these are the extremum values for all orientations of the plane of polarization. This hat notation will soon be used to denote the principal values of a tensor associated with the transmission of light through the plate. The principal values of this tensor and the extremums in the values of the indices of refraction are related.

For light propagating with the fast speed, to pass through thickness h, the elapsed time, t_2, is

$$t_2 = \frac{h}{c_2} \, . \tag{3}$$

Similarly, for light propagating with the slow speed, the elapsed time, t_1, to pass through thickness h is

$$t_1 = \frac{h}{c_1} \, . \tag{4}$$

If a vacuum occupied that region of space instead of a birefringent medium, then the elapsed time to move through the distance h would be

$$t_0 = \frac{h}{c_0} \, . \tag{5}$$

Figure 6 illustrates this thickness geometry. The time difference between when the fast light emerges from the plate and when the slow light emerges from the plate, Δt, is given by

16
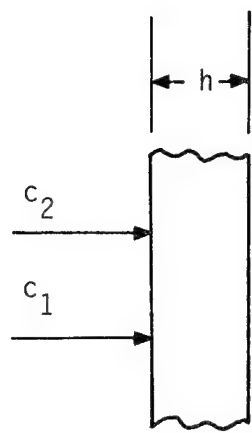
Fig. 6 Light passing through plate.

$$\Delta t = t_1 - t_2 = \frac{h}{c_1} - \frac{h}{c_2} \, . \tag{6}$$

Using eqs. 1-4 in eq. 6 leads to

$$\Delta t = \frac{h}{c_0} (\hat{n}_1 - \hat{n}_2) \, . \tag{7}$$

In terms of distance (e.g. meters, inches, etc.), the two light vectors are out of phase by an amount

$$c_0 \Delta t = h (\hat{n}_1 - \hat{n}_2) \, . \tag{8}$$

Relative to the wavelength of light , λ, entering the plate, the phase difference, in cycles, between the two light vectors is

$$\frac{c_0 \Delta t}{\lambda} = \frac{h}{\lambda} (\hat{n}_1 - \hat{n}_2) \, . \tag{9}$$

To put this phase difference in terms of radians, multiply eq. (9) by 2π, i.e.

$$\Delta = \frac{2\pi c_0 \Delta t}{\lambda} = \frac{2\pi h}{\lambda} (\hat{n}_1 - \hat{n}_2) \, . \tag{10}$$

Thus the phase difference, Δ, is expressed in terms of the wavelength of incident light, the plate thickness, and the difference in the principal indices of refraction. The quantity Δ is the relative retardation between the two components of reemerging polarized light.

In this discussion the quantity $\hat{n}_2$ is arbitrarily associated with the direction that transmitts the light the fastest and $\hat{n}_1$ is associated with the direction that transmitts the light the slowest. Thus $(\hat{n}_1 - \hat{n}_2)$ is a positive quantity.

18

Causes of Birefringence in Solids

The interaction of the electromagnetic field of the light with the electromagnetic fields associated with the bonding of the atoms in a transparent solid changes the speed of light from the vacuum condition. In addition, anything that changes the spatial distribution and/or strength of the bonding electric fields in a solid will affect the propagation speed of light within the solid. A way to change the bonding electric fields in a solid is to physically move the molecules of the solid relative to each other. Such a condition could be caused by applying a mechanical load (stress) to the solid. If the solid is elastically isotropic, and if there is a stress applied in a particular direction, then the strength and distribution of the bonding fields would be different in different directions. In this case the electric field of the incident light would be acted upon by one field strength if it was polarized in one direction and it would be acted upon by another field strength if it was polarized in another direction. This leads to directionally-dependent propagation speeds. This phenomenon would also occur if the material was elastically orthotropic. In fact, even with the solid in its natural (unstrained or unstressed) state, an orthotropic solid has different bonding field strengths in different directions. Thus it is possible to conceive of multiple indices of refraction in an orthotropic media with the molecules in their natural (unstressed) positions. In the context of these discussions, the multiple indices of refraction with no load applied can be considered a residual difference in the indices of refraction or residual birefringence. If a mechanically induced alteration of the bonds occurs, and if superposition of birefringent effects is assumed valid, then the total differences in indices

19

of refraction would be the sum of the effects of the residual bire-
fringence and the effects of the mechanically induced birefringence.

Details of Birefringence in Solids

The fundamental quantities for the study of birefringence in solids
are the dielectric constants of the material. The plural connotation in
the word 'constants' is important because oftentimes the dielectric
properties of a material are thought of as being described by a single
number. In general, the dielectric properties of a material are direc-
tionally-dependent and they can be represented as a tensor called the
dielectric tensor. The dielectric tensor relates the electric field
strength vector to the electric displacement vector. The index of re-
fraction of a solid is related to the dielectric tensor. Due to the di-
rectionally-dependent nature of a tensor, the speed of propagation of
light in a transparent solid depends strongly on the directional-depen-
dence of the dielectric properties of the solid. For the case of a thin
plate, referred to here by analogy to 'plane stress' as 'plane birefrin-
gence,' the dielectric tensor can be written as

$$
\begin{bmatrix} e_x & e_{xy} \\ e_{xy} & e_y \end{bmatrix} \quad \text{or} \quad \begin{Bmatrix} e_x \\ e_y \\ e_{xy} \end{Bmatrix} \tag{11}
$$

With the above notation, the dielectric properties are being referred to
an x-y coordinate system. The x-y coordinate system is a global coordi-

20

nate system with the x and y axes in the plane of the plate. At the moment the orientation of the x and y axes within the plane are not important. Later, stresses will be computed in the x-y system and its orientation will be specified. Figure 7 depicts the coordinate system. The light can be considered to be propagating into the page and perpendicular to it.

In an electrically isotropic material the dielectric tensor takes the form

$$
\begin{bmatrix} e & 0 \\ 0 & e \end{bmatrix} = \begin{Bmatrix} e \\ e \\ 0 \end{Bmatrix} . \tag{12}
$$

A vacuum, or free space, is isotropic and so the dielectric tensor is given by

$$
\begin{bmatrix} e_0 & 0 \\ 0 & e_0 \end{bmatrix} = \begin{Bmatrix} e_0 \\ e_0 \\ 0 \end{Bmatrix} , \tag{13}
$$

the subscript 'o' denoting free vacuum. The fast and slow indices of refraction of a solid are related to the principal values of the dielectric tensor. The principal values of the dielectric tensor are given by

$$
\hat{e}_1, \hat{e}_2 = \frac{e_x + e_y}{2} \pm \sqrt{(\frac{e_x - e_y}{2})^2 + e_{xy}^2} . \tag{14}
$$

21
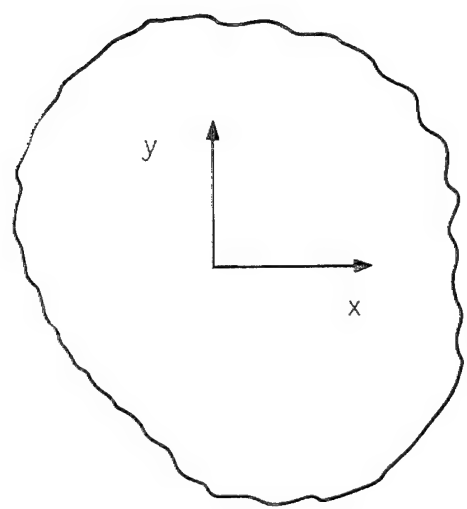
Fig. 7 The x-y coordinate system.

The fast and slow indices of refraction are defined [2] to be

$$\hat{n}_1 \equiv \sqrt{\frac{\hat{e}_1}{e_o}} \quad \text{and} \quad \hat{n}_2 \equiv \sqrt{\frac{\hat{e}_2}{e_o}} \quad . \tag{15}$$

$$\tag{16}$$

For the transparent solids considered here and for the levels of birefringence encountered in photoelasticity, certain simplifying approximations can be made. If e_{ave} is defined as

$$e_{ave} = \frac{e_x + e_y}{2} , \tag{17}$$

then eq. 14 becomes

$$\hat{e}_1, \hat{e}_2 = e_{ave} \pm \Delta e, \tag{18}$$

where

$$\Delta e = \sqrt{(\frac{e_x - e_y}{2})^2 + e_{xy}{}^2} \quad . \tag{19}$$

It is shown in Appendix A that Δe is an order of magnitude smaller than e_{ave}. Then, using the binomial approximation, eqs. 15 and 16 become

$$\hat{n}_1, \hat{n}_2 \approx \sqrt{\frac{e_{ave}}{e_o}} \left[1 \pm \frac{1}{2} \frac{\Delta e}{e_{ave}} \right] \quad . \tag{20}$$

$$\tag{21}$$

The relative retardation can be related to the dielectric constants by substituting eqs. 20 and 21 into eq. 10. This relation is important because the application of stress directly affects the dielectric constants of a transparent material. The above substitution results in

23

$$\Delta = \frac{2\pi h}{\lambda n_{ave}} \frac{\Delta e}{e_o} , \qquad (22)$$

where n_{ave} is the average index of refraction of the medium and is defined as

$$n_{ave} = \sqrt{\frac{e_{ave}}{e_o}} . \qquad (23)$$

It should be mentioned at this point that it has been assumed that the magnetic permeability, μ, has been assumed to be an isotropic property of the material. Furthermore, the permeability is assumed to be equal to the permeability in a vacuum, μ_o. Generally the velocity of propagation of electromagnetic waves depends on the permeability as well as the dielectric constant. For an isotropic material, the velocity of propagation is proportional to $1/\sqrt{e\mu}$. In a vacuum the velocity becomes $1/\sqrt{e_o \mu_o}$. The index of refraction of a medium is thus given by thus

$$n = \sqrt{\frac{e\mu}{e_o \mu_o}} . \qquad (24)$$

If μ is assumed to be equal to μ_o, then the index of refraction is related only by the ratios of the dielectric constants.

For an orthotropic material, particularly fiber reinforced composite materials, there is a coordinate associated with the stiff (fiber) direction and a coordinate, perpendicular to the first, associated with the soft (matrix) direction. Much of the analysis of fiber-reinforced composites uses these directions as the reference for defining stress, strains, elastic constants, failure stresses, etc. In orthotropic photoelasticity it is also convenient to use this coordinate system as a basis. Herein, these directions will be referred to as 1M and 2M.

24

These directions will refer to the fiber and matrix direction, respectively, with the M denoting that it is a material coordinate system. When computing stresses in the x-y system, the angle the +1M axis makes with to the +x axis will be denoted ϕ. This coordinate system orientation is shown in fig. 8. In the material coordinate system, the dielectric tensor can be identified as

$$
\begin{bmatrix} e_{1M} & e_{12M} \\ e_{12M} & e_{2M} \end{bmatrix} \quad or \quad \begin{Bmatrix} e_{1M} \\ e_{2M} \\ e_{12M} \end{Bmatrix} \quad . \tag{25}
$$

Birefringence in Fiber-Reinforced Solids

Because of differences in the thermoelastic properties of the fiber and matrix constituents in fiber-reinforced composites, the fabrication of fiber-reinforced composites can lead to residual stresses in the fibers and the matrix. Since the dielectric properties of solids can depend on the stress state in the solid, these residual stresses can lead to residual birefringence. As mentioned in the Introduction, such birefringence is considered here. In the material coordinate system, residual dielectric effects generally have three components,

$$
\begin{Bmatrix} e_{1M}^R \\ e_{2M}^R \\ e_{12M}^R \end{Bmatrix} \quad . \tag{26}
$$

The superscript R identifies properties associated with residual effects. There is no a priori reason to believe, in general, that the

25
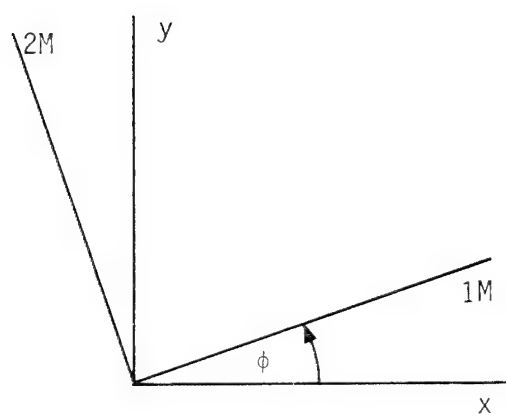
Fig. 8   Orientation of the material system (1M-2M) relative to
         the x-y system.

26

principal directions of the residual dielectric tensor are aligned with the material directions. There is, however, a principal direction associated with the residual tensor, i.e. directions associated with the fastest and slowest propagation directions for the solid when there is no mechanical load applied. Assume that the principal residual directions are rotated from the material directions by an amount θ_R. The orientation of the 1R-2R system relative to the 1M-2M system is shown in fig. 9. The residual dielectric tensor principal coordinate system is identified by 1R and 2R. The principal values of the residual dielectric tensor are given by $\hat{e}_{1R}$ and $\hat{e}_{2R}$. The representation of the residual dielectric tensor in the principal residual coordinate system is

$$\left\{ \begin{array}{c} \hat{e}_{1R} \\ \\ \hat{e}_{2R} \\ \\ 0 \end{array} \right\} \quad . \tag{27}$$

The components of the residual dielectric tensor in the material system, eq. 26, can be related to the principal values of the residual dielectric tensor, eq. 27, by the usual two-dimensional tensor transformations, i.e.

$$e_{1M}^R = \left(\frac{\hat{e}_{1R} + \hat{e}_{2R}}{2}\right) + \left(\frac{\hat{e}_{1R} - \hat{e}_{2R}}{2}\right) \cos\left(-2\theta_R\right) \tag{28}a$$

$$e_{2M}^R = \left(\frac{\hat{e}_{1R} + \hat{e}_{2R}}{2}\right) - \left(\frac{\hat{e}_{1R} - \hat{e}_{2R}}{2}\right) \cos\left(-2\theta_R\right) \tag{28}b$$

$$e_{12M}^R = -\left(\frac{\hat{e}_{1R} - \hat{e}_{2R}}{2}\right) \sin\left(-2\theta_R\right) \tag{28}c$$

27
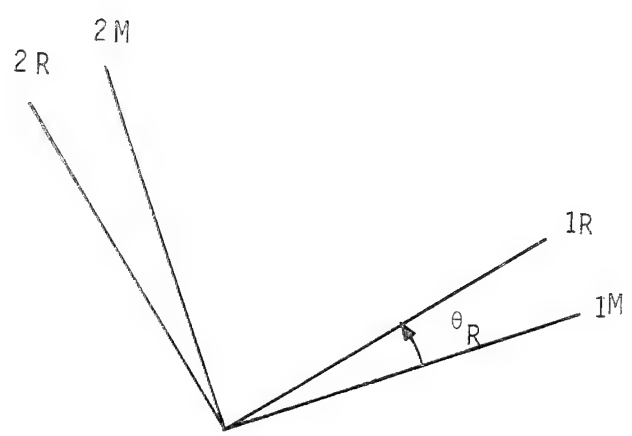
Fig. 9 Orientation of 1R-2R system relative to 1M-2M system.

28

The minus sign is left with the angle as a reminder that in these equations one is transforming back to the material system. If the components of the residual dielectric tensor are known in the material system, the principal values and principal directions of the residual dielectric tensor can be determined by the familiar formulas

$$\hat{e}_{1R}, \ \hat{e}_{2R} = \frac{e_{1M}^R + e_{2M}^R}{2} \pm \sqrt{\left(\frac{e_{1M}^R - e_{2M}^R}{2}\right)^2 + (e_{12M}^R)^2} \qquad (28)d$$

$$\tan (2\theta_R) = \frac{2e_{12M}^R}{e_{1M}^R - e_{2M}^R} . \qquad (28)e$$

If loads are applied to the solid and there are residual birefringent effects present, then there will exist a state of total birefringence. This situation is associated with the total dielectric tensor. The total dielectric tensor will have principal values and principal directions. The coordinate system of the principal total dielectric tensor will be denoted as 1T and 2T, the T signifying association with total effects. The principal values of the total dielectric tensor can be written as

$$\begin{Bmatrix} \hat{e}_{1T} \\ \hat{e}_{2T} \\ 0 \end{Bmatrix} . \qquad (29)$$

In the material coordinate system, the components of the total dielectric tensor are given by

29

$$\begin{Bmatrix} e_{1M}^T \\ e_{2M}^T \\ e_{12M}^T \end{Bmatrix}.$$
(30)

The angle between the material coordinates and the coordinate system of the principal total dielectric tensor is denoted as θ_T and is illustrated in fig. 10. The components of the total dielectric tensor in the material coordinate system, eq. 30, are related to the principal values of the total dielectric tensor, eq. 29, by

$$e_{1M}^T = \left(\frac{\hat{e}_{1T} + \hat{e}_{2T}}{2}\right) + \left(\frac{\hat{e}_{1T} - \hat{e}_{2T}}{2}\right) \cos(-2\theta_T)$$
(31)a

$$e_{2M}^T = \left(\frac{\hat{e}_{1T} + \hat{e}_{2T}}{2}\right) - \left(\frac{\hat{e}_{1T} - \hat{e}_{2T}}{2}\right) \cos(-2\theta_T).$$
(31)b

$$e_{12M}^T = -\left(\frac{\hat{e}_{1T} - \hat{e}_{2T}}{2}\right) \sin(-2\theta_T)$$
(31)c

Conversely, knowing the components of the total dielectric tensor in the material system, the principal values and principal directions of total effects can be computed by

$$\hat{e}_{1T}, \hat{e}_{2T} = \left(\frac{e_{1M}^T + e_{2M}^T}{2}\right) \pm \sqrt{\left(\frac{e_{1M}^T + e_{2M}^T}{2}\right)^2 + (e_{12M}^T)^2}$$
(31)d

$$\tan(2\theta_T) = \frac{2e_{12M}^T}{(e_{1M}^T - e_{2M}^T)}$$
(31)e

Finally, there are principal values, principal directions, and material system components of the dielectric tensor associated with the application of mechanical loads. In the material system, the components of the dielectric tensor due to the applied loads are given by

30
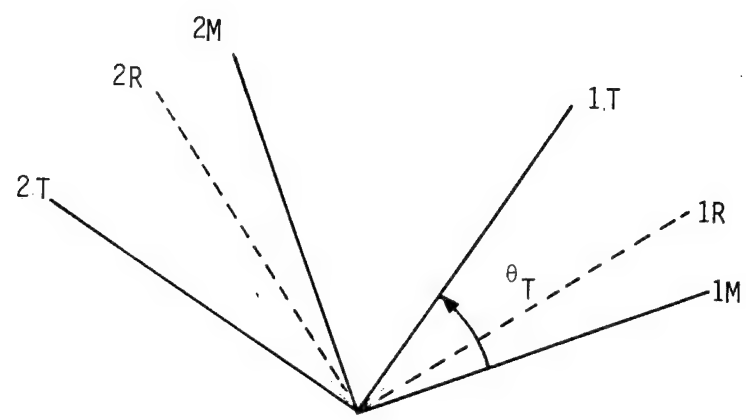
Fig. 10 Orientation of 1T-2T system relative to the 1M-2M system.

$$\left\{ \begin{array}{c} e^{\sigma}_{1M} \\ e^{\sigma}_{2M} \\ e^{\sigma}_{12M} \end{array} \right\} \, . \qquad (32)$$

The mechanically induced dielectric tensor has its own principal coordinate system $1\sigma - 2\sigma$. The principal values of the dielectric tensor due to applied loads can be referred to this system and can be written as

$$\left\{ \begin{array}{c} \hat{e}_{1\sigma} \\ \hat{e}_{2\sigma} \\ 0 \end{array} \right\} \, . \qquad (33)$$

Assume the $1\sigma - 2\sigma$ coordinate system is oriented at an angle θ_{σ} relative to the material system. Figure 11 shows the angle θ_{σ} and four of the five coordinate systems discussed. (The x-y coordinate system is not depicted.) Equations similar to eqs. 28a - 28e and 31a-31e can be written to relate e^{σ}_{1M}, e^{σ}_{2M}, e^{σ}_{12M}, $\hat{e}_{1\sigma}$, $\hat{e}_{2\sigma}$, and θ_{σ}. These equations are

$$e^{\sigma}_{1M} = \left(\frac{\hat{e}_{1\sigma} + \hat{e}_{2\sigma}}{2} \right) + \left(\frac{\hat{e}_{1\sigma} - \hat{e}_{2\sigma}}{2} \right) \cos \left(-2\theta_{\sigma} \right) \qquad (34)a$$

$$e^{\sigma}_{2m} = \left(\frac{\hat{e}_{1\sigma} + \hat{e}_{2\sigma}}{2} \right) - \left(\frac{\hat{e}_{1\sigma} - \hat{e}_{2\sigma}}{2} \right) \cos \left(-2\theta_{\sigma} \right) \qquad (34)b$$

$$e^{\sigma}_{12M} = - \left(\frac{\hat{e}_{1\sigma} - \hat{e}_{2\sigma}}{2} \right) \sin \left(-2\theta_{\sigma} \right) \qquad (34)c$$

and
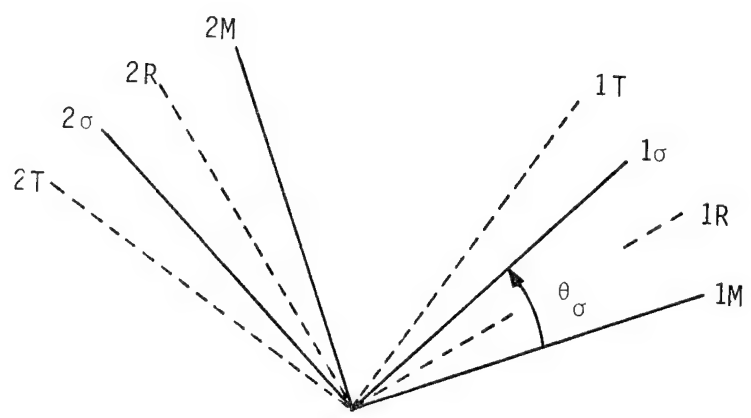
Fig. 11 Four of the coordinate systems discussed and the definition of θ_σ.

$$e_{1\sigma}, e_{2\sigma} = \left(\frac{\hat{e}_{1M} + \hat{e}_{2M}}{2}\right) \pm \sqrt{\left(\frac{e_{1M}^{\sigma} - e_{2M}^{\sigma}}{2}\right)^2 + (e_{12M}^{\sigma})^2} \quad (34)d$$

$$\tan(2\theta_\sigma) = \frac{2e_{12M}^{\sigma}}{e_{1M}^{\sigma} - e_{2M}^{\sigma}} \quad (34)e$$

Hypothesis Regarding Dielectric Effects Due to Applied Loads

It will be hypothesised here that the dielectric effects due to applied loads can be superimposed onto the residual dielectric effects. Due to the tensorial nature of dielectric effects, the total dielectric tensor can be represented, in the material system, as follows:

$$\begin{Bmatrix} e_{1M}^{T} \\ e_{2M}^{T} \\ e_{12M}^{T} \end{Bmatrix} = \begin{Bmatrix} e_{1M}^{\sigma} \\ e_{2M}^{\sigma} \\ e_{12M}^{\sigma} \end{Bmatrix} + \begin{Bmatrix} e_{1M}^{R} \\ e_{2M}^{R} \\ e_{12M}^{R} \end{Bmatrix} \quad (35)$$

It has been hypothesized by previous investigators [3,4] that the dielectric tensor due to the applied loads is related to the applied stress by the following orthotropic relation:

$$\begin{Bmatrix} e_{1M}^{\sigma} \\ e_{2M}^{\sigma} \\ e_{12M}^{\sigma} \end{Bmatrix} = \begin{bmatrix} q_{11} & q_{12} & 0 \\ q_{21} & q_{22} & 0 \\ 0 & 0 & q_{66} \end{bmatrix} \begin{Bmatrix} \sigma_1 \\ \sigma_2 \\ \sigma_{12} \end{Bmatrix}. \quad (36)$$

The q_{ij} are constants for a given material and can be thought of as the material's stress-dielectric coefficients. Equation 35, representing the total dielectric tensor in the material system, can be written as

34

$$
\begin{Bmatrix} e_{1M}^T \\ e_{2M}^T \\ e_{12M}^T \end{Bmatrix} = \begin{bmatrix} q_{11} & q_{12} & 0 \\ q_{21} & q_{22} & 0 \\ 0 & 0 & q_{66} \end{bmatrix} \begin{Bmatrix} \sigma_1 \\ \sigma_2 \\ \sigma_{12} \end{Bmatrix} + \begin{Bmatrix} e_{1M}^R \\ e_{2M}^R \\ e_{12M}^R \end{Bmatrix} \quad . \quad (37)
$$

Several approaches can be taken to check the validity of eq. 37 or to check the consequences of it, assuming it is valid. It is on the basis of eq. 36 that much of the work in orthotropic photoelasticity has been done to date. The hypothesis represented by eq. 36 has been termed ad hoc [5] because there is no a priori reason to believe that orthotropic elastic behavior implies orthotropic optical behavior. The crux of the discussion about the validity of eq. 36 is whether or not it correlates with experimental observation. Equation 35 has not been verified to any great extent. Previous investigators [6,7,8,9] have mentioned residual birefringent effects. However eq. 35, and the just-derived relations involving the residual dielectric tensor, treat residual effects with more formalism.

Consequences of the Hypothesized Relation

Since, as stated previously, standard polariscopes measure relative retardation, Δ, it is useful to relate the retardation Δ to the applied stresses via the just stated hypotheses. This is done by using eq. 37 in eq. 22, the expression for Δ. In the present context the dielectric properties in eq. 22 refer to the total dielectric properties, i.e. residual effects plus mechanically induced effects. Thus eq. 22 becomes

$$
\Delta = \frac{2\pi h}{\lambda n_{ave}^T} \frac{\Delta e^T}{e_o} \tag{38}
$$

35

with

$$\Delta e^T = \frac{1}{2} \sqrt{(e_{1M}^T - e_{2M}^T)^2 + (2e_{12M}^T)^2} \quad , \tag{39}a$$

$$n_{ave}^T = \sqrt{\frac{e_{ave}^T}{e_0}} \tag{39}b$$

and

$$e_{ave}^T = \frac{e_{1M}^T + e_{2M}^T}{2} \quad . \tag{39}c$$

Since e_{ave}^T is related to the trace of the total dielectric tensor, e_{ave}^T is independent of coordinate system. To use eq. 37 in eq. 39, it is useful to write the residual dielectric effects in eq. 37 in terms of principal residual values. This can be done using eqs. 28a - 28c. Doing this, eq. 37 becomes

$$
\left\{ \begin{array}{c} e_{1M}^T \\ \\ e_{2M}^T \\ \\ e_{12M}^T \end{array} \right\} = \left[\begin{array}{ccc} q_{11} & q_{12} & 0 \\ \\ q_{21} & q_{22} & 0 \\ \\ 0 & 0 & q_{66} \end{array} \right] \left\{ \begin{array}{c} \sigma_1 \\ \\ \sigma_2 \\ \\ \tau_{12} \end{array} \right\} + \left\{ \begin{array}{c} (\frac{\hat{e}_{1R} + \hat{e}_{2R}}{2}) + (\frac{\hat{e}_{1R} - \hat{e}_{2R}}{2}) \cos(-2\theta_R) \\ \\ (\frac{\hat{e}_{1R} + \hat{e}_{2R}}{2}) - (\frac{\hat{e}_{1R} - \hat{e}_{2R}}{2}) \cos(-2\theta_R) \\ \\ - (\frac{\hat{e}_{1R} - \hat{e}_{2R}}{2}) \sin(-2\theta_R) \end{array} \right\} \quad . \tag{40}
$$

Substituting eq. 40 into eq. 39 and then substituting those results into eq. 38 leads to an expression for Δ, namely

$$\Delta = \frac{\pi h}{\lambda n_{ave}^T e_0} \sqrt{\{(q_{11} - q_{21})\sigma_1 - (q_{22} - q_{12})\sigma_2 + (\hat{e}_{1R} - \hat{e}_{2R}) \cos(2\theta_R)\}^2}$$

$$\overline{+ \{2q_{66}\tau_{12} + (\hat{e}_{1R} - \hat{e}_{2R}) \sin(2\theta_R)\}^2} \tag{41}$$

With a darkfield polariscope arrangement, for example, fringes occur when

$$\frac{\Delta}{2} = 0, \pi, 2\pi, 3\pi, \ldots, N\pi \qquad (42)$$

N an integer.

Combining eqs. 41 and 42 gives the condition for integer fringe orders in a darkfield polariscope due to applied loads and residual effects. Specifically, integer order fringes occur when

$$\frac{h}{2\lambda n_{ave}^T e_o} \sqrt{\{(q_{11} - q_{21})\sigma_1 - (q_{22} - q_{12})\sigma_2 + (\hat{e}_{1R} - \hat{e}_{2R}) \cos(2\theta_R)\}^2}$$

$$\overline{+ \{2q_{66}\tau_{12} + (\hat{e}_{1R} - \hat{e}_{2R}) \sin(2\theta_R)\}^2} = N_T$$

$$(43)$$

N_T being the integer fringe order. The subscript T has been added to N to signify it is the fringe order associated with total birefringence, residual and mechanically induced. Practically speaking, N_T does not have to be an integer. Standard polariscopes are capable of displaying any fringe order, fractional or integer. In any case, the residual effects and the applied load effects combine in the manner as indicated by the left hand side of eq. 43 to produce the observed fringe order. This is a direct consequence of eq. 37 and the optics of a darkfield polariscope. Knowing the material constants q_{ij} and the residual effects, eq. 43 can be used to determine the fringe order produced by a certain stress state. It is important to note that in eq. 43 the five optical constants q_{ij} appear as differences in two of the coefficients of stress. In reality, only $(q_{11} - q_{21})$, $(q_{12} - q_{22})$, and q_{66} are neces-

37

sary for determining the effects of applied stress on fringe order. This constitutes three quantities instead of five. In addition, only the difference in principal values of the residual dielectric tensor is involved, along with the principal residual directions.

It is legitimate at this point to be concerned with the fact that to use eq. 43, such unfamiliar physical constants as the average total index of refraction, n_{ave}^T, the stress-dielectric coefficients, q_{ij}, the residual dielectric effects, etc. have to be determined. In the next section many of these constants will be lumped together into stress-optic coefficients and another tensor called the birefringent tensor. Then instead of having to be concerned with all of the quantities in eq. 43, concern will be with, for example, the slopes of the fringe order vs. applied stress relations.

Birefringence Tensor

To examine other consequences of eq. 37, it is convenient to define several quantities which can be thought of as components of another tensor. These components combine tensorially to produce the fringe order N_T. Define

$$\begin{Bmatrix} N_{1M}^{\sigma} \\ N_{2M}^{\sigma} \\ N_{12M}^{\sigma} \end{Bmatrix} \equiv \frac{h}{2\lambda n_{ave}^T e_o} \begin{Bmatrix} e_{1M}^{\sigma} \\ e_{2M}^{\sigma} \\ e_{12M}^{\sigma} \end{Bmatrix} \tag{44}$$

or

$$\begin{Bmatrix} N_{1M}^{\sigma} \\ N_{2M}^{\sigma} \\ N_{12M}^{\sigma} \end{Bmatrix} = \begin{bmatrix} a_{11} & a_{12} & 0 \\ a_{21} & a_{22} & 0 \\ 0 & 0 & a_{66} \end{bmatrix} \begin{Bmatrix} \sigma_1 \\ \sigma_2 \\ \tau_{12} \end{Bmatrix} \tag{45}$$

where $a_{ij} \equiv \dfrac{h}{2\lambda n_{ave}^T e_o} \; q_{ij}$ $i, j = 1, 2, 6.$ (46)

Also define

$$\hat{N}_{1R} \equiv \frac{h}{2\lambda n_{ave}^T e_o} \; \hat{e}_{1R} \text{ and } \hat{N}_{2R} \equiv \frac{h}{2\lambda n_{ave}^T e_o} \; \hat{e}_{2R} \; . \quad (47)$$

The various quantities N have been called components of the _birefringent_ _tensor_ (as opposed to components of the dielectric tensor). Having particular values of the components N_{1M}^σ, N_{2M}^σ, and N_{12M}^σ is having a particular _state of birefringence._ Using eqs. 46 and 47, eq. 43 becomes

$$N_T = \sqrt{\{(a_{11} - a_{21})\sigma_1 - (a_{22} - a_{12})\sigma_2 + (\hat{N}_{1R} - \hat{N}_{2R})\cos(2\theta_R)\}^2} \quad (48)$$
$$+ \{2a_{66}\tau_{12} + (\hat{N}_{1R} - \hat{N}_{2R})\sin(2\theta_R)\}^2$$

Using eq. 45 this becomes

$$N_T = \sqrt{\{(N_{1M}^\sigma - N_{2M}^\sigma) + (\hat{N}_{1R} - \hat{N}_{2R})\cos(2\theta_R)\}^2}$$
$$+ \{2N_{12M}^\sigma + (\hat{N}_{1R} - \hat{N}_{2R})\sin(2\theta_R)\}^2 \quad (49)$$

This equation indicates that the observed fringe count N_T is due in part to the effect of normal stresses, N_{1M}^σ and N_{2M}^σ, the shear stress, N_{12M}^σ, and the residual birefringence. The equation indicates that the fringe productions due to normal stresses, N_{1M}^σ and N_{2M}^σ, subtract algebraically and the difference is added vectorially to the fringe production due to the shear stress, $2N_{12M}^\sigma$. Residual effect fringe production adds algebraically to the fringe production due to applied load. Equation 49 states that all effects contribute to the observed fringe. In standard polariscopes, the individual components, i.e. N_{1M}^σ, N_{2M}^σ,....etc., cannot be observed. Only the total effect, N_T, is observable. In a sense,

39

then, the quantities N_{1M}^σ, N_{2M}^σ,...etc. are simply convenient abstractions which essentially replace the dielectric tensor.

Mohr's Circle of Birefringence

Equation 49 has an interesting physical interpretation. Consider, for the moment, the case where the residual effects are zero. Equation 49 becomes

$$N_T = \sqrt{\{N_{1M}^\sigma - N_{2M}^\sigma\}^2 + \{2N_{12M}^\sigma\}^2} \tag{50}$$

If a Mohr's circle is constructed with N_{1M}^σ and N_{2M}^σ on the horizontal axis (i.e., where σ_x and σ_y are located on Mohr's circle of stress) and N_{12M}^σ on the vertical axis, then the state of birefringence due to the applied load can be located on these axes. The state of birefringence is shown as closed circles on fig. 12a. By geometry, the quantity

$$\sqrt{(\frac{N_{1M}^\sigma - N_{2M}^\sigma}{2})^2 + (N_{12M}^\sigma)^2} \tag{51}$$

is the radius of the circle. Then twice the quantity in eq. 51 is the diameter of the circle. Thus, by eq. 50, with no residual effects present, the diameter of Mohr's circle of birefringence is the fringe order, N_T, seen in a polariscope. Equation 50 is the form originally introduced by Sampson [10] for utilizing the idea of a birefringent tensor. He essentially postulated eq. 50 and worked from there. Figure 12b shows other important aspects of Mohr's circle of birefringence.

A Mohr's circle interpretation can be implied even in the presence of residual birefringence. This circle is Mohr's circle of total birefringence. Referring to eq. 40, define
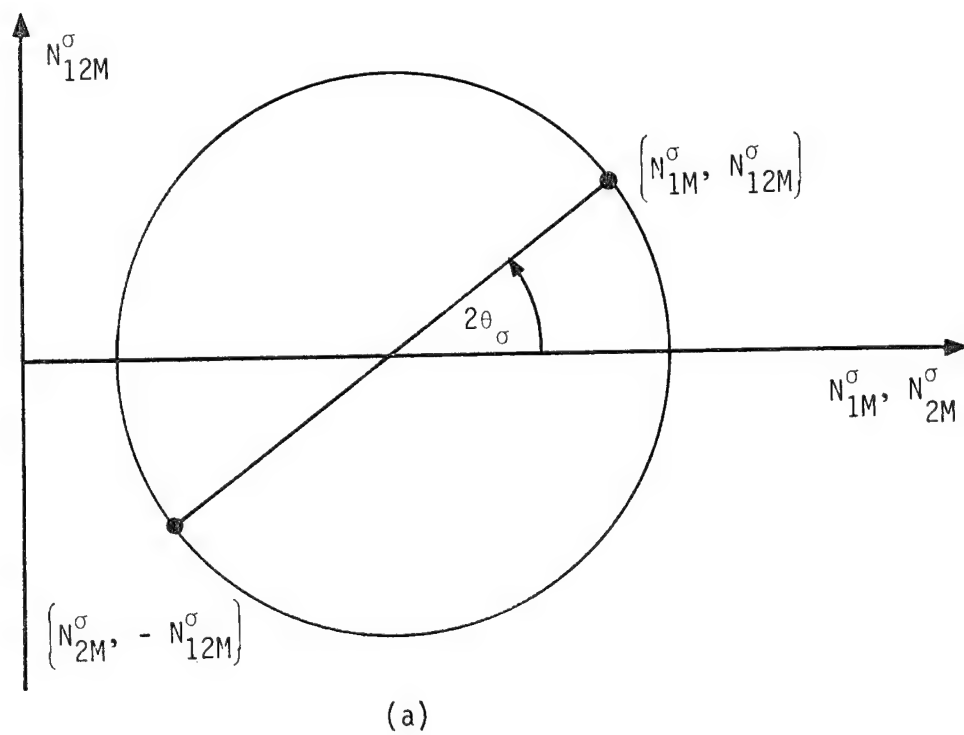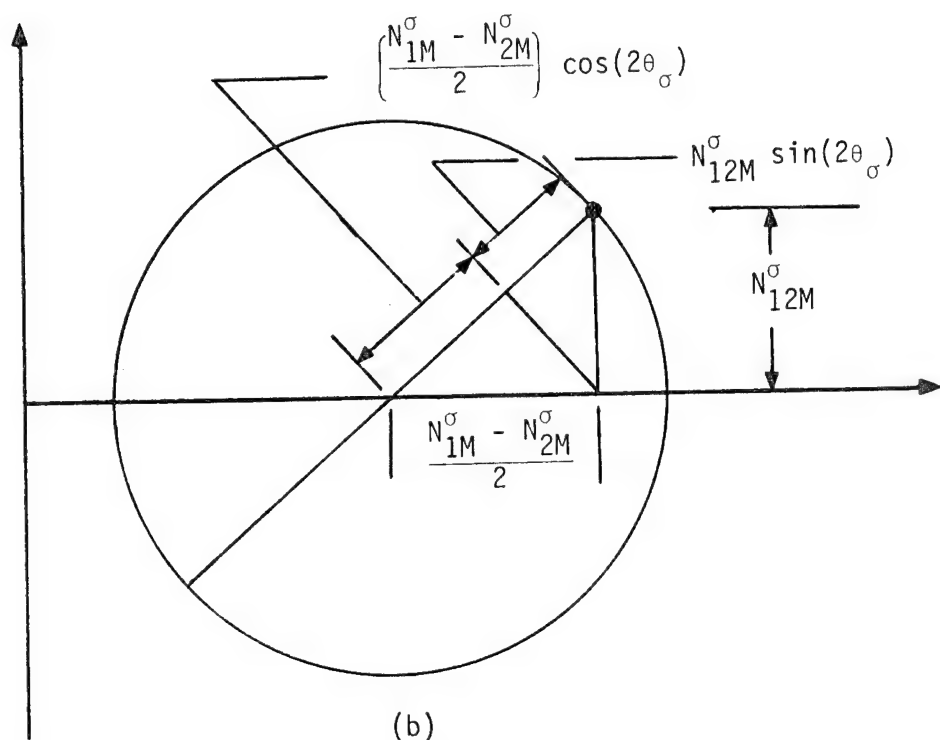
Fig. 12 Mohr's circle of birefringence (no residual effects)

41

$$\begin{Bmatrix} N_{1M}^T \\ N_{2M}^T \\ N_{12M}^T \end{Bmatrix} = \frac{h}{2\lambda n_{ave}^T e_o} \begin{Bmatrix} e_{1M}^T \\ e_{2M}^T \\ e_{12M}^T \end{Bmatrix} . \tag{52}$$

Construct Mohr's circle by locating N_{1M}^T and N_{2M}^T on the horizontal axis and N_{12M}^T on the vertical axis. The diameter of the circle is

$$\sqrt{(N_{1M}^T - N_{2M}^T)^2 + (2N_{12M}^T)^2} . \tag{53}$$

Using the definitions of eqs. 45-47 and substituting into eq. 53, the diameter expression becomes

$$\sqrt{\{(N_{1M}^\sigma - N_{2M}^\sigma) + (\hat{N}_{1R} - \hat{N}_{2R})\cos(2\theta_R)\}^2 + \overline{\{2N_{12M}^\sigma + (\hat{N}_{1R} - \hat{N}_{2R})\sin(2\theta_R)\}^2}} . \tag{54}$$

Thus an interpretation of eq. 49 is that the diameter of Mohr's circle of total birefringence is equal to the total fringe order, N_T, observed in the polariscope. Mohr's circle of total birefringence is illustrated in fig. 13. Because of the connection with Mohr's circle, it is obvious that the observed total fringe order N_T is also equal to the difference in principal values of total birefringence, i.e.

$$N_T \equiv \hat{N}_{1T} - \hat{N}_{2T}, \tag{55}$$

where

$$\hat{N}_{1T} = \frac{h}{2\lambda n_{ave}^T e_o} \hat{e}_{1T} \text{ and } \hat{N}_{2T} = \frac{h}{2\lambda n_{ave}^T e_o} \hat{e}_{2T}. \tag{56}$$

$$\tag{57}$$

42
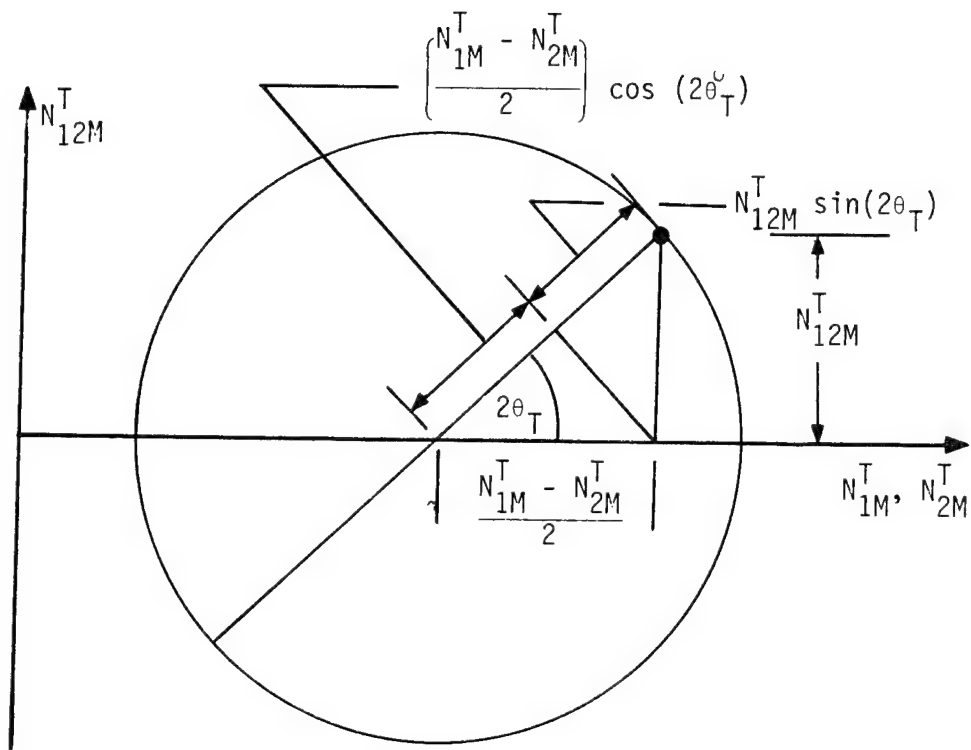
Fig. 13 Mohr's circle of total birefringence.

When there are no applied loads, $N_{1M}^{\sigma} = N_{2M}^{\sigma} = N_{12M}^{\sigma} = 0$. In this case the diameter of Mohr's circle, and the value of the fringe order seen in the polariscope, is $|\hat{N}_{1R} - \hat{N}_{2R}|$. This is the difference in the principal values of birefringence. Also for this no-load case, as will be seen, the isocline observed in the polariscope is θ_R. Thus, the no-load case can be used to calculate several important parameters regarding the material's optical behavior.

Redefinition of Coefficients

If the following definitions are used

$$f_1 = \frac{1}{a_{11} - a_{21}} \tag{58a}$$

$$f_2 = \frac{1}{a_{22} - a_{12}} \tag{58b}$$

$$f_{12} = \frac{1}{a_{66}} \tag{58c}$$

$$N_R \equiv \hat{N}_{1R} - \hat{N}_{2R} , \tag{59}$$

eq. 48 becomes

$$N_T = \sqrt{\{\frac{\sigma_1}{f_1} - \frac{\sigma_2}{f_2} + N_R \cos(2\theta_R)\}^2 + \{\frac{2\tau_{12}}{f_{12}} + N_R \sin(2\theta_R)\}^2} . \tag{60}$$

With no residual effects, eq. 60 becomes

$$N_T = \sqrt{\{\frac{\sigma_1}{f_1} - \frac{\sigma_2}{f_2}\}^2 + \{\frac{2\tau_{12}}{f_{12}}\}^2} . \tag{61}$$

This is another form proposed by Sampson [10]. He introduced the three stress-optic coefficients f_1, f_2, and f_{12}. These coefficients can be determined for a particular material by applying a known stress and observing the fringe order. Specifically, if $\sigma_1 = \sigma$, $\sigma_2 = 0$, and $\tau_{12} = 0$, then f_1 can be computed. If $\sigma_1 = 0$, $\sigma_2 = \sigma$, and $\tau_{12} = 0$, then f_2 can be determined. If $\sigma_1 = 0$, $\sigma_2 = 0$, and $\tau_{12} = \tau$, then f_{12} can be calculated. Alternatively, knowing f_1 and f_2 and performing an off-axis tensile test, f_{12} can be computed.

For the case of residual birefringence, calibration of the material is more involved. With a no-load condition, N_R and θ_R can be determined. Then with various known stress states, f_1, f_2, and f_{12} can be computed.

For a general case, knowing N_R, θ_R, f_1, f_2, and f_{12}, the fringe order can be predicted from a given stress state, σ_1, σ_2, and τ_{12}, using eq. 60. This is exactly what will be done later to predict the fringe patterns in the disk.

In addition, for a given stress state, the optical isocline, θ_T, can be predicted. Using eqs. 31e and 35, $\tan(2\theta_T)$ becomes

$$\tan(2\theta_T) = \frac{2e^{\sigma}_{12M} + 2e^{R}_{12M}}{(e^{\sigma}_{1M} - e^{\sigma}_{2M}) + (e^{R}_{1M} - e^{R}_{2M})} \qquad (62)$$

With the aid of eq. 28a-c this becomes

$$\tan(2\theta_T) = \frac{2e^{\sigma}_{12M} + (\hat{e}_{1R} - \hat{e}_{2R})\sin(2\theta_R)}{(e^{\sigma}_{1M} - e^{\sigma}_{2M}) + (\hat{e}_{1R} - \hat{e}_{2R})\cos(2\theta_R)} \ . \qquad (63)$$

Multiplying the numerator and denominator by $\dfrac{h}{2\lambda n_{ave}e_o}$ and using eqs. 44 and 47 results in

45

$$\tan(2\theta_T) = \frac{2N^\sigma_{12M} + (\hat{N}_{1R} - \hat{N}_{2R}) \sin(2\theta_R)}{(N^\sigma_{1M} - N^\sigma_{2M}) + (\hat{N}_{1R} - \hat{N}_{2R}) \cos(2\theta_R)} \,. \tag{64}$$

Using eqs. 45 leads to

$$\tan(2\theta_T) = \frac{2a_{66}\tau_{12} + (\hat{N}_{1R} - \hat{N}_{2R}) \sin(2\theta_R)}{(a_{11} - a_{21})\sigma_1 - (a_{22} - a_{12})\sigma_2 + (\hat{N}_{1R} - \hat{N}_{2R}) \cos(2\theta_R)} \,.$$

$$\tag{65}$$

The definitions of eqs. 58 and 59 produce the final form, namely,

$$\tan(2\theta_T) = \frac{2\,\dfrac{\tau_{12}}{f_{12}} + N_R \sin(2\theta_R)}{\dfrac{\sigma_1}{f_1} - \dfrac{\sigma_2}{f_2} + N_R \cos(2\theta_R)} \,. \tag{66}$$

This equation relates the optical isocline to the residual effects, the material constants f_1, f_2, and f_{12}, and the stress state. The optical isocline is the parameter observed in the polariscope. It is important to note that the optical isocline is a function of the stress level! Doubling each stress, for example, changes θ_T. The mechanical isocline, as θ_σ is often called, can be related to stress from eq. 66 by setting residual effects equal to zero. The result is

$$\tan(2\theta_\sigma) = \frac{2\,\dfrac{\tau_{12}}{f_{12}}}{\dfrac{\sigma_1}{f_1} - \dfrac{\sigma_2}{f_2}} \,. \tag{67}$$

In the presence of residual birefringence, θ_σ will never be observed. Its existence can only be hypothesized. In the absence of residual effects, the mechanical and optical isocline coincide. The mechanical

46

isocline is not a function of stress level. Doubling each stress has no effect on $\tan(2\theta_\sigma)$.

Finally, with no applied stress eq. 66 indicates

$$\tan(2\theta_T) = \frac{N_R \sin(2\theta_R)}{N_R \cos(2\theta_R)} = \tan(2\theta_R) \qquad (68)$$

or, as stated earlier,

$$\theta_T = \theta_R. \qquad (69)$$

The observed isocline with no applied load is the residual isocline, θ_R.

With the material calibrated for a given stress state, the observed isocline can be predicted using eq. 66. This prediction, along with the prediction of N_T, will be done for the disk.

Determining Stresses from Optical Data

To this point the equations have been manipulated so that if the stress state is known, the optical response of the material can be determined. Specifically, eq. 60 relates the observed fringe order with the stress state and residual birefringence. Equation 66 relates the observed isocline to the stress state. To determine the stress state from the optical data, the equations must be used differently. As with isotropic photoelasticity, an auxiliary condition such as the shear difference method or a finite-difference form of the two plane-stress equilibrium equations is needed to completely determine the stress state. However, photoelastic data from polariscope observations provides part of the needed information. There are several ways to

47

determine just what information is available from a polariscope in the way of the state of stress in fiber-reinforced composites. The approach taken here starts with eq. 37.

In eq. 37, subtract the 2nd equation from the 1st and multiply the 3rd equation by 2. The result is, with a slight rearrangement

$$(q_{11} - q_{21})\sigma_1 - (q_{22} - q_{12})\sigma_2 = (e_{1M}^T - e_{2M}^T) - (e_{1M}^R - e_{2M}^R) \qquad (70)$$

$$2q_{66}\tau_{12} = 2e_{12M}^T - 2e_{12M}^R . \qquad (71)$$

Using eqs. 28a-c and 31a-c in the right hand sides lead to

$$(q_{11} - q_{21})\sigma_1 - (q_{22} - q_{12})\sigma_2 = (\hat{e}_{1T} - \hat{e}_{2T}) \cos(2\theta_R) - (\hat{e}_{1R} - \hat{e}_{2R}) \cos(2\theta_R) \qquad (72)$$

$$2q_{66}\tau_{12} = (\hat{e}_{1T} - \hat{e}_{2T}) \sin(2\theta_T) - (\hat{e}_{1R} - \hat{e}_{2R}) \sin(2\theta_R) \qquad (73)$$

It is obvious at this point that multiplying any dielectric tensor quantity by $\dfrac{h}{2\lambda n_{ave}^T e_0}$ defines a similar birefringent tensor quantity. Thus multiplying both sides of eqs. 72 and 73 by $\dfrac{h}{2\lambda n_{ave}^T e_0}$ and using eqs. 46, 47, and 55-59 results in

$$\frac{\sigma_1}{f_1} - \frac{\sigma_2}{f_2} = N_T \cos(2\theta_T) - N_R \cos(2\theta_R) \qquad (74)$$

and

$$\frac{\tau_{12}}{f_{12}} = \frac{N_T}{2} \sin(2\theta_T) - \frac{N_R}{2} \sin(2\theta_R) . \qquad (75)$$

For isotropic photoelasticity, with no residual effects,

48

$$f_1 = C = f_2 = f_{12}, \qquad (76)$$

and

$$N_R = 0 = \theta_R, \qquad (77)$$

C being the material's stress-optic coefficient. Then eqs. 74 and 75 simplify to

$$\sigma_x - \sigma_y = C \ N \cos(2\theta) \qquad (78)$$

$$\tau_{xy} = \frac{CN}{2} \sin(2\theta) \ , \qquad (79)$$

where the x-y system has been substituted for the 1-2 material system. These are the classical equations of isotropic photoelasticity.

Equations 74 and 75 indicate that to determine the stress state from the optical data, the difference in the principal values of residual birefringence, N_R, and the direction of residual birefringence, θ_R, must be known. As stated previously, both these quantities can be determined in a polariscope with a no-load condition.

Transformation of Equations to Global x-y System

In reality, it is not always convenient to reference the stresses, the residual effects, and the material constants to the material system. Equations 74 and 75 can be transformed to a global x-y system which makes an angle of ϕ with the 1M-2M system as shown previously. The angle ϕ is positive as measured counter-clockwise from +x axis to the +1M axis. With this definition of ϕ, the stresses in the material system are related to the stresses in the x-y system as follows:

49

$$\begin{Bmatrix} \sigma_1 \\ \sigma_2 \\ \tau_{12} \end{Bmatrix} = \begin{bmatrix} \cos^2\phi & \sin^2\phi & 2\sin\phi\cos\phi \\ \sin^2\phi & \cos^2\phi & -2\sin\phi\cos\phi \\ -\sin\phi\cos\phi & \sin\phi\cos\phi & (\cos^2\phi - \sin^2\phi) \end{bmatrix} \begin{Bmatrix} \sigma_x \\ \sigma_y \\ \tau_{xy} \end{Bmatrix}. \quad (80)$$

Substituting for σ_1, σ_2, and τ_{12} in eqs. 74 and 75 results in

$$\frac{\cos^2\phi\ \sigma_x + \sin^2\phi\ \sigma_y + 2\sin\phi\cos\phi\ \tau_{xy}}{f_1} -$$

$$\frac{\sin^2\phi\ \sigma_x + \cos^2\phi\ \sigma_y - 2\sin\phi\cos\phi\ \tau_{xy}}{f_2} = N_T \cos(2\theta_T) \quad (81)$$

$$- N_R \sin(2\theta_R)$$

and

$$\frac{-\sin\phi\cos\phi\ \sigma_x + \sin\phi\cos\phi\ \sigma_y + (\cos^2\phi - \sin^2\phi)\tau_{xy}}{f_{12}} =$$

$$\frac{N_T}{2} \sin(2\theta_T) - \frac{N_R}{2} \sin(2\theta_R) .$$

$$(82)$$

Gathering terms results in

$$\left(\frac{\cos^2\phi}{f_1} - \frac{\sin^2\phi}{f_2}\right)\sigma_x + \left(\frac{\sin^2\phi}{f_1} - \frac{\cos^2\phi}{f_2}\right)\sigma_y +$$

$$(83)$$

$$2\left(\frac{1}{f_1} + \frac{1}{f_2}\right) \sin\phi\cos\phi\ \tau_{xy} = N_T \cos(2\theta_T) - N_R \cos(2\theta_R) ,$$

and

$$\left(\frac{-\sin\phi\cos\phi}{f_{12}}\right)\sigma_x + \left(\frac{\sin\phi\cos\phi}{f_{12}}\right)\sigma_y + \left(\frac{\cos^2\phi - \sin^2\phi}{f_{12}}\right)\tau_{xy} =$$

$$(84)$$

$$\frac{N_T}{2} \sin(2\theta_T) - \frac{N_R}{2} \sin(2\theta_R) .$$

If the following definitions are made:

$$\frac{1}{C_1} = \left(\frac{\cos^2\phi}{f_1} - \frac{\sin^2\phi}{f_2}\right) \tag{85)a}$$

$$\frac{1}{C_2} = \left(\frac{\cos^2\phi}{f_2} - \frac{\sin^2\phi}{f_1}\right) \tag{85)b}$$

$$\frac{1}{C_3} = 2\left(\frac{1}{f_1} + \frac{1}{f_2}\right) \sin\phi \cos\phi \tag{85)c}$$

$$\frac{1}{C_4} = - \frac{\sin\phi \cos\phi}{f_{12}} \tag{85)d}$$

$$\frac{1}{C_5} = \frac{\cos^2\phi - \sin^2\phi}{f_{12}} , \tag{85)e}$$

then the stress-optic equations become

$$\frac{\sigma_x}{C_1} - \frac{\sigma_y}{C_2} + \frac{\tau_{xy}}{C_3} = N_T \cos(2\theta_T) - N_R \cos(2\theta_R) \tag{86}$$

and

$$\frac{\sigma_x - \sigma_y}{C_4} + \frac{\tau_{xy}}{C_5} = \frac{N_T}{2} \sin(2\theta_T) - \frac{N_R}{2} \sin(2\theta_R). \tag{87}$$

Couple these with the plane stress equilibrium equations

$$\frac{\partial\sigma_x}{\partial x} + \frac{\partial\tau_{xy}}{\partial y} = 0 \tag{88)a}$$

and

$$\frac{\partial\tau_{xy}}{\partial x} + \frac{\partial\sigma_y}{\partial y} = 0, \tag{88)b}$$

and a complete determination of the stresses is possible. Since ϕ, f_1, f_2, and f_{12} are known, $C_1 - C_5$ are known. Note that the quantities observed in the polariscope, N_T, N_R, θ_T, and θ_R, enter directly, independent of the x-y system. With certain situations, $1/C_4$ and/or $1/C_5$ might

51

be zero. This implies $C_4 = \infty$ and $C_5 = \infty$. If eqs. 86 and 87 are being implemented on a computer, it is more convenient to define

$$\bar{C}_1 = \frac{1}{C_1} \qquad (89)a$$

$$\bar{C}_2 = \frac{1}{C_2} \qquad (89)b$$

$$\bar{C}_3 = \frac{1}{C_3} \qquad (89)c$$

$$\bar{C}_4 = \frac{1}{C_4} \qquad (89)d$$

$$\bar{C}_5 = \frac{1}{C_5} \qquad (89)e$$

so that the governing equtions become

$$\bar{C}_1 \, \sigma_x - \bar{C}_2 \, \sigma_y + \bar{C}_3 \, \tau_{xy} = N_T \cos(2\theta_T) - N_R \cos(2\theta_R) \qquad (90)$$

$$\bar{C}_4 \, \sigma_x - \bar{C}_4 \, \sigma_y + \bar{C}_5 \, \tau_{xy} = \frac{N_T}{2} \sin(2\theta_T) - \frac{N_R}{2} \sin(2\theta_R). \qquad (91)$$

This circumvents having transformed stress-optic properties becoming infinite. It is interesting to note that when $\phi = 45°$, $\bar{C}_5 = 0$ and the equation usually associated with computation of the shear stress, eq. 91, contains no information about the shear. Also note that for certain materials the values of f_1, f_2, and ϕ may combine to produce zero values for $\bar{C}_1$ or $\bar{C}_2$.

In a later section, eqs. 86 and 87 or 90 and 91 will be used to determine the stresses in a disk using the photoelastic data and a finite-difference representation of eqs. 88a and b.

CALIBRATION OF THE MATERIAL

Uniaxial Tests

From the previous section it is clear that to predict N_T and θ_T for a given stress state, the material properties f_1, f_2, f_{12}, N_R and θ_R must be known. Conversely, to predict the stress state from N_T and θ_T, these same material properties must be known. In the present work, following the approach of previous investigators [e.g. 11], an uniaxial loading of three specimens was initially used to determine f_1, f_2, f_{12}. Residual birefringence was not even considered. Thus N_R and θ_R were implicitly set to zero by using equations which didn't account for residual effects, for example eqs. 61 and 67. Three calibration specimens were cut from the same unidirectional material that was cut into a disk for later testing. The calibration specimens were cut as follows: one parallel to the fibers (0°), one perpendicular to the fibers (90°), and one at 45° to the fiber direction. The material used in these experiments was manufactured by the Illinois Institute of Technology Research Institute under contract with the NASA-Langley Research Center [11]. The material had a volume fraction of fibers of 55-60%. This was determined by the acid ingestion method with small pieces from the uniaxial specimens. The specimens were strain gaged, to determine elastic properties, and then subjected to uniaxial loading. The fringe order was observed as the load level was varied. For the tensile specimens, at a given load, the entire specimen should have been in the same state of birefringence. Bending effects and other eccentricities were minimized and felt to be negligible. Yet, during the uniaxial tests it was not possible to have the entire specimen in what was felt to be a uniform state of birefringence. It was slightly lighter or darker toward the

54

top of the specimen or to one side, never 100% uniform. This was particularly true for the higher load levels. Two observers were used to minimize value-judgement biases in deciding at what load level the specimen appeared to exhibit, say, the first fringe. Observations were made while loading, while unloading, on different days, and for different specimen orientations in the loading frame. At the time the testing was being conducted, it was felt local variations in volume fraction or index of refraction properties of the fibers and matrix caused the slight spatial non-uniformities. This idea was reinforced somewhat by the fact that independent of orientation in the loading frame, the same particiular region of the specimen always exhibited slightly different birefringence effects. For the high load levels in the 0° specimen and for all load levels in the 90° and 45° specimen, the material was such that the fibers were clearly at a different level of birefringence than the matrix.

Figure 14 shows the 0° specimen with no load in the lightfield polariscope arrangement. The specimen was 0.625 in. wide, about 12 in. long, and 0.090 in. thick. In the photograph the strain gages are visible, as are the spots of adhesive securing the lead wires. Excessive strain gage adhesive caused the opaqueness in the region around the strain gages. There was a long hair-sized flaw along the length of the specimen at the bottom end. This is visible in the photograph. This flaw did not appear to affect birefringence in the region around it. Light centerlines scribed on the specimen are visible between the two strain gages. The intersection of these lines was chosen as the point at which to count the fringe number. As stated earlier, the birefringent effect was not spatially uniform on the

55
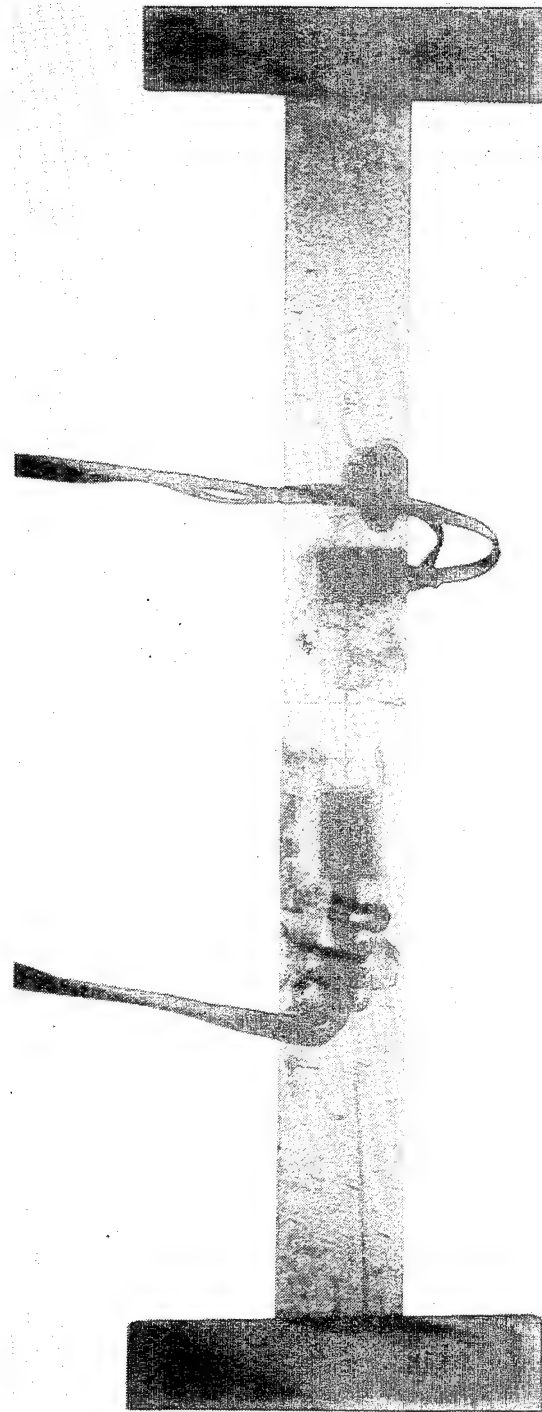
Fig. 14 The 0° tensile specimen in light field with no load.

specimen and so for consistency the fringe count was always evaluated at this same specific point. In the figure the central part of the specimen appears lighter than the upper and lower portions. This is because the polariscope light source and the specimen centerline were aligned on the optical axis of the polariscope and the light source was a bit too intense. This is not related to the aforementioned slight lack of uniformity of birefringence in the specimen. Figure 15 shows the 0° specimen in the light field at what was judged to be a fringe order of 1/2. Figure 16 shows the 1st fringe in the light field. Generally, the eye discerns spatial variation in light intensity differently than photographic film. Because of this, except for the aforementioned difference in intensity in the central portion of the specimen, the birefringence of the specimens in the photographs presented so far has appeared quite uniform and is representative of the uniformity until high load levels were reached. Figure 17 shows fringe order 4 in the dark-field polariscope. The lack of uniformity of the birefringence is evident in this photograph. Bundles of fibers could be clearly distinguished and there was a region in the specimen at the lower left which always had a markedly different level of birefringence. This is the lighter region in the photo. If this had been due to bending effects, there would have been an accompanying light region at the top of the test specimen. The concern with lack of uniform birefringence was as follows: With a spatially varying stress state there is a spatial variation of birefringence. If the stress state is spatially uniform and the photoelastic sensitivity of the material varies spatially, then there is also spatial variation in birefringence. If both the state of stress and the photoelastic sensitivity vary spatially in an unknown manner, it would be

57
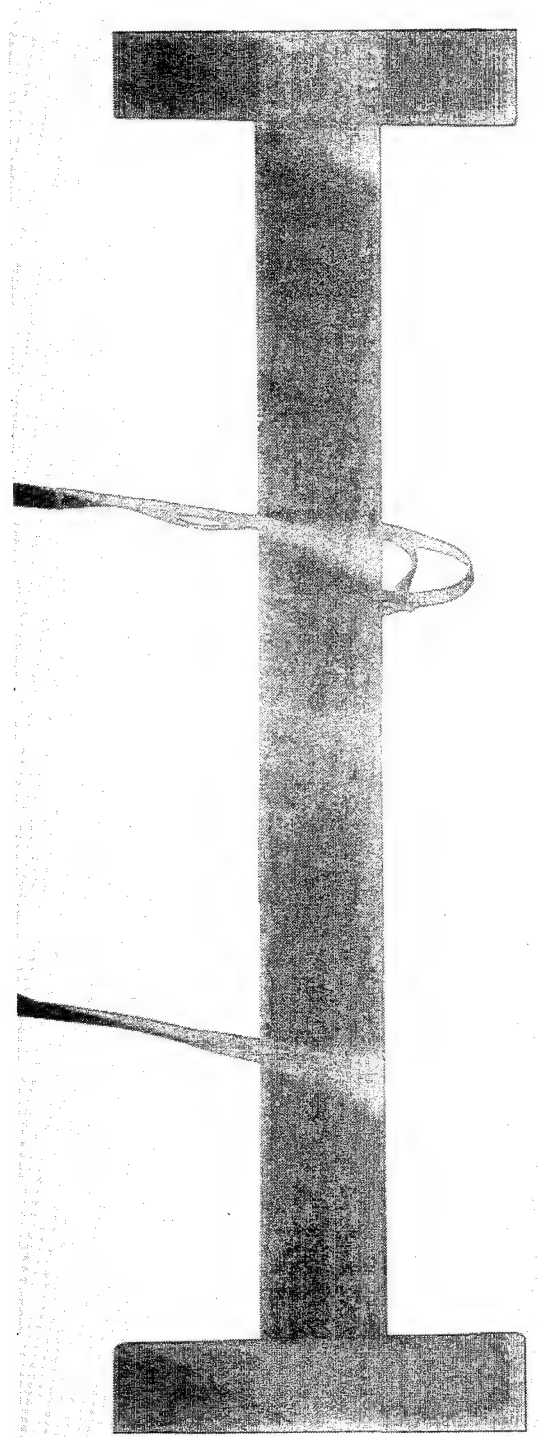
Fig. 15   The 0° tensile specimen in light field with fringe order 1/2.
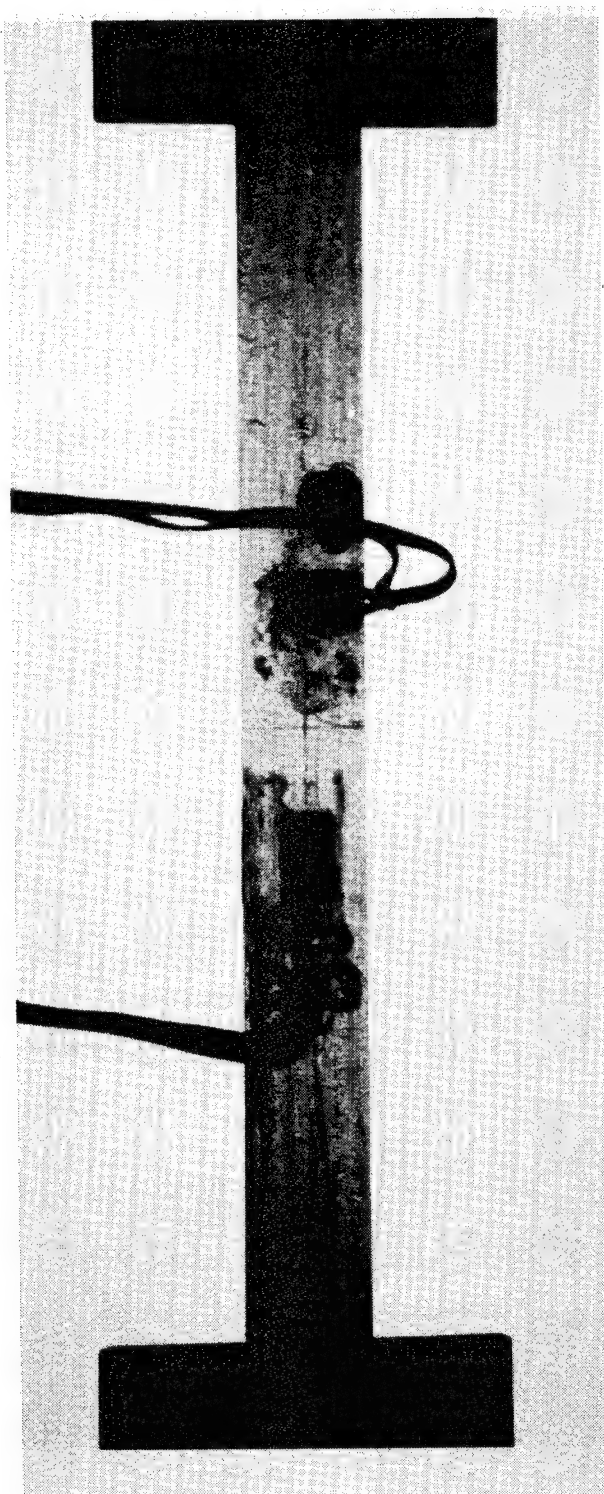
Fig. 16   The 0° tensile specimen in light field with fringe order 1.
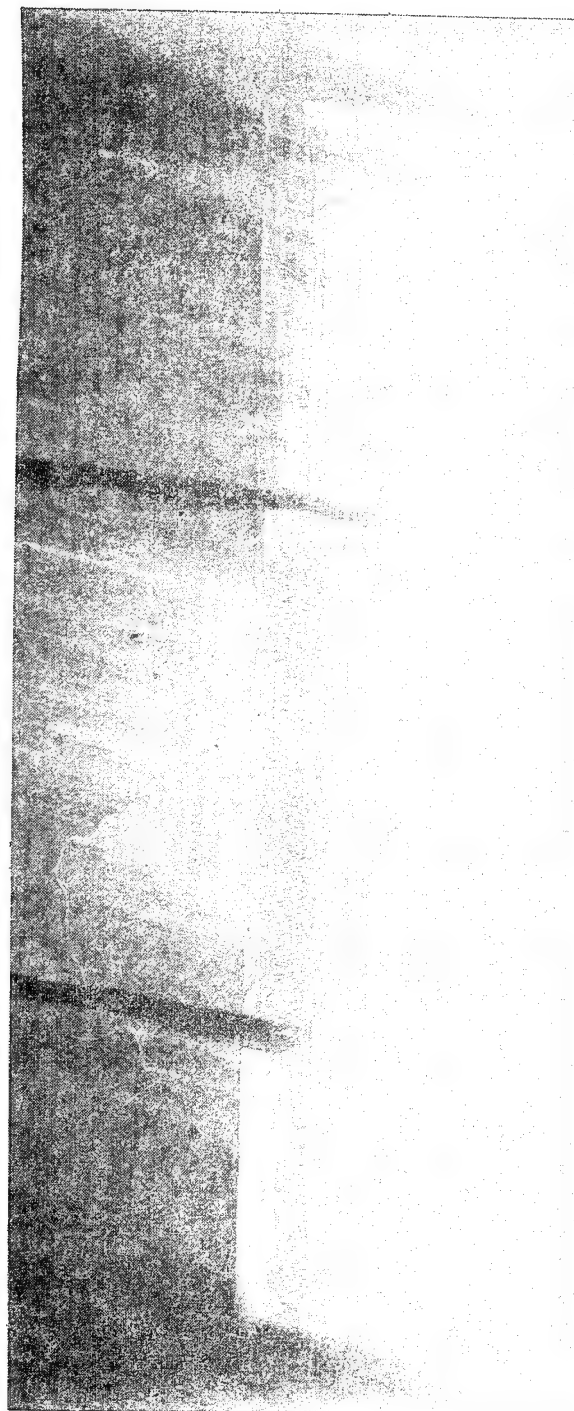
Fig. 17   The 0° tensile specimen in dark field with fringe order 4.

difficult, if not impossible, to extract information regarding the stresses from the fringe pattern. Figure 18 shows the 4th order fringe in the light field. The lighter region at the lower left of the specimen in fig. 17 appears slightly darker in the situation of fig. 18.

Figure 19 shows the fringe order as a function of stress for the 0° specimen. The experimental data are represented by the solid circles. The results of several tests on different days using two observers are lumped together. If it is assumed that there was no initial birefringence in the material, then when $\sigma_1 = 0$, N_T is assumed to be zero. For the case of no initial birefringence, the hypothesis regarding the effect of stress on the dielectric tensor ultimately resulted in eq. 61. With $\sigma_2 = \tau_{12} = 0$ in eq. 61, the relation between N and σ_1 is a simple straight line through the origin. Assuming no initial birefringence, i.e. including the point $\sigma_1 = 0$, $N = 0$, a least-square linear fit of the data from the 0° specimen produced the solid line in fig. 19. This line has a slope of 0.121×10^{-3} fringe/psi and an intercept of 0.08 fringe. The slope led to a value for f_1 of 744 psi/fringe/in. If, as was done after seeing these data along with the data from the 90° specimen, it is assumed that there was some initial birefringence, then when $\sigma_1 = 0$, N_T is not necessarily zero. This nonzero value of N_T at $\sigma_1 = 0$ is really N_R. The value of N_R could be estimated from the data of fig. 19 by not using the points $\sigma_1 = 0$, $N_T = 0$ in the least-squares analysis. Not including this data point resulted in the linear least-squares fit dotted line in fig. 19. The slope of this line is 0.119×10^{-3} fringe/psi and it has an intercept of 0.13 fringe. The slope led to $f_1 = 756$ psi/fringe /in. The calibration thus depended on whether or not initial birefringence was assumed. It should be pointed out that if at the onset of

61
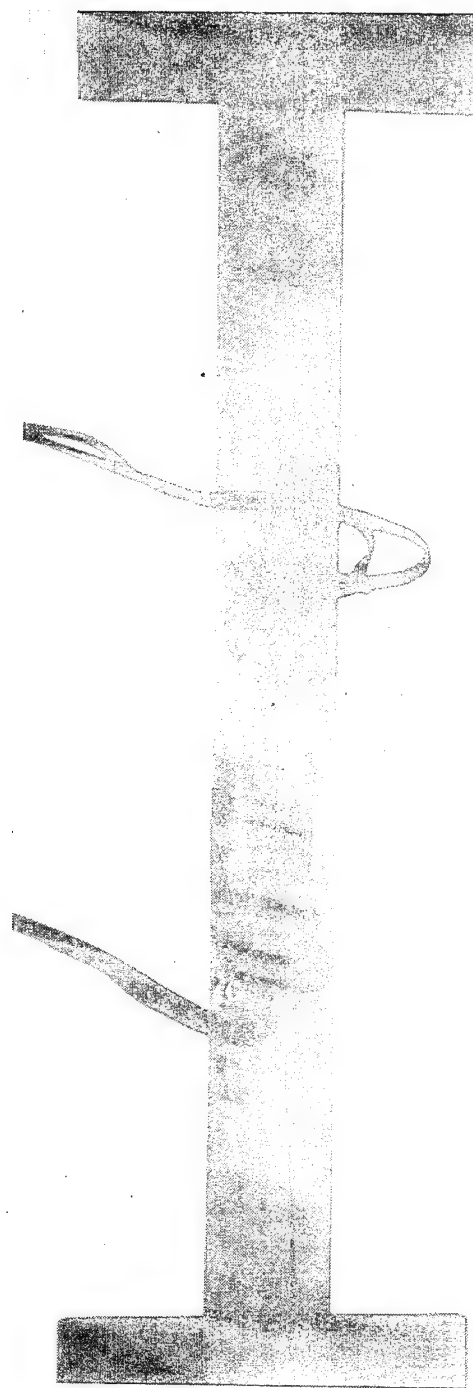
Fig. 18 The 0° tensile specimen in light field with fringe order 4.
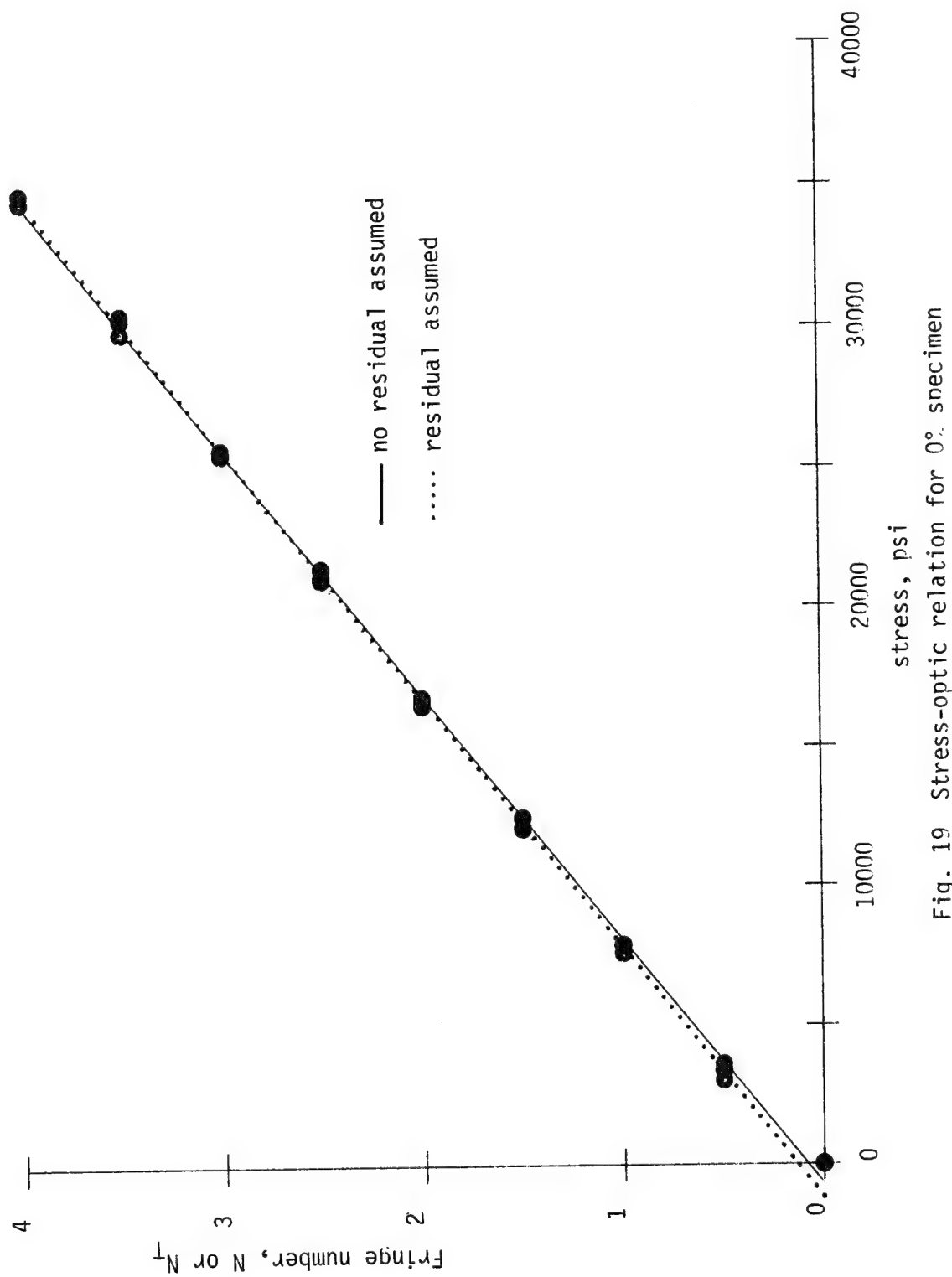
Fig. 19 Stress-optic relation for 0° specimen

63

calibration residual birefringence is suspected, the Tardy method can be used to determine the level.

Figure 20 shows the longitudinal stress-longitudinal strain relation for the 0° specimen while fig. 21 shows the lateral strain-longitudinal strain relation for that specimen. From least-square fits, Young's modulus in the fiber direction, E_1, for the specimen was 5.4 x 10^6 psi and the major Poisson's ratio, ν_{12}, was 0.3.

Testing the 90° specimen was more difficult than testing the 0° specimen. The ultimate tensile strength of the material in the matrix direction was low compared to the tensile strength in the fiber direction. In addition, there was some variation in the ultimate tensile strength in the matrix direction from one point to the next in the material. Thus it was not always possible to obtain the same maximum fringe count in replicate 90° specimens. A 90° specimen was tested in tension until failure and then a portion of the failed specimen was tested in compression. Figure 22 shows the set-up used for testing the 90° specimen in compression. The loading frame was a hand-operated screw device. The 1000 lb. load cell used to measure the compressive load is shown. The specimen was strain gaged and it was restrained from buckling by sandwiching it between two pieces of plexiglas. The specimen was 0.625 in. wide, 3.6 in. long, and 0.90 in. thick. There were holes in the plexiglas restraints so that the restraints were not in contact with the strain gages. The plexiglas was not being compressed even though the specimen was and so the fringes observed in the specimen through the plexiglas were the true fringes in the 90° specimen.

Figure 23 shows the no-load, lightfield state of birefringence in the specimen. Figure 24 shows the 1/2 order, lightfield fringe
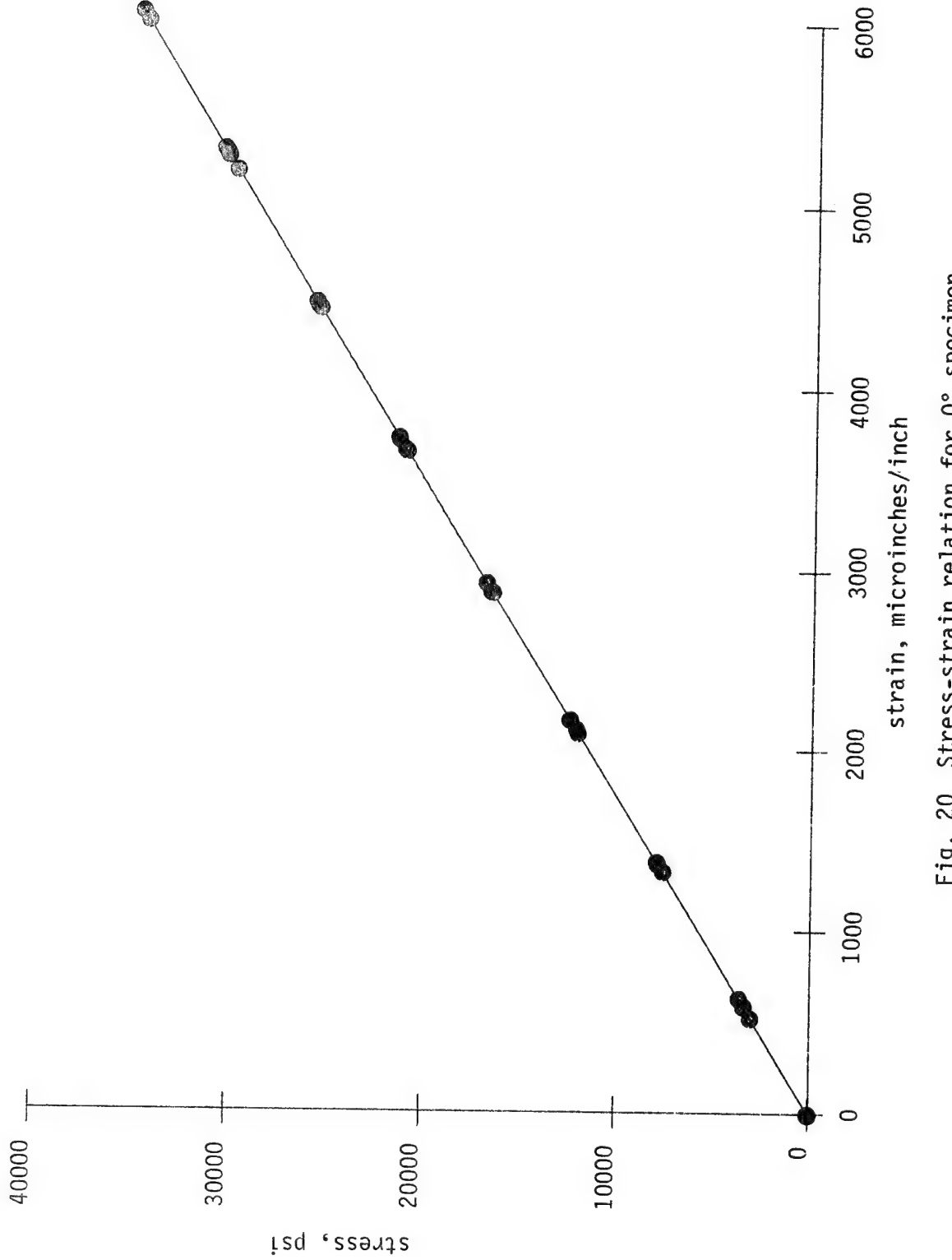
Fig. 20 Stress-strain relation for 0° specimen.
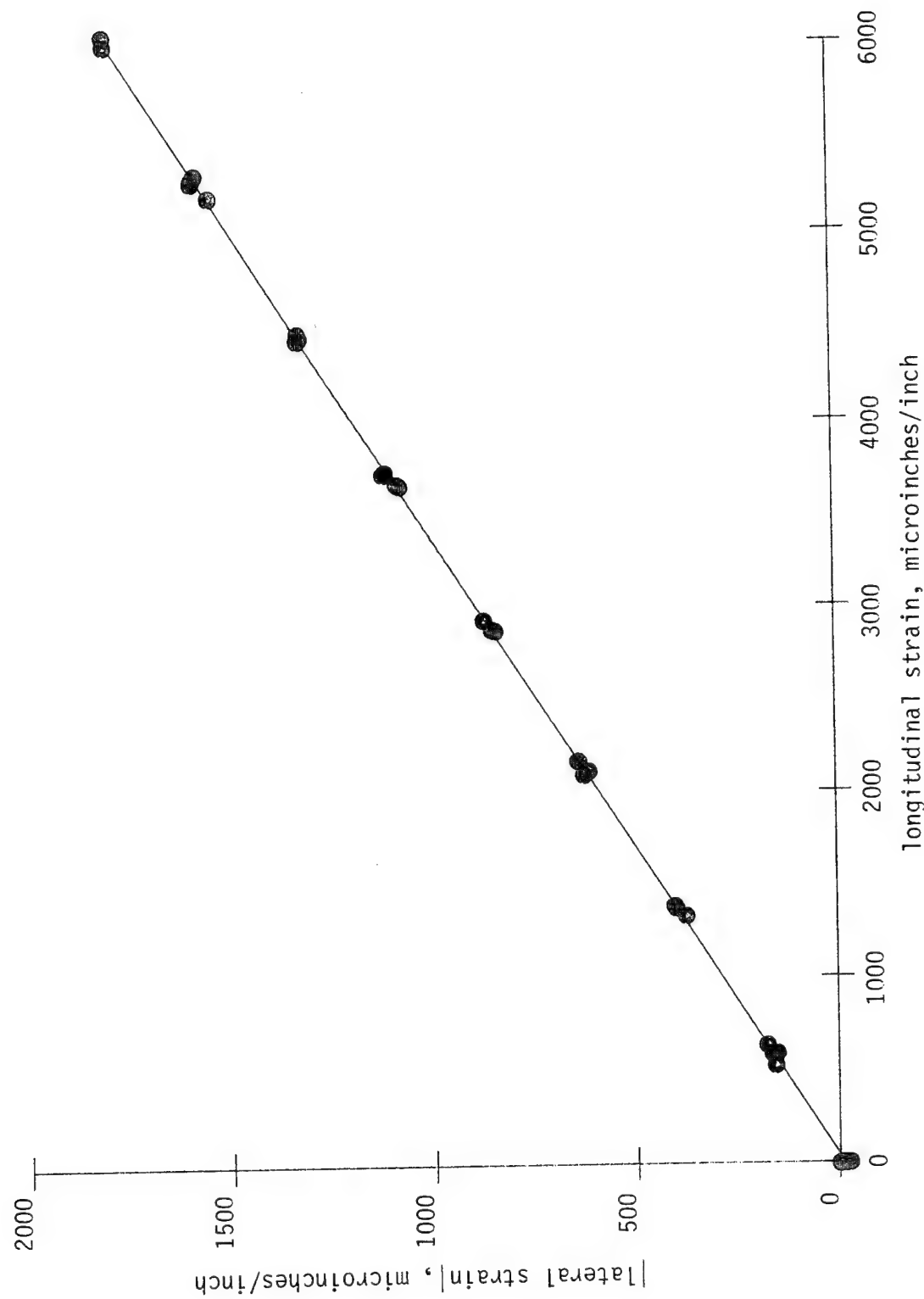
Fig. 21 Poisson's relation for 0° specimen.

longitudinal strain, microinches/inch

|lateral strain|, microinches/inch
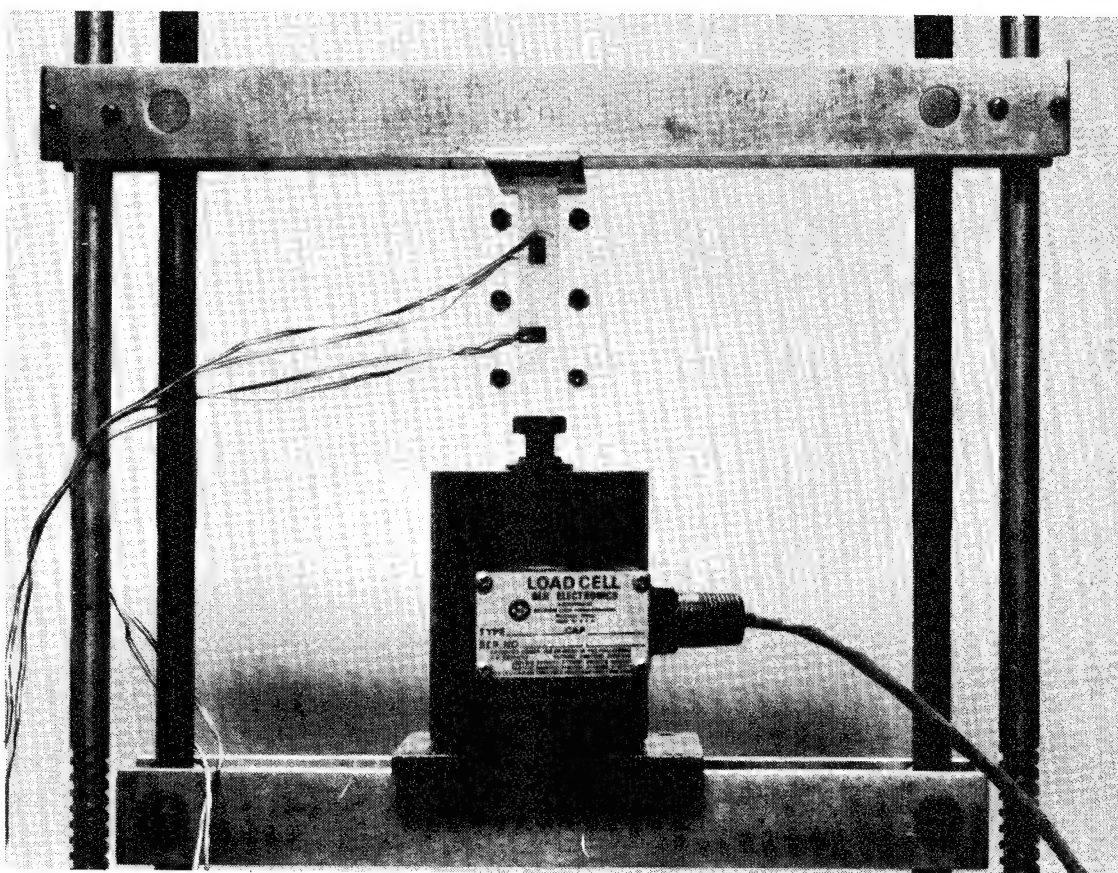
Fig. 22 Fixture for loading 90° specimen in compression.
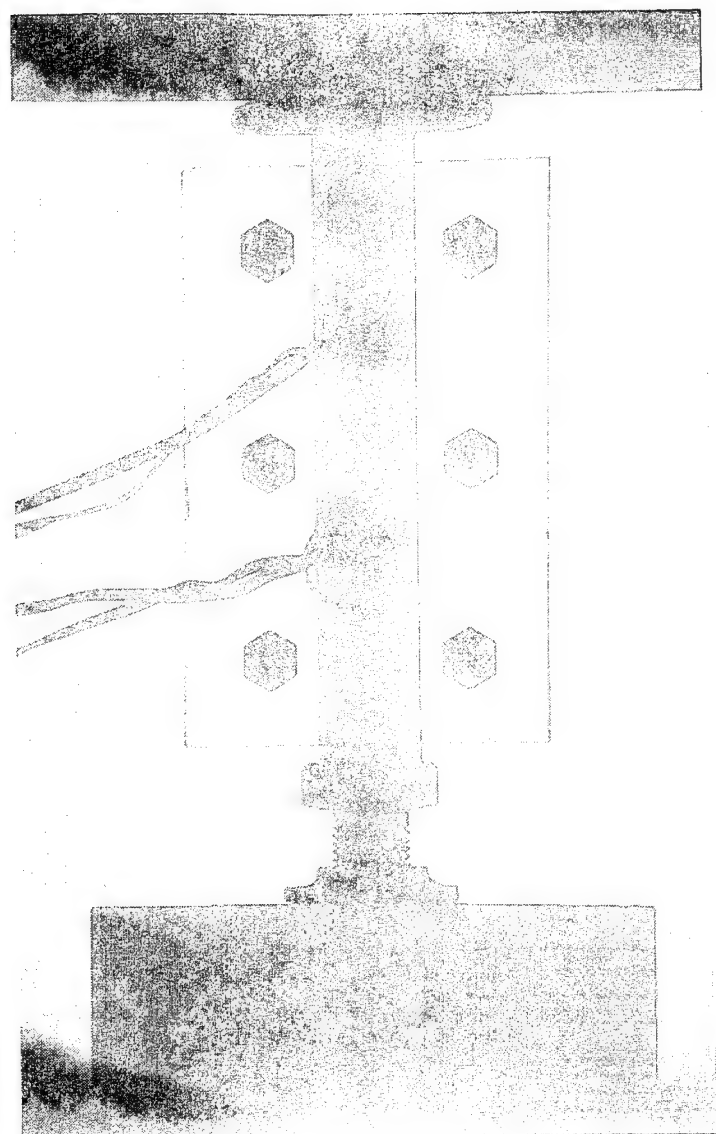
Fig. 23 The 90° compression specimen in light field with no load.

condition. Figure 25 illustrates the darkfield state of birefringence
at a fringe order of about 1.25. The spatial nonuniformity of the bire-
fringence is quite evident here, with nonuniformity both widthwise and
lengthwise. As one moves from the top of the specimen toward the bot-
tom, the image of the birefringence is darker near the centerline of the
specimen than it is near the edges. This indicates the center of the
specimen was at a different level of birefringence than the edges.
About one-half way down, just above the lower (lateral) strain gage, the
birefringence suddenly becomes more nearly uniform with width. This
phenomenon is felt to be related to inhomogeneities in the material
rather than inhomogeneities in the stress state. In the 90° direction,
the orthotropic photoelastic material crushes quite easily. Thus any
deviations from flatness of the ends of the specimen, where the compres-
sive loads are transmitted to the specimen, would be eliminated by the
application of load. In addition, in the 90° direction end effects at-
tenuate quite rapidly due to the low stiffness. Thus any deviations
from flatness or other end effects would be very unlikely to cause
abrupt changes in the widthwise uniformity of birefringence at the cen-
ter of the specimen. The halos aound the hexagonal bolts were due to
stresses induced in the plexiglas when the holes were drilled. With the
situation depicted in fig. 25 it is evident why at times it was diffi-
cult to determine exactly what fringe order was being observed. For
this 90° specimen, the fringe order at the center of the specimen was
used as the fringe order for calibration.

Figure 26 illustrates the relation between applied stress and
fringe order for the 90° specimen. Note both tensile and compressive
stresses are shown. As mentioned previously, N_T is being considered as

69
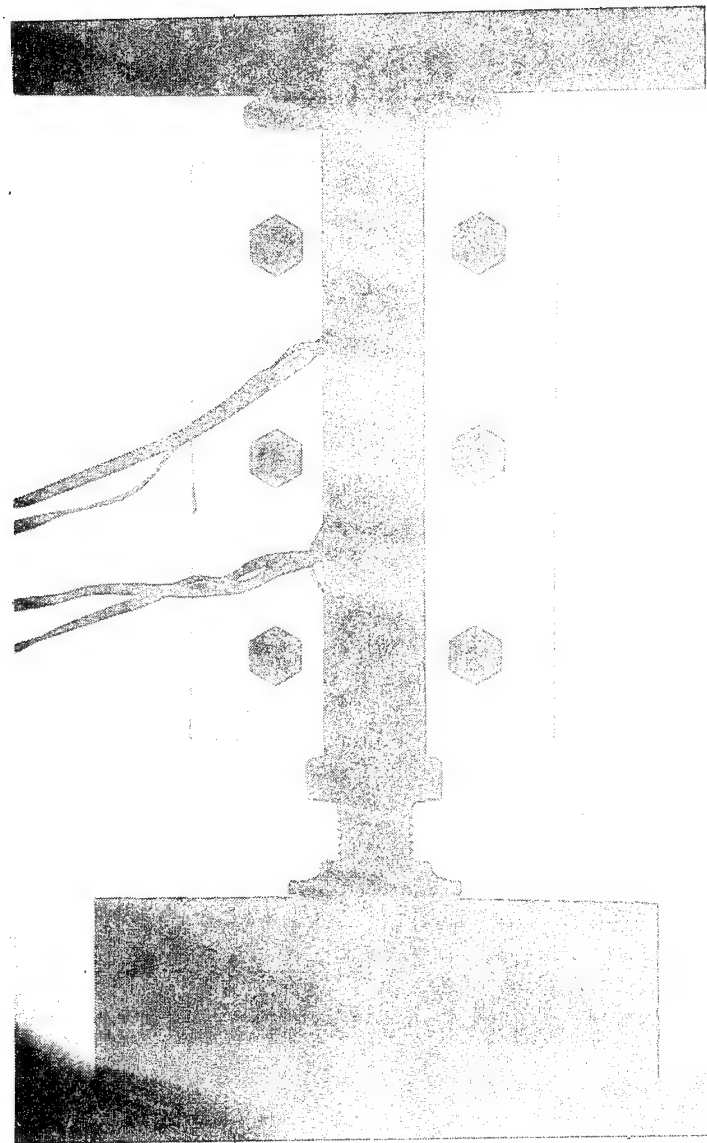
Fig. 24 The 90° compression specimen in light field with fringe order 1/2.
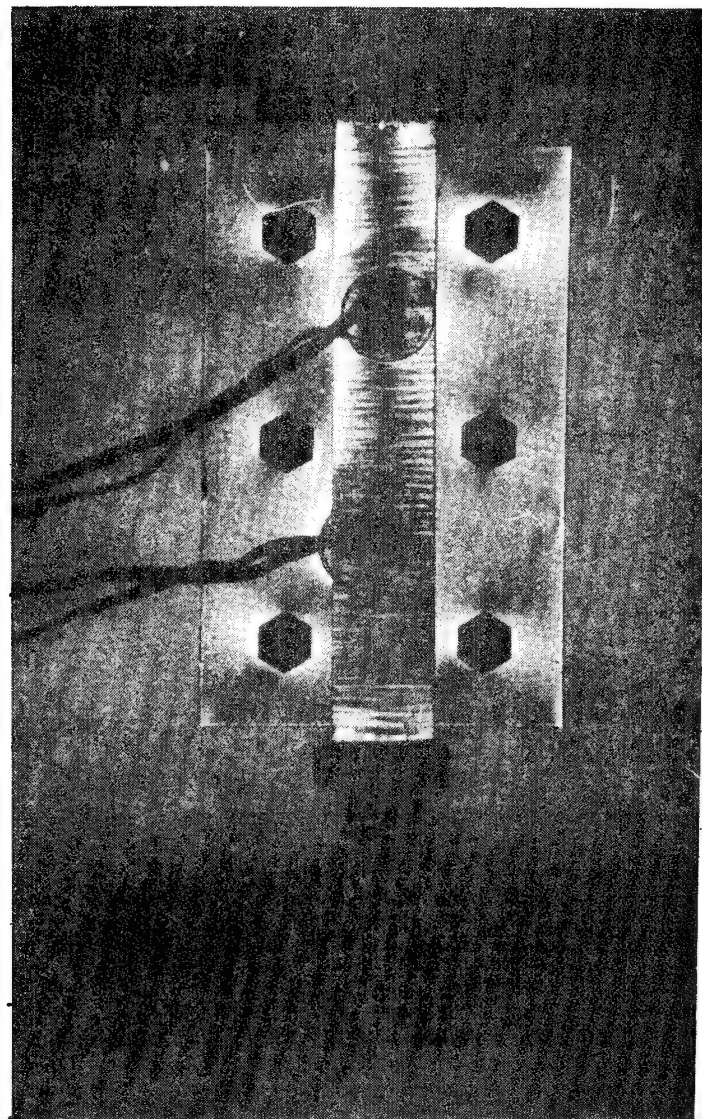
Fig. 25   The 90° compression specimen in dark field with fringe order
            1.25.

Fig. 26 Stress-optic relation for 90° specimen.

— no residual assumed

...... residual assumed

stress, psi

Fringe order, N or N_T

72
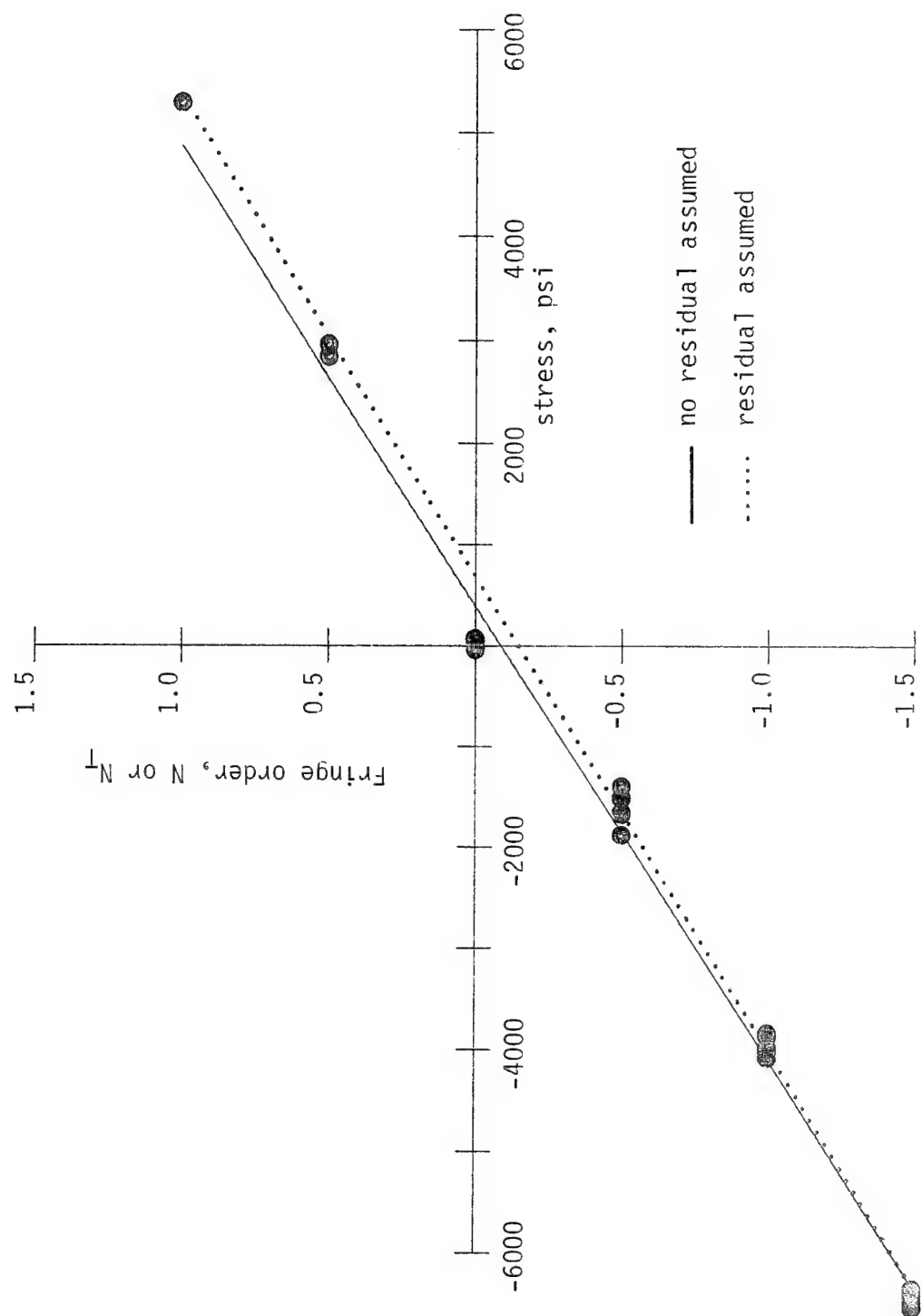
a positive quantity and so fig. 26 should actually be plotted as shown schematically in fig. 27. However, for purposes of conveniently using least-square techniques and for strictly asthetic reasons, plots such as in fig. 26 will be used.

If it is assumed that there was no residual birefringence, then when $\sigma_2 = 0$, the fringe order is zero (see eq. 61 with $\sigma_1 = \tau_{12} = 0$). The solid line in fig. 26 shows the least-square calibration with the no residual stress assumption. This line has a slope of 0.237×10^{-3} fringe/psi and intercept of 0.09 fringe. The slope led to a value of f_2 = 380 psi/fringe/in. If it is assumed that residual birefringence existed, the least-square data fit produced the dotted line. This line has a slope of 0.227×10^{-3} fringe/psi and an intercept of 0.15 fringe. From this slope f_2 = 396 psi/fringe/inch. Reiterating an earlier discussion to avoid ambiguity, the solid line was obtained by using the points $\sigma_2 = 0$, $N_T = 0$ in the least-square analysis. The dotted line was obtained by omitting those data in the least-squares analysis. The former approach tends to force the line through the origin when in fact it should not go through the origin.

With both figs. 19 and 26 in hand, residual birefringence was suspected. With fig. 19 alone it was not clear whether the nonzero intercept on the N axis was due to the data scatter or due to residual birefringence. The nonzero intercepts of both figures were, however, strong arguments for residual effects. If there were residual effects, were figs. 19 and 26 consistent? To determine this, consider eq. 60. With $\sigma_2 = \tau_{12} = 0$, eq. 60 becomes

$$N_T = \sqrt{\{\frac{\sigma_1}{f_1} + N_R \cos(2\theta_R)\}^2 + \{N_R \sin(2\theta_R)\}^2} \quad . \qquad (92)$$

73
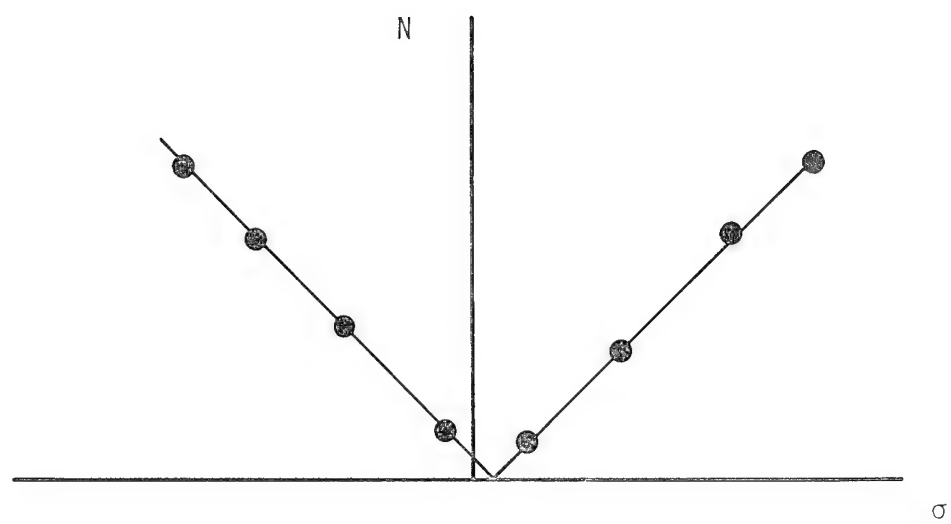
Fig. 27   Correct way to plot stress-optic data for tension and
compression.

With $\sigma_1 = \tau_{12} = 0$, eq. 60 becomes

$$N_T = \sqrt{\{-\frac{\sigma_2}{f_2} + N_R \cos(2\theta_R)\}^2 + \{N_R \sin(2\theta_R)\}^2} \quad . \qquad (93)$$

With an actual polariscope measurement it was quickly established that for the uniaxial material, θ_R was very close to zero. Thus eqs. 92 and 93 become

$$N_T = \sqrt{\{\frac{\sigma_1}{f_1} + N_R\}^2} \qquad (94)$$

and

$$N_T = \sqrt{\{-\frac{\sigma_2}{f_2} + N_R\}^2} \quad . \qquad (95)$$

Figures 28a and b illustrate the N vs. σ relations for these two equations. The presence of residual birefringence, with the residual isocline aligned with the fibers, results in shifts in the calibration relations. The 0° calibration is shifted in a direction opposite to the shift of the 90° specimen. The experimentally observed shifts in the two specimens were consistent with the notion of residual birefringence being present, particularly the sense of the shifts.

Figures 29 and 30 illustrate the elastic properties of the 90° specimen. Figure 29 indicates that Young's modulus in the matrix direction , E_2, was 1.78 x 10^6 psi and fig. 30 indicates the minor Poisson's ration was 0.094.

A third tensile specimen, with the fibers at 45° relative to the tensile direction, was used to complete the calibration. The data from this third specimen could be used in several ways. The use depended on whether or not residual effects were felt to be important. Figure 31 shows the no-load state of birefringence in the 45° specimen in the

75

a) N_T vs. σ_1

b) N_T vs. σ_2

Fig. 28 N_T vs. σ in the presence of residual birefringence.

76
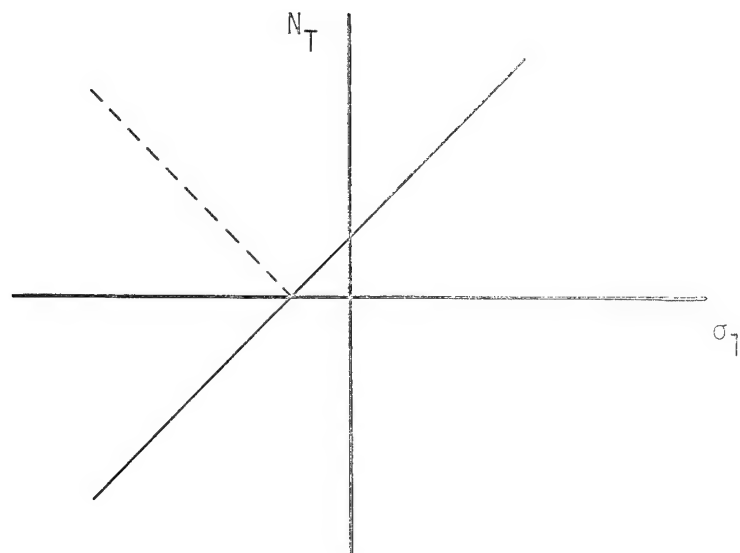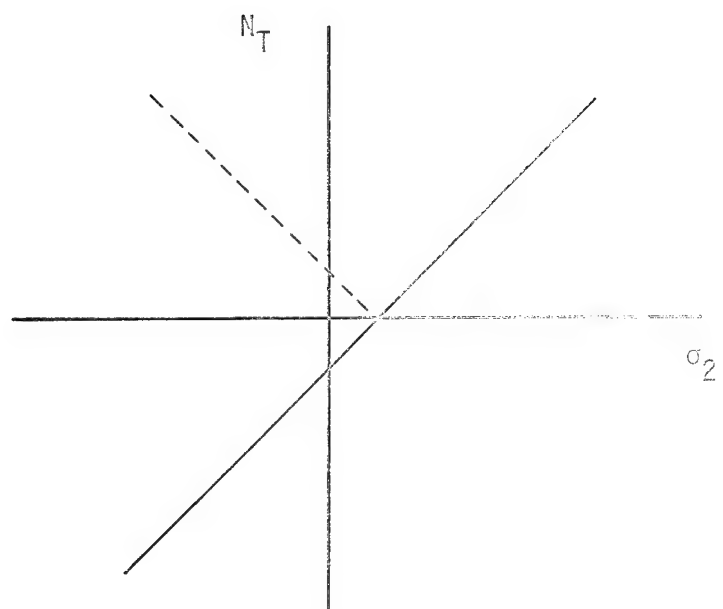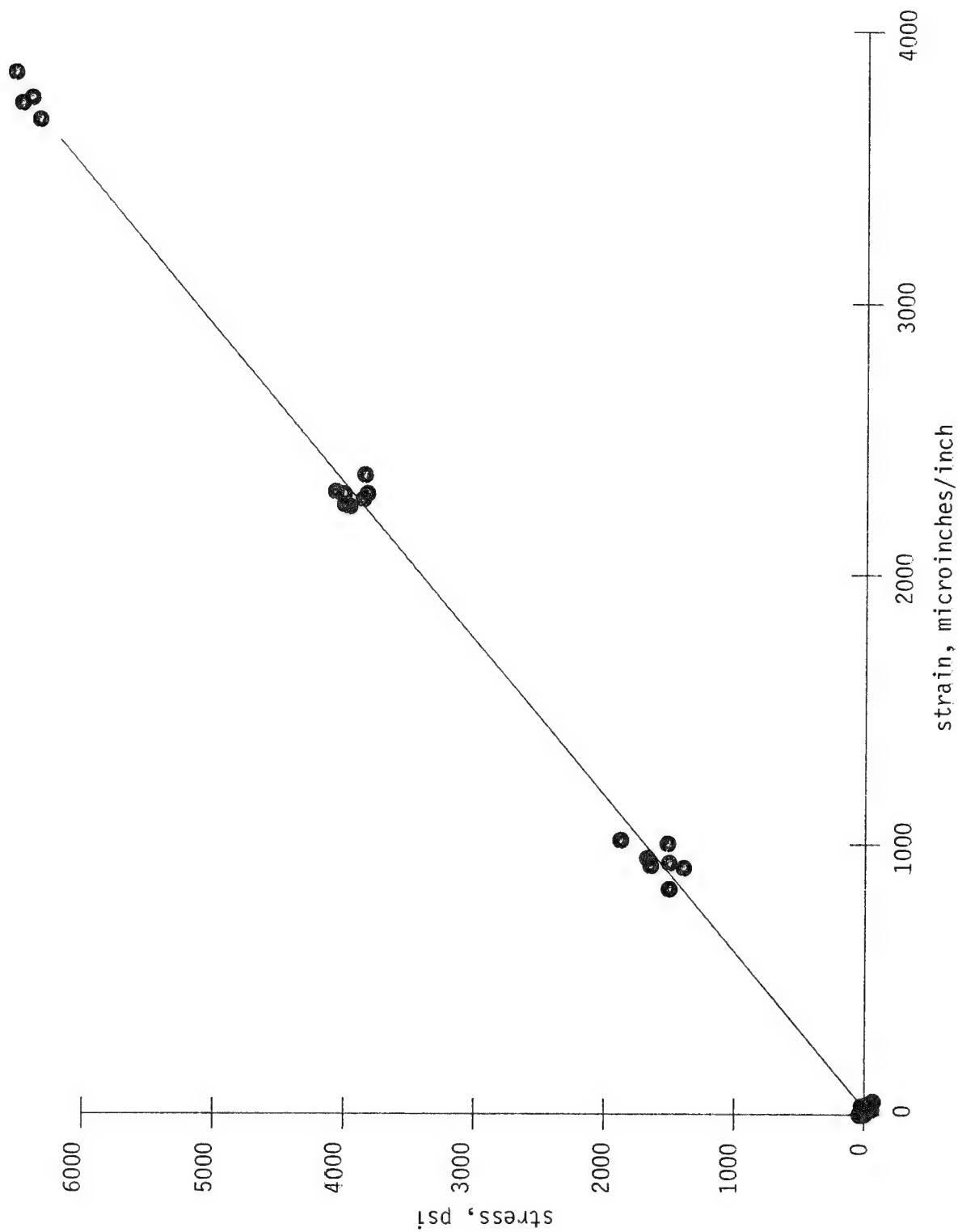
Fig. 29 Stress-strain relation for 90° specimen.
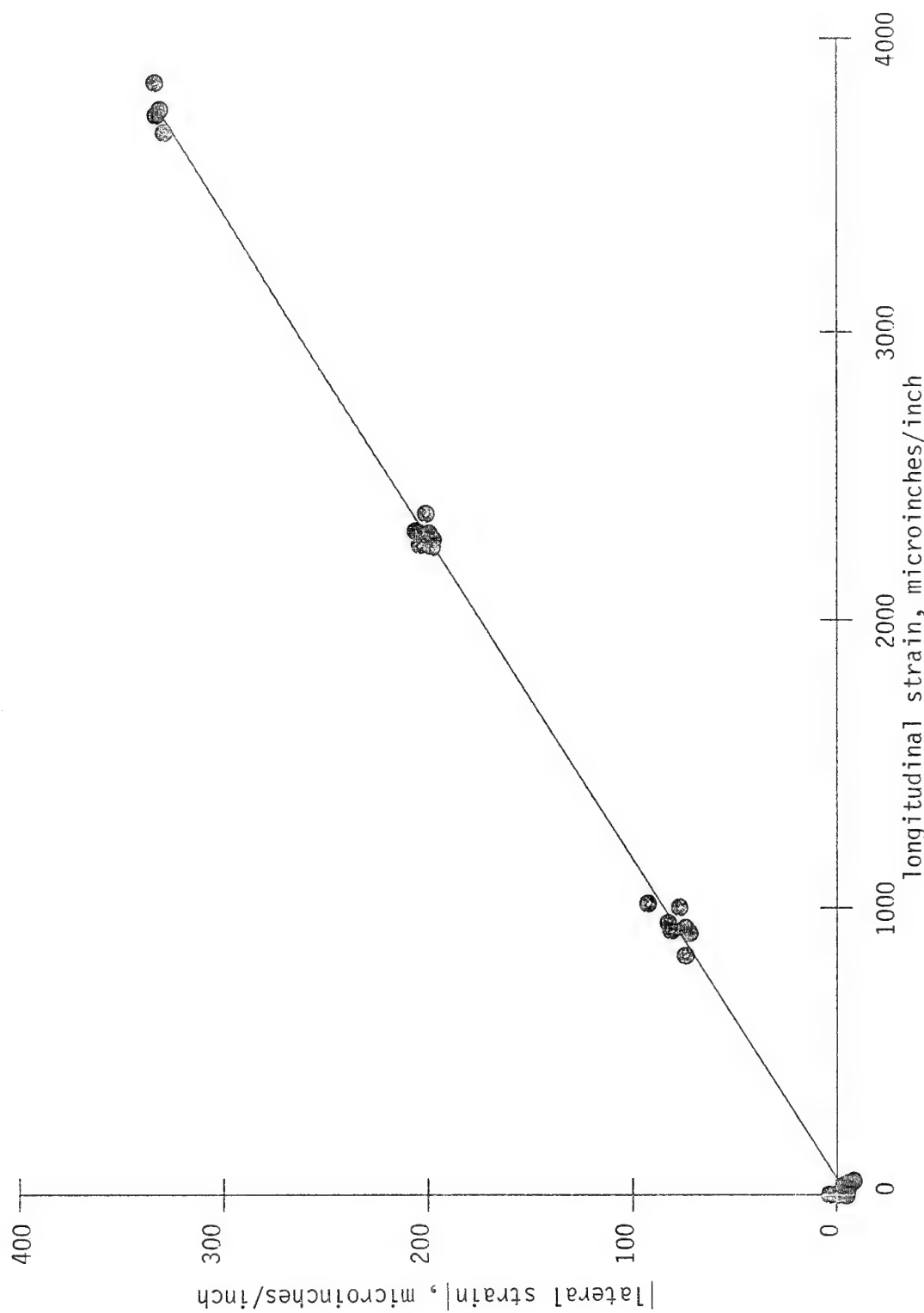
Fig. 30 Poisson's ratio for 90° specimen.

78

light field. Back-to-back strain gage rosettes were used to measure the elastic response of the specimen. Figure 32 shows the lightfield 1/2-order state of birefringence of the 45° specimen. This was a relatively low load level and yet the fibers caused striations in the birefringence. This could have been due to very high shear stresses at the fiber-matrix interfaces. Figure 33 shows the 45° specimen in the dark field at what was judged to be the 1st fringe order. As can be seen, it was quite difficult to determine what constituted a specific level of birefringence. For this specimen the striations were present at all load levels. The specimen did, however, go through lighter and darker states of 'striated' birefringence. The lightest or darkest states, as the load was varied, were used to define the fringe order.

For the 45° specimen the combined stress state was related to the applied stress, σ, by the following:

$$\sigma_1 = \sigma_2 = \frac{\sigma}{2} \qquad (96)a$$

$$\tau_{12} = \frac{\sigma}{2} \qquad (96)b$$

If residual effects were ignored, these stresses could be substituted into eq. 61 to yield

$$N = \sigma \sqrt{\frac{1}{4}\left(\frac{1}{f_1} - \frac{1}{f_2}\right)^2 + \left(\frac{1}{f_{12}}\right)^2} \; . \qquad (97)$$

The slope of the fringe order vs. applied stress relation, N vs σ, can be used along with previously obtained values of f_1 and f_2 to determine the value of f_{12}. Figure 34 shows the fringe order-applied stress relation for the 45° specimen and also indicates a least-square straight

79
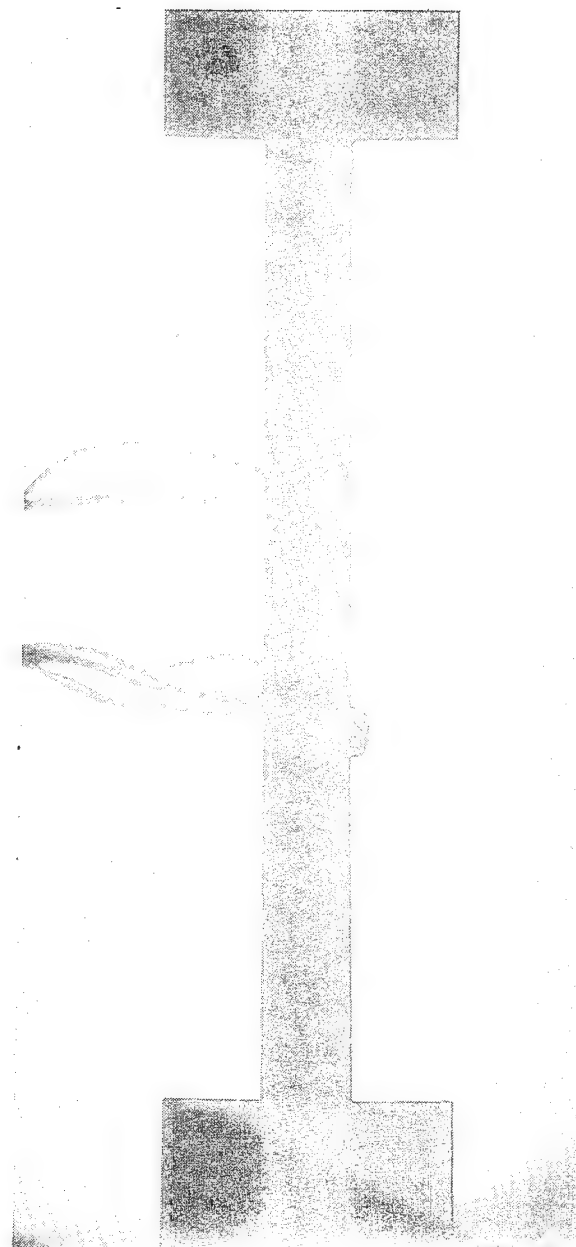
Fig. 31   The 45° tensile specimen in light field with no load.
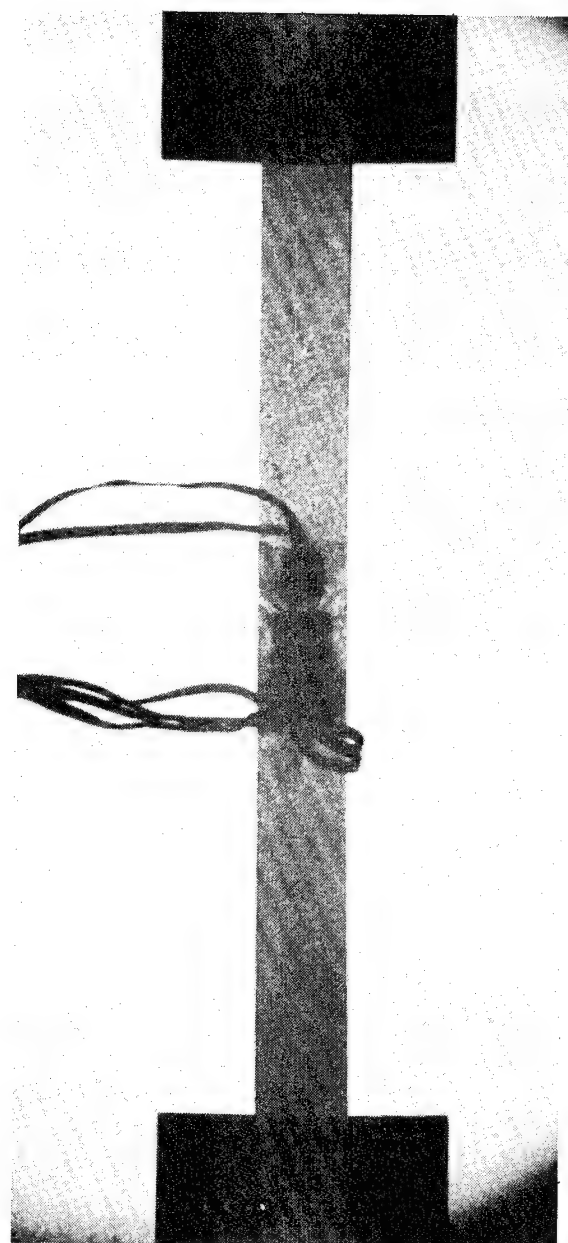
Fig. 32   The 45° tensile specimen in light field with fringe order 1/2.
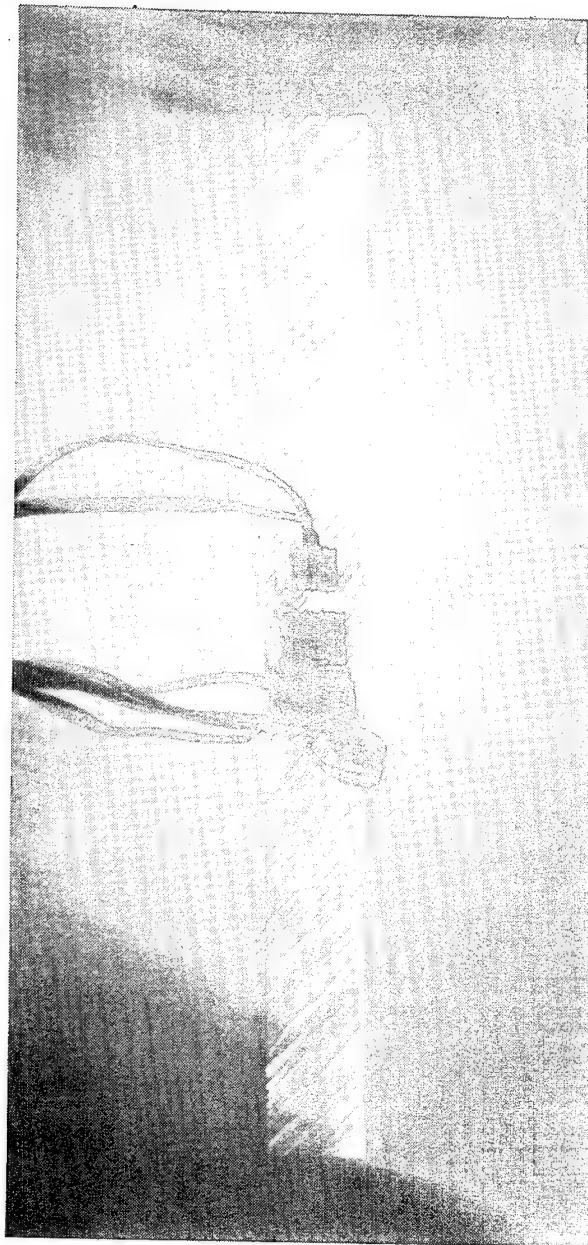
Fig. 33   The 45° tensile specimen in dark field with fringe order 1.

line. Since it was assumed in fig. 34 that residual effects were not important, the points $\sigma = 0$, $N_T = 0$ were used as data in the least-square scheme. The slope of the line, 0.288×10^3 fringe/psi, resulted in a value of 312 psi/fringe/in for f_{12}.

If it is assumed residual effects were important in the 45° specimen, eq. 60 must be used. It is more convenient to square eq. 60 to obtain

$$N_T^2 = [\frac{1}{4}(\frac{1}{f_1} - \frac{1}{f_2})^2 + (\frac{1}{f_{12}})^2]\sigma^2 + [N_R(\frac{1}{f_1} - \frac{1}{f_2})]\sigma + N_R^2 , \qquad (98)$$

where eq. 96 has been used along with the fact that $\theta_R = 0$. If A, B, and C are defined as

$$A = [\frac{1}{4}(\frac{1}{f_1} - \frac{1}{f_2})^2 + (\frac{1}{f_{12}})^2] , \qquad (99)a$$

$$B = N_R(\frac{1}{f_1} - \frac{1}{f_2}) , \qquad (99)b$$

$$C = N_R^2 , \qquad (99)c$$

then eq. 98 is of the form

$$N_T^2 = A\sigma^2 + B\sigma + C . \qquad (100)a$$

If the experimental measurements of N_T and σ are plotted as N_T^2 vs. σ, and a least-squares parabola of the form

$$N_T^2 = \alpha\sigma^2 + \beta\sigma + \gamma \qquad (100)b$$

is fit to the data, then A, B, and C can be estimated from

83
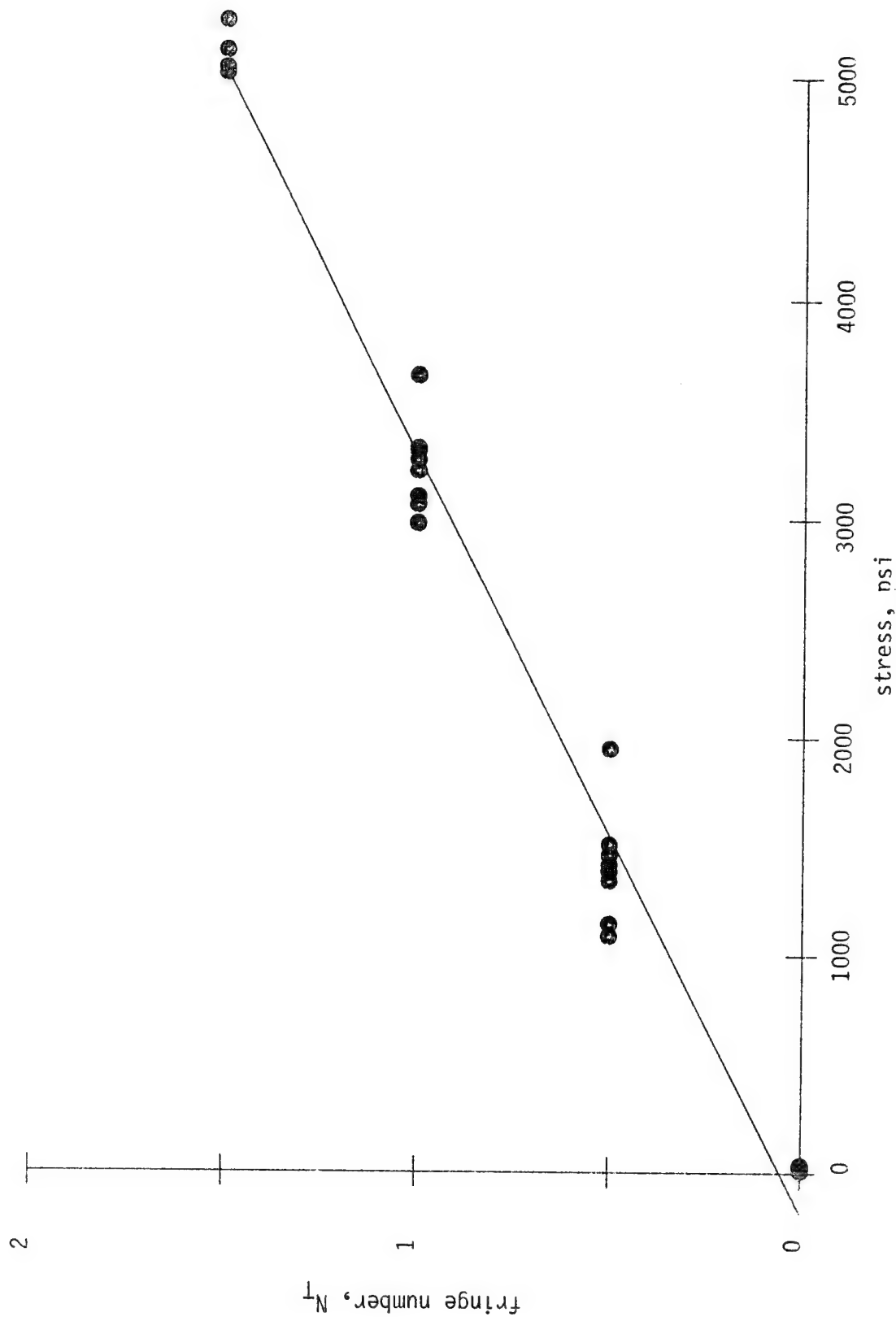
Fig. 34 Stress-optic relation for 45° specimen.

84

$$A \approx \alpha \qquad\qquad (101)a$$

$$B \approx \beta \qquad\qquad (101)b$$

$$C \approx \gamma \ . \qquad\qquad (101)c$$

If f_1 and f_2 have been determined from previous calculations, then α can be used to determine f_{12}. The value of γ should give a value of N_R^2 consistent with the value obtained in 0° and 90° tests. The value of B should be consistent with the values of N_R, f_1, and f_2. Figure 35 shows the relation between N_T^2 and σ. The least-squares parabola has the following coefficients,

$$\alpha = 0.75 \times 10^{-7} (\text{fringe/psi})^2 \qquad\qquad (102)a$$

$$\beta = 0.45 \times 10^{-4} (\text{fringe})^2/\text{psi} \qquad\qquad (102)b$$

$$\gamma = 0.049 \ (\text{fringe})^2 \qquad\qquad (102)c$$

This value of α led to a value for f_{12} of 335 psi/fringe/in. The value of γ predicted a value of $N_R = 0.22$. This value of N_R was higher than the value of N_R computed from the 0° or 90° specimens. However, there was much more difficulty in determining the level of birefringence in the 45° specimen and so, as seen in figs. 34 and 35, there was much scatter to the $N_T - \sigma$ data. Hence, stress-optic properties obtained from this specimen may not be as reliable as properties taken from the 0° and 90° specimens. Unfortunately, with this approach to calibration, f_{12} must be determined from this 45° specimen.

In addition to the value of N_R being different than previous calculations, the value of β, eq. 102b, was inconsistent. The quantity β

85
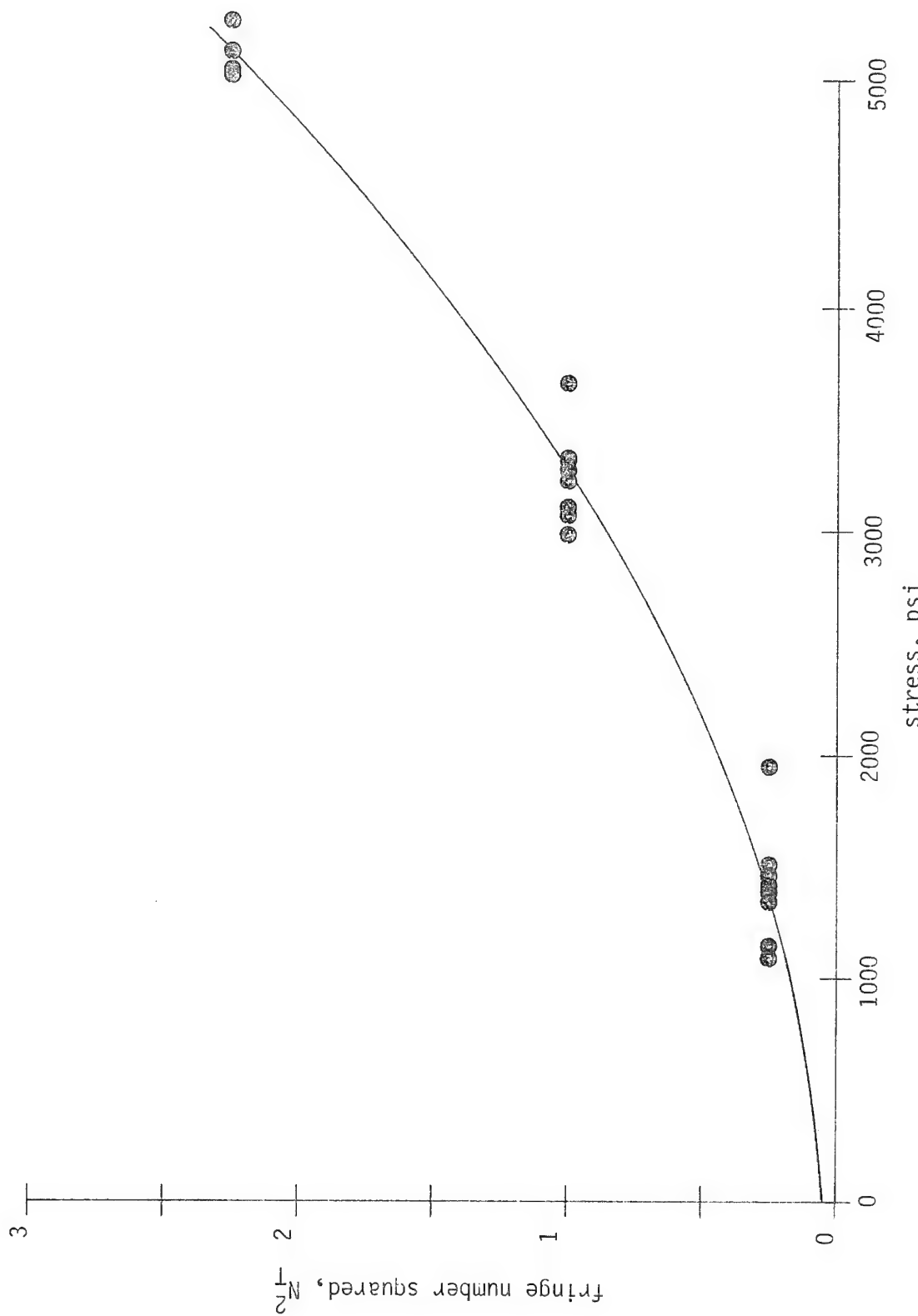
Fig. 35 Stress-optic relation for 45° specimen, alternative display of data.

86

approximates β in eq. 100 (see eq. 99b). Since $f_1 > f_2$, β will be a negative number. The value of β from the least-squares approximation was positive. The reason for this inconsistency was not evident. It is not felt to be due entirely to the data scatter responsible for the inconsistent value of N_R.

Figure 36 shows a plot of the shear stress τ_{12} as a function of the sheer strain γ_{12}. The shear strain was determined from the rosette gages while the shear stress was computed using eq. 96b. For some reason the strain gage readings were erratic and so the elasticity data had scatter. A least-square straight line through the τ - γ data yields a value of G_{12} of 570,000 psi. The longitudinal stress-longitudinal strain ralation for this 45° specimen resulted in a Young's modulus, i.e. E_{45}, of 1.56×10^6 psi.

Table 1 summarizes the optical properties and Table 2 summarizes the elastic properties of the material as obtained from the uniaxial tests.

Four Point Bend Tests

After it was hypothesized that residual birefringence was present in the material, it was decided to use four-point bending tests to optically calibrate the material. There were several reasons for this. First, it was felt the stress gradients in a bending specimen would result in sharp, more well defined fringes. It would thus be easier to judge the presence of, say, the first fringe order. Using the flexure formula and determining the distance from the neutral bending axis to a particular fringe, the stress levels producing that fringe order could be accurately determined. Second, with residual birefringence in the

87
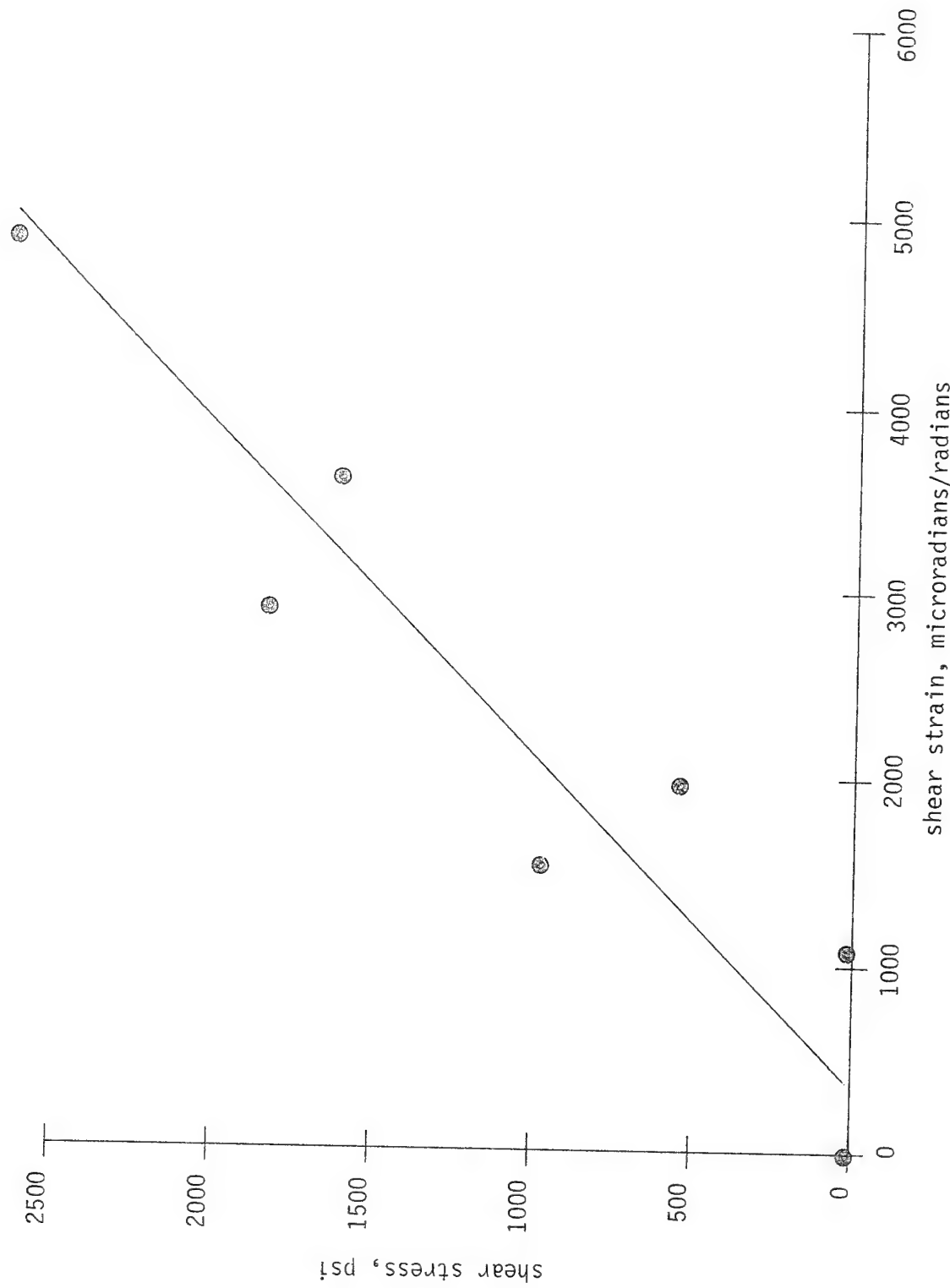
Fig. 36 Shear stress-strain relation for 45° specimen.

shear strain, microradians/radians

shear stress, psi

Table 1

Optical properties of unidirectional material as determined from uniaxial tests

Specimen Type	No Initial Birefringence Assumed	Initial Birefringence Assumed[1]
0°	f_1 = 744 psi/fringe/in	f_1 = 756 psi/fringe/in N_R = 0.13
90°	f_2 = 380 psi/fringe/in	f_2 = 396 psi/fringe/in N_R = 0.15
45°	f_{12} = 312 psi/fringe/in	f_{12} = 335 psi/fringe/in N_R = 0.22[2]

(1) θ_R measured to be zero

(2) N_R and β not consistent with previous computations

Table 2

Elastic properties of unidirectional material
as determined from uniaxial tests

Specimen Type   Elastic Properties

0° E_1 = 5.4 x 10^6 psi ν_{12} = 0.3

90° E_2 = 1.78 x 10^6 psi ν_{21} = 0.09

45° G_{12} = 0.57 x 10^6 psi E_{45} = 1.5 x 10^6 psi

material, the fringes would not be symmetrically disposed on either side of the bending neutral axis. The 'optical neutral axis' would be off-set from the conventional neutral axis, i.e. the centerline of the bending specimen. This off-set could be used to determine the residual fringe order N_R. Finally, one test could be used for both tensile and compressive stresses. With a known applied bending moment and using Tardy compensation to determine fractional fringe orders, considerable stress-optic data could be obtained from the four-point bending arrangement.

All the previously discussed uniaxial specimens were used as four-point bending specimens. These specimens were reused as bending specimens for two reasons. First, it conserved valuable photoelastic material. Second, it insured that variability of optical properties from location to location on the panel would not contribute to any differences in the calibration constants between the uniaxial tests and the four-point bend tests. There was one disadvantage in using the uniaxial specimen. These particular specimens, as stated before, were approximately 0.625 in. wide. Wider specimens would have resulted in more accuracy in resolving distances from the neutral bending axis. Actually, photographs of the four-point bend test fringe patterns were enlarged to aid in determining distances from the neutral axis. Thus the size of the specimen was not important from that standpoint. However, using a wider specimen as the basis for scaling would have resulted in more resolution than using a narrower one.

Figures 37-39 show the three four-point bending tests. Figure 37 shows the 0° specimen. In this case the fibers were parallel to the neutral bending axis (horizontal in the figure). Figures 38 and 39,

Fig. 37 Four-point bend test of 0° specimen.
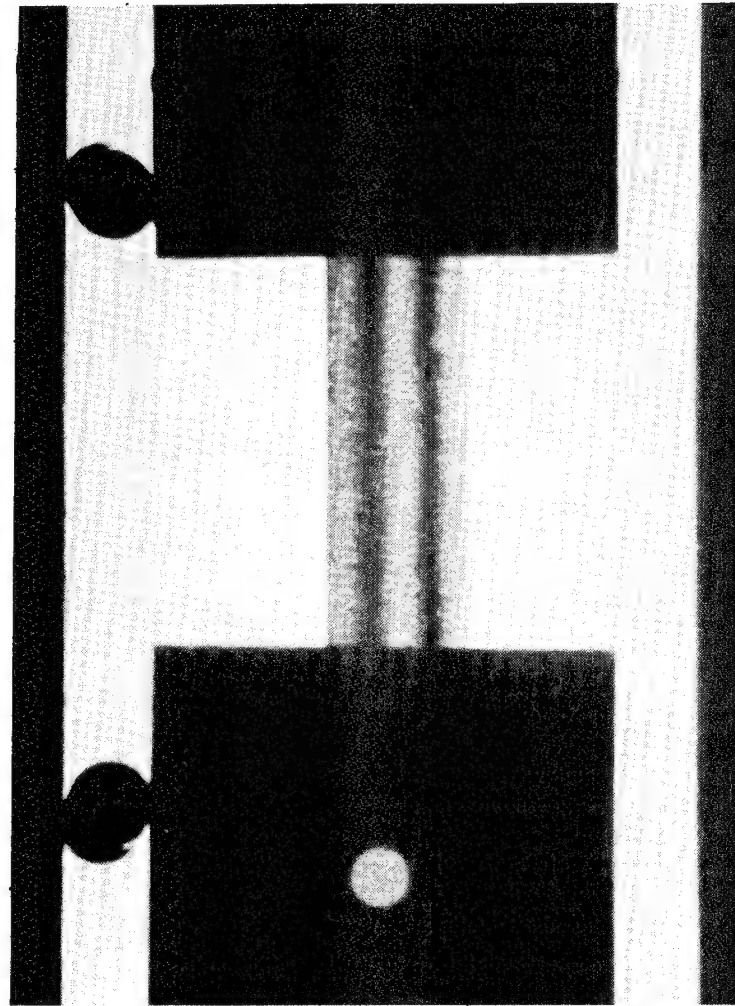
Fig. 38 Four-point bend test of 90° specimen.
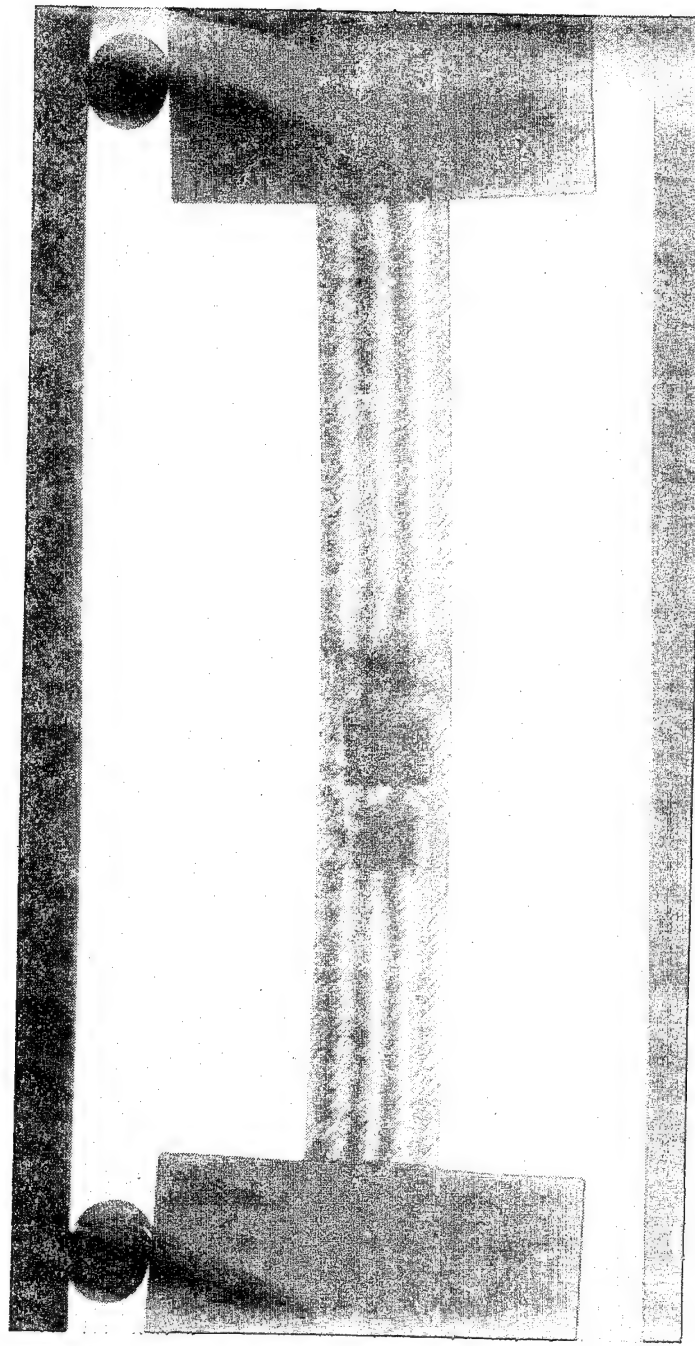
Fig. 39 Four-point bend test of 45° specimen.

respectively, show the 90° and 45° specimens. With the 90° orientation, the fibers were perpendicular to the neutral axis. The 90° specimen was somewhat shorter than the other two since it was the remains of a failed tensile specimen. Recall, the 90° tensile specimens were tested in tension to failure and then one of the remaining pieces was tested in compression with the buckling restraints.

With the specimens as shown in figs. 37-39, the portion of the beam above the neutral axis was in compression. For the 0° specimen,

$$\sigma_1 = \frac{Mz}{I} . \tag{103}$$

where z was measured positive downward from the neutral axis and M and I have their usual meaning. Equation 94 provides the relation between σ_1 and N_T, i.e.

$$N_T = \sqrt{(\frac{\sigma_1}{f_1} + N_R)^2} \tag{94}$$

Using various values of moment, looking at several z locations, and using Tardy compensation, sufficient data could be generated to reliably determine f_1 and N_R. Figure 40 shows the relation between σ_1 and N_T. The maximum stress levels used in the four-point tests were not necessarily identical to the stress levels in the uniaxial tests because interest here was in residual birefringence. The slope of the line in fig. 40 is 0.106×10^{-3} fringe/psi and the intercept, N_R, is 0.11. The slope led to a value of f_1 of 849 psi/fringe/ inch. This is 11% higher than the value of the f_1 using the tensile tests, assuming an initial birefringence.

95
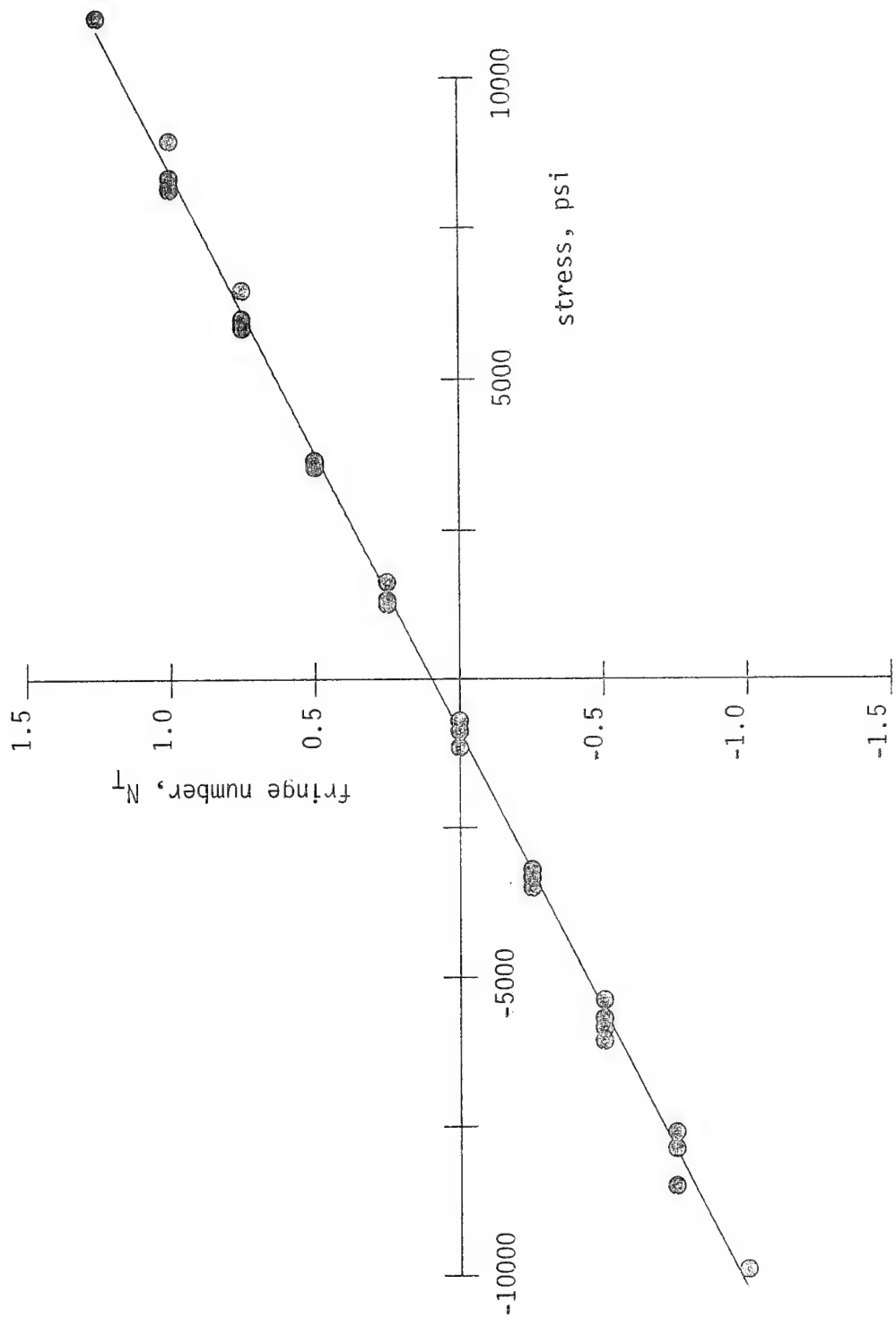
Fig. 40 Stress-optic relation for 0° specimen from four-point bend test.

For the 90° specimen,

$$\sigma_2 = \frac{Mz}{I} \qquad (104)$$

and eq. 95 provides the relationship between σ_2 and N_T, i.e.

$$N_T = \sqrt{\left(-\frac{\sigma_2}{f_2} + N_R\right)^2} \; . \qquad (95)$$

Figure 41 shows the relation between N_T and σ_2. The slope of the relationship is 0.234×10^{-3} fringe/psi and the intercept is -0.07 fringe. The slope resulted in a value of f_2 of 385 psi/fringe/inch. This is about 3% lower than the value obtained in uniaxial tests.

For the 45° specimen, eqs. 96 and 98 are applicable, where in those equations

$$\sigma = \frac{Mz}{I} \; . \qquad (105)$$

Figure 42 shows the relation between N_T^2 and σ. A least-squares parabola of the form eq. 100b was fit through the data. The coefficients were

$$\alpha = 0.837 \times 10^{-7} \; (fringes)^2/(psi)^2 \qquad (106)a$$

$$\beta = 0.34 \times 10^{-4} \; (fringes)^2/psi \qquad (106)b$$

$$\gamma = 0.0451 \; fringes \; . \qquad (106)c$$

Using the values of f_1 and f_2 from the 0° and 90° bending tests, the value of α led to a value of f_{12} of 319 psi/fringe/in. This is about 10% lower than the value of f_{12} obtained from the uniaxial tests. The value of γ led to a residual fringe value of 0.21. The sign of β was again inconsistent with the other data. Table 3 summarizes the optical calibration from the four-point bending tests.
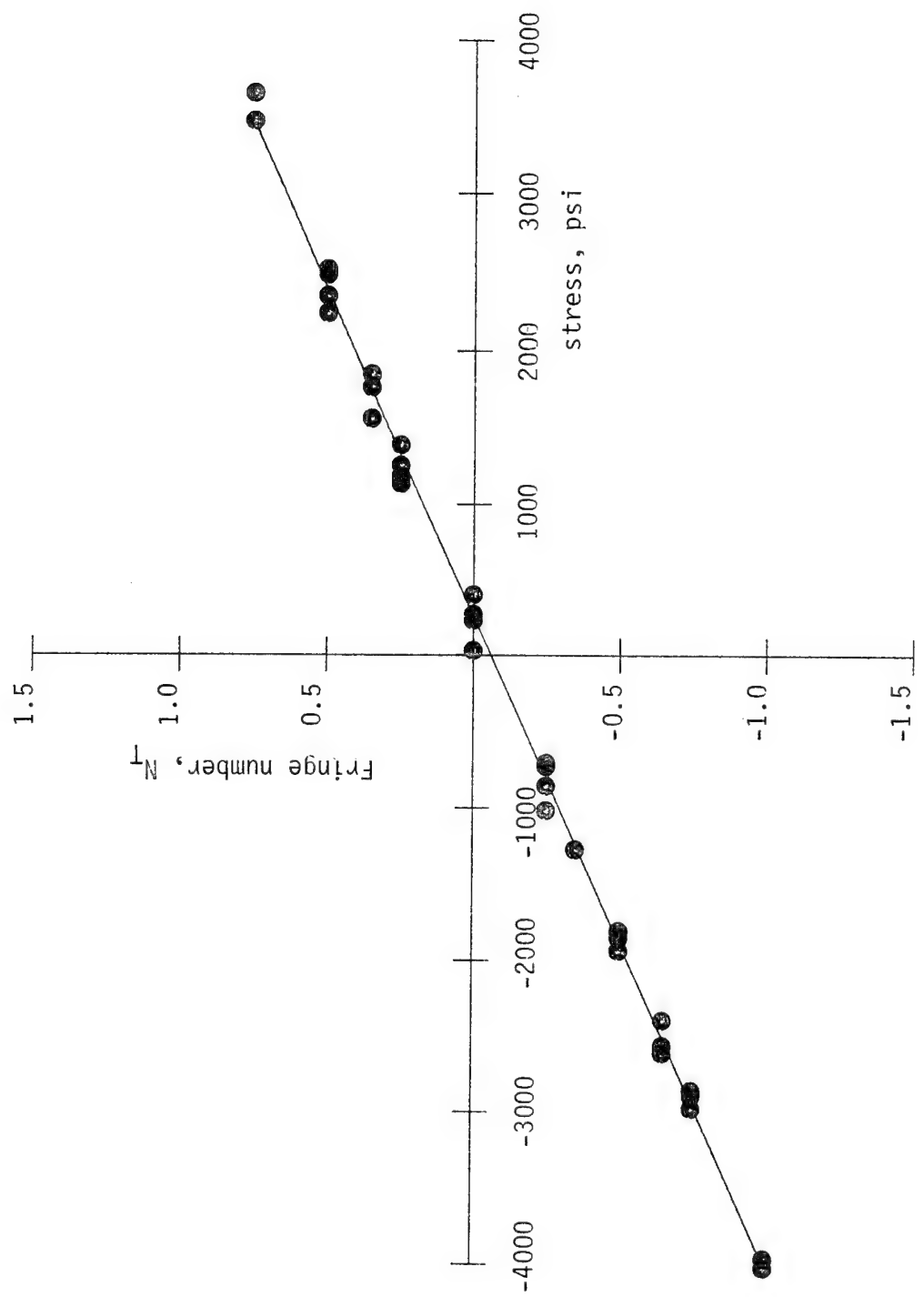
Fig. 41 Stress-optic relation for 90° specimen from four-point bend test.

98
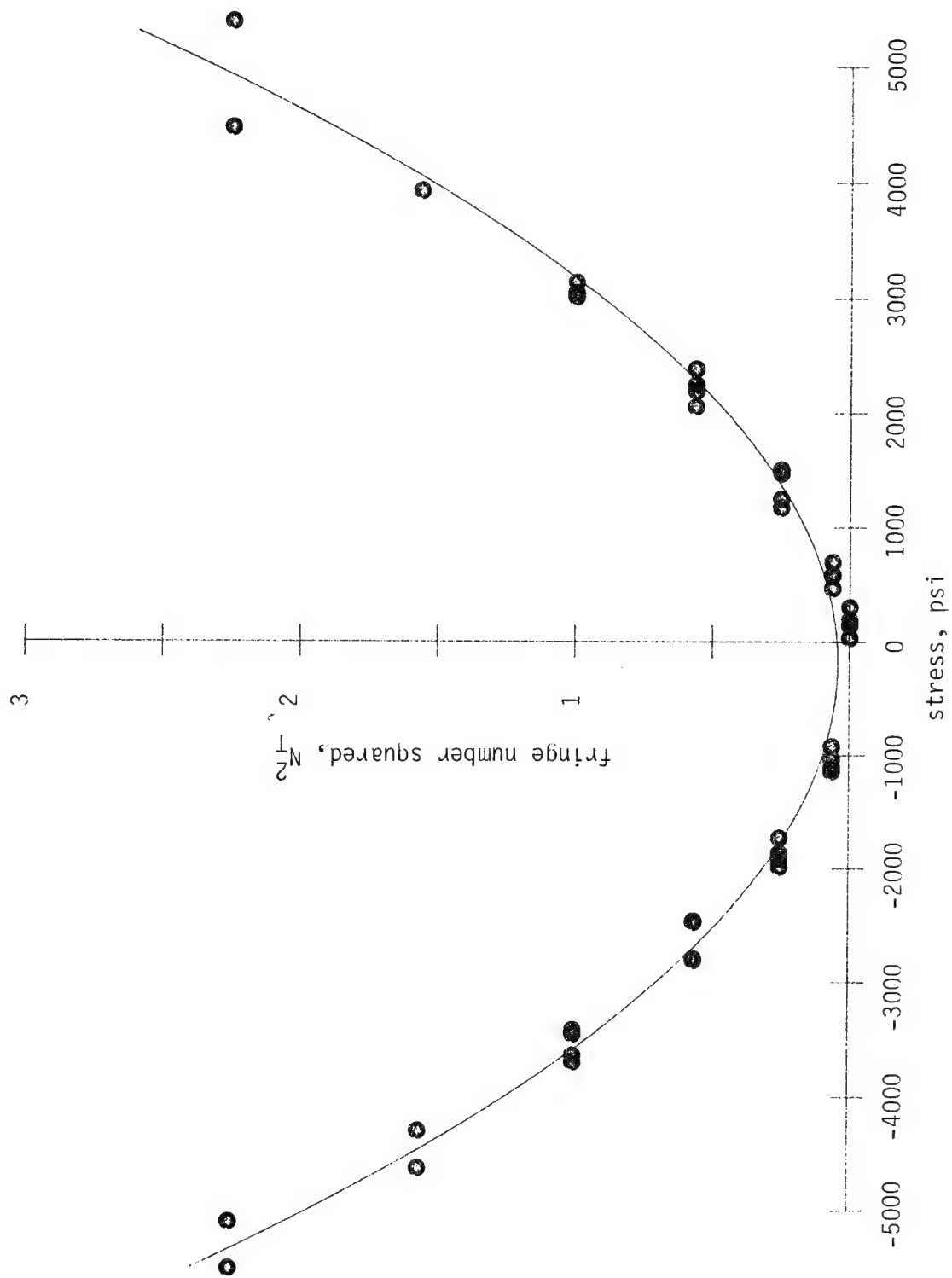
Fig. 42 Stress-optic relation for 45° specimen from four-point bend test.

99

Table 3

Optical properties of unidirectional material
as determined from four-point bend tests.

Specimen Type	Data[1]
0°	f_1 = 849 psi/fringe/in
	N_R = 0.11
90°	f_2 = 385 psi/fringe/in
	N_R = 0.07
45°	f_{12} = 319 psi/fringe/in
	N_R = 0.21[2]

(1) θ_R measured to be zero

(2) β not consistent with previous computations

100

In summary, it is felt that the four-point bending tests yielded a more accurate calibration. The ambiguity concerning fringe definition in the uniaxial tests did not occur in the bending tests. Furthermore, having tensile stresses and compressive stresses at the same time was felt to be valuable. Since the transition between tension and compression is associated with determining the value of N_R, having a single testing fixture and simultaneously determining the value of N_T associated with tension and the value associated with compression should reduce the variance in the determination of N_R.

101

FORWARD TESTING: GLOBAL BEHAVIOR

With the material calibrated, eqs. 60 and 66 could be used to pre-
dict the isochromatic and isoclinic fringes in a disk, assuming the
stresses were known. Alternatively, using eqs. 74 and 75, in addition
to a third condition, the stresses could be computed, assuming the iso-
chromatic and isoclinic fringe patterns were known. The former has been
referred to here as forward testing while the latter has been referred
to as backward testing. The forward testing is discussed in this and in
the next section

The comparing of the predicted fringe patterns with the experiment-
ally observed fringe patterns was done using two approaches. Both com-
parisons were done using an orthotropic disk in diametral compression.
The first comparison was done by looking at the disk as-a-whole. This
is discussed in this section and is referred to as global behavior. The
second approach is described in the next section and is referred to as
local behavior. To study the global behavior, photographs of fringe
patterns in the disk were compared with computer-generated fringe pat-
terns. These computer-generated fringe patterns were based on eq. 60
and the elasticity solution of Appendix B. This solution is based on
the complex variable approach of Lekhnitskii [12]. The stress-optic
data required in eq. 60 was taken from the tensile and four-point bend-
ing tests and the stresses, σ_1, σ_2, and τ_{12}, were determined from the
elasticity solution. Figure 43 shows the set-up used to load the disks
in diametral compression. The disk used was 3.12 in. in diameter and
0.090 in. in thickness. Shown in the photograph is the plexiglas sand-
wiching plates used to prevent the disk from buckling under the
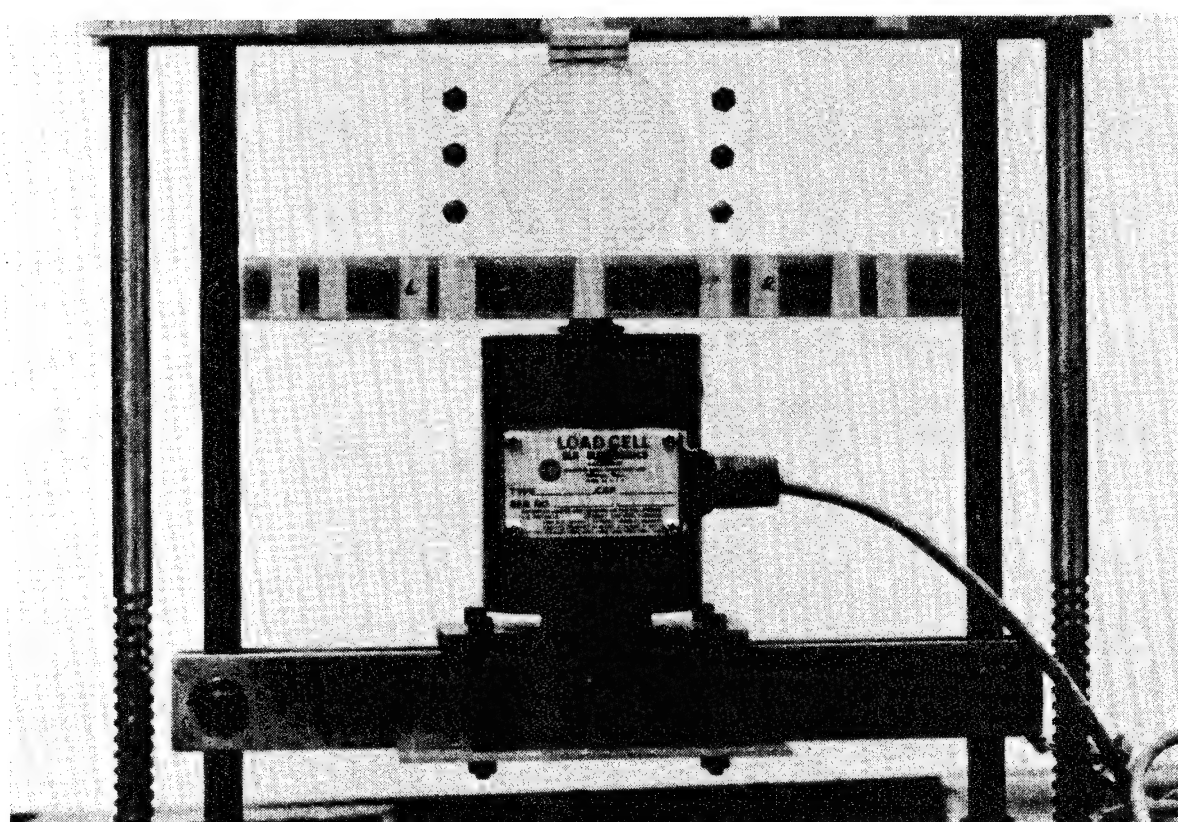
Fig. 43   Fixture for loading disks in diametral compression.

compressive load. This loading fixture is the fixture described in conjunction with the discussion of the 90° compression calibration specimens.

One dilemma in the comparison of theory and experiment was the choice of the numerical values of the stress-optic parameters, particularly N_R. The calibration tests produced several values of N_R, ranging from 0.07 to 0.22. Realistically, the 0.22 value from Table 1 and the 0.21 value from Table 3 were unreliable. As previously indicated, they were not consistent with the other calibration data from the same specimen. It was not clear a simple average of the various values would be a valid choice for the value of N_R. A value of 0.15 was chosen, somewhat arbitrarily, for N_R. This certainly was a good approximation to the values measured from the tests. The values of the other stress-optic coefficients were as follows:

$$f_1 = 849 \text{ psi/fringe/in.} \qquad (107)a$$

$$f_2 = 385 \text{ psi/fringe/in.} \qquad (107)b$$

$$f_{12} = 319 \text{ psi/fringe in.} \qquad (107)c$$

These data are from Table 3.

Figure 44 shows a typical computer-generated fringe pattern for the disk. For the case shown, the fringe order is $N_T = 0.5$ and the fibers are 30° relative to the loaded diameter. Figures 45, 48, 51, 54, and 57 show the comparisons between the observed fringe patterns in the disk and the computer-generated fringe patterns. The figures show the fringe patterns for the disk with the load at various angles relative to the fibers. In all figures the primary fringe order is $N_T = 0.5$. Other
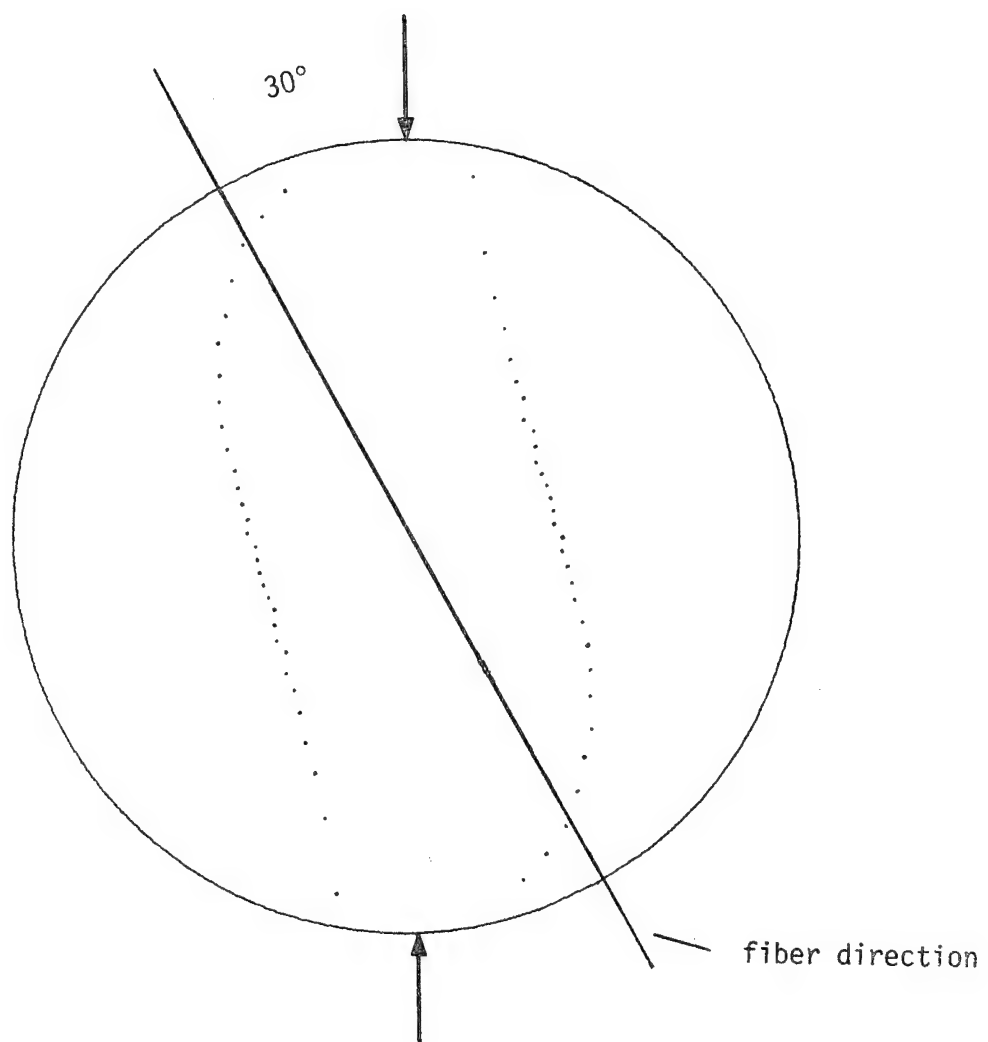
Fig. 44 Computer-generated fringe pattern for disk in diametral compression, N_T=0.5.

fringes are visible near the application of the load. These fringes were not studied because of the lack of ideal loading and lack of accuracy in the elasticity solution in this region. Visible in the photographs of the disk is crazing damage on the disk edge appearing as dark spots on the edge. When the load was applied, the disk material in the immediate vicinity of the load application point would craze and thus become opaque to light transmission. At first, the load was introduced into the disk with a rounded contact point. The radius of curvature of the rounded contact was 0.125 in. This small radius was used to simulate point loads. However, the damage induced in the disk was severe. Thus the flat contacts seen in the figure were used. Still some crazing would always occur, especially when loading the disk perpendicular to the fibers.

Figure 45 shows the observed and predicted fringe pattern when the load was applied along the fibers. The load level was 500 lb. Certainly the characteristics, such as the vertical bow-tie shape, correlated well. On the one hand, it is quite remarkable how good the correlation was. The state of stress in the disk was quite complex. The stress-optic law is a hypothesis and the calibration of the stress-optic coefficients was done with simple tests. The three main ingredients seemed to combine well to lend credibility to the whole notion of orthotropic photoelasticity. On the other hand, a closer scrutiny of the results shows the predicted horizontal distance from the center of the disk to the $N_T = 0.5$ fringe was less than observed. Scaled to the disk's actual size, the distance from the center to the fringe was predicted to be 0.33 in. From the photograph the distance was closer to 0.40 in. Interestingly enough, if it was assumed the residual fringe value, N_R, was

106
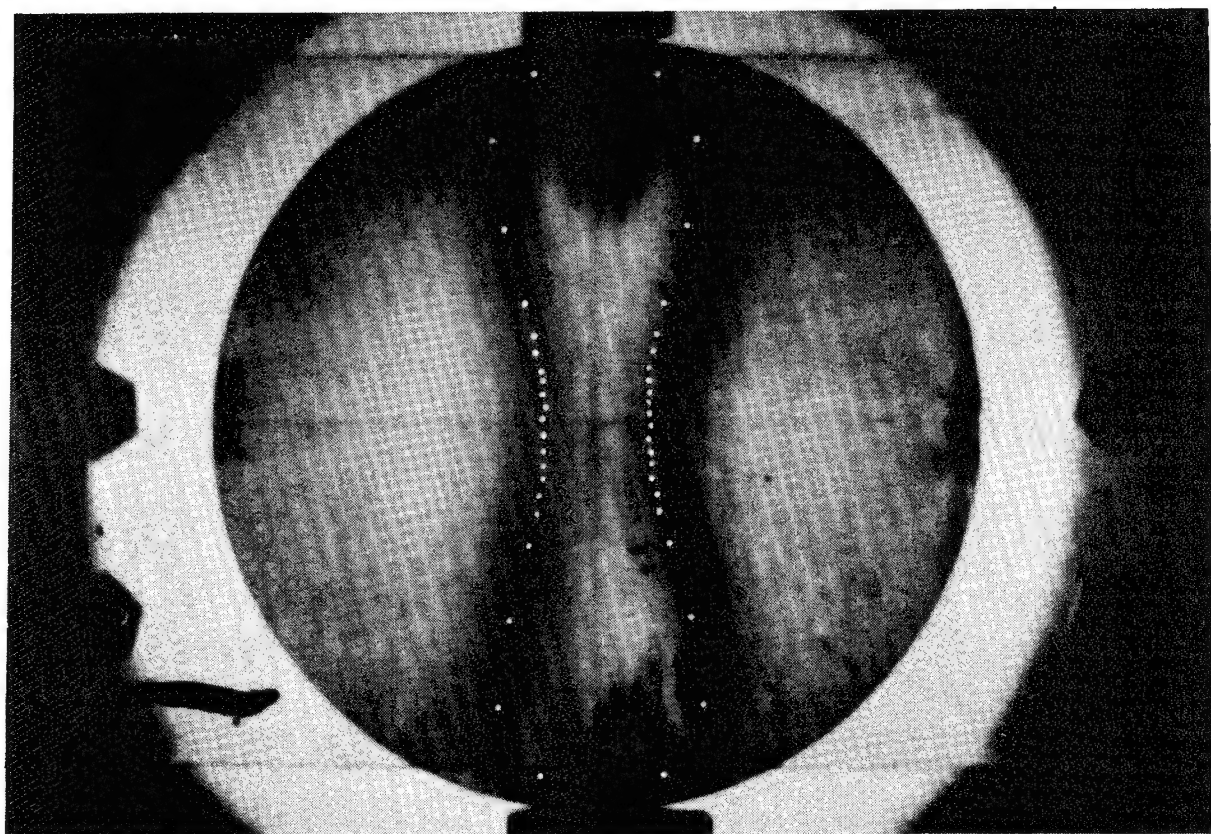
Fig. 45   Comparison between predicted and observed fringe pattern, fibers aligned with load, $N_T=0.5$ (predicted=white dots).

0.07, one-half the value being assumed, the distance prediction was very close to the value observed. Figure 46 shows the predicted fringe pattern as a function of three levels of residual birefringence, $N_R = 0$, $N_R = 0.07$, and $N_R = 0.15$. The level of residual birefringence obviously makes a difference in the fringe pattern generated in the disk. Figure 47 shows another interesting aspect of the effects of residual birefringence. The figure shows the predicted effects of simply reversing the load and subjecting the disk to diametral tension. For no residual birefringence, the sign of the load has no influence on the observed fringe pattern. With residual birefringence, the sign of the load influences the fringe pattern produced.

Figure 48 shows a comparison between predicted and observed fringe pattern in the disk when the load was oriented 30° relative to the fibers. The load level was 325 lb. (With the sign convention adapted in Appendix B, this corresponds to $\alpha = -30^0$.) The fibers caused the streaking in the photo and also contributed to the lack of sharp fringe definition in some regions of the disk. This obscuring was the same as observed in the testing of the uniaxial specimens described earlier. The distance from the disk center to the fringe location, along the diameter perpendicular to the fibers, was slightly overpredicted by the theory. Figure 49 shows the effect of various levels of residual birefringence on the predicted fringe patterns. The differences are subtle but there are slight differences. When shear stresses, in the $1M - 2M$ coordinate system, dominate the stresses, small changes in residual birefringent effects become less important. This is because for this material $\theta_R = 0$ and only the term involving σ_1 and σ_2 in eq. 60 is affected by varying N_R. Figure 50 shows the effect of a load reversal on the
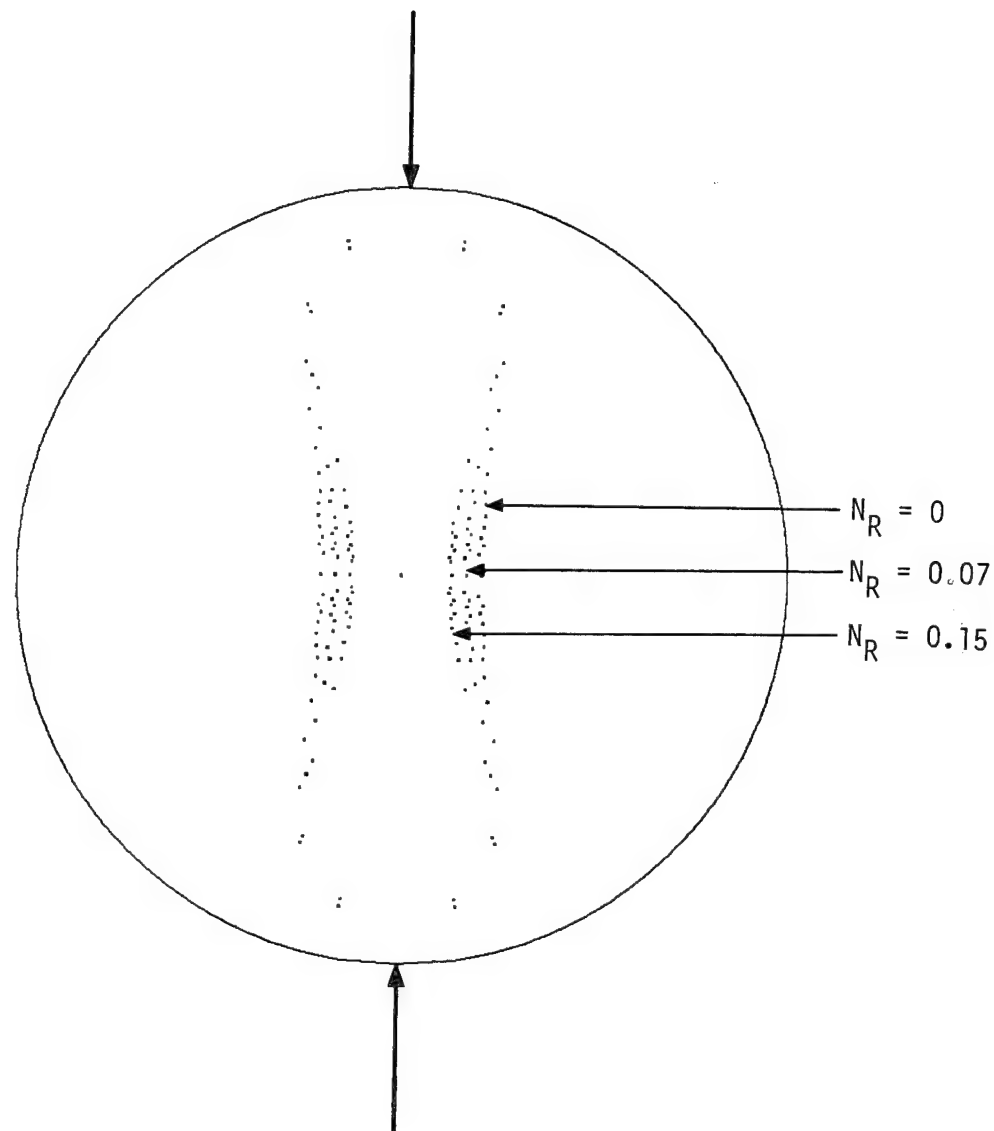
Fig. 46   Effect of level of residual birefringence on predicted fringe
pattern, fibers aligned with load, $N_T=0.5$.

109
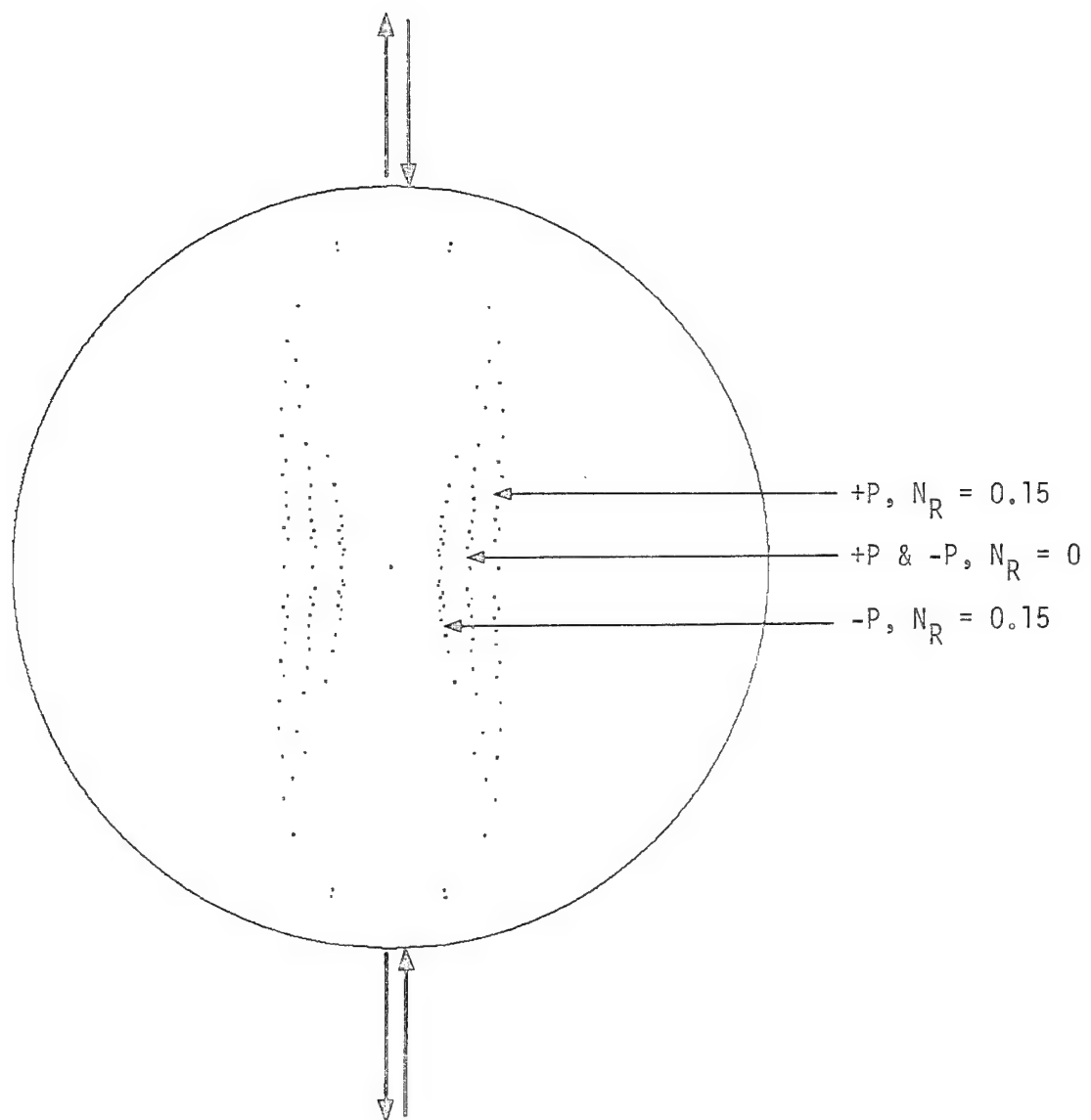
Fig. 47   Effect of residual birefringence on the load reversal fringe
          pattern, fibers aligned with load, $N_T=0.5$.
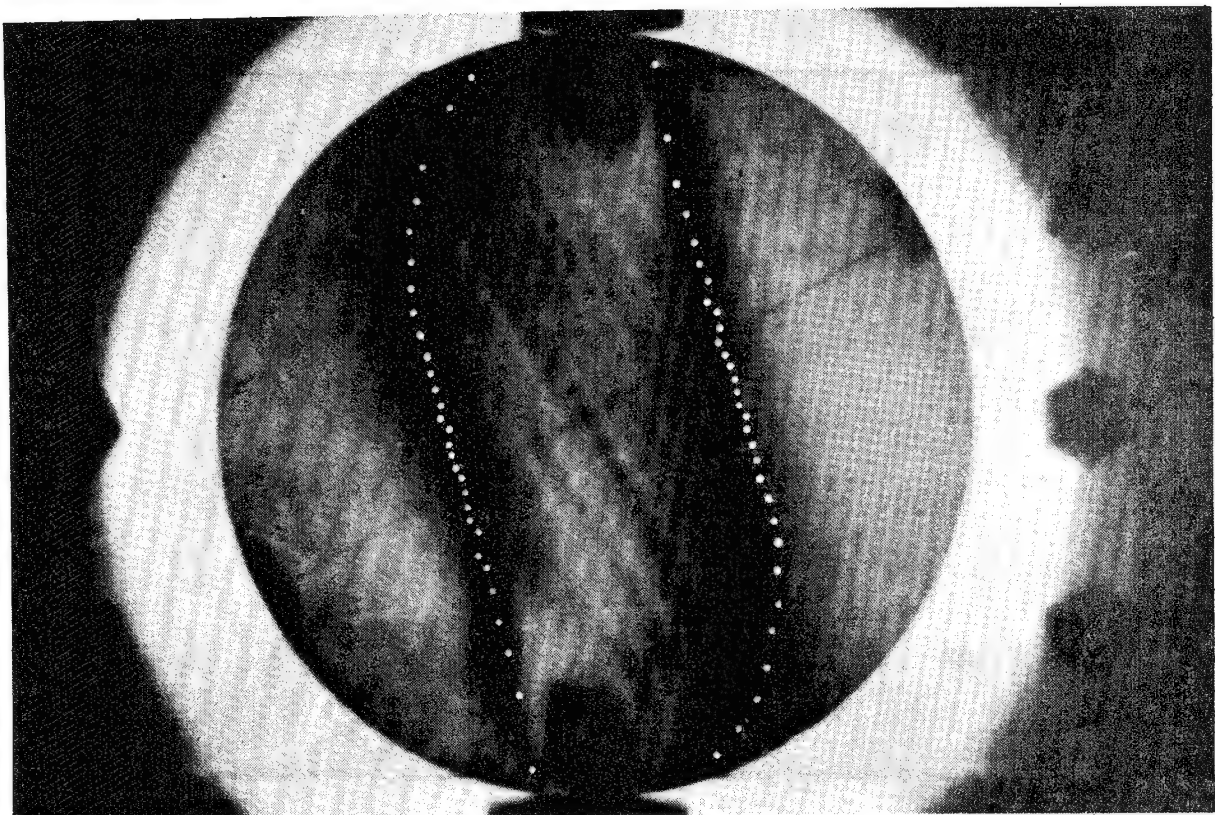
Fig. 48 Comparison between predicted and observed fringe pattern, fibers 30° relative to load, N_T=0.5 (predicted=white dots).

111
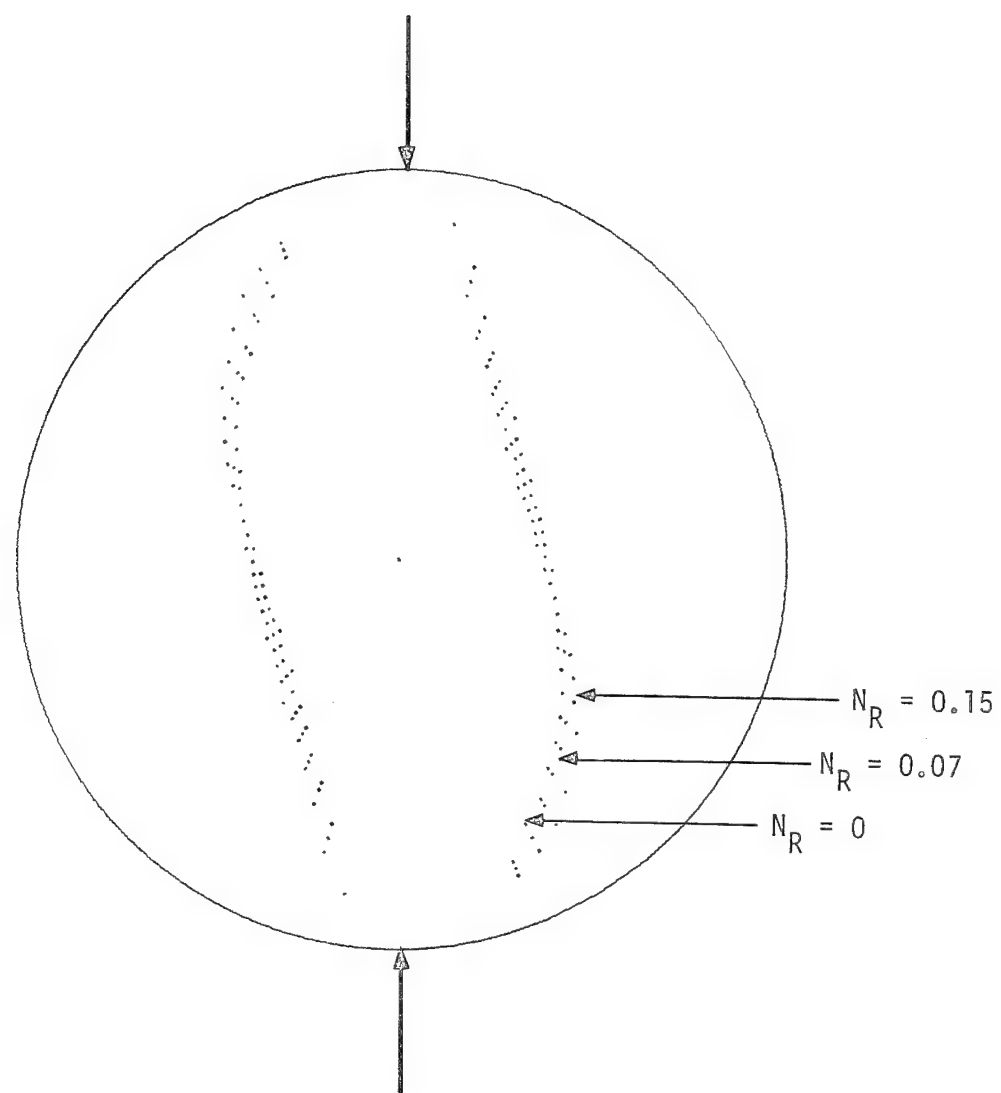
Fig. 49 Effect of level of residual birefringence on predicted fringe
         pattern, fibers 30° relative to load, $N_T=0.5$

predicted fringe pattern for this 30° orientation. Again, it is clear that simply reversing the load direction has an impact on the fringe pattern.

Figure 51 shows the predicted and observed fringe patterns for the case of the fibers making a 45° angle with the diametral compressive load. The load level was 325 lb. (This orientation corresponds to α = +45°.) Again the fibers tended to spread the fringe but the pattern was quite close to the predicted configuration. A close scrutiny of the distance from the disk's center to the half-order fringe, along a diameter perpendicular to the fibers, showed the predicted value to be quite close to the observed value. Figures 52 and 53 show the effects of residual level and load reversal, respectively.

Figures 54-56 shows similar comparisons for the case with the fibers 60° relative to the load direction. Again the load level was 325 lb. (This corresponds to α = +60 in the nomenclature of Appendix B). The spreading of the fringe by the fibers was quite severe. However, the computer-generated fringe pattern shows good correlation between the dots of the predicted fringe pattern and the center of the fringe.

Figure 57 shows the observed and predicted fringe pattern for the situation when the load was 90° relative to the fibers. Here the load level was 520 lb. The correlation for this case was the poorest of all cases. Using a residual birefringence of 0.07 made the correlation better. Figure 58 shows that the predicted fringe pattern for this orientation of load and fibers is fairly sensitive to the level of residual birefringence. As expected, Fig. 59 shows that with residual birefringence the sign of the load is important in determining the nature of the observed fringe pattern.

113

+P, N_R = 0.15

+P & -P, N_R = 0

-P, N_R = 0.15
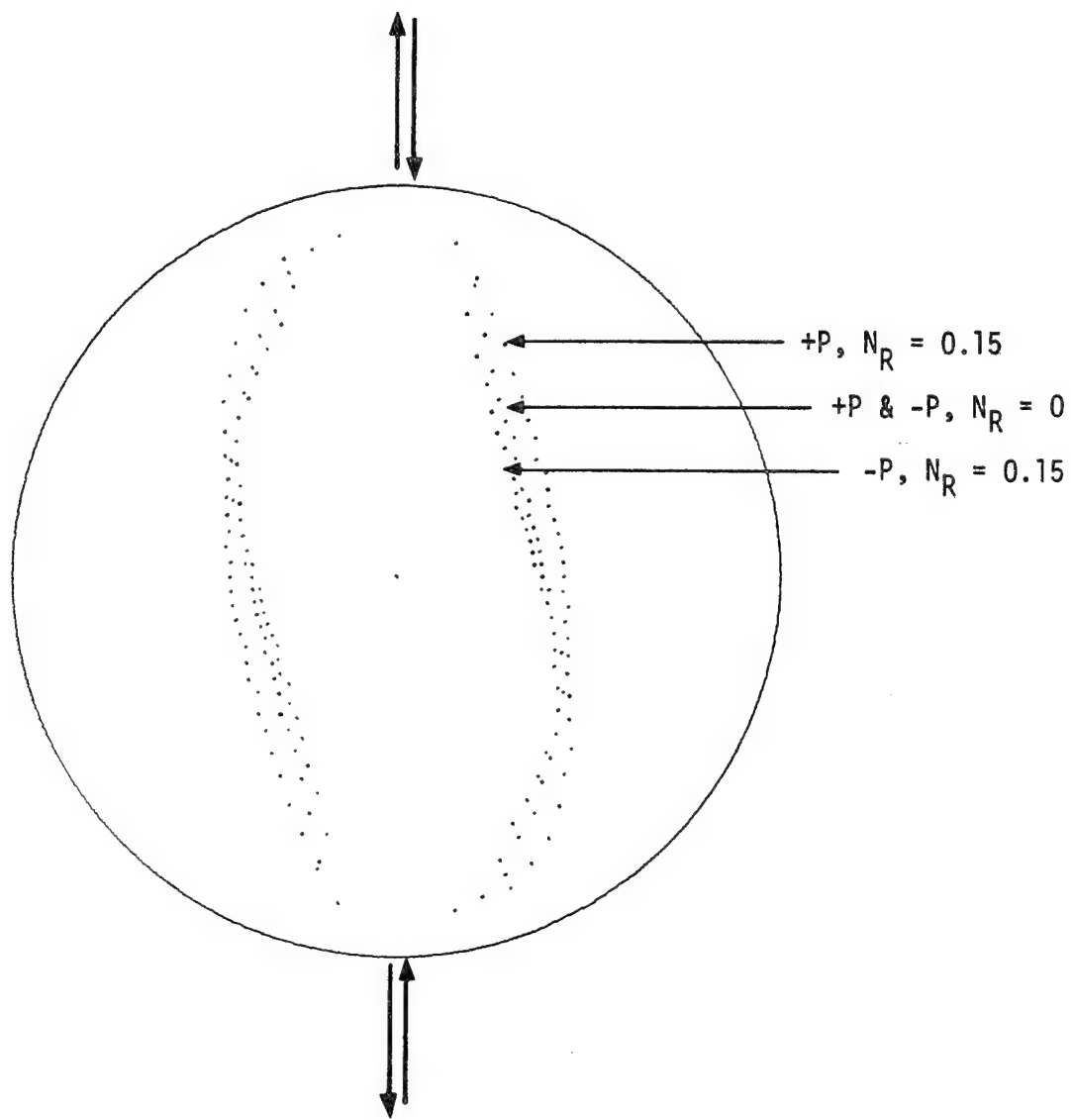
Fig. 50 Effect of residual birefringence on the load reversal fringe
pattern, fibers 30° relative to load, N_T=0.5.
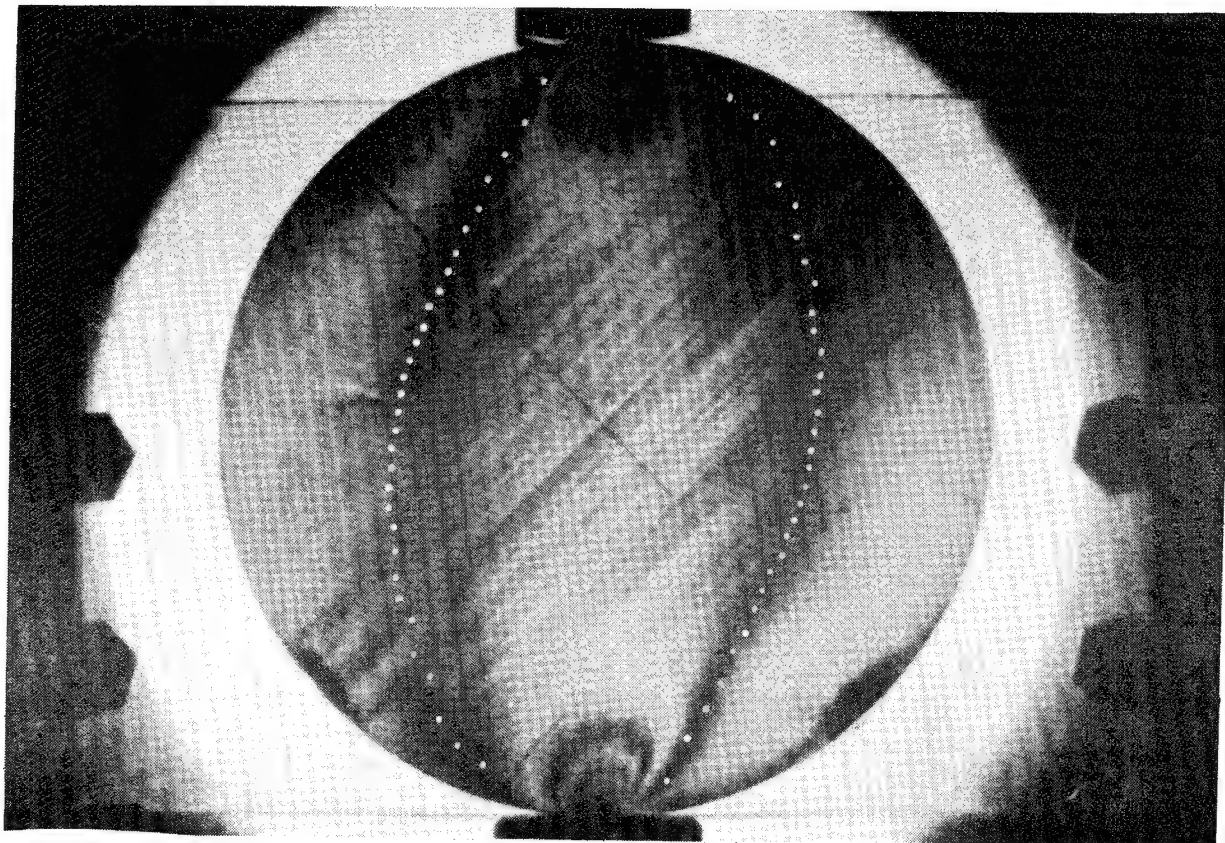
Fig. 51   Comparison between predicted and observed fringe pattern,
fibers 45° relative to load, N_T=0.5 (predicted=white dots).

115
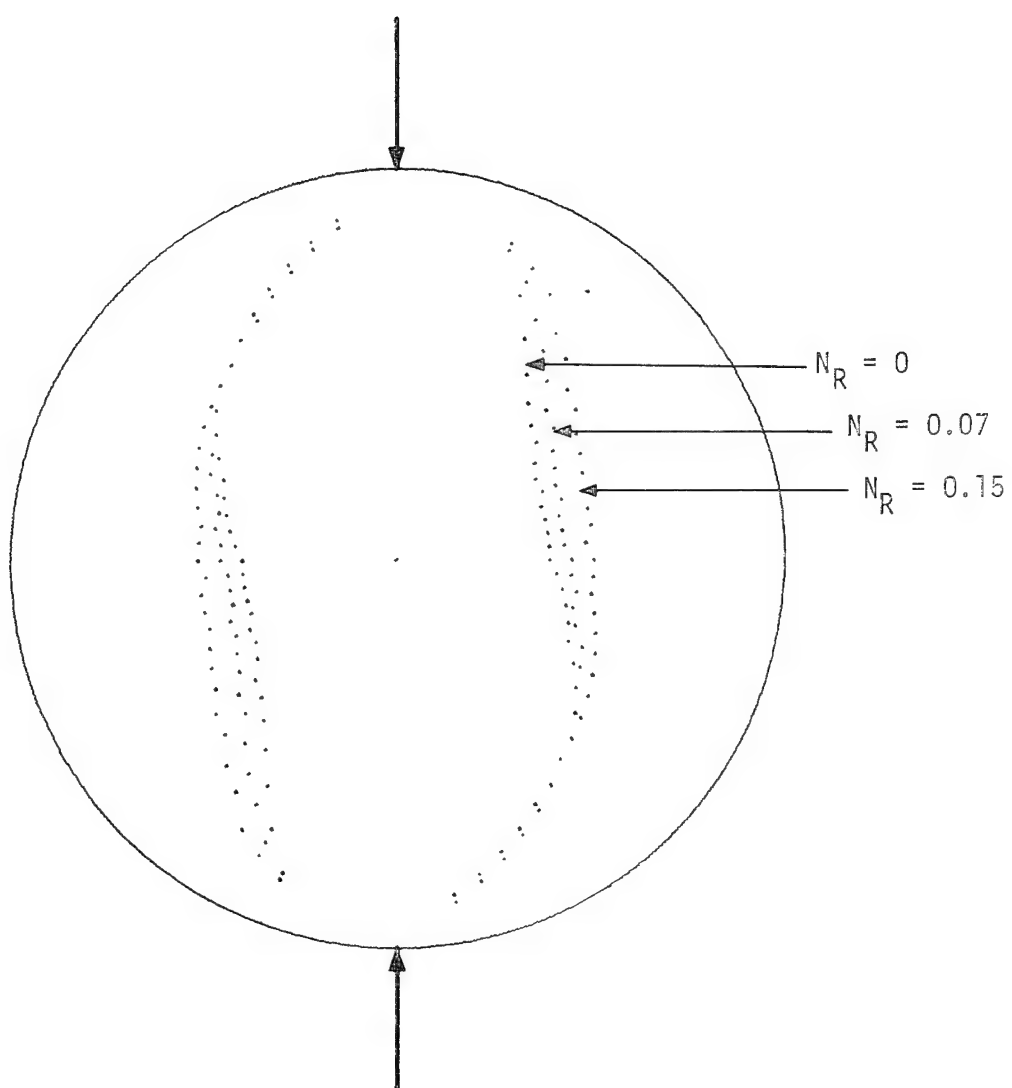
Fig. 52 Effect of level of residual birefringence on predicted fringe
pattern, fibers 45° relative to load, $N_T=0.5$.
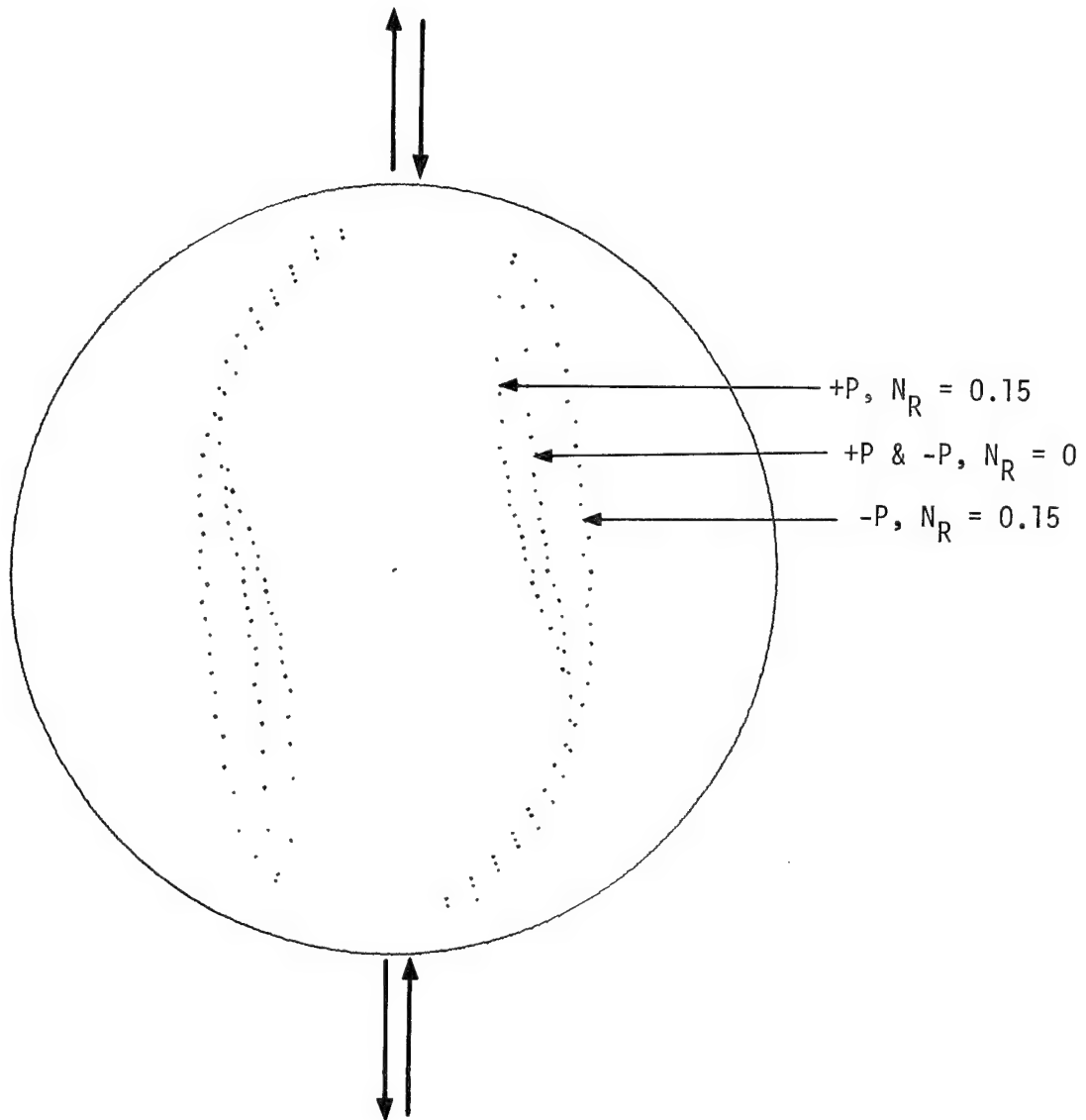
Fig. 53 Effect of residual birefringence on the load reversal fringe
pattern, fibers 45° relative to load, N_T=0.5.
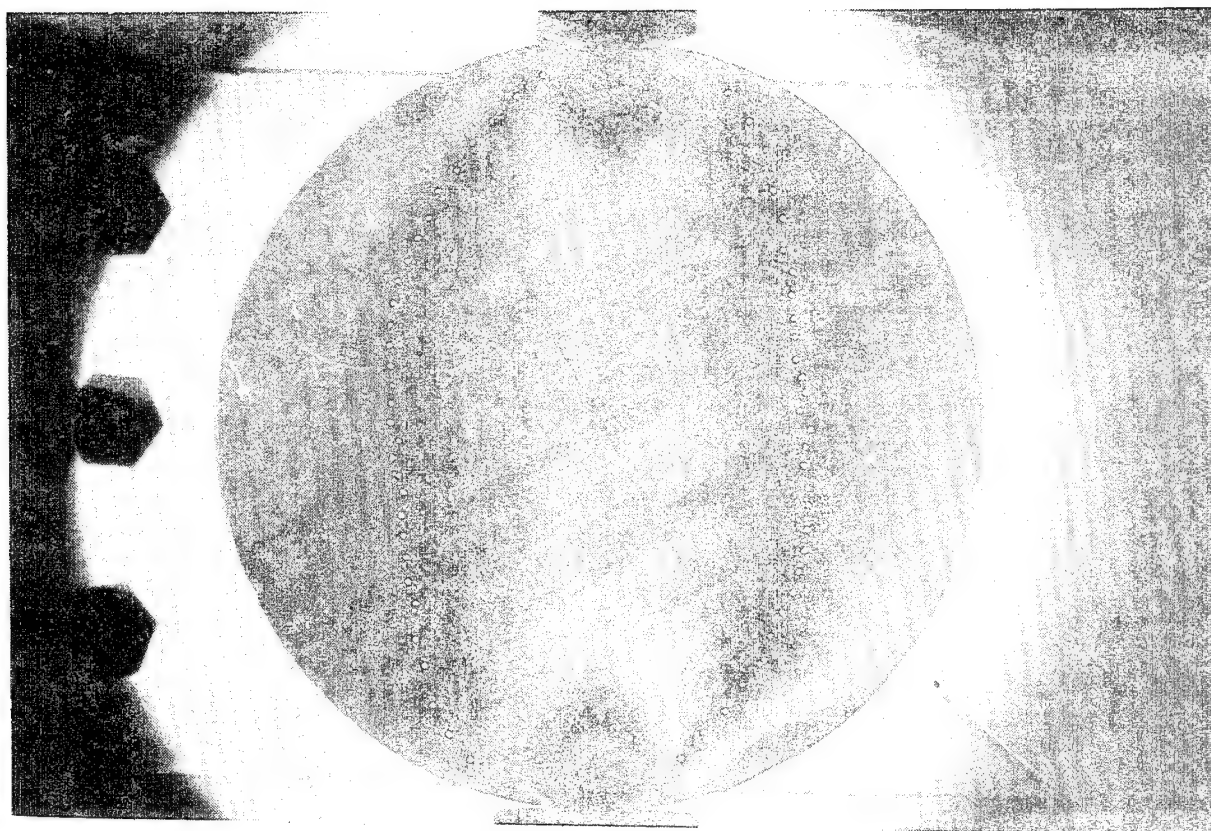
Fig. 54   Comparison between predicted and observed fringe pattern,
fibers 60° relative to load, $N_T=0.50$ (predicted=white dots).
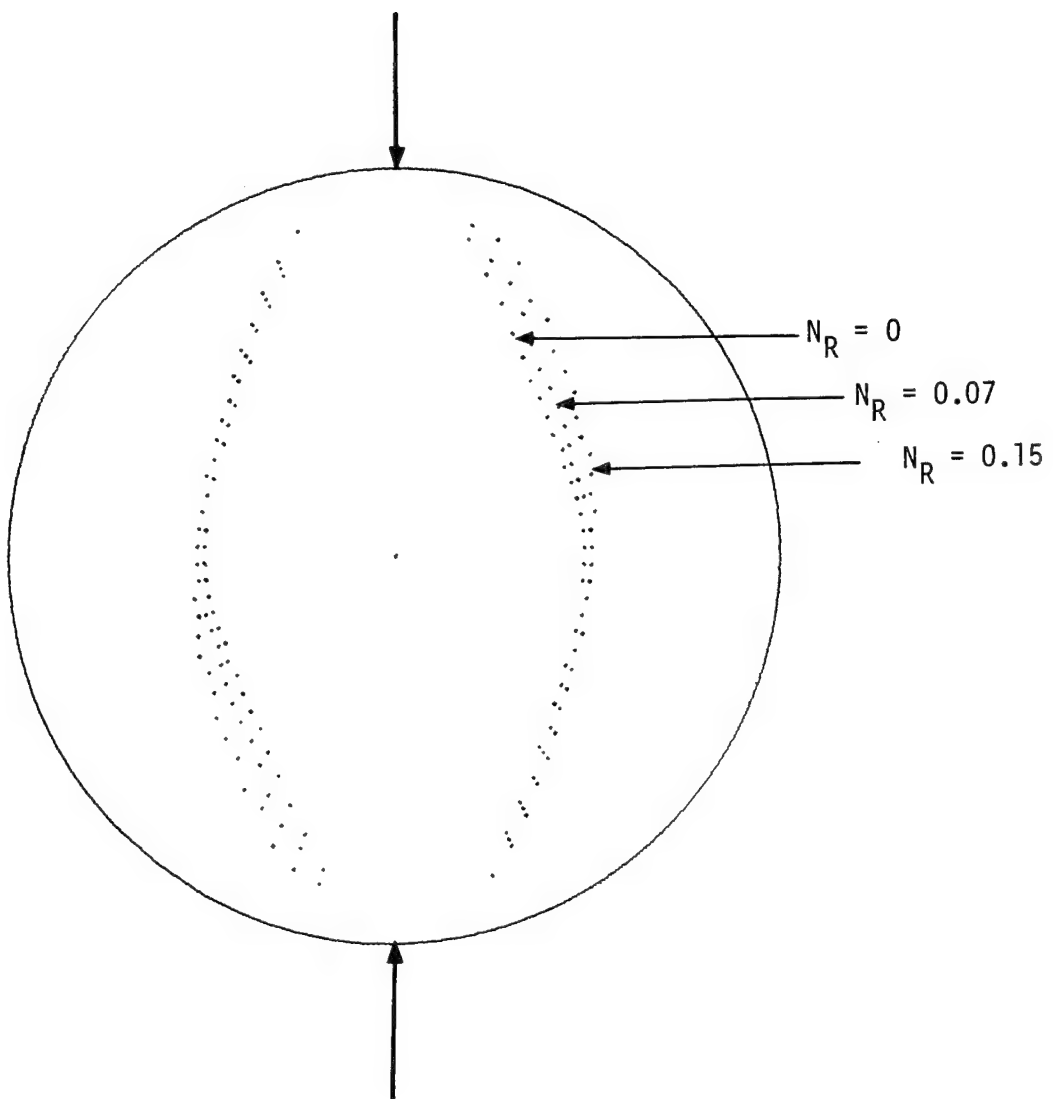
Fig. 55 Effect of level of residual birefringence on predicted fringe
         pattern, fibers 60° relative to load, N_T=0.5.

119

+P, N_R = 0.15

+P & -P, N_R = 0

-P, N_R = 0.15
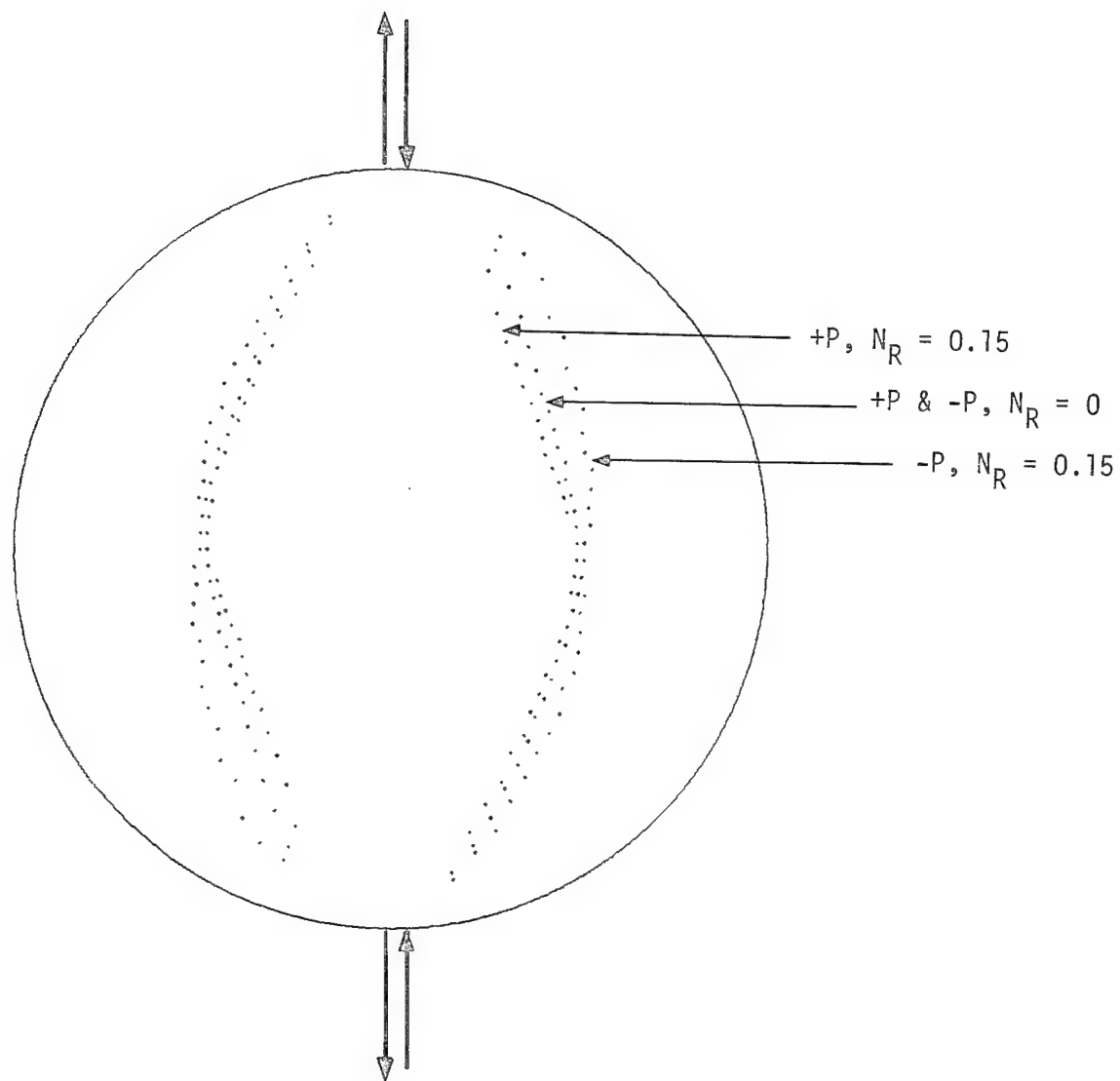
Fig. 56 Effect of residual birefringence on the load reversal fringe
pattern, fibers 60° relative to load, N_T=0.5.

120
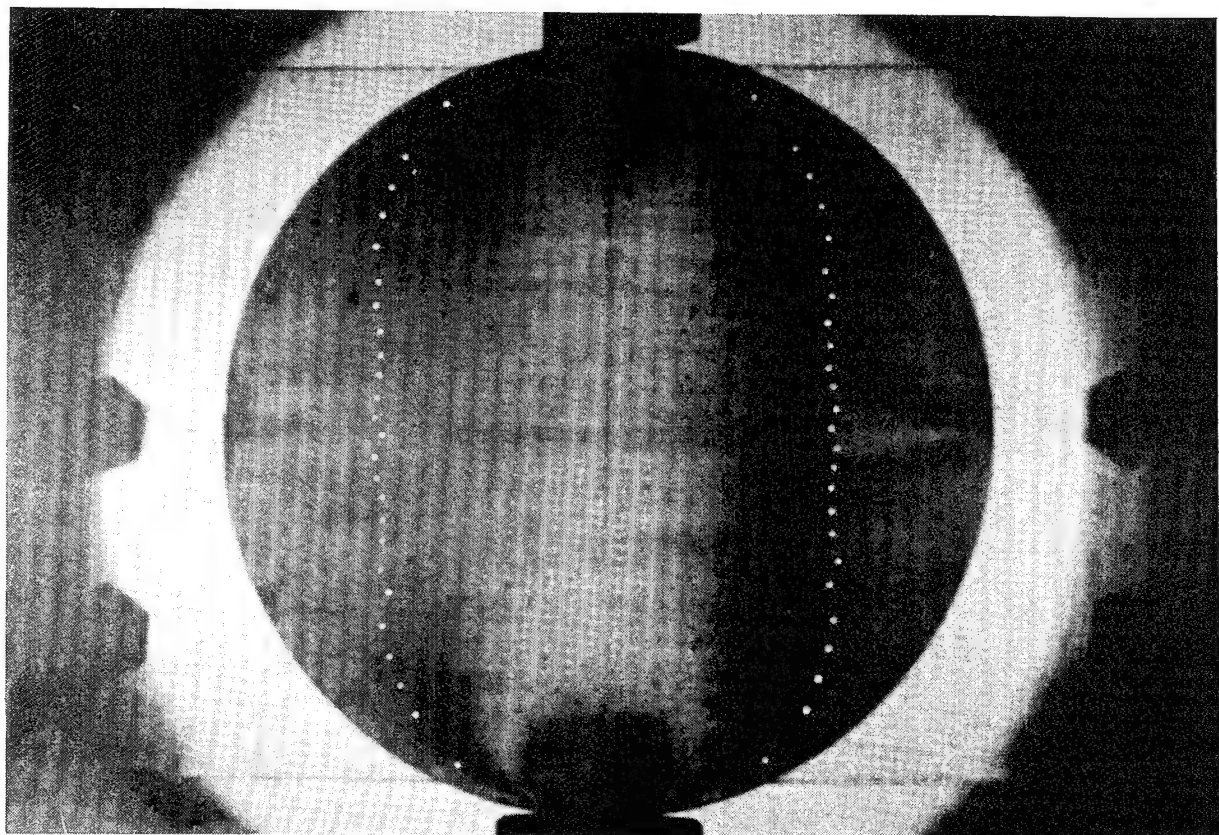
Fig. 57 Comparison between predicted and observed fringe pattern,
fibers perpendicular to load, $N_T=0.5$ (predicted=white dots).
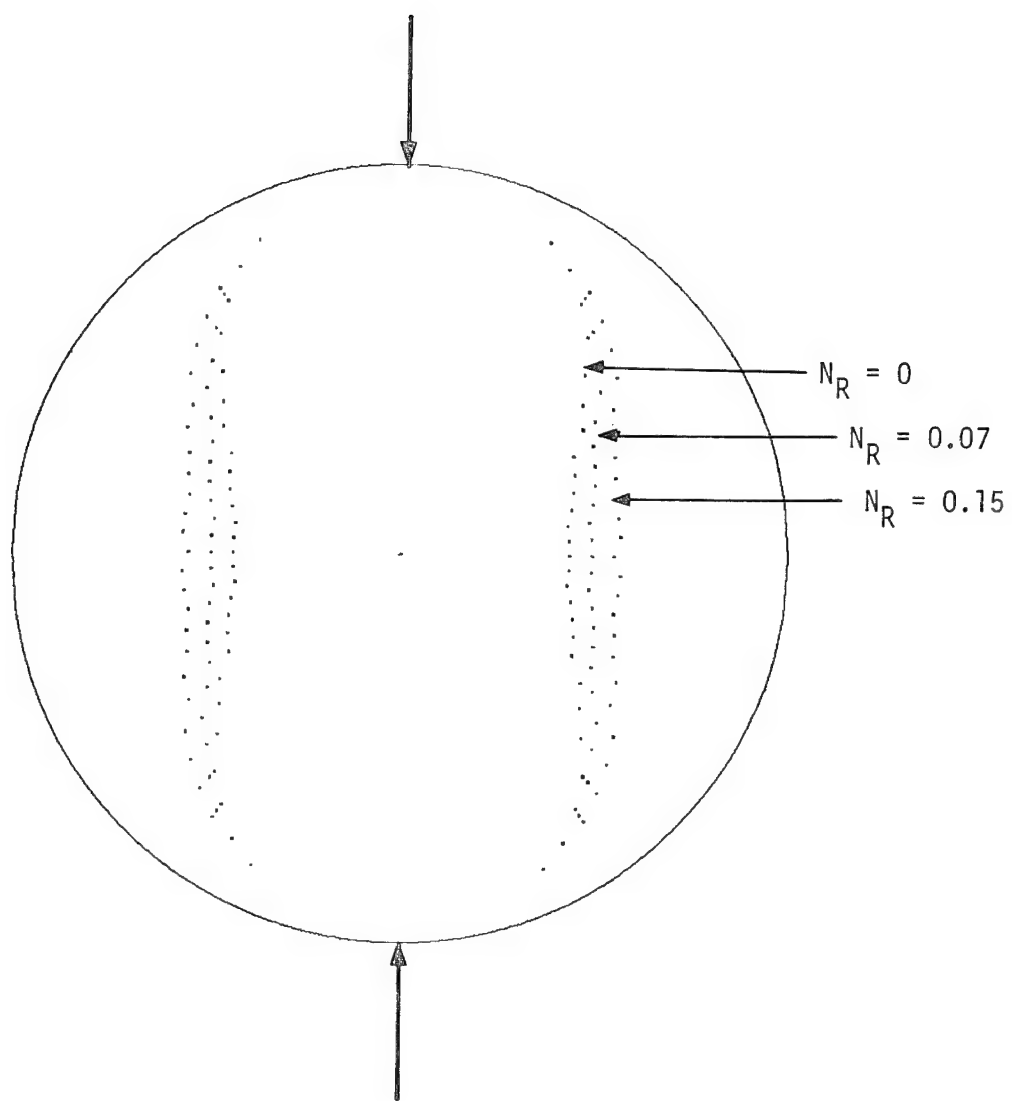
Fig. 58 Effect of level of residual birefringence on predicted fringe
pattern, fibers perpendicular to load, N_T=0.5.
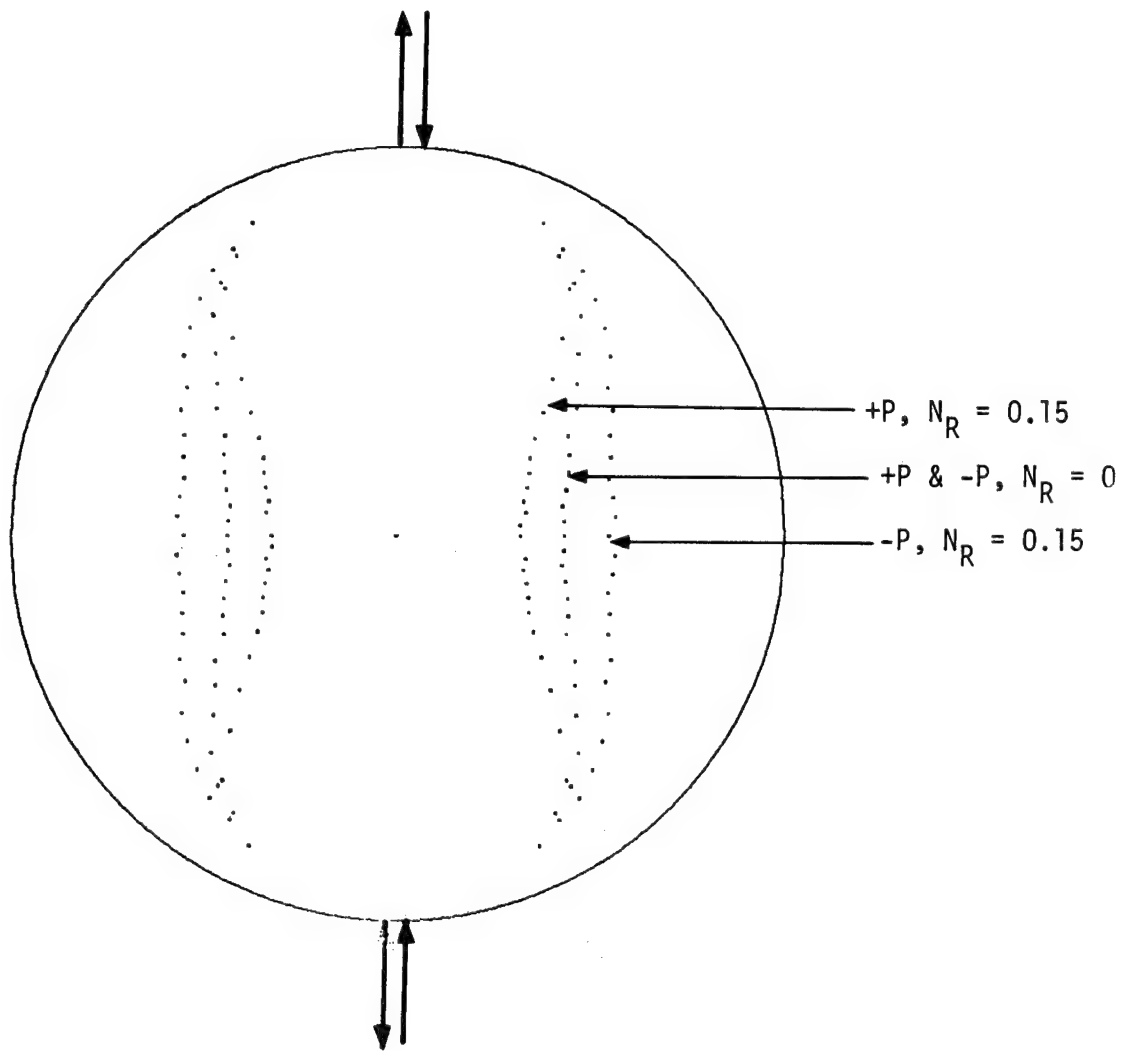
Fig. 59 Effect of residual birefringence on the load reversal fringe
pattern, fibers perpendicular to load, $N_T=0.50$.

123

In conclusion, it appears that the idea of orthotropic photoelasticity is, on-the-whole, a valid concept. However, fringe definition can definitely be a problem. In the cases here, the 'answer' was known and so it is easy to conclude the fringes were, more or less, where they should have been. However, for the 60° orientation (fig. 54), at the two o'clock and eight o'clock locations on the disk (high noon being at the upper load application point), it may not have been possible to sketch in the fringes if it were not known a priori where they were supposed to be located. This is a serious concern in the practical application of orthotropic photoelasticity. This prompted the series of tests described in the following section, namely, a closer look at the predicted and observed fringes.

FORWARD TESTING: LOCAL BEHAVIOR

Whereas forward testing of the global behavior indicated an overall comparison between theory and experiment, a more detailed comparison was of value. For this reason another series of comparisons between theoretical and experimental fringe data was made. Specifically, the total isochromatic fringe order, N_T, and the optical isocline, θ_T, were compared point-by-point across a diameter perpendicular to the load and across a diameter perpendicular to the fibers. These comparisons were made for diametral loads at various angles relative to the fibers. These comparisons are shown in figs. 60-75. The figures show the experimentally measured values and their theoretical predictions. On each figure there are several theoretical predictions, each prediction corresponding to a different level of assumed residual birefringence, N_R. The three levels are the same as in the previous section, $N_R = 0$, 0.07, and 0.15. The isochromatic fringe predictions were based on eq. 60, the stress-optic data for the material, and the complex variable elasticity solution. The optical isocline predictions were based on eq. 66, the stress-optic data for the material, and the elasticity solution. On each figure the horizontal axis shows the nondimensional distance across a diameter as measured from the left edge of the specimen. Measurements were only made from one edge of the disk to the center. The vertical axes show the isochromatic or isoclinic measure, depending on the figure. On the figures, the open squares represent the experimentally measured values. The solid circles represent the theoretical predictions for the case of no residual birefringence ($N_R = 0$). The solid triangles represent the predictions for the case of $N_R = 0.07$ and the solid squares represent the theoretical values for the case $N_R = 0.15$.

Figure 60 shows the comparison of isochromatic fringe order for the case when the loading was aligned with the fibers. The load level used was 407 lb. Obviously the diameter perpendicular to the load and the diameter perpendicular to the fibers were the same for this case. As can be seen, starting at the left edge of the disk and moving toward the center, the experimentally measured isochromatic fringe count decreased to practically zero and then increased to a value slightly greater than one-half at the center. Independent of the assumed level of initial bi-refringence, the theoretically predicted fringe count also approached zero somewhere along the radius. The initial level of birefringence only affected where it went to zero. For no initial birefringence (sol-id circles) the fringe count dropped to zero at $x/D = 0.15$. Experimen-tal measurements (open squares) showed minimial fringe value at $x/D = 0.21$. A residual level of birefringence of 0.07 caused the predicted fringe level to drop to zero at $x/D = 0.23$. The zero fringe was pre-dicted to occur at $x/D \simeq 0.3$ when the residual birefringence was 0.15. Except for near the left edge, the experimental observation correlated well with the predictions based on low (N_R between 0 and 0.07), as op-posed to high ($N_R = 0.15$), levels of residual birefringence.

Figure 61 shows the predicted and observed optical isocline for the case of the load aligned with the fibers. This figure is quite inter-esting. In reality all symbols should be plotted at $\theta = 0^0$ or $\theta = -90^0$. To illustrate an important point, the symbols have been shifted slightly off the $0°$ and $-90°$ values. It was the rapid jump of the isocline from $0°$ to $-90°$ as one moved in along a radius that was important. The x/D location at which the optical isocline jumped from $0°$ to $-90°$ was the same location at which the total isochromatic fringe count dropped

126
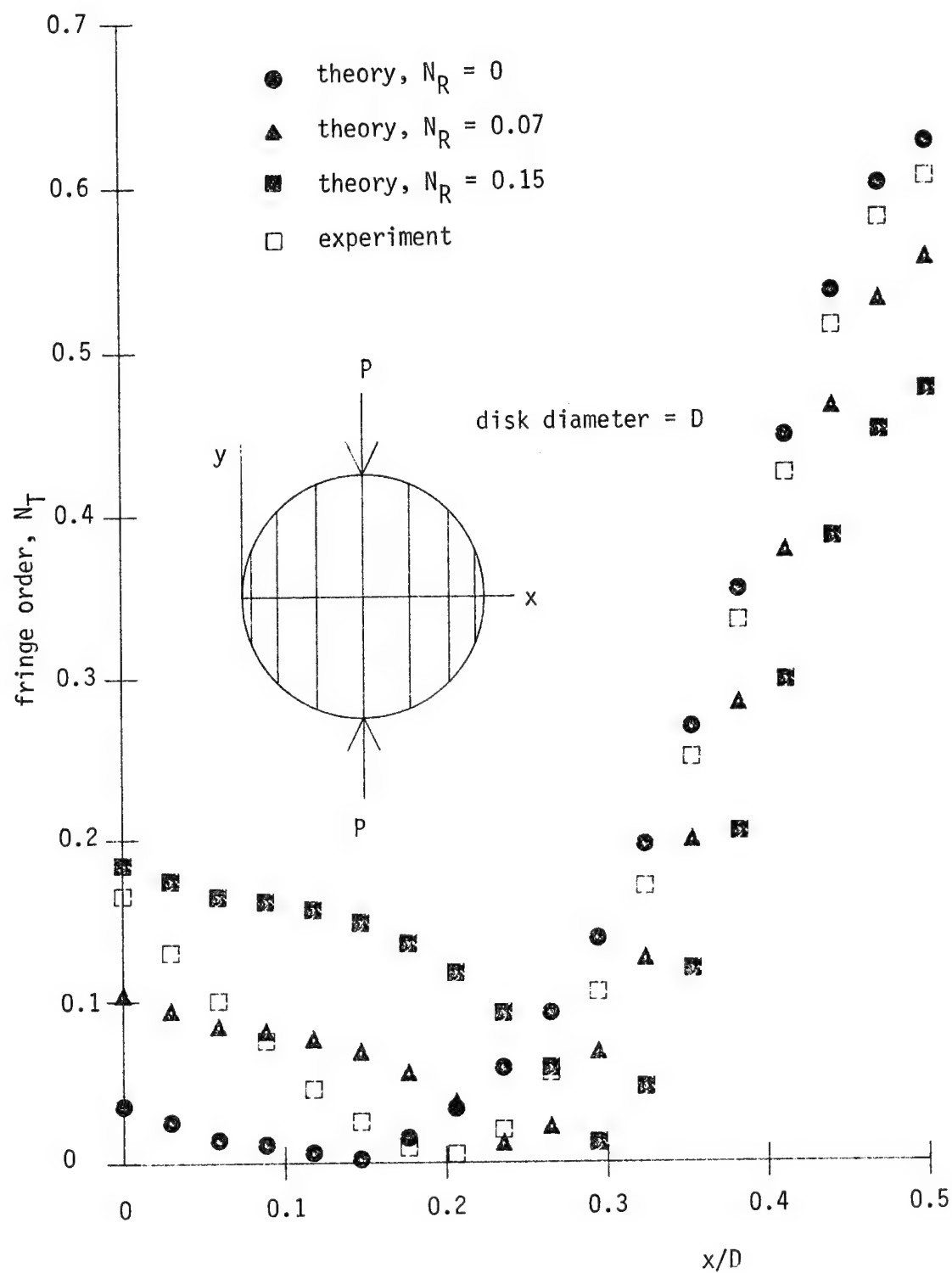
Fig. 60 Comparison between predicted and observed isochromatic fringe order along diameter perpendicular to load, fibers aligned with load.

127
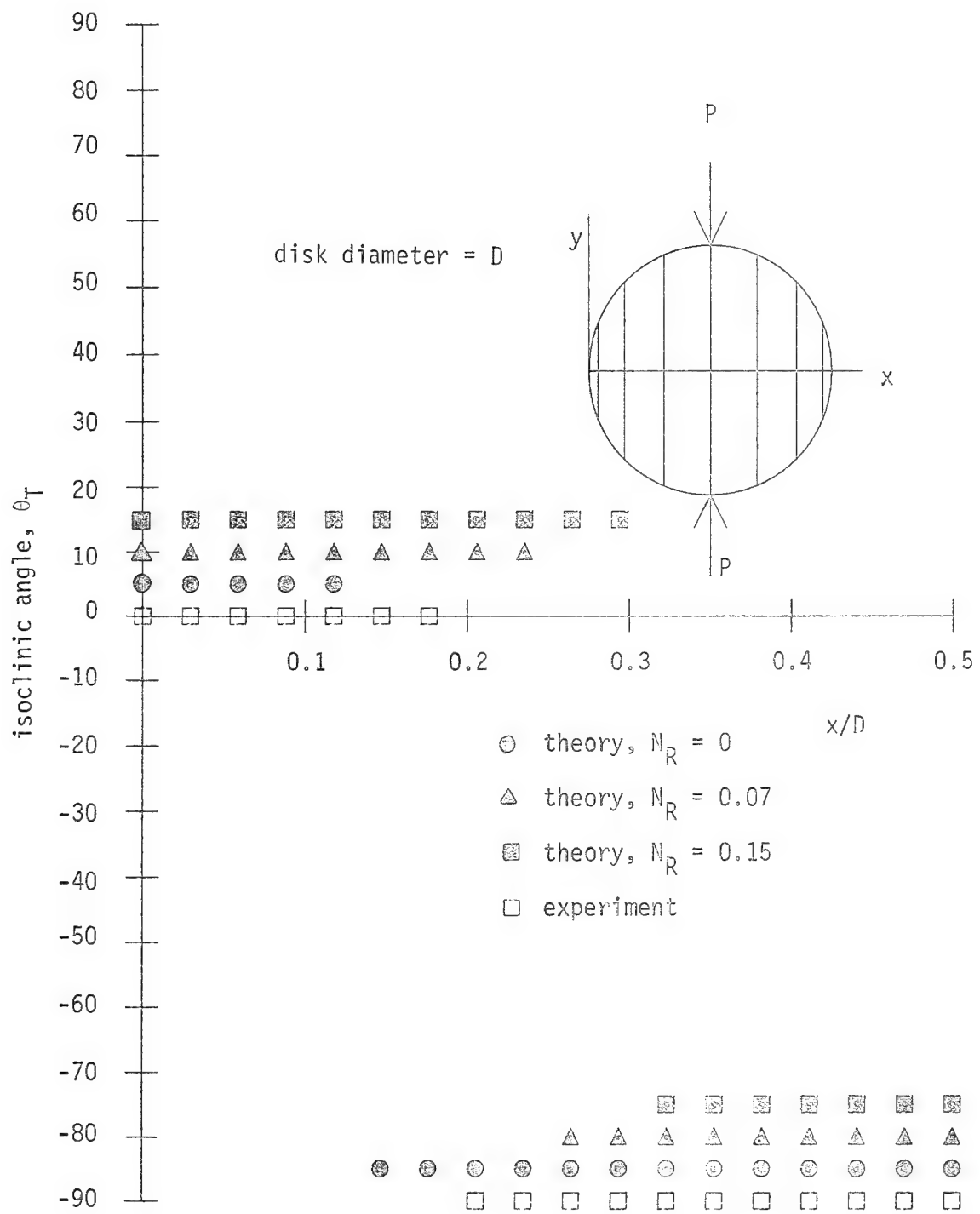
Fig. 61 Comparison between predicted and observed isoclinic angle along diameter perpendicular to load, fibers aligned with load.

128

to zero. This location can be thought of as an optical isotropic point. At such a point the total isochromatic fringe order is zero and the isoclinic is indeterminant. Referring to eq. 60, the second squared bracketed term is zero along the diameter. There is no shear stress, τ_{12}, and the residual isocline, θ_R, is zero. With a proper combination of normal stresses, σ_1 and σ_2, the first squared bracketed term can be made zero. This was precisely the case at the various x/D locations. As can be seen from eq. 60, the value of N_R affects this term going to zero. Examining eq. 66, if the first and second terms of eq. 60 are zero, eq. 66 becomes

$$\tan 2\theta_T = \frac{0}{0} . \qquad (108)$$

This leads to indeterminent values for θ_T. It should be noted, not only does the value of N_R affect the location of the isotropic point, but the load level does also. Since N_R is fixed and σ_1 and σ_2 can be varied by varying the load level, the physical location of the optical isotropic point can be controlled. This was not explored in this study.

From the above discussion, it seems that it may be possible to determine N_R by comparing the theoretical and experimental isotropic point location along the diameter. Since the isotropic point in the experiment was located between the predicted isotropic point for no initial birefringence and the case $N_R = 0.07$, the assumed lower levels of residual birefringence seem to correlate better with experiment than does the assumed higher level.

Figures 62 and 63 show further isochromatic and isoclinic data for the disk with the load aligned with the fibers. Since the diameter perpendicular to the load and the diameter perpendicular to the fiber
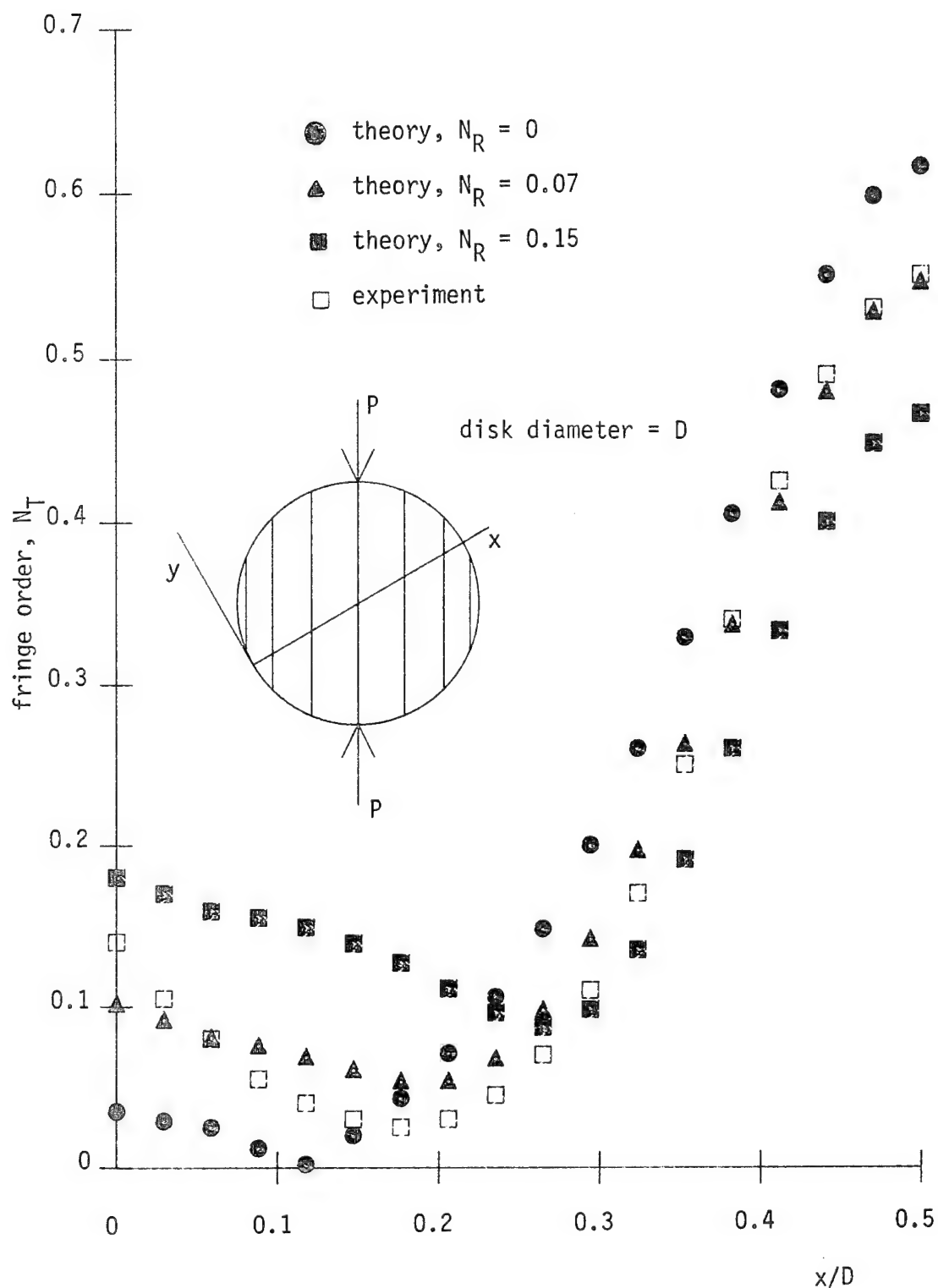
Fig. 62 Comparison between predicted and observed isochromatic fringe order along 30° diameter, fibers aligned with load.
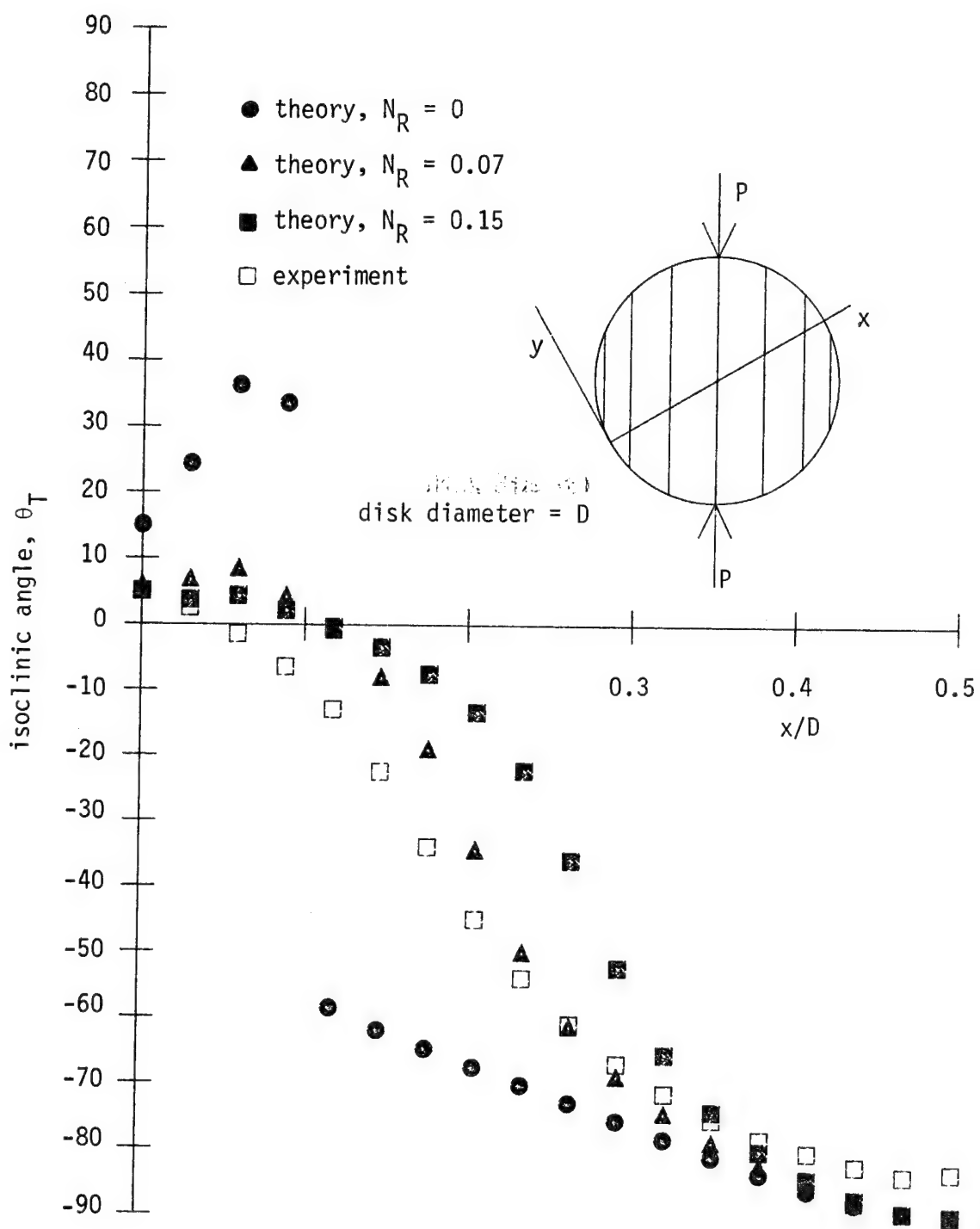
Fig. 63 Comparison between predicted and observed isocline
angle along 30° diameter, fibers aligned with load.

131

were the same, data was studied along another diameter. This diameter was arbitrarily picked to be a diameter which made a 30° angle with the horizontal diameter.

Moving from the edge of the disk toward the center along the 30° diameter produced trends in the data similar to the horizontal diameter data. The isochromatic fringe number decreased and then increased to about 0.5. The minimum value of the theoretically predicted isochromatic varied, depending on the assumed value of initial birefringence. For no assumed initial birefringence (solid circles), the isochromatic fringe value dropped to zero at x/D = 0.12. The experimentally measured isochromatic never dropped to zero. The same was true for the theoretical predictions based on assumed initial birefringence values of 0.07 and 0.15.

Figure 63 shows the theoretically predicted and the experimentally measured optical isocline parameter for the 30° diameter. There were vast differences, depending on the assumed level of initial birefringence, between the predicted and the measured values. The experimentally measured isocline varied smoothly from about 5° at the outer edge, through 0° at x/D = 0.06, to -85° at the center of the disk. The theoretical cases of N_R = 0.07 and N_R = 0.15 also varied smoothly but the case N_R = 0 exhibited a sharp jump at x/D = 0.12. This was the same location that N_T = 0 for this theoretical case. This behavior was similar to the jump behavior in the optical isocline along the horizontal diameter for this fiber/load orientation. Again, except for the outer edge, the theoretical predictions for the case N_R = 0.07 seemed to correlate the best with experimental observations. The isochromatic predictions almost coincided and the isocline predictions were close.

Recall, there was concern over choosing the value of N_R from the tensile and compression test data. There were values, though unreliable, of N_R as high as 0.21. There was strong evidence from the tensile and compression data that N_R was in the range 0.07 - 0.15. The value of 0.15 was chosen from the test data of the 0°, 90°, and 45° specimens. Yet the experimentally observed global and local behavior correlated better with theoretical predictions obtained by using a lower value of assumed residual birefringence, specifically N_R = 0.0 or 0.07. This trend toward good correlation with $0 < N_R < 0.07$ in the global and local tests contradicted the findings of the 0°, 90°, 45° tests. The contradiction is still a puzzle.

Figures 64 and 65 show the isochromatic and the isoclinic behavior along a horizontal diameter for the case of the fibers rotated 30° from the applied diametral load. The observed isochromatic and isoclinic behavior was similar to the other two cases discussed. The experimentally observed isocline changed from negative values to positive values at x/D of about 0.08. The theoretical prediction for the case N_R = 0 showed a very sharp jump in isocline at this x/D location. At the same time, the isochromatic prediction for this level of birefringence practically dropped to zero at this same location. Throughout the testing of all cases presented in the figures in this section, when the isocline experienced a rapid change with spatial location, the isochromatic fringe number was going to a minimum value. This was true with the experimental observations and all theoretical predictions. It seemed that the closer the isochromatic fringe approached zero, the more dramatic was the jump in the isoclinic.
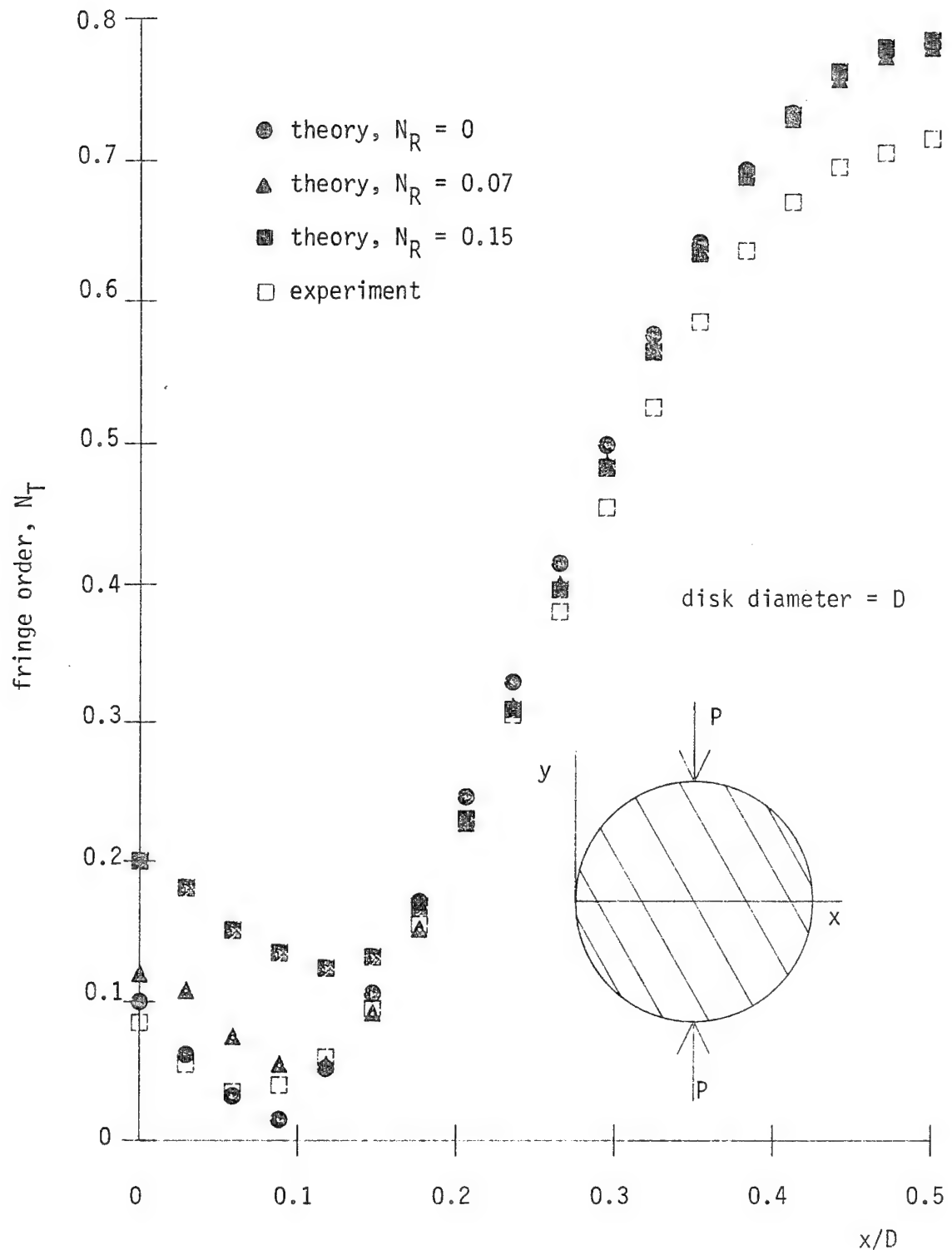
Fig. 64 Comparison between predicted and observed isochromatic
fringe order along diameter perpendicular to load,
fibers 30° relative to load.
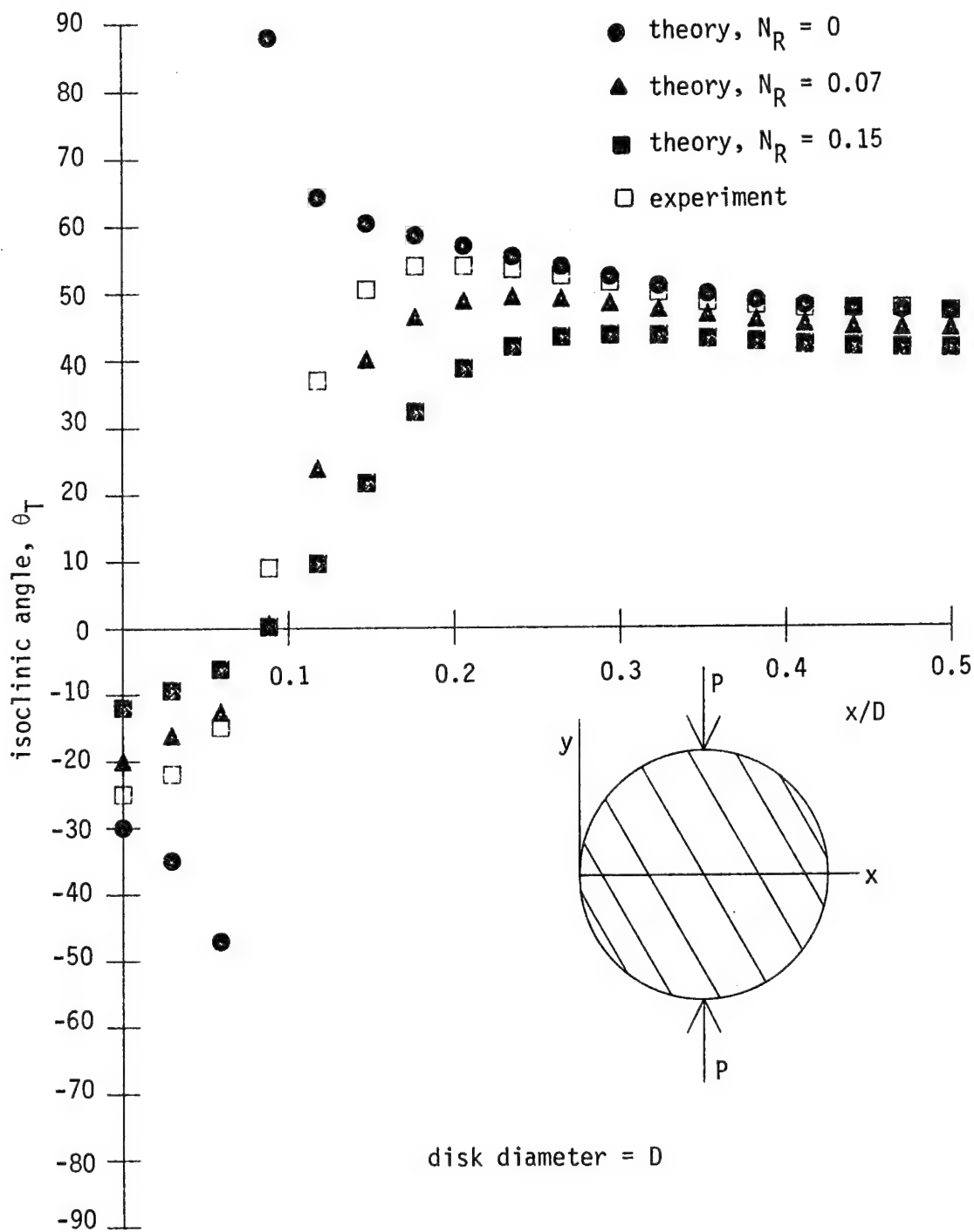
Fig. 65 Comparison between predicted and observed isoclinic
angle along diameter perpendicular to load, fibers
30° relative to load.

135

Several additional comments should be made regarding the data in figs. 64 and 65. In the range $0.2 \leqslant x/D \leqslant 0.5$, the assumed level of residual birefringence did not affect the predicted isochromatic. All predictions coincided. Because of this, in that same range along the diameter, the correlation between predicted and observed isochromatics didn't seem to favor any particular level of N_R. However, the isoclinic figure showed reasonable correlation with the $N_R = 0.07$ case, particularly the characteristics near the change in sign in the isoclinic.

Figures 66 and 67 show more isochromatic and isocline data for the case with the fibers oriented 30° relative to the load. These figures are for the diameter perpendicular to the fiber direction. Observations and comments similar to the discussion of previous figures can be made regarding these two figures. As seen in fig. 67, for example, the experimentally observed isoclinic experienced a sharp change at $x/D \approx 0.14$. It was at this location N_T was a minimum. At first, the sharp changes in isoclines were viewed as an undesirable feature. Eventually, however, these sharp changes were a welcome characteristic. They served as sort of a datum for minimum isochromatic fringe counts and a point where there was most likely a change in sign in the isoclinic. Polariscopes, by their nature, respond similarly to isoclinics of complementary values, i.e., isoclinics that differ in value by 90°. When the sign of the isoclinic changes, or the isoclinic otherwise goes to zero, interpretation of the data can be confusing. The existence of the sharp changes helped clarify the interpretation.

Figures 68-75 show the isoclinc and isochromatic data for cases when the fibers were at 45° and 90 to the load direction. These cases will not be discussed in detail. In light of previous discussions, some

136
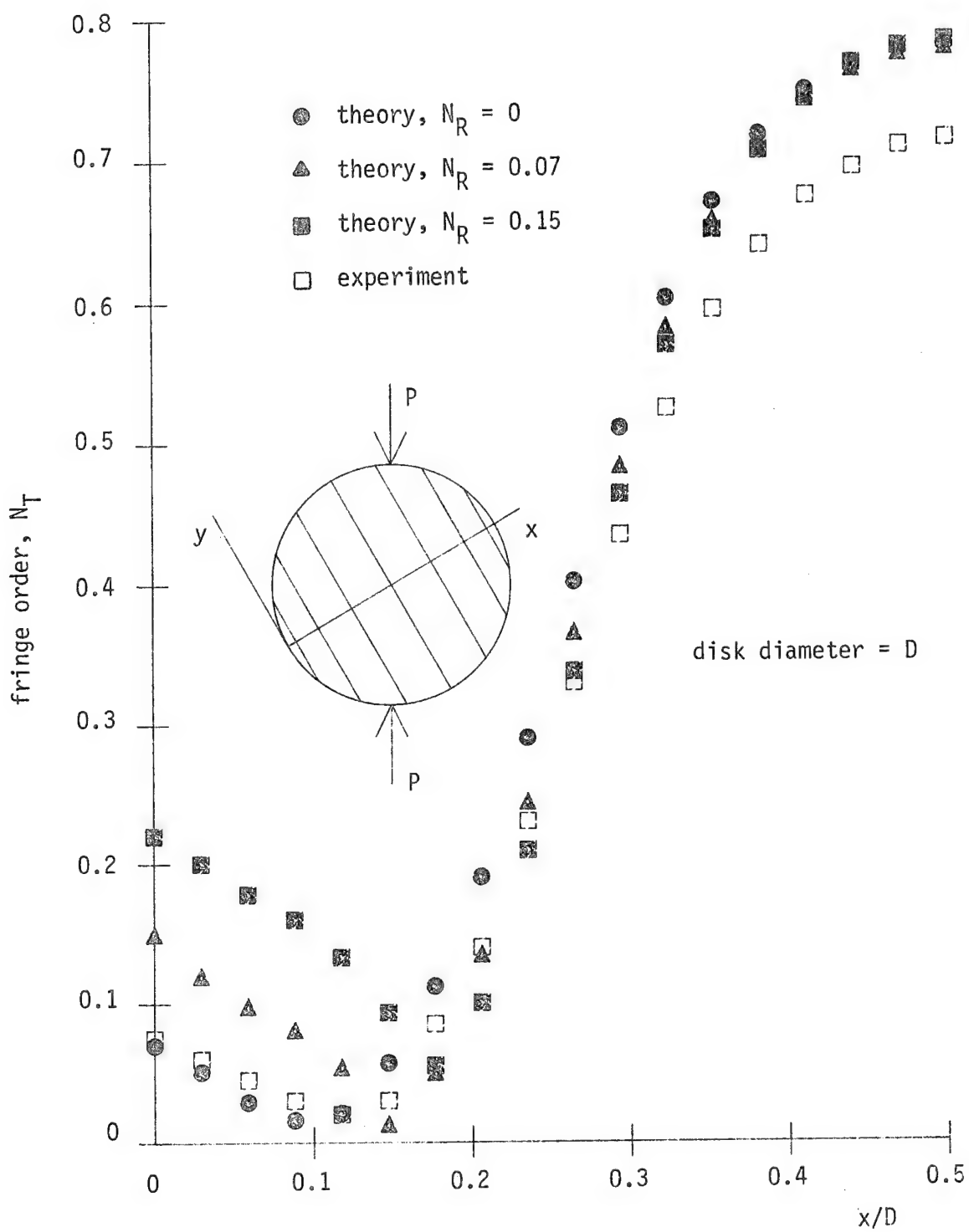
Fig. 66   Comparison between predicted and observed isochromatic
fringe order along diameter perpendicular to fibers,
fibers 30° relative to load.

137
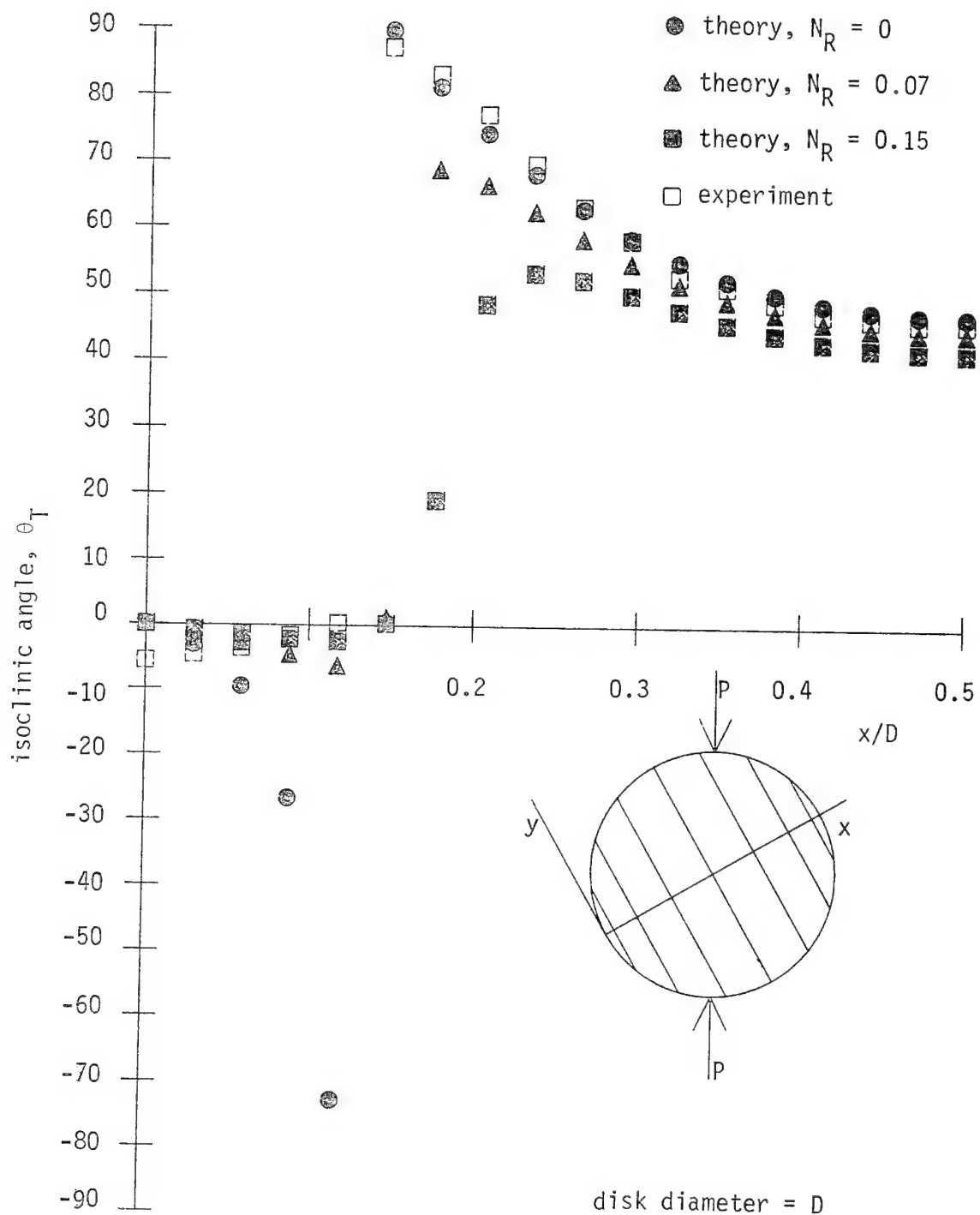
Fig. 67   Comparison between predicted and observed isoclinic
angle along diameter perpendicular to fibers, fibers
30° relative to load.

138
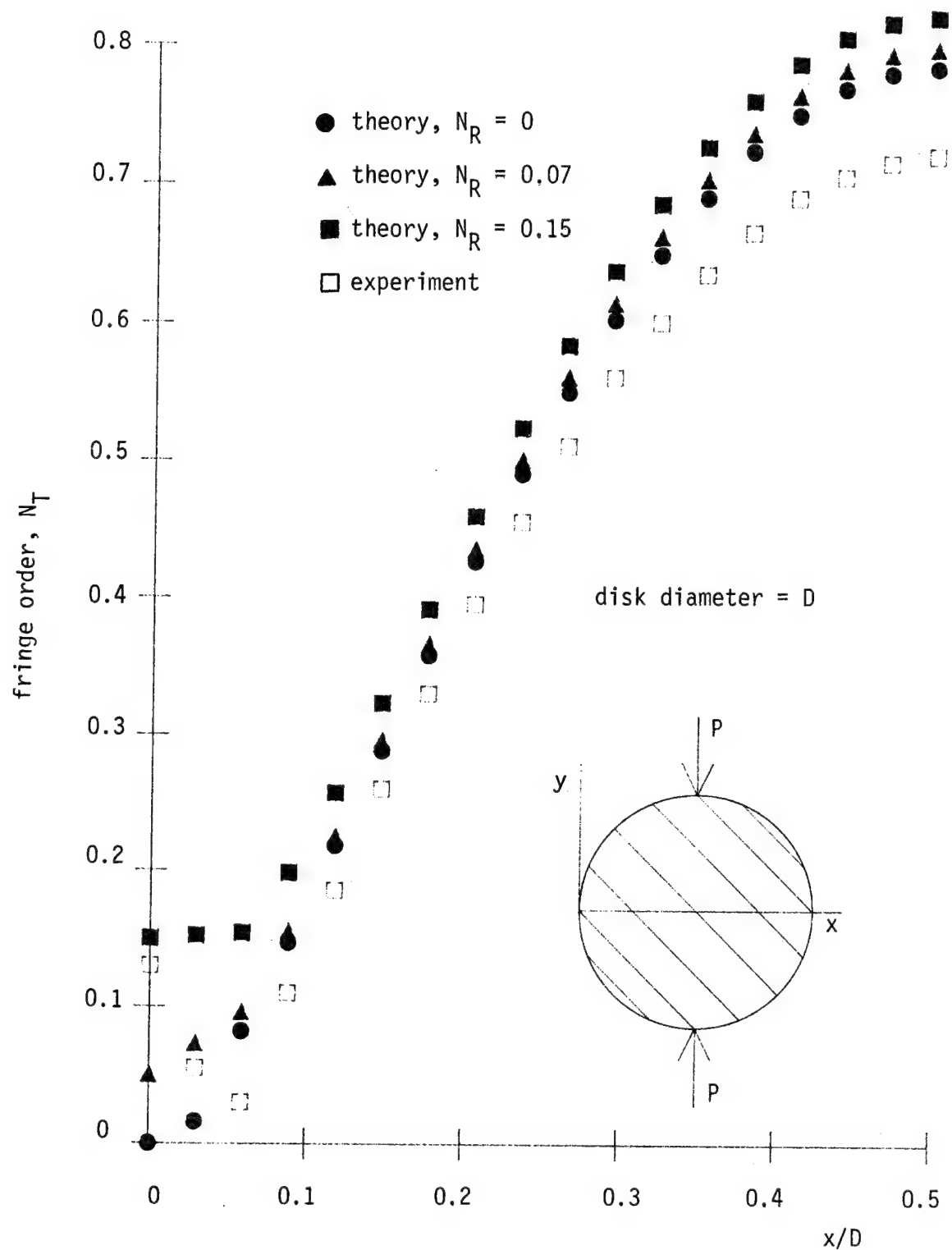
Fig. 68 Comparison between predicted and observed isochromatic fringe
order along diameter perpendicular to load, fibers 45° relative
to load.
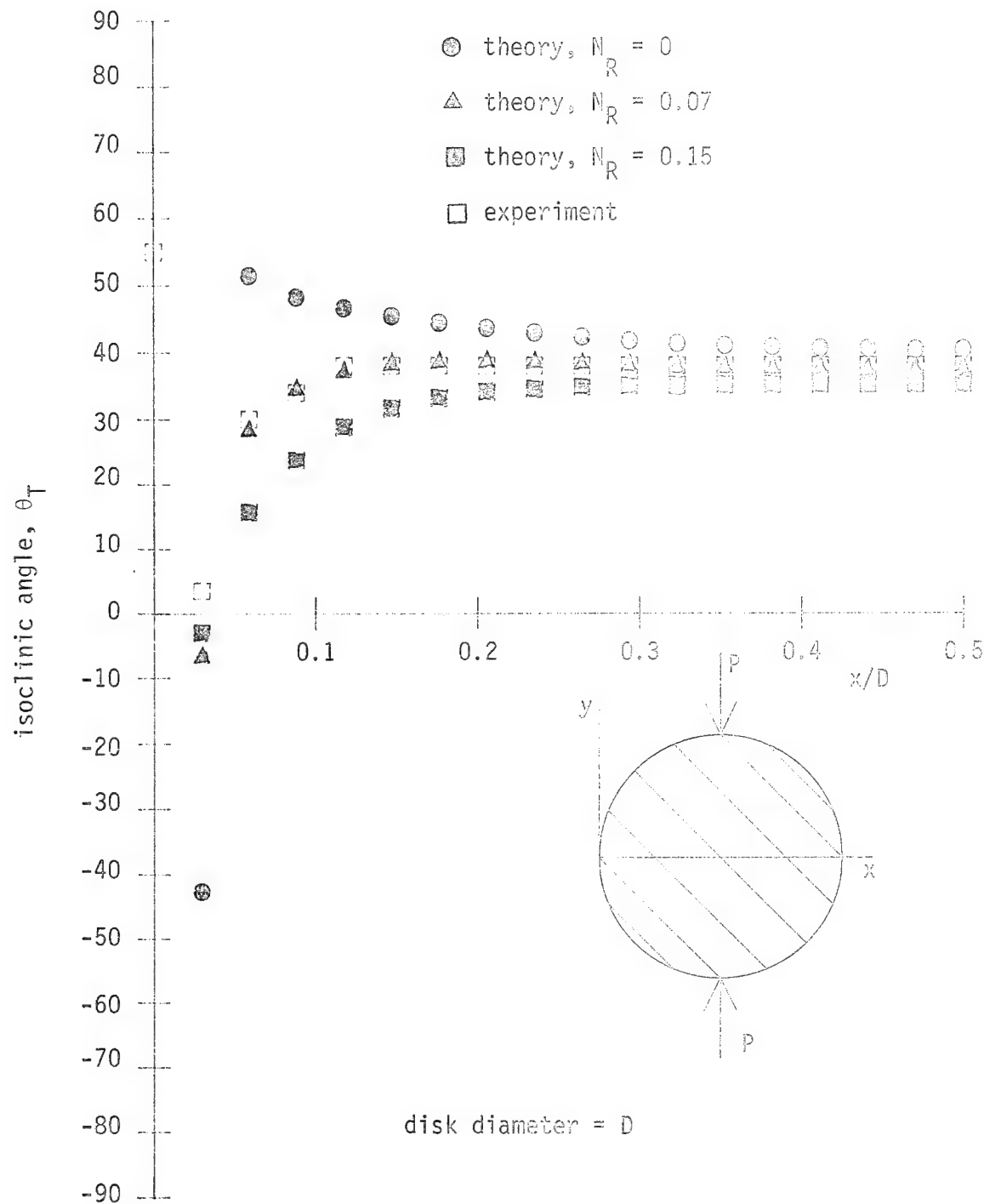
Fig. 69 Comparison between predicted and observed isocline angle along diameter perpendicular to applied loads, fibers 45° relative to load.
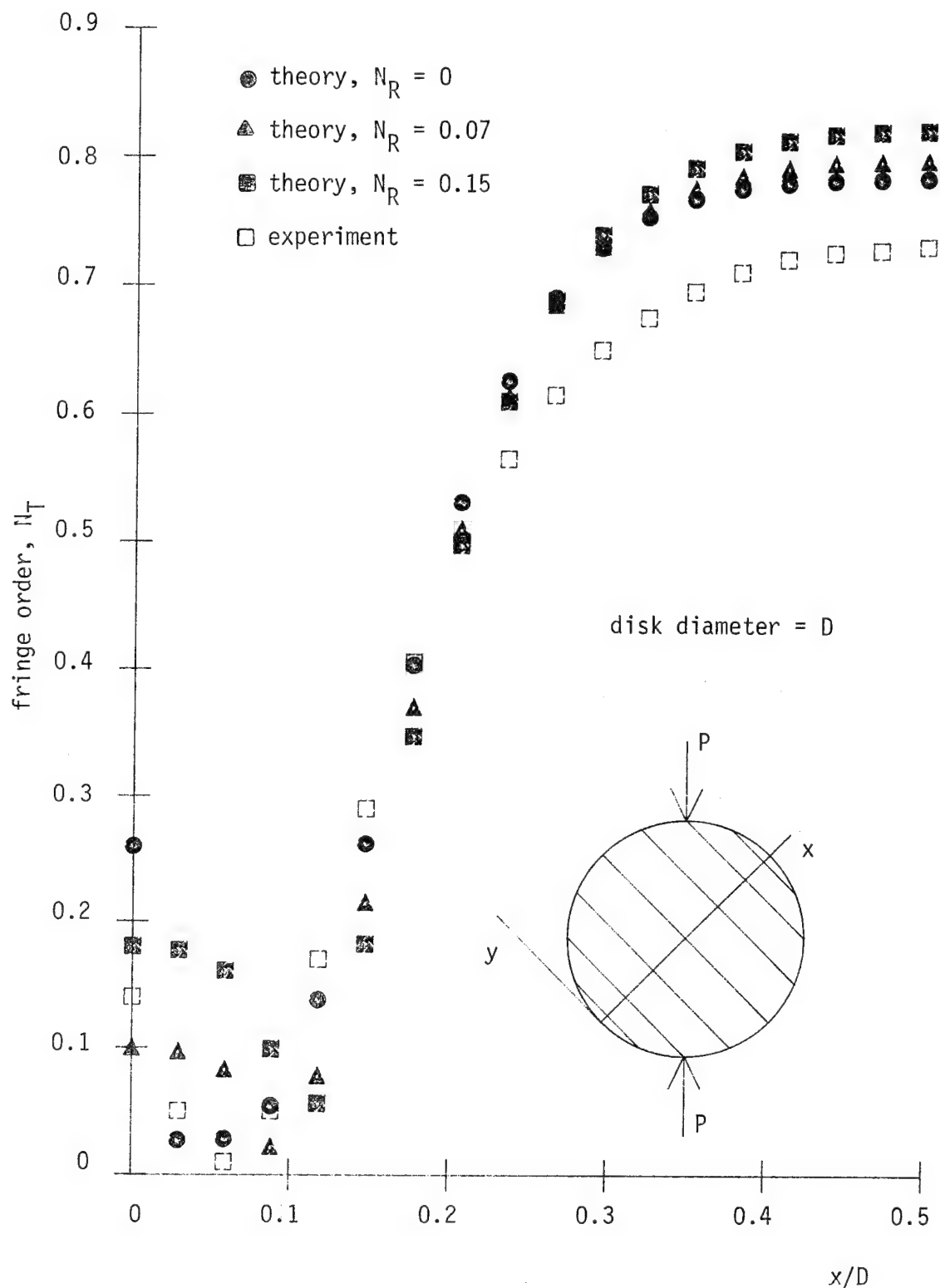
Fig. 70   Comparison between predicted and observed isochromatic
          fringe order along diameter perpendicular to fibers,
          fibers 45° relative to load.

141
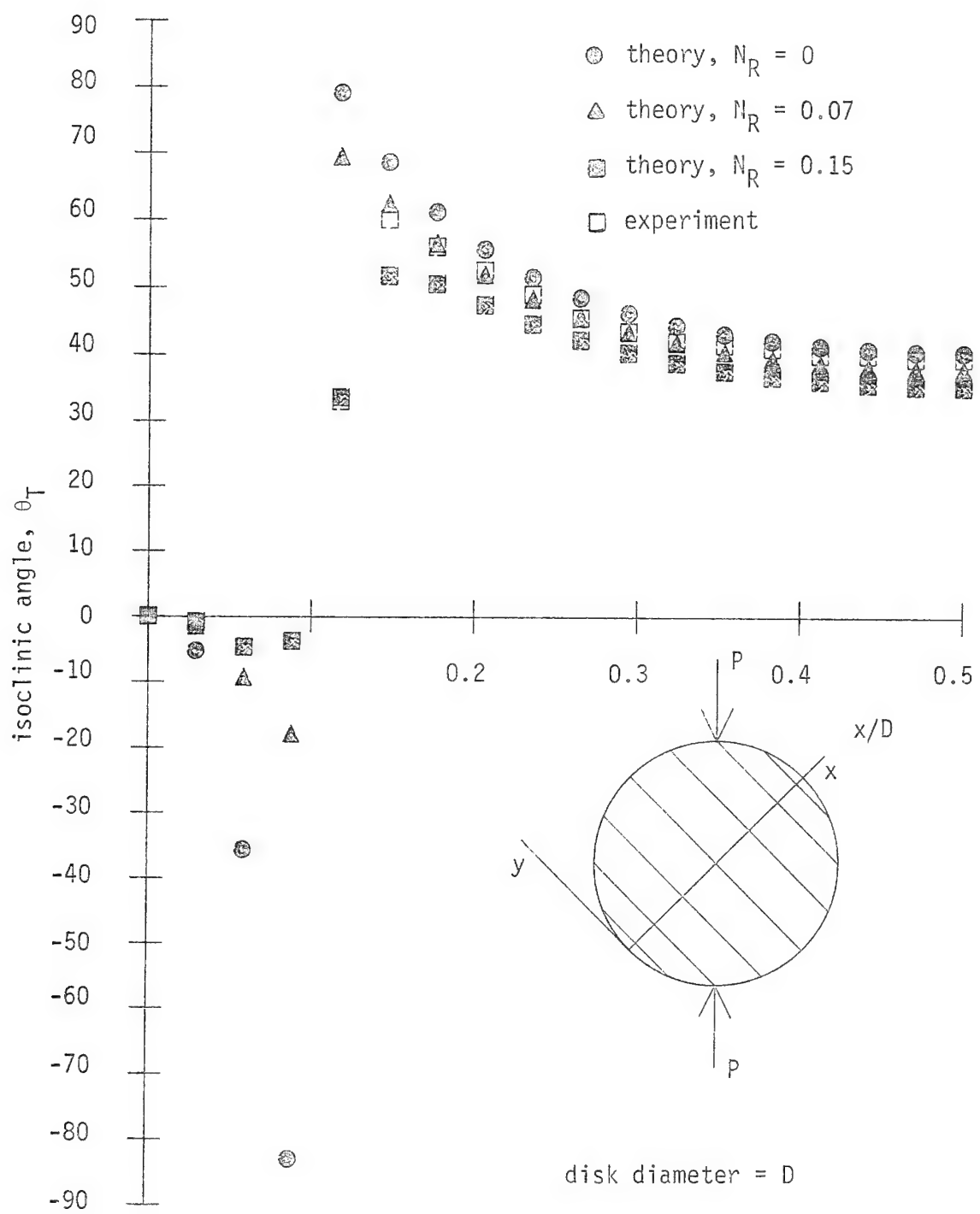
Fig. 71 Comparison between predicted and observed isoclinic angle along diameter perpendicular to fibers, fibers 45° relative to load.
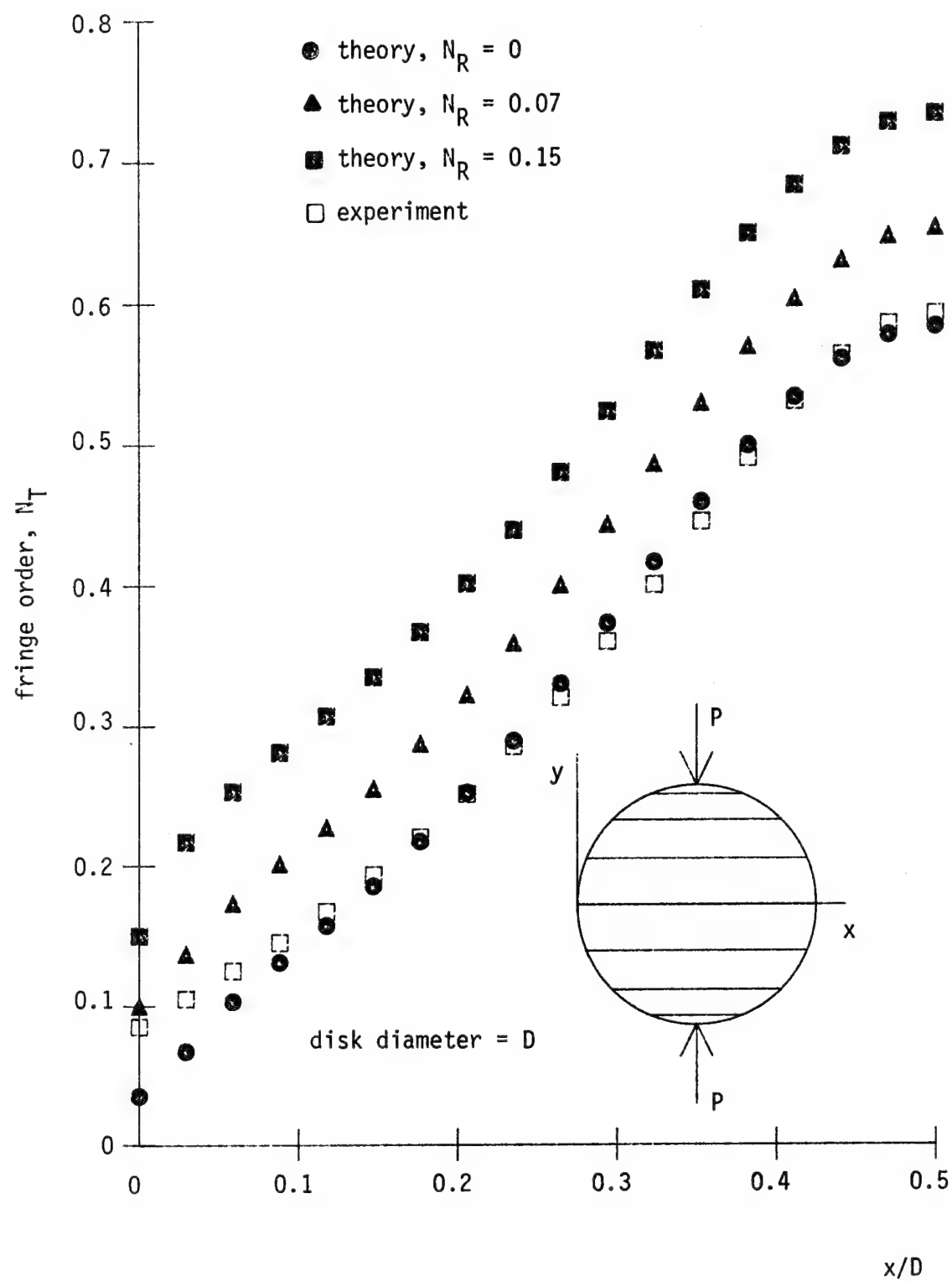
Fig. 72 Comparison between predicted and observed isochromatic
fringe order along diameter parallel to fibers, fibers
perpendicular to load.

143
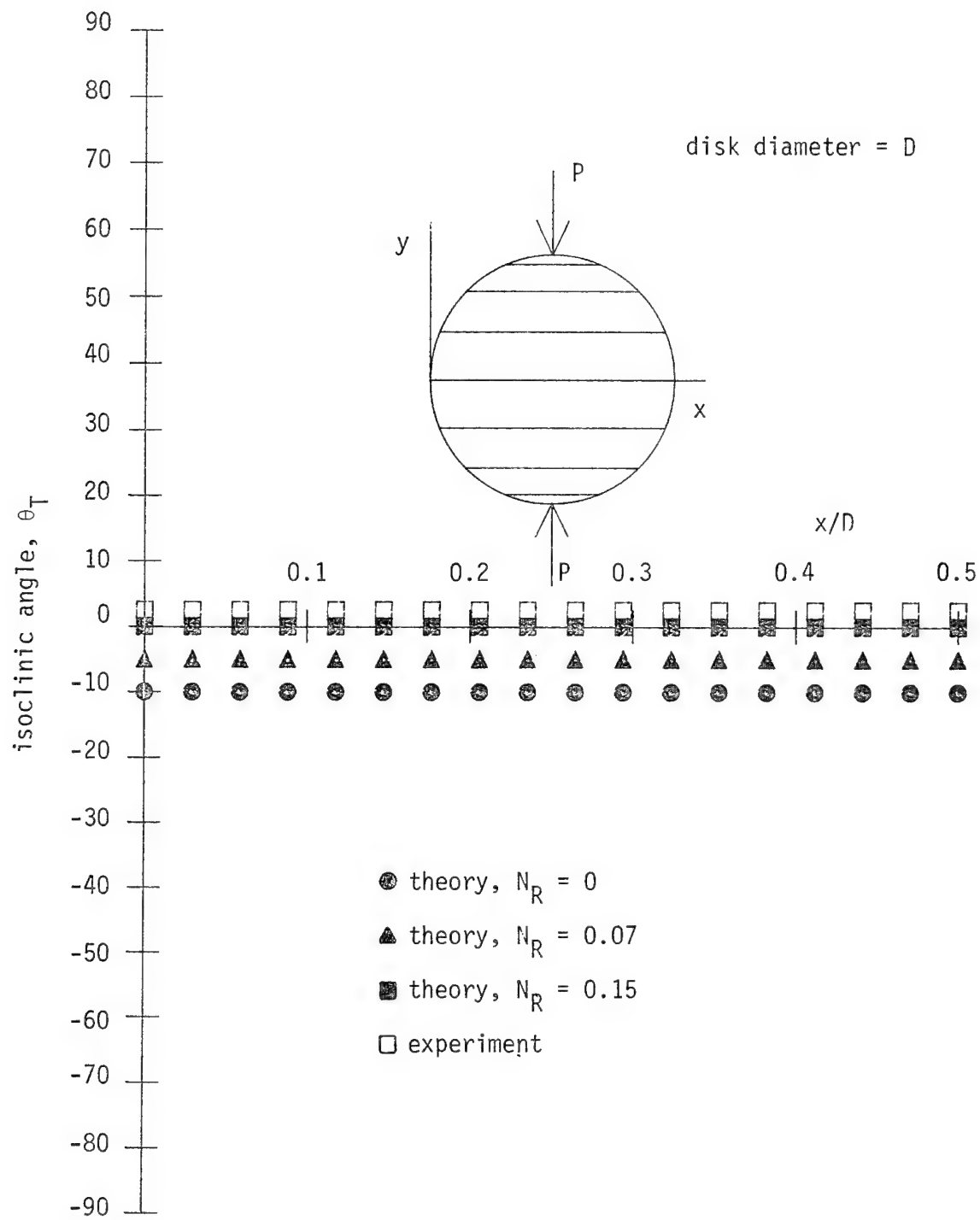
Fig. 73 Comparison between predicted and observed isoclinic angle along diameter parallel to fibers, fibers perpendicular to load.

144
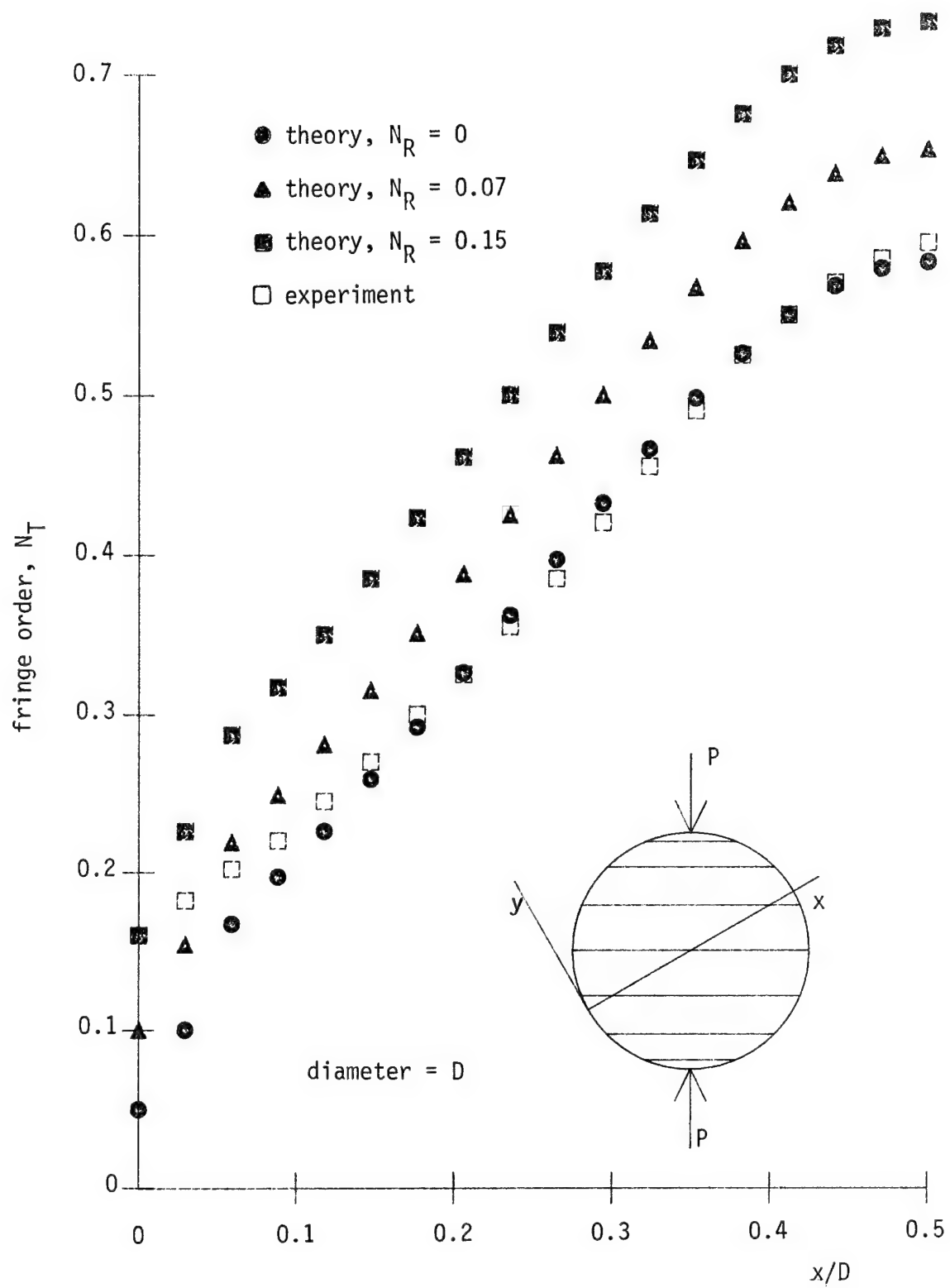
Fig. 74 Comparison between predicted and observed isochromatic
fringe order along 30° diameter, fibers perpendicular
to load.

145
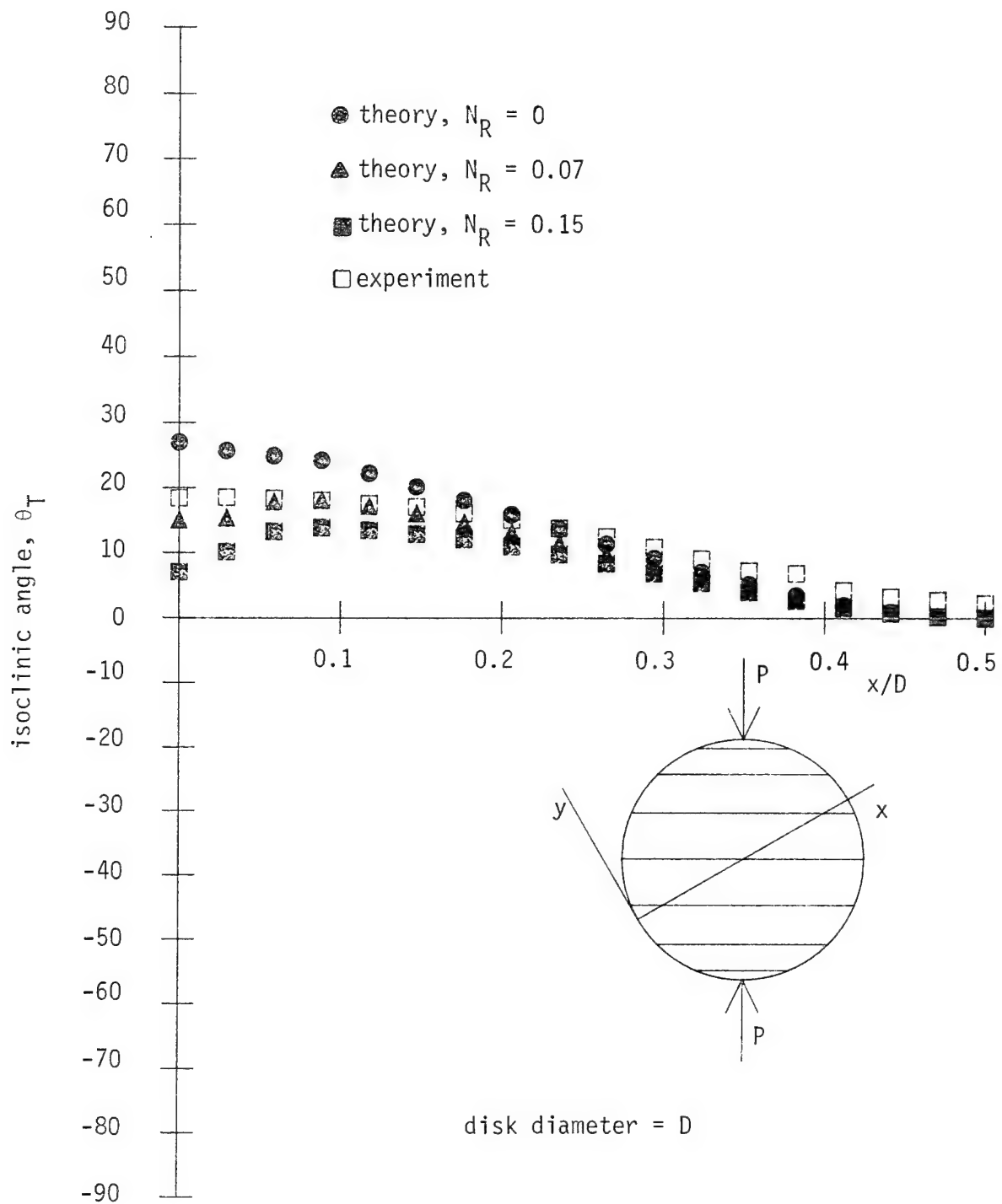
Fig. 75 Comparison between predicted and observed isoclinic
angle along 30° diameter, fibers perpendicular to load.

of the observations and comments are obvious. The load level used for the 45° and 90° orientations was 350 lb. It can be seen from the figures that the experiments correlated better with the lower levels of assumed residual birefringence than they did with the higher levels.

It was of interest to put these experiments of local behavior into context by repeating the experiments with a standard isotropic disk. A great effort is made in the manufacture of isotropic photoelastic material to eliminate residual birefringence. Thus the isotropic tests could not be used to check the effects of residual birefringence. However, the tests could certainly be used to check the spatial distribution of isochromatic and isoclinic data. If it is assumed the theoretically predicted data were correct, then the experiments would evaluate how well photoelastic data was being measured. If it was assumed that the photoelastic measurements were correct, then the comparison between experiment and theory could be viewed as an evaluation of the theory of isotropic photoelasticity. The theory of isotropic photoelasticity has been verified time and time again and so experiments with the isotropic disk should be looked upon as an indication of the accuracy to which isochromatic and isoclinic fringe data could be recorded with the polariscope.

Figures 76-79 show the comparison between the measured and the predicted isochromatic and isoclinic fringe information for the isotropic disk. The predictions are based on the exact elasticity solution for an isotropic disk as presented in Frocht [13]. The load level used was 125 lb. The isotropic disk material was PSM-1. Figure 76 shows the isochromatic fringe numbers across a diameter perpendicular to the load.

147
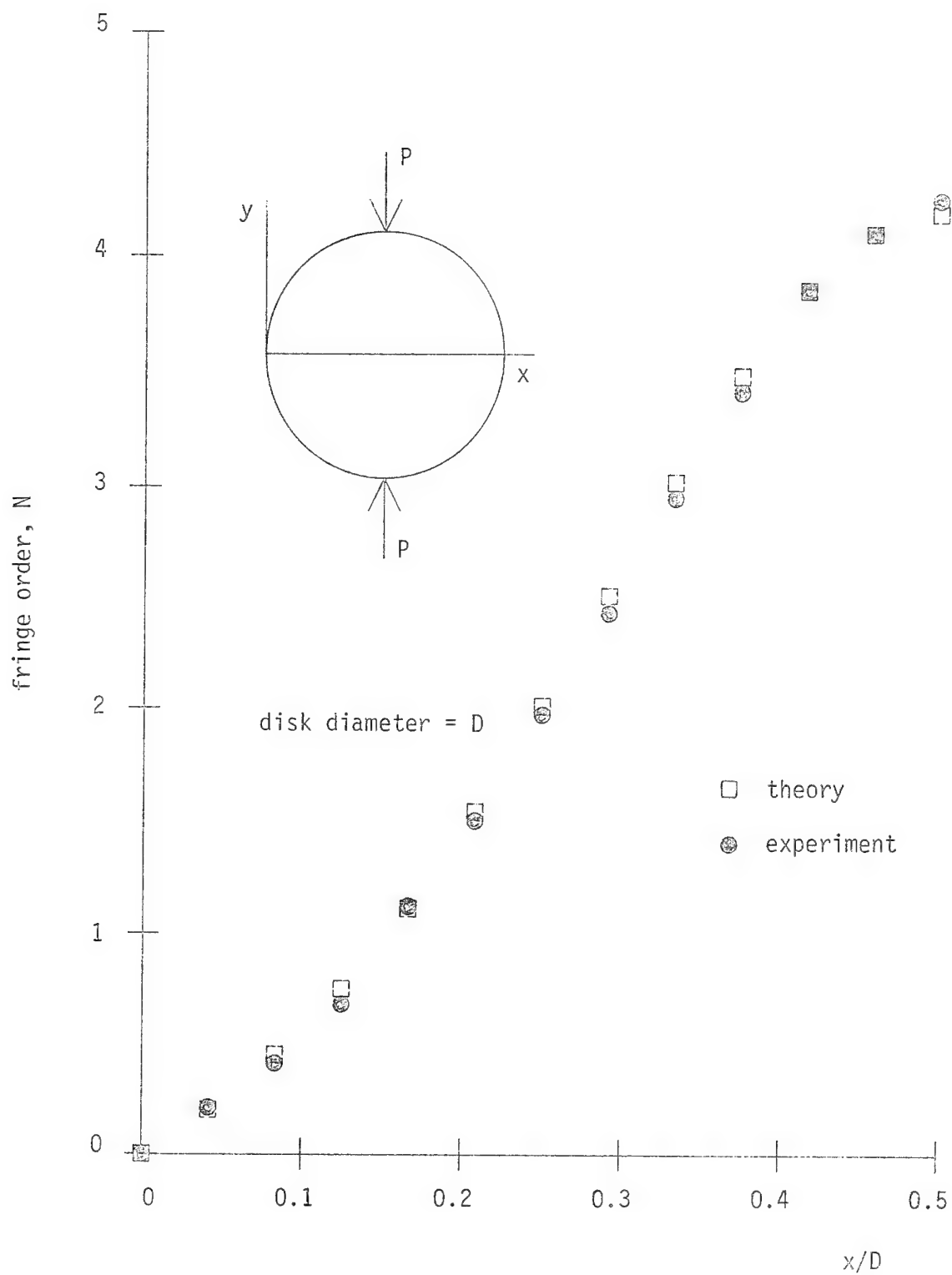
Fig. 76   Comparison between predicted and observed isochromatic fringe order along diameter perpendicular to load, isotropic disk.

148

Figure 77 shows the isoclinic data for that diameter. The correlation was very good. Figures 78 and 79 show similar information for a diameter oriented at 30° to the horizontal diameter. Again the correlation was excellent. From these four figures, there was no question as to the ability to make accurate measurements with the polariscope.

From these studies with the orthotropic and isotropic disks, one conclusion is certain. Orthotropic photoelasticty, as it is hypothesised here, is not as accurate as isotropic photoelasticity. Although the conclusion is straightforward, it is not so clear why there is a difference in accuracy. It can, however, be traced to two sources. Possibly, the hypothesis regarding the stress-optic behavior, given by eq. 36, is not entirely valid. The averaging of the effects of the fibers and matrix, in a through-the-thickness sense, may not be as accurate for optical behavior as it is for, say, elastic behavior. In addition, there may be an interaction between shear and elongation effects. That is, maybe eq. 36 should not be orthotropic in any coordinate system. These issues are directed at the theory itself. Perhaps the inaccuracy comes in the practicing of the theory. Fringe definition in orthotropic photoelastic material is not as good as it is in isotropic materials. This can be seen in a number of previous figures, for example, fig. 54. Thus the discrepancies between theory and experiment may result from not being able to accurately locate the center of a fringe. Fringe count was kept low in the orthotropic material, $N_T \approx 0.5$, whereas it was made high in the isotropic material, $N \approx 5.0$. Due to streaking by the fibers, the higher order fringes (greater than 3 or 4) are difficult to define in the orthotropic material. In an isotropic material, higher order fringes are narrower and more distinct than the lower order
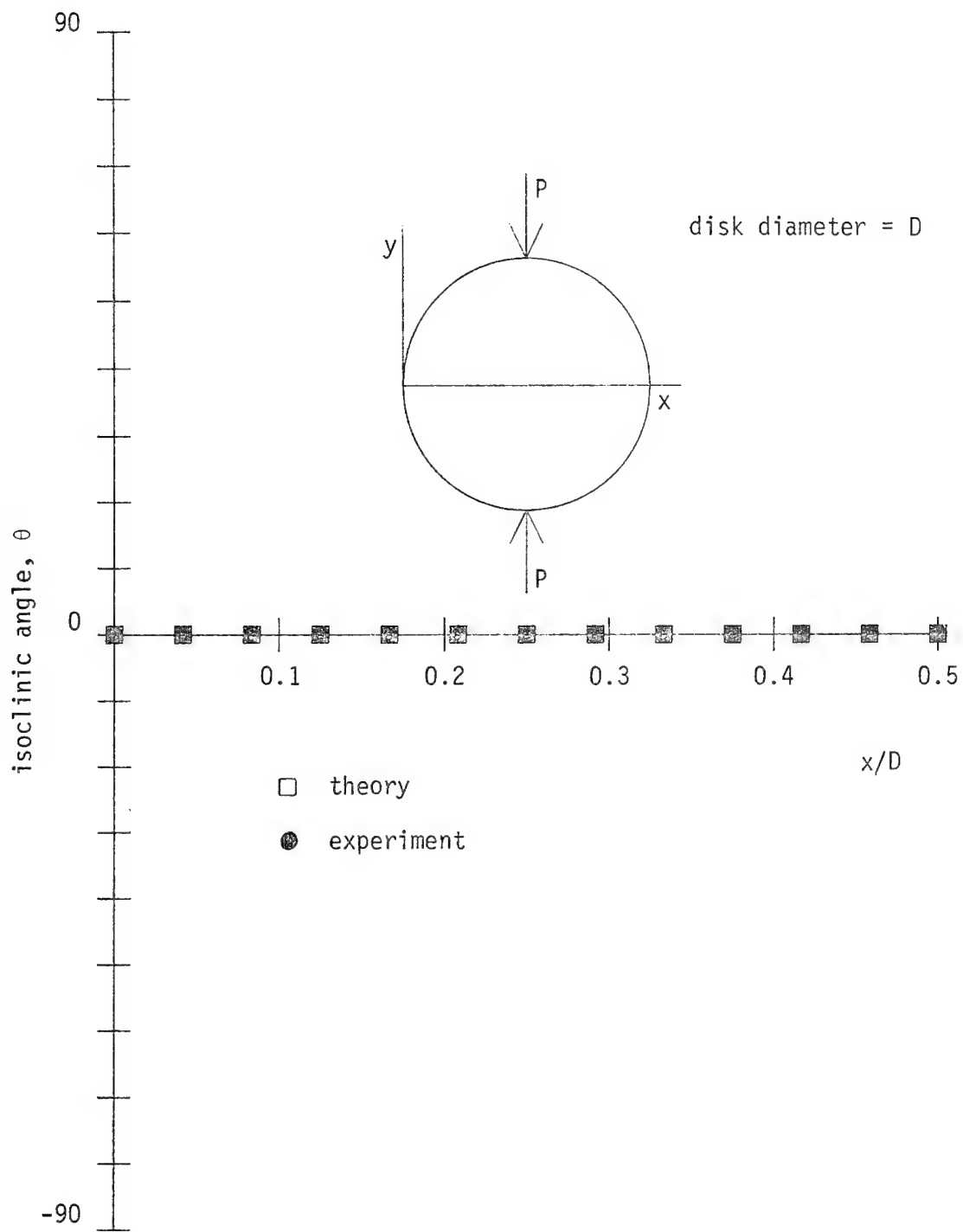
Fig. 77 Comparison between predicted and observed isoclinic
         angle along diameter perpendicular to load,
         isotropic disk.

150
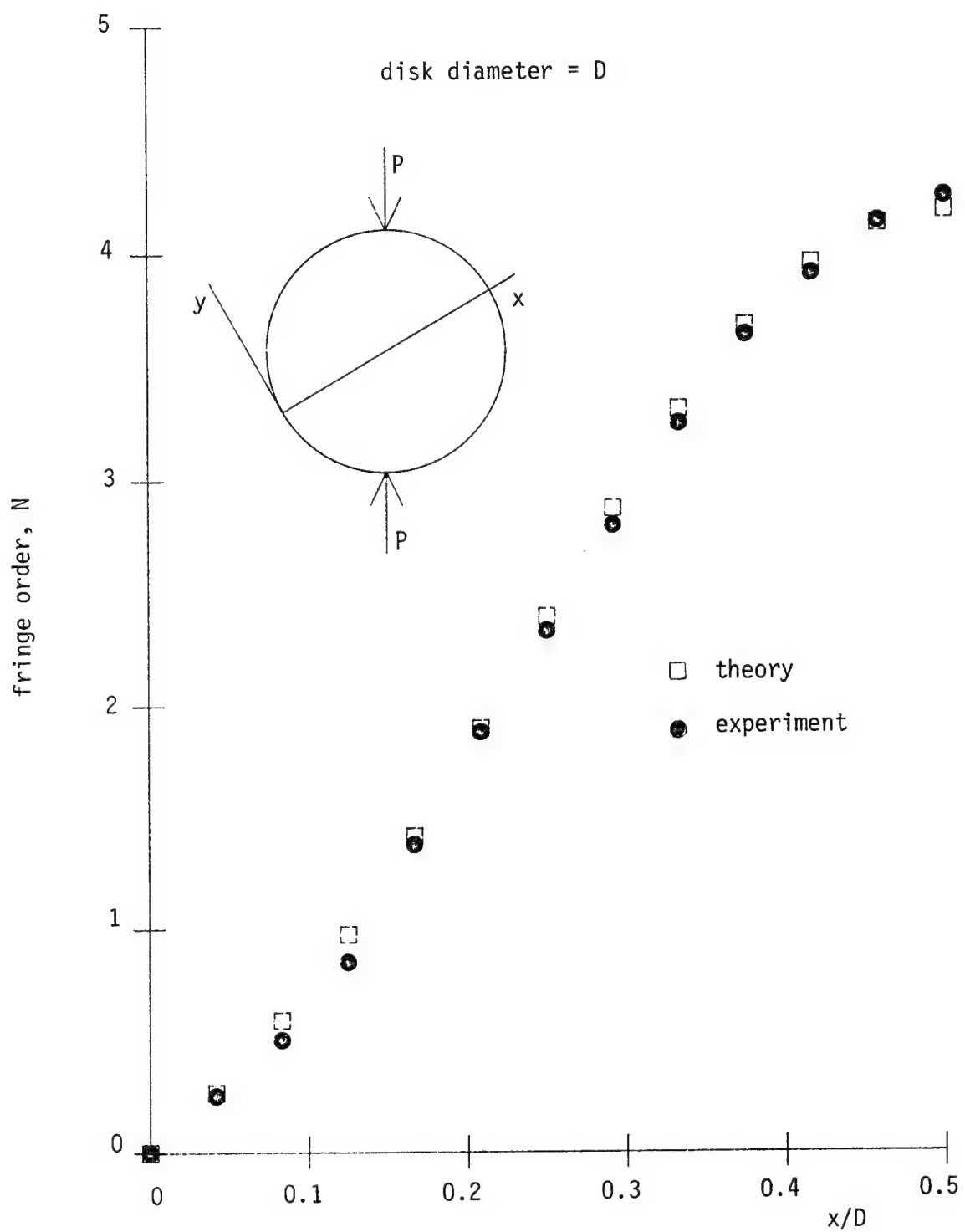
Fig. 78   Comparison between predicted and observed isochromatic
fringe order along 30° diameter, isotropic disk.
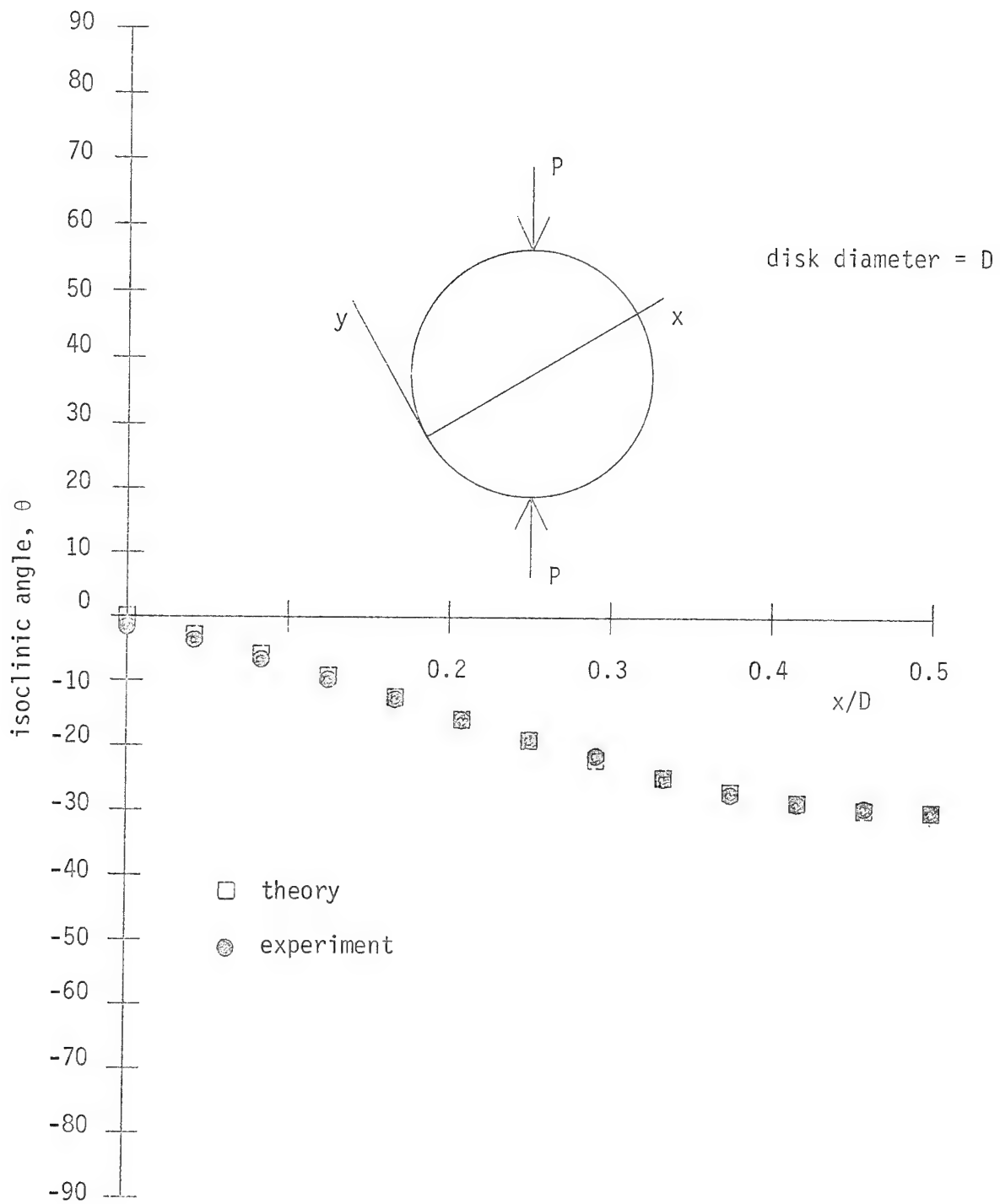
Fig. 79   Comparison between predicted and observed isoclinic
          fringe order along 30° diameter, isotropic disk.

fringes. Thus the two materials respond in an opposite manner to high fringe numbers. Where the stresses are high and changing rapidly, the isotropic material responds in an ideal manner. The orthotropic material responds exactly opposite to the ideal manner. This lack of spatial resolution of fringes in the orthotropic material is felt to be the major reason for the discrepancies between theory and experiment. Also, perhaps a lack of spatially uniform residual birefringence contributes to the behavior.

The real issue, though, is how accurately can stresses be predicted using orthotropic photoelasticity. This is the subject of the next section.

BACKWARD TESTING: PREDICTION OF STRESSES

Historically, photoelasticity has been used to predict stresses
from known isochromatic and isoclinic fringe information. For a general
state of stress, at each point in a body the two normal stresses, σ_x
and σ_y, and the shear stress, τ_{xy}, are to be determined. At each point
in the body, the isochromatic fringe count gives one quantity of experi-
mental information and the isoclinic gives a second quantity of experi-
mental information. A third quantity or condition is needed if three
stresses are to be uniquely determined at the point. In isotropic ma-
terials, interferometric measurements have been used to provide informa-
tion regarding the sum of principal stresses. This is a third quantity
and thus σ_x, σ_y, and τ_{xy} can be determined. Interferometric measure-
ments are not that easy to obtain so experimenters tend to rely on other
relations among the stresses as a third condition. One other condition
is that the unknown stresses must satisfy the compatibility equations.
Compatability is a second order partial differential equation. For iso-
tropic materials the compatibility equation reduces to Laplace's equa-
tion for the quantity $\left(\sigma_x + \sigma_y\right)$. Since the solution to Laplace's equa-
tion on simple domains such as a circle or rectangle is well estab-
lished, investigators have used the compatibility equation as the auxil-
iary condition. For orthotropic materials, the compatibility equation
in terms of stresses does not reduce to Laplace's equation.

Another condition often used by photoelasticians is that the un-
known stresses must satisfy equilibrium. Equilibrium is represented by
two first-order partial differential equations. These two equations in-
volve the three stresses and by themselves cannot be solved, as

Laplace's equation can, on any domain. In addition, the two equilibrium equations plus the isochromatic and the isoclinic fringe data result in four conditions from which to solve for the three stresses. In this situation the stresses are overdetermined. To have a unique solution, one of the equilibrium equations can be simply discarded. This is done in the so-called shear difference approach. If both equilibrium equations are retained the stresses computed are the three stresses which satisfy the four conditions in a least-squares sense. It is also possible to use the equilibrium equations in such a way that in the region of interest in a photoelastic model there are exactly as many unknown stresses as there are equations. This approach was used in this present study and it relies on applying the equilibrium equations in an average sense.

Independent of how the equilibrium equations are used as an auxiliary condition, the equilibrium equations are usually represented in finite-difference form. The partial derivations are approximated by using central, forward, and backward differences in the stresses at the gird, or mesh, points of a finite-difference grid. The partial differential equations thus become algebraic equations relating the three stresses at the mesh points. In isotropic photoelasticity, eqs. 78 and 79 are then used as two more algebraic equations at each mesh point. Since the isochromatic, N, and the isoclinic, θ, are known at each point, eqs. 78 and 79 represent algebraic relations the normal and shear stresses must satisfy at each point. The two finite-difference forms of the equilibrium equations and eqs. 78 and 79 represent the four equations which are used to compute the three stress components. A previous photoelastic study [14] of isotropic double-lapped, double-pin connectors used this four-

155

equation scheme to estimate stresses. This scheme was adapted to orthotropic photoelastic materials by using eqs. 86 and 87 in place of eqs. 78 and 79. This is possible because the form of the equilibrium equations, unlike the form of the compatibility equation, does not depend on the material properties. The finite-difference representation of the plane-stress equilibrium equation remains unaltered. Appendix C describes the scheme.

To determine the degree to which orthotropic photoelasticity could be used to predict stresses, a final series of experiments was conducted with the disk using the finite-difference formulation. The disk was loaded in diametral compression and the isochromatic and the isoclinic fringe data determined along various diameters of the disk. These data were used in the finite-difference formulation to calculate the three stresses along these diameters. These stresses were then compared with the values computed using the elasticity solution of Appendix A. Since the level of residual birefringence was an issue, the experimentally predicted stresses were computed using various values of assumed residual birefringence. The values of N_R assumed were: 0, 0.07, and 0.15. The value of θ_R was assumed to be 0. For given values of N_T and θ_T, the experimentally computed values of σ_x, σ_y, and τ_{xy} would be dependent on N_R. Changing N_R and θ_R changes the right-hand side of eqs. 86 and 87. Physically, changes in the right hand side of the equation 'adjust' the fringe data so only those data due to the applied load generate numerical values for the stresses. Obviously if $N_T = N_R$ and $\theta_T = \theta_R$, the right hand side 'adjusts' to zero and the system of equations predicts that there are no stresses due to applied loads.

Before using actual photoelastic data in the finite-difference scheme, the accuracy of the finite-difference formulation was assessed. This was done by using the exact elasticity solution and the stress-optic law to generate N_T and θ_T at each point of the finite-difference mesh. These values of N_T and θ_T were used in the finite-difference scheme as if they were experimental data. The values of σ_x, σ_y, and τ_{xy} were then computed. These values of stress were compared with the values of stress at each mesh point as predicted by the elasticity solution used to generate N_T and θ_T. This exercise tested the accuracy of the finite-difference formulation. In essence, if the exact values of N_T and θ_T were used, could the finite-difference scheme compute the exact value of the stresses? Generally the answer to the question was a resounding yes. For a few cases, as will be seen, there were some differences between the exact values of σ_x, σ_y, and τ_{xy} from the elasticity solution and the values from the finite-difference scheme.

Figure 80 shows the finite-difference mesh used. In the following figures the stresses along the middle line of the three-line mesh, i.e. the diametral line, are reported. The mesh consisted of 0.092 in.by 0.092 in. squares. With the disk 3.12 in. in diameter, there were 18 grid points along the disk radius. Studies were not conducted to determine the effects of mesh refinement on predicted stresses. Because of the aforementioned good agreement between the elasticity solution stresses and the finite-difference predictions using the exact values of N_T and θ_T, such refinement studies were felt to be superfluous.

Figures 81-83 show the stresses along the diameter perpendicular to the load for the case of the fibers aligned with the load. The stresses have been normalized by the absolute value of the mean stress across the

157
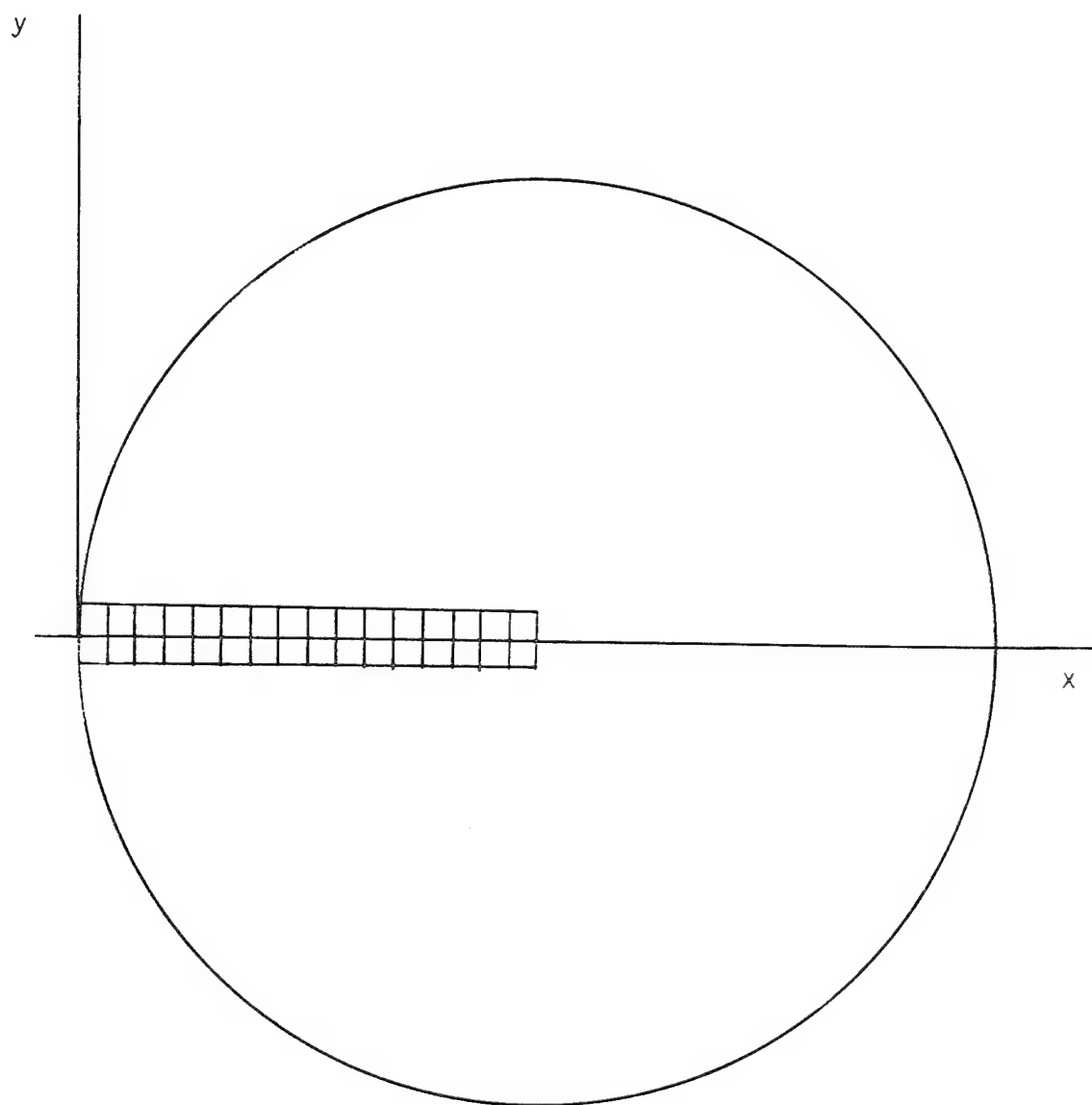
Fig. 80 Finite-difference mesh on disk.

158

disk diameter, $|P|/Dt$, where P is the load, D is the disk diameter, and t is the disk thickness. (In the elasticity solution P is negative if compressing the disk.) The normalized stresses are plotted on the vertical axes and the distance along the diameter is plotted on the horizontal axis. The diametral distance is measured from the left edge of the disk. Experimental measurements of N_T and θ_T were obtained for only one-half the disk. The inset in each figure indicates the fiber orientation relative to the load, and the diameter being considered.

Figure 81 shows variation of the major compressive stress, σ_y, with diametral distance. There are several sets of data on this and on subsequent figures. The solid squares represent the predictions of the elasticity solution. The open diamonds represent the predictions of the finite-difference scheme when the elasticity solution values of N_T and θ_T were used as 'experimental' data. This is the aforementioned finite difference check. In fig. 81 the diamonds are almost entirely obscured by the solid squares, indicating the aforementioned good accuracy of the finite-different approach. The slight differences that did occur were at the outer edge of the disk where the stresses were quite low. The open squares represent the stress predictions when the values of N_T and θ_T, as measured from the actual disk, are used in the finite-difference scheme and the residual birefringence was assumed to be $N_R = 0.15$. The open triangles indicate the experimentally predicted stresses when N_R was assumed to be 0.07. The open circles indicate the case when N_R was assumed to be zero. As can be seen, and as could be expected, the level of assumed residual birefringence affected the stress predictions. The close agreement between the elasticity solution (solid squares) and the $N_R = 0.07$ case was in keeping with the findings of the forward testing

159
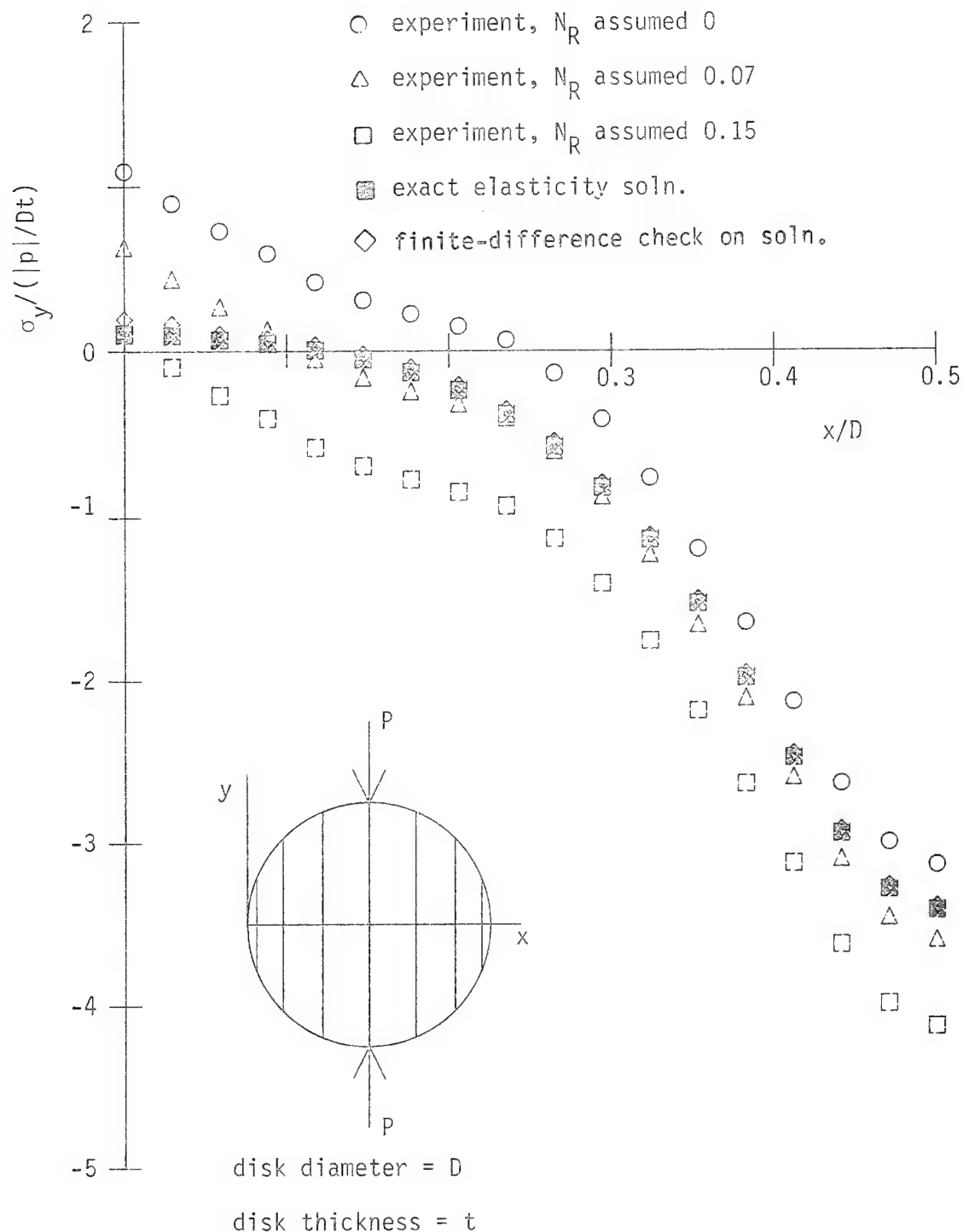
Fig. 81 Comparison of σ_y stresses along diameter perpendicular to load, fibers aligned with load.

experiments described in the previous section. There, recall, with N_R = 0.07 or lower, the level of residual birefringence resulted in better correlation with experimental findings than other levels of assumed residual birefringence.

Figure 82 shows the matrix direction stress, σ_x, for this same case. In this figure the open diamonds are not obscured by the exact solution's solid squares. It is important to note these stresses are an order of magnitude less than the σ_y stresses of the previous figure and the scale for the stress coordinate has been expanded to fill the figure. Plotting this figure with the same scale as used in fig. 81 would significantly 'squeeze' the σ_x data together. What was interesting about the experimental σ_x computation is that it did not depend on the assumed level of residual birefringence. This is evidenced by the fact that the open circles, squares, and triangles are coincident. This always occurred when the x-y system coincided with the principal material axes.

Figure 83 shows the shear stress calculations, τ_{xy}, for the case being discussed. Due to symmetry in geometry, loading, and material properties the shear stress was zero across the horizontal diameter. The shear stresses shown in fig. 83 were the values for the upper mesh points of the three-line finite-difference grid of fig. 80. These shear stress were quite small and really almost meaningless. The calculations could be easily influenced by any inaccuracy in measurement or computation. However, the trend and magnitude of the theoretically predicted shear stresss were well matched by the experimentally determined values.

161
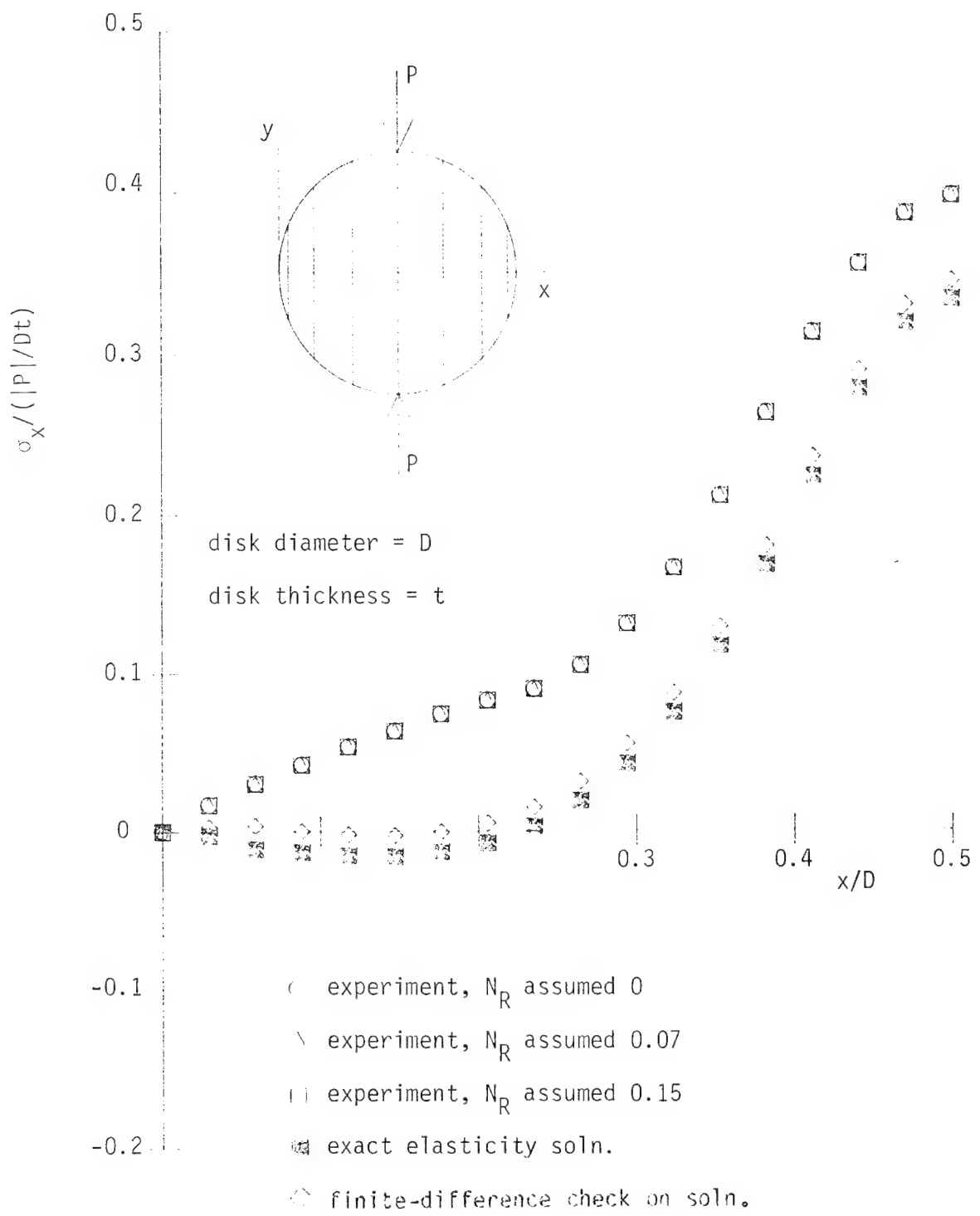
Fig. 82   Comparison of σ_x stresses along diameter perpendicular
to load, fibers aligned with load.

162
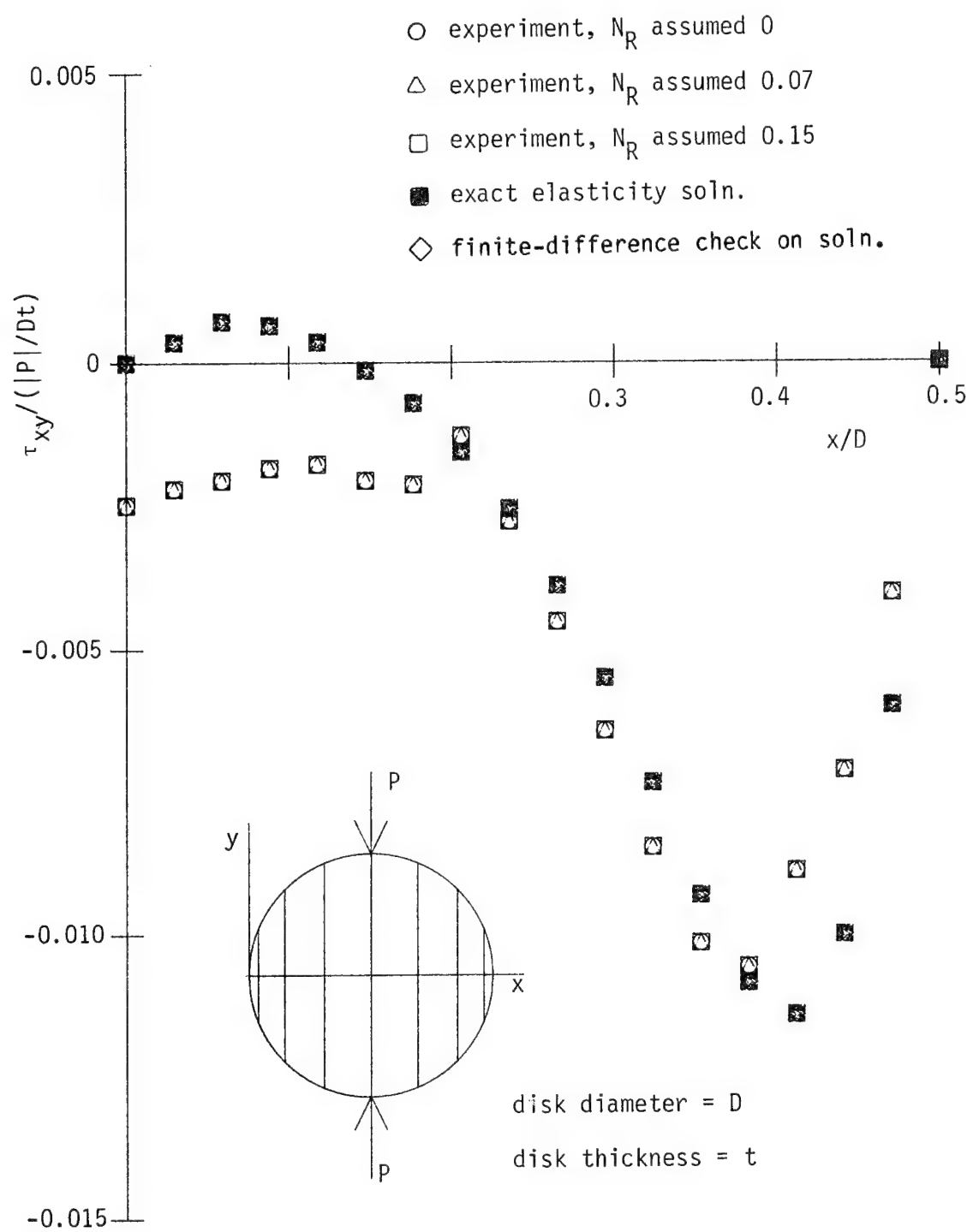
Fig. 83 Comparison of τ_{xy} stresses just off diameter perpendicular to load, fibers aligned with load.

163

Figures 84-86 show the three stress components along a diameter oriented 30° relative to the horizontal. The stresses are computed in a coordinate system which has its x axis along this diameter and the y direction perpendicular to this. The orientation of the x-y system is shown in the figures.

Figure 84 shows the variation of σ_y along this diameter. The symbol designations are, and will be, consistent with previous notation. Here the stress calculations based on the experimental values of N_T and θ_T did not seem to align with any particular level of assumed residual birefringence. However, the experimental calculations were more closely aligned with the theoretical predictions when low levels of residual birefringence were assumed in the finite-difference calculations.

Figure 85 illustrates the σ_x stress computations. Again the scale differences between this figure and fig. 84 should be noted.

Figure 86 illustrates the τ_{xy} stress calculations for the 30° diameter. These stresses were on the true diameter rather than for an off-set line as in fig. 83. For the majority of the diameter, the experimental calculations using $N_R = 0.07$ coincided with the theoretical elasticity solution.

Figures 87-104 show the stresses for other load orientations relative to the fibers. These situations will not be discussed in detail except for cases where there were some unusual features. In some cases the correlation between the exact solution and calculations based on experimental data was similar to the reasonable correlation for the cases just discussed in detail. In the other case, correlation was not as good.
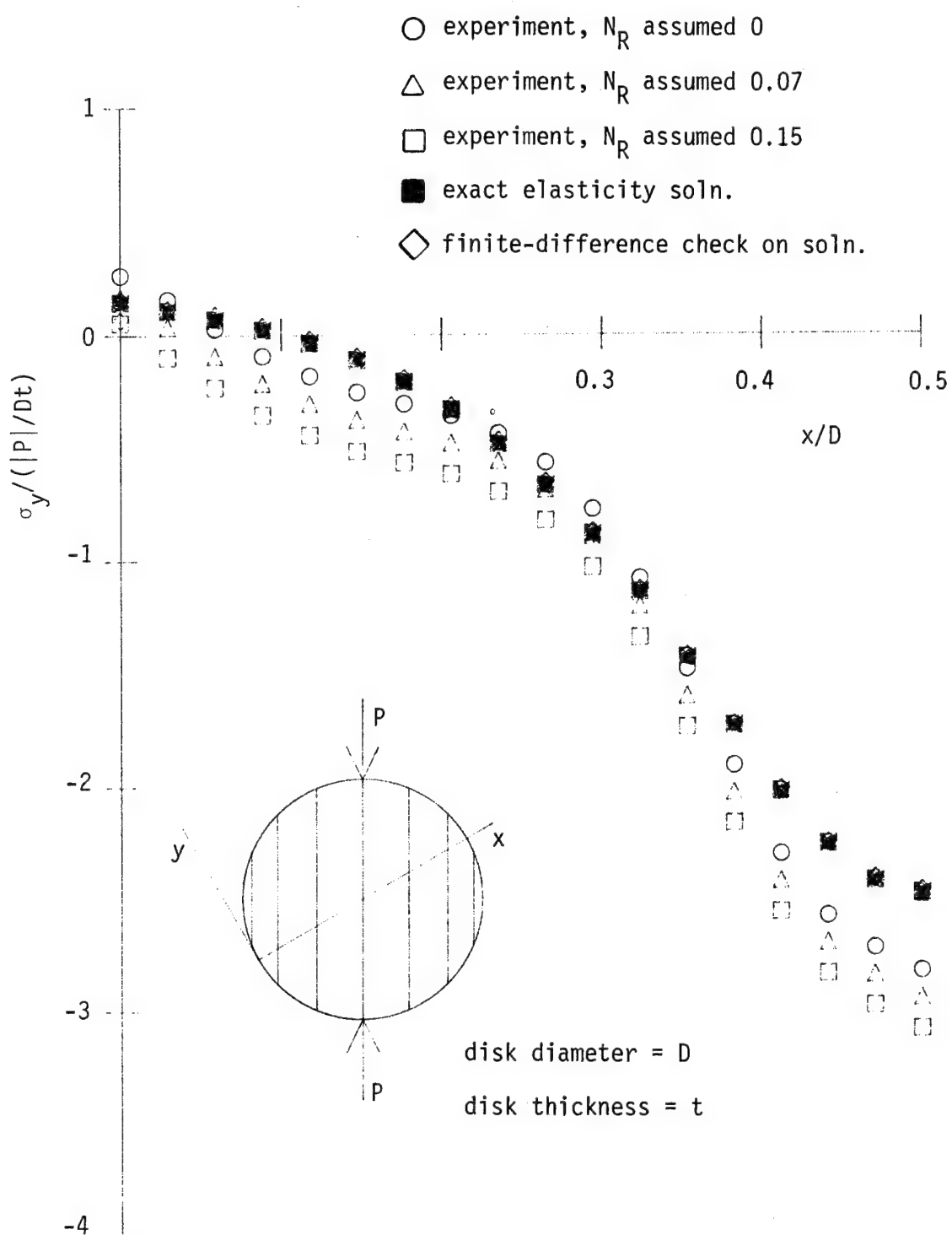
Fig. 84 Comparison of σ_y stresses along 30° diameter, fibers aligned with load.

165
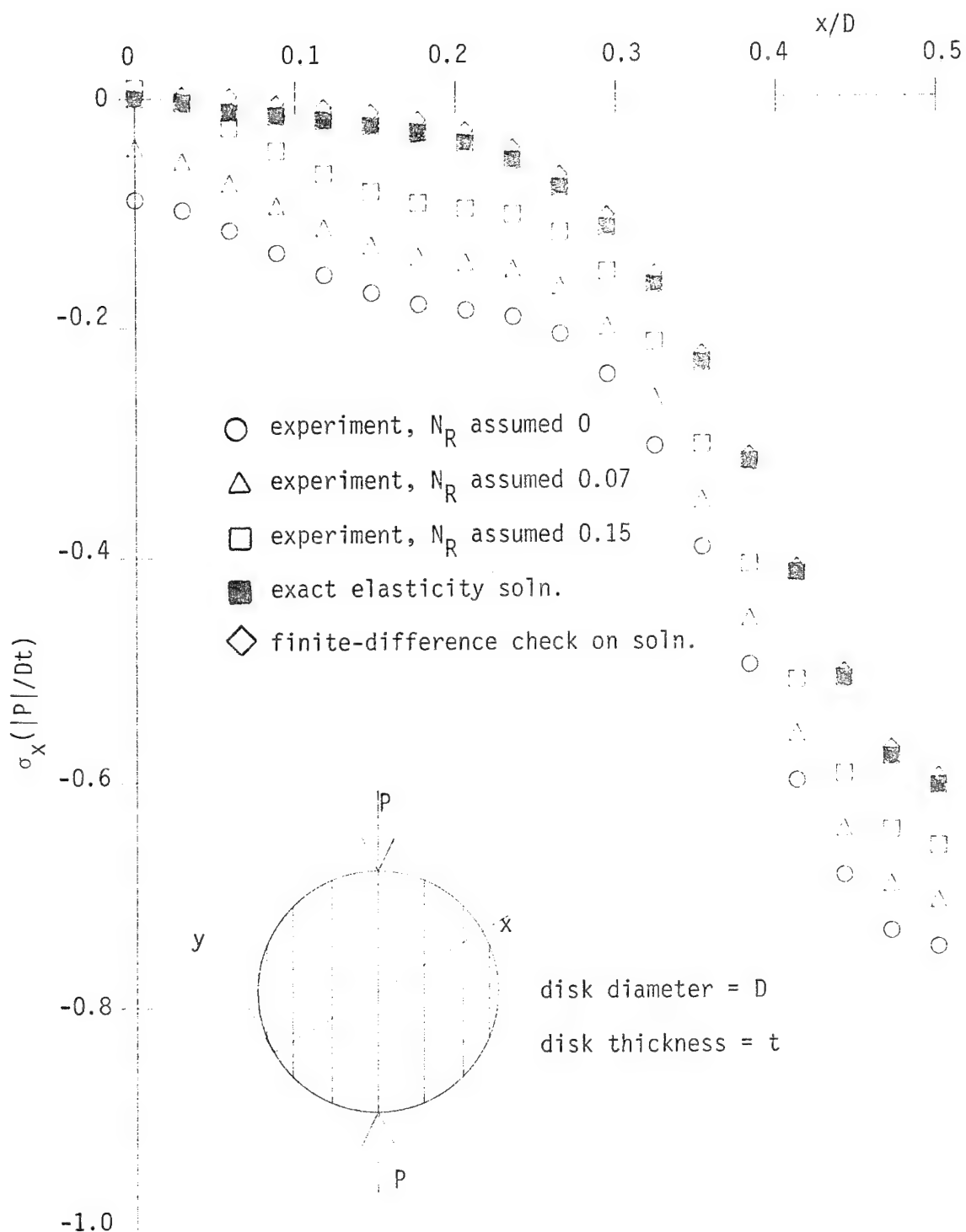
Fig. 85 Comparison of σ_x stresses along 30° diameter, fibers aligned with load.
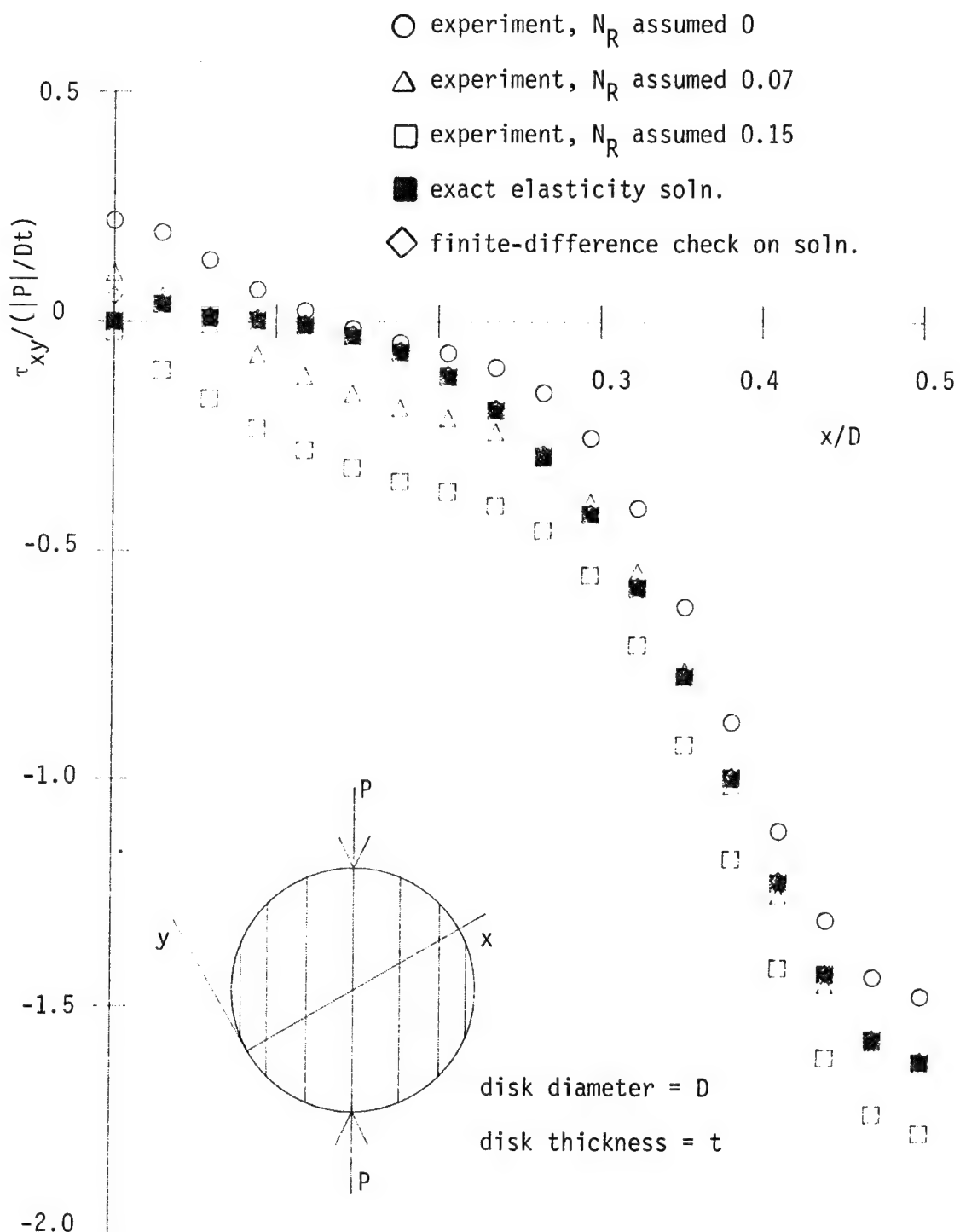
Fig. 86 Comparison of τ_{xy} stresses along 30° diameters, fibers aligned with load.

167
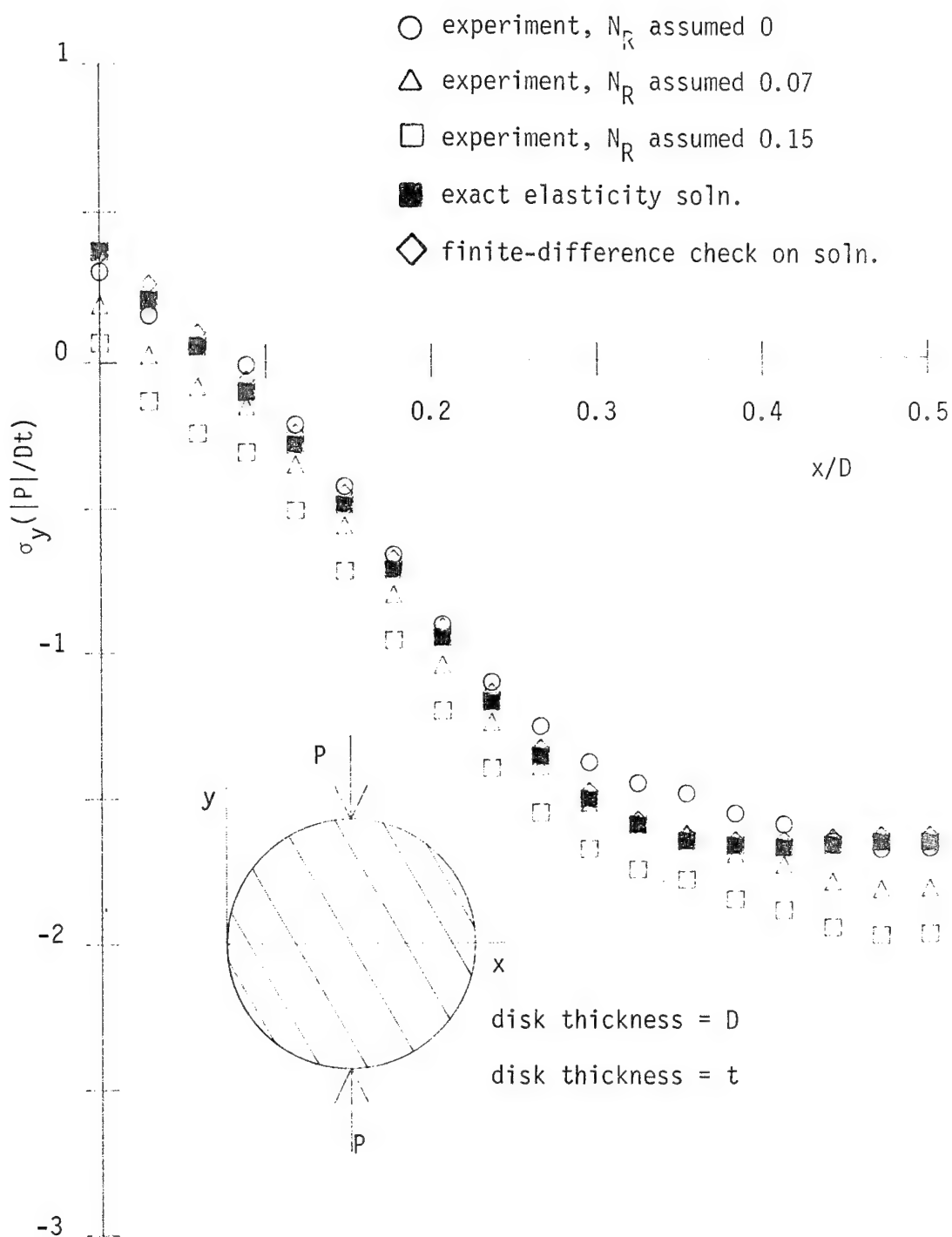
Fig. 87 Comparison of σ_y stresses along diameter perpendicular to load, fibers 30° relative to load.
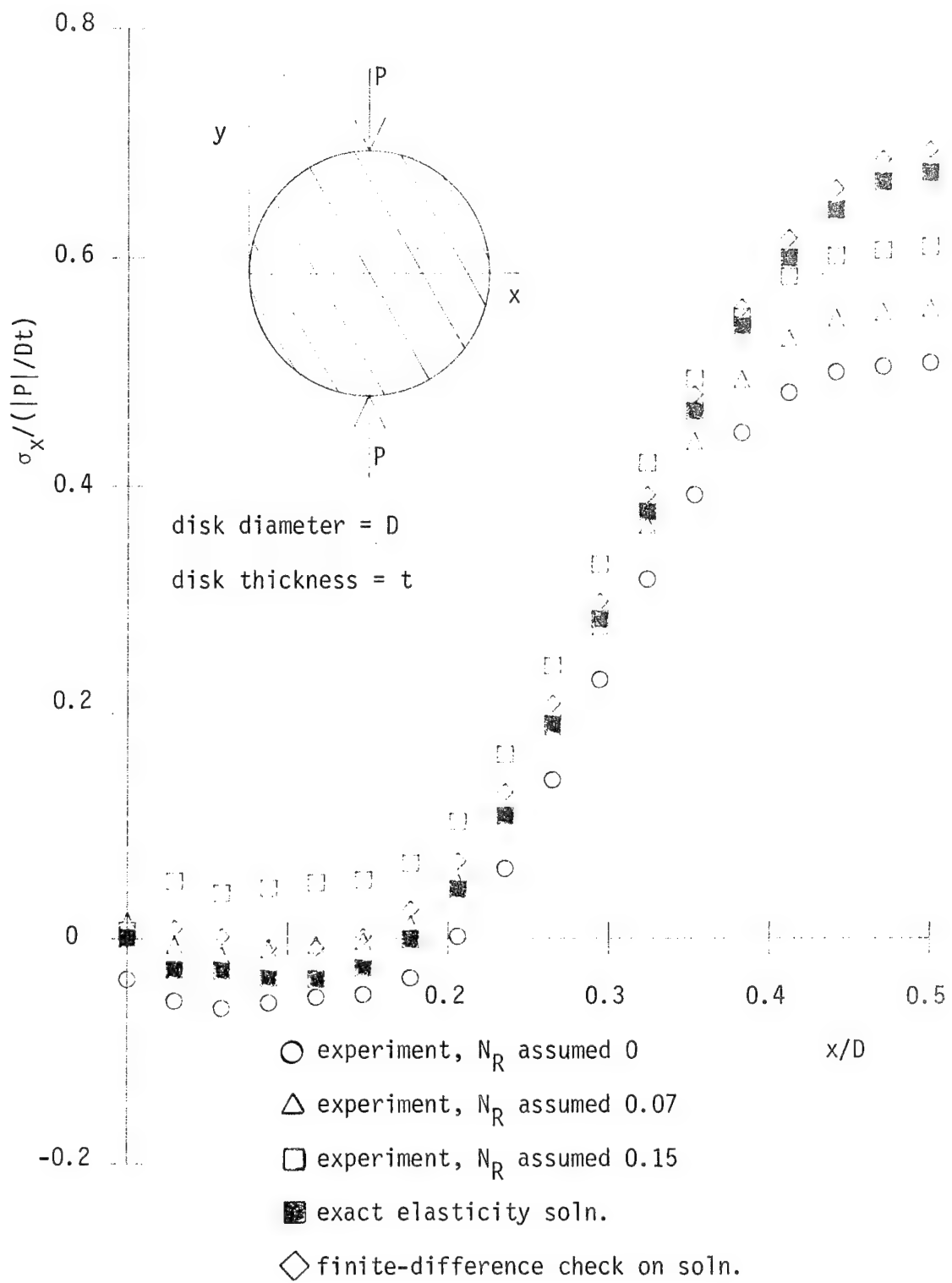
Fig. 88 Comparison of σ_x stresses along diameter perpendicular to load, fibers 30° relative to load.

169
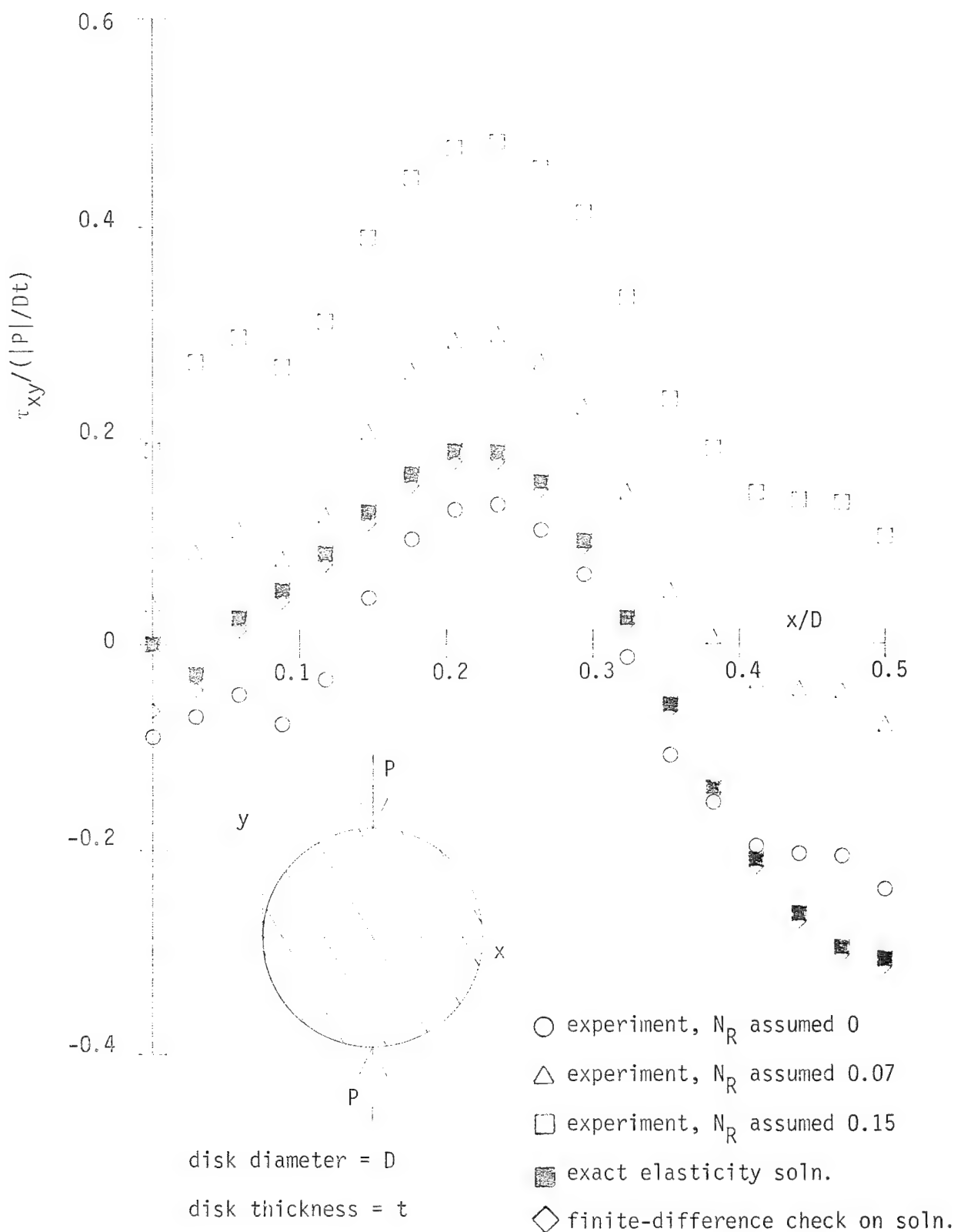
Fig. 89 Comparison of τ_{xy} stresses along diameter perpendicular to load, fibers 30° relative to load.
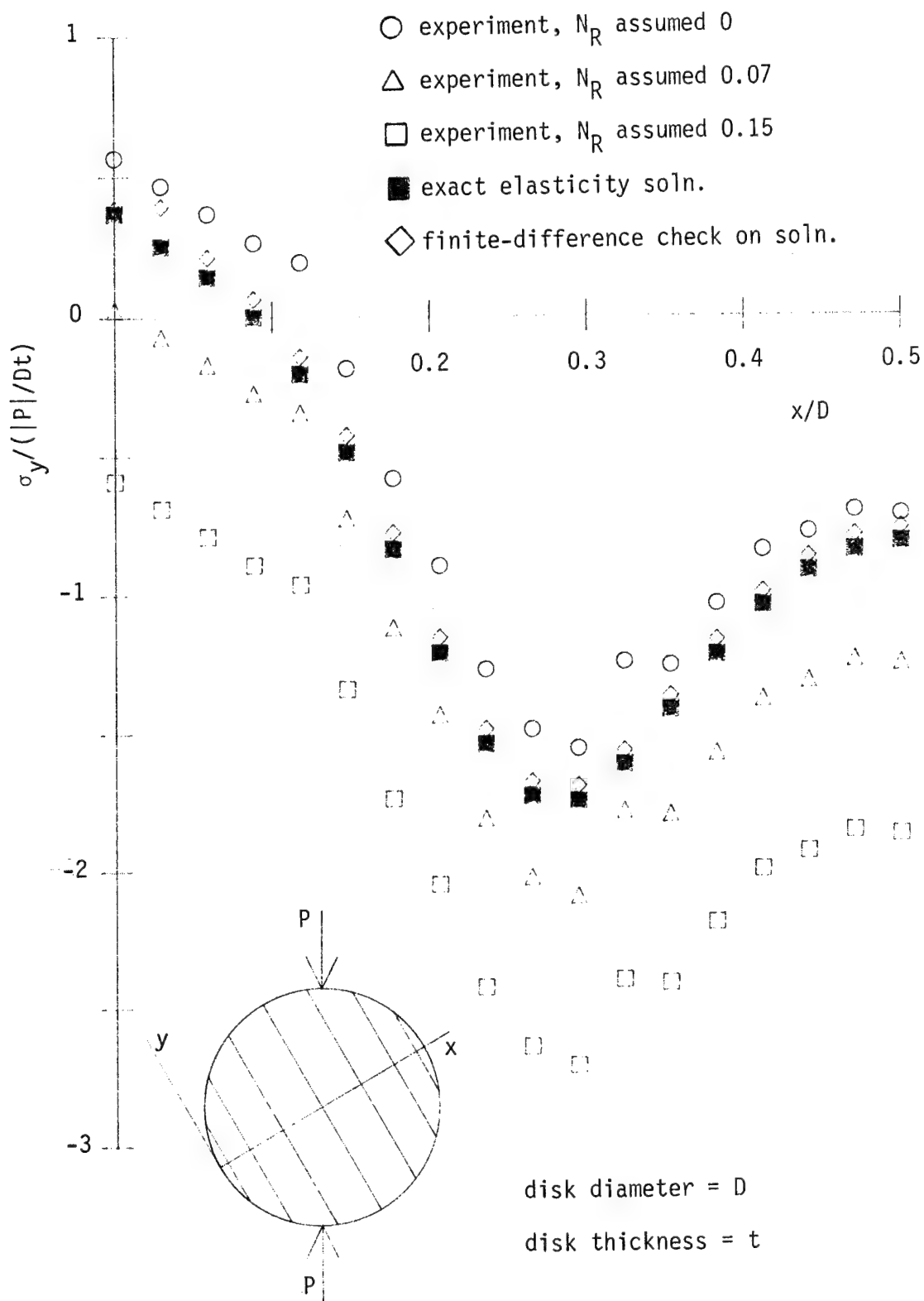
Fig. 90 Comparison of σ_y stresses along diameter perpendicular to fibers, fibers 30° relative to load.

171
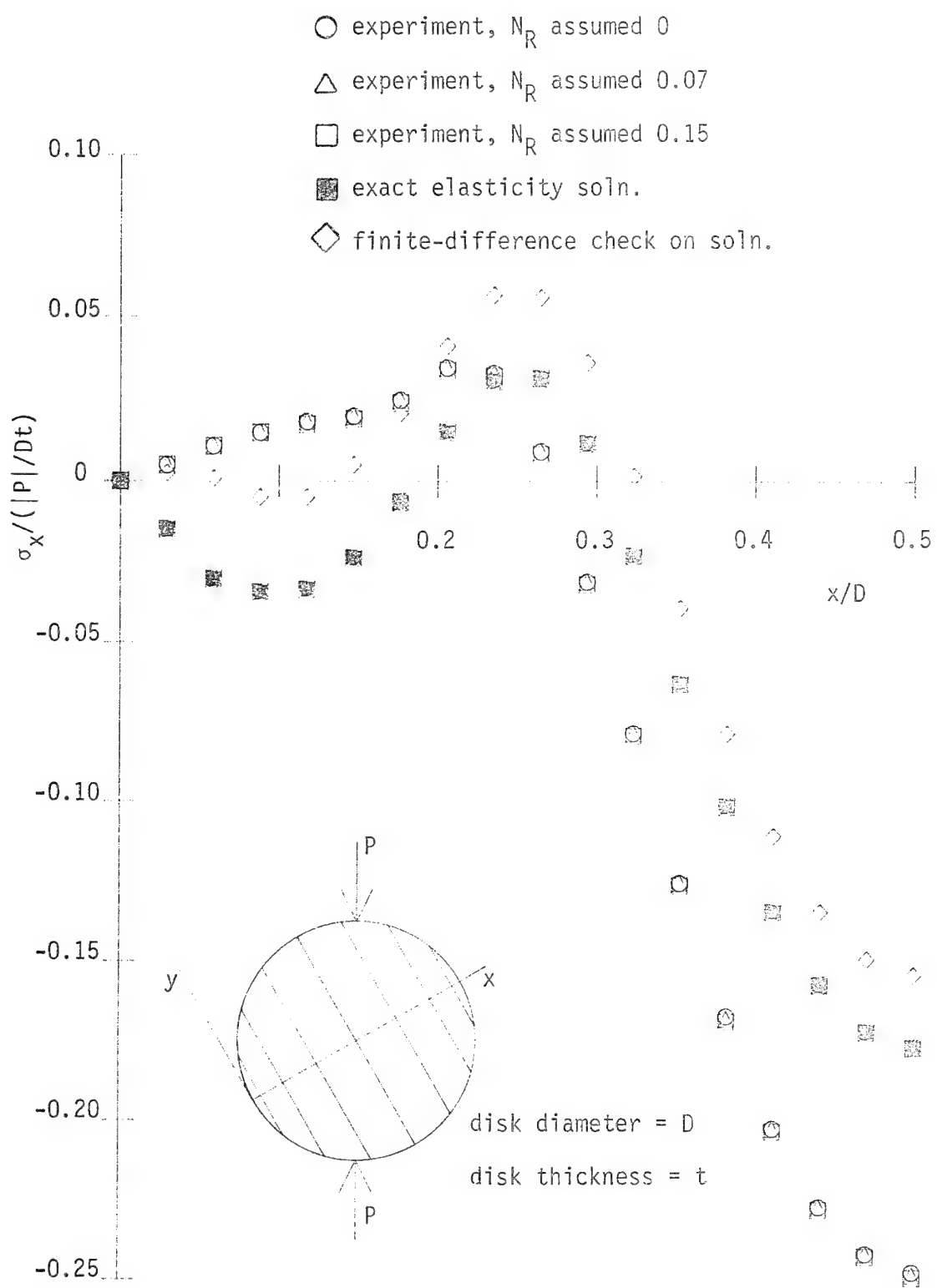
Fig. 91 Comparison of σ_x stresses along diameter perpendicular to fibers, fibers 30° relative to load.
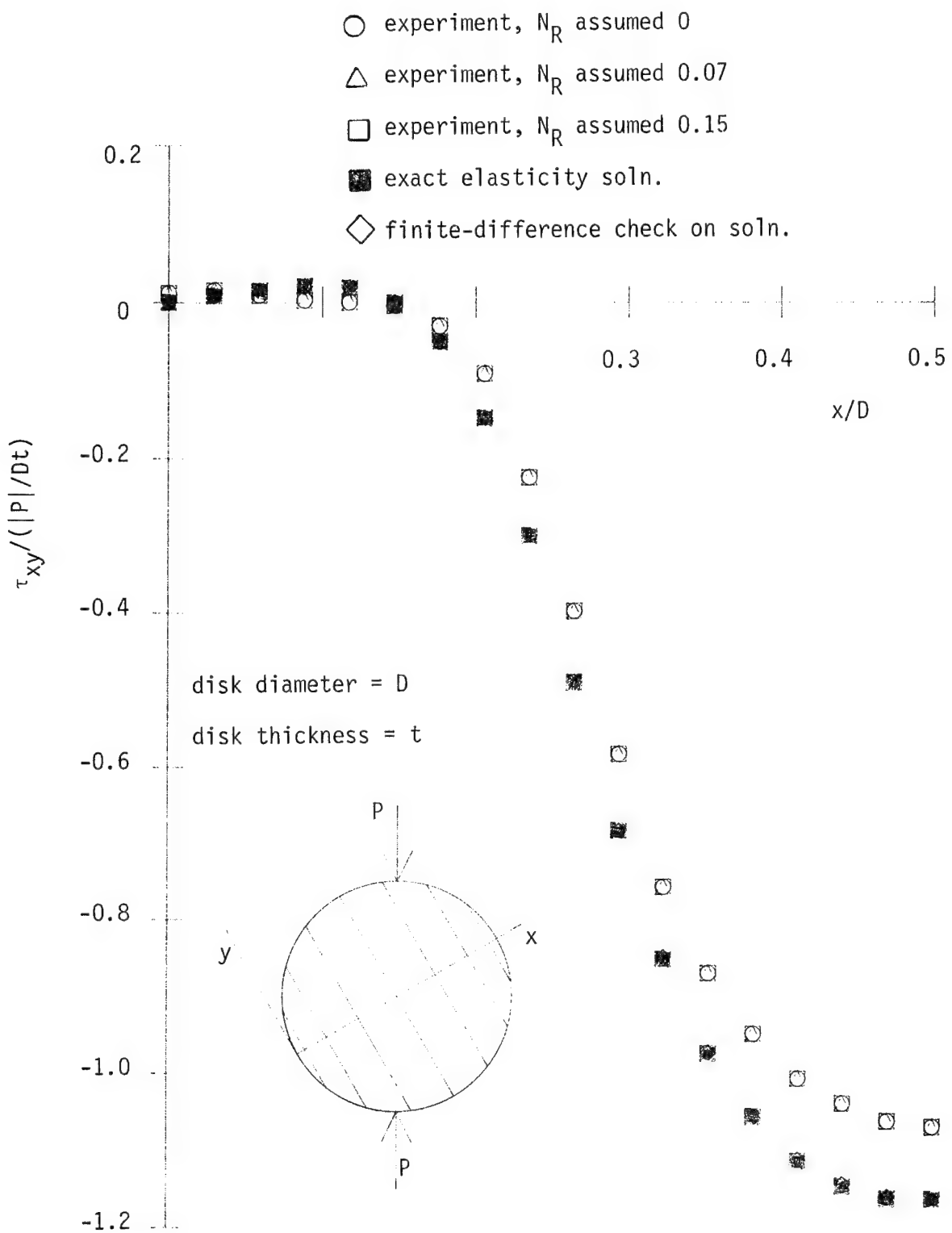
Fig. 92 Comparison of τ_{xy} stresses along diameter perpendicular to fibers, fibers 30° relative to load.

173
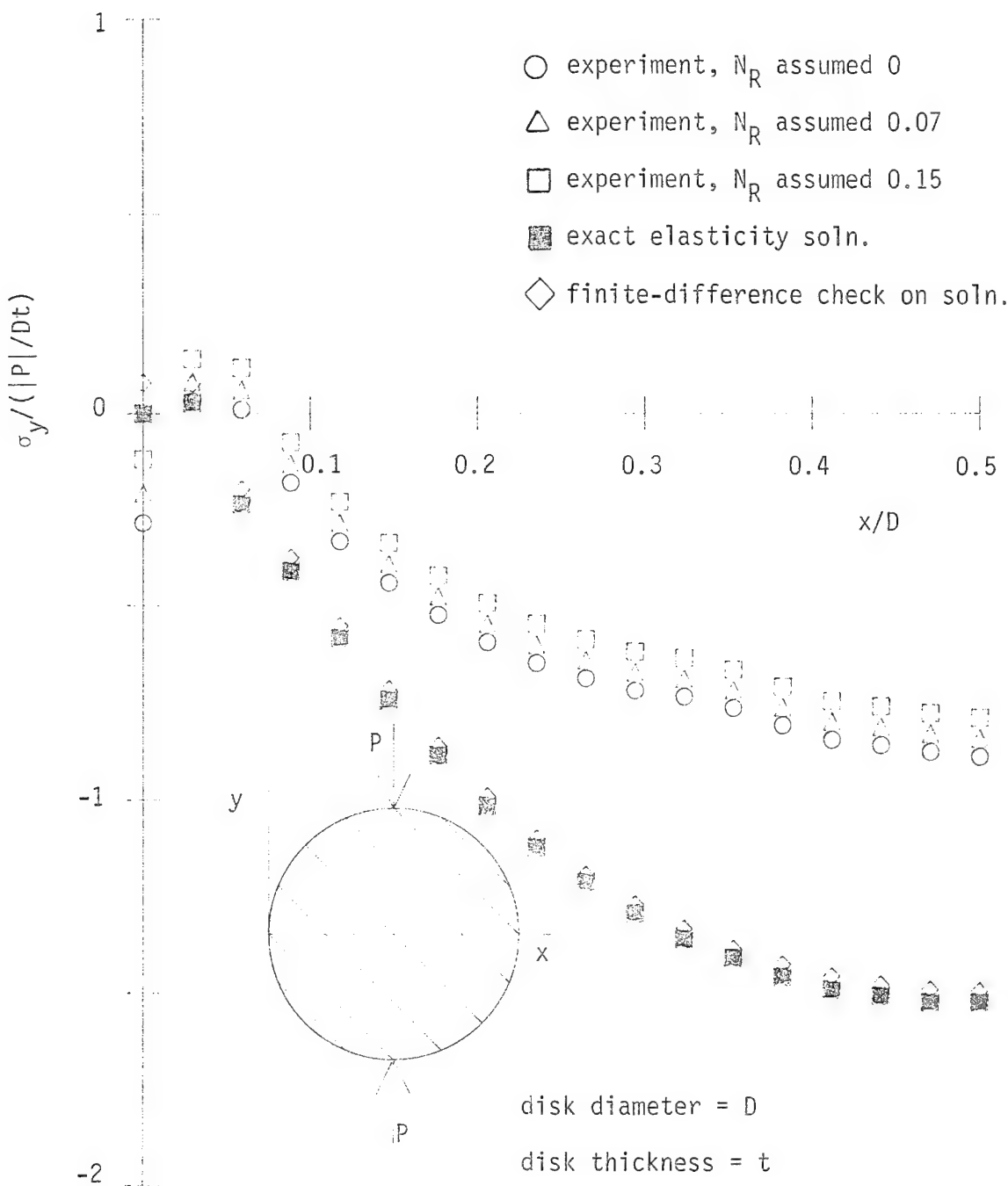
Fig. 93 Comparison of σ_y stresses along diameter perpendicular to load, fibers 45° relative to load.

Fig. 94 Comparison of σ_x stresses along diameter perpendicular to load, fibers 45° relative to load.

175

disk diameter = D

disk thickness = t
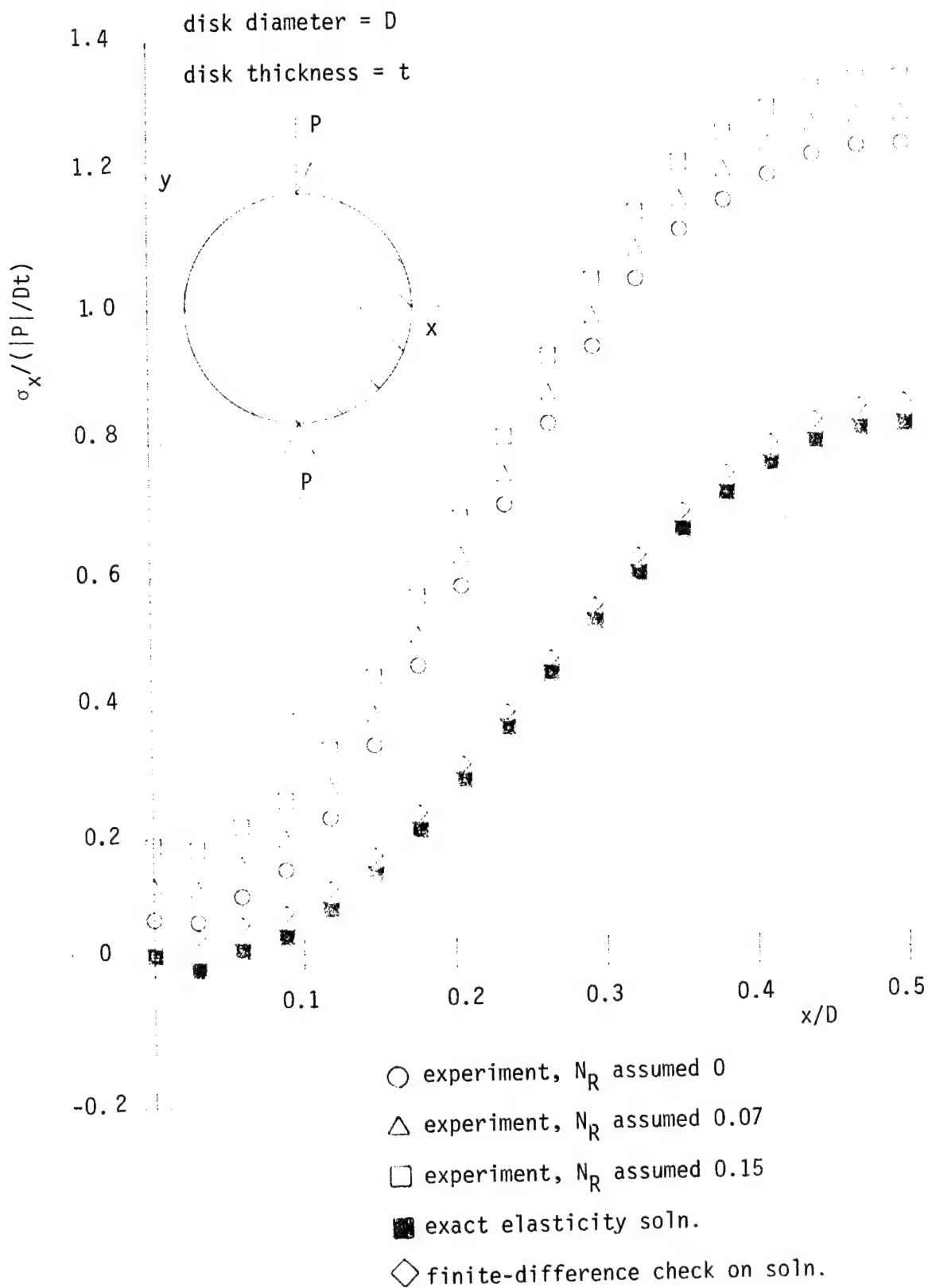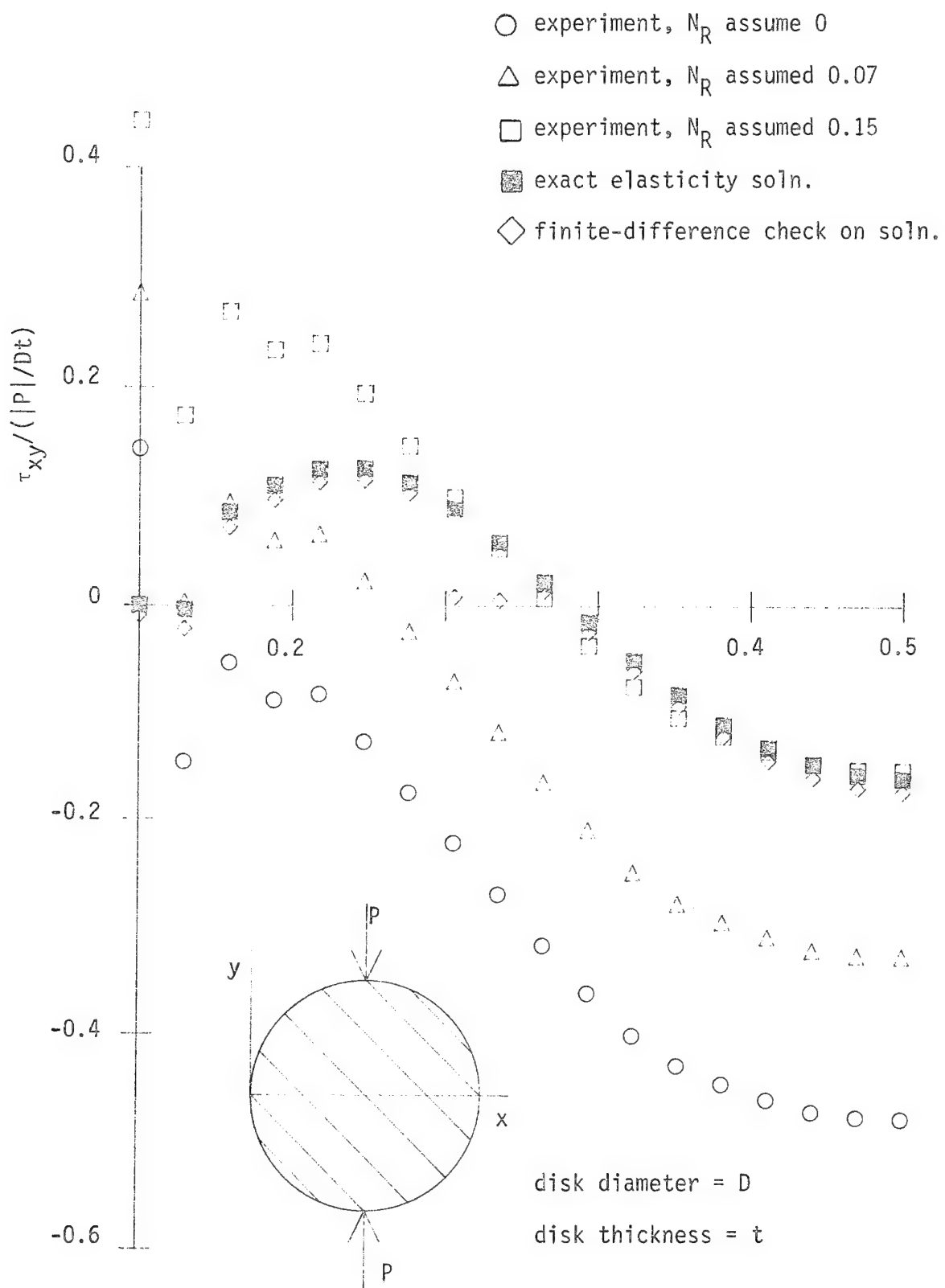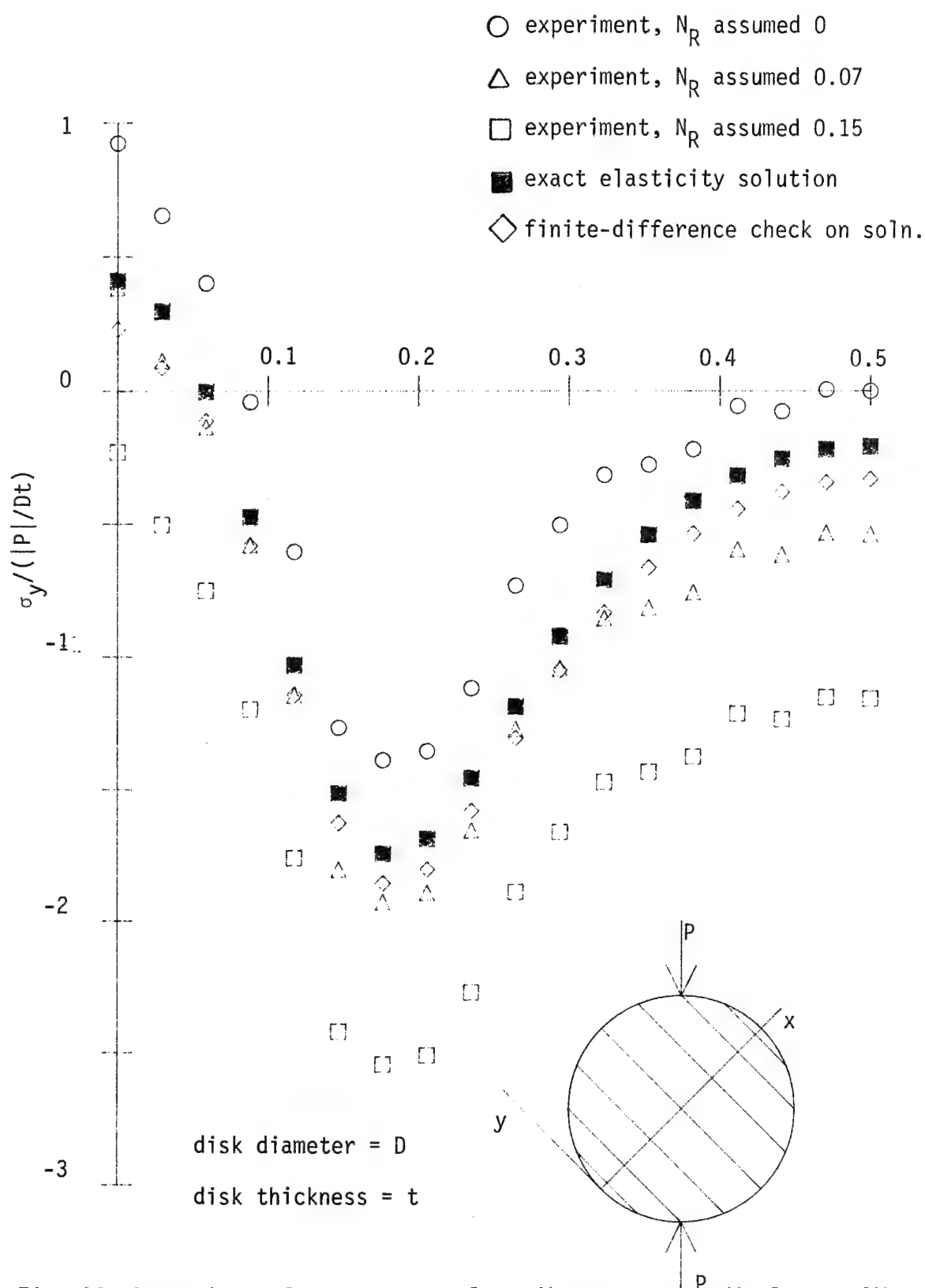
Fig. 96 Comparison of σ_y stresses along diameter perpendicular to fibers, fibers 45° relative to load.

177
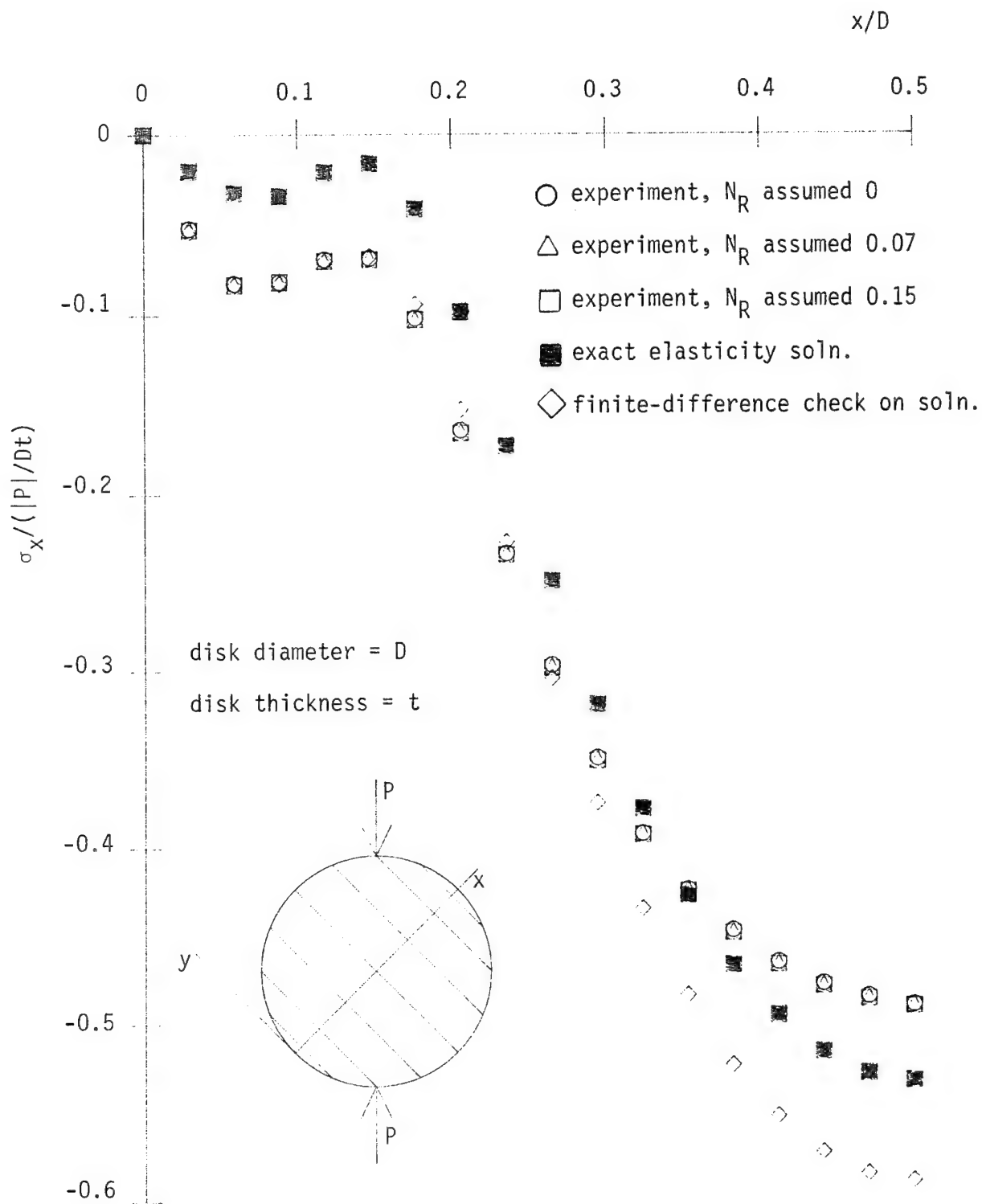
Fig. 97 Comparison of σ_x stresses along diameter perpendicular to fibers, fibers 45° relative to load.
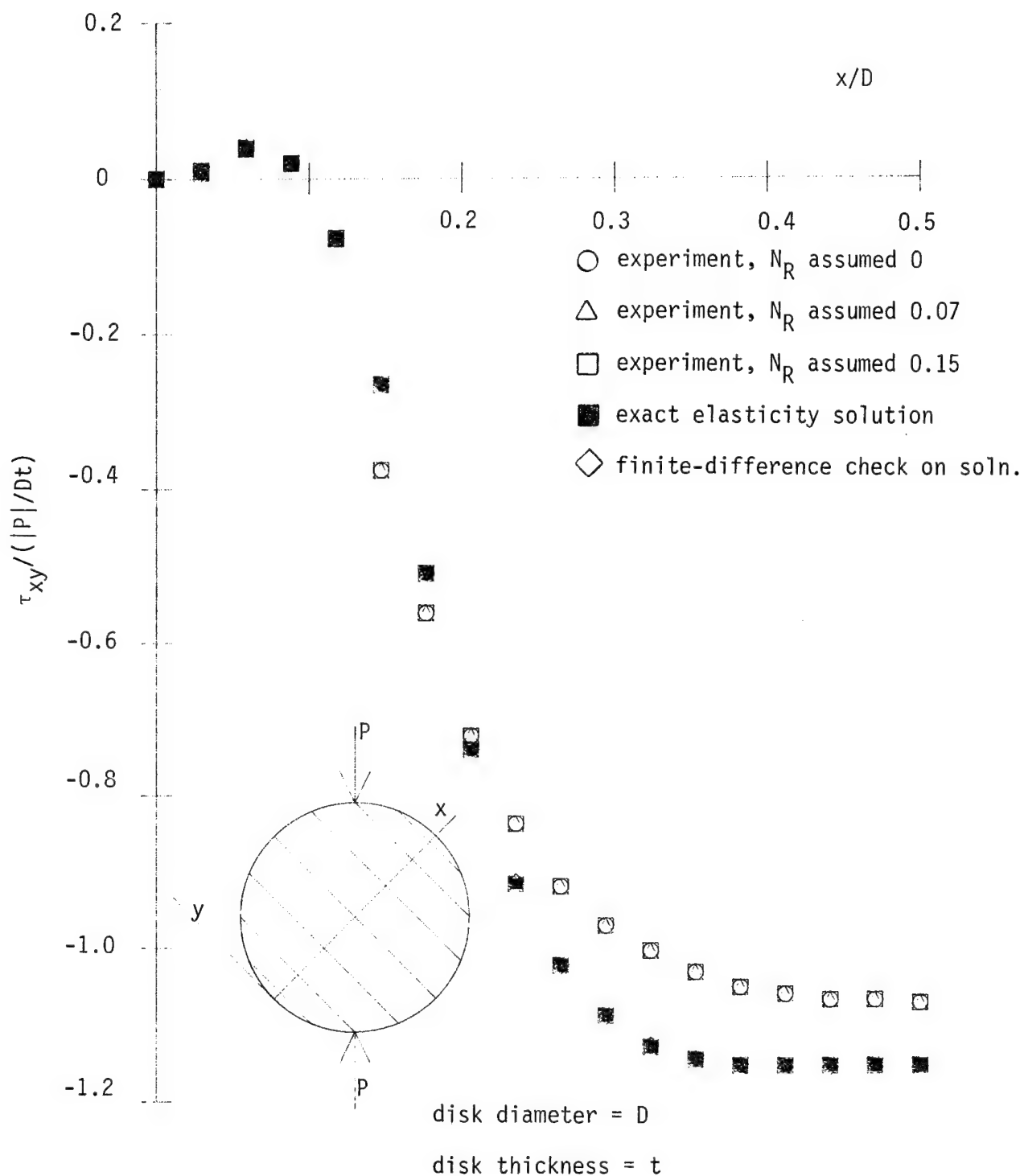
Fig. 98 Comparison of τ_{xy} stresses along diameter perpendicular to fibers, fibers 45° relative to load.

179
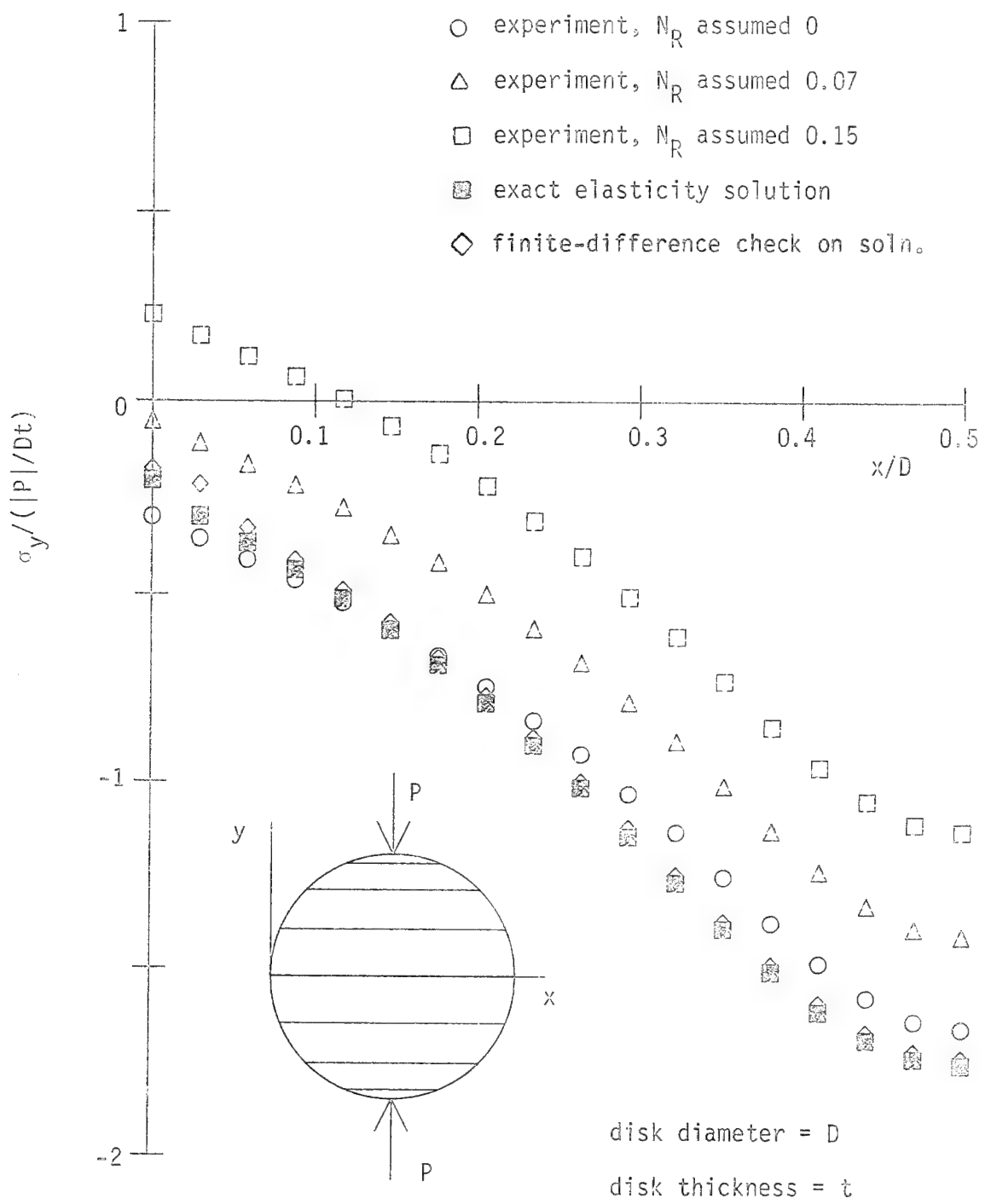
Fig. 99 Comparison of σ_y stresses along diameter perpendicular to load, fibers perpendicular to load.
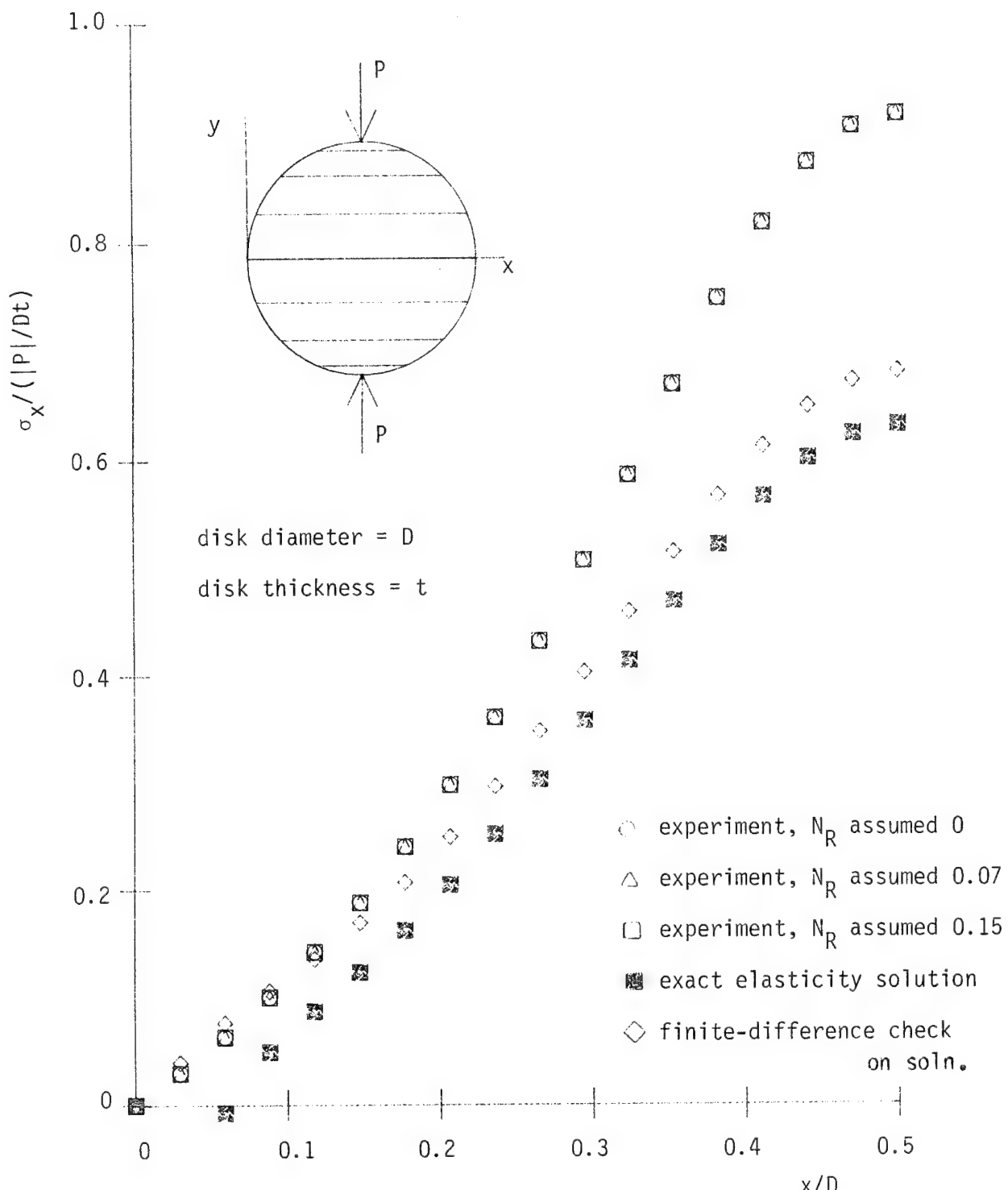
Fig. 100   Comparison of σ_x stresses along diameter perpendicular to load, fibers perpendicular to load.

181
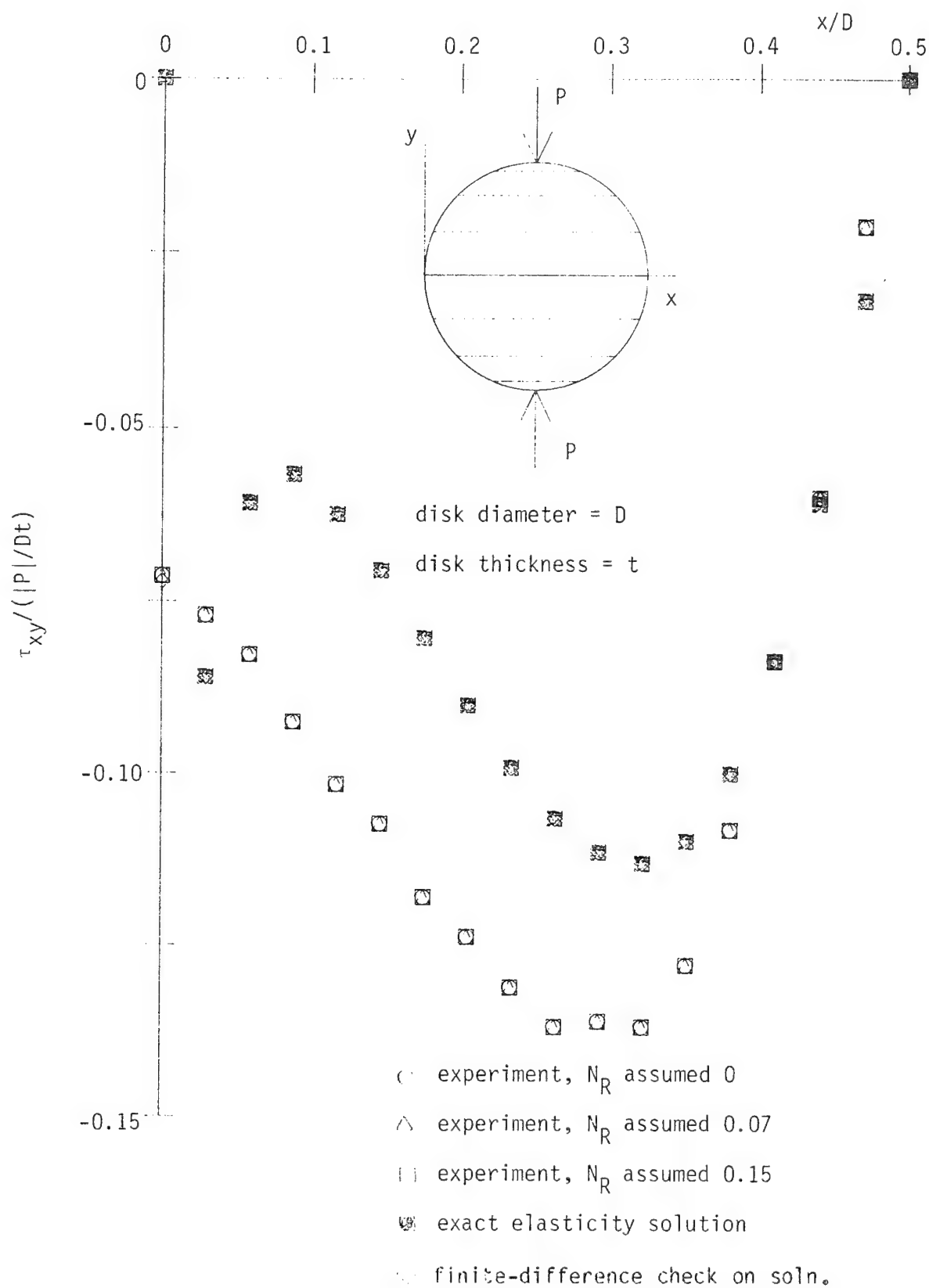
Fig. 101 Comparison of τ_{xy} stresses just of diameter perpendicular to load, fibers perpendicular to load.
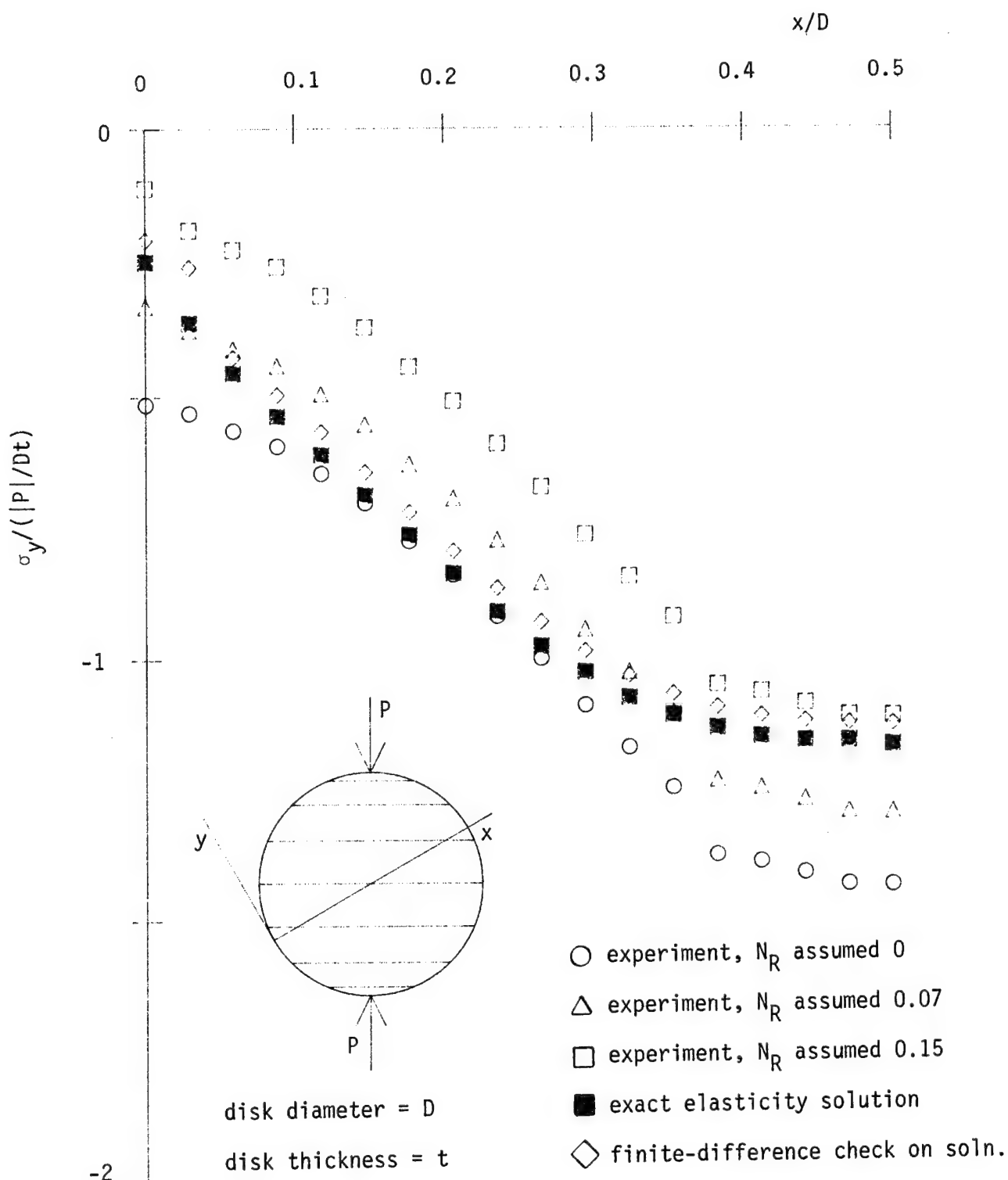
Fig. 102 Comparison of σ_y stresses along 30° diameter, fibers perpendicular to load.

183
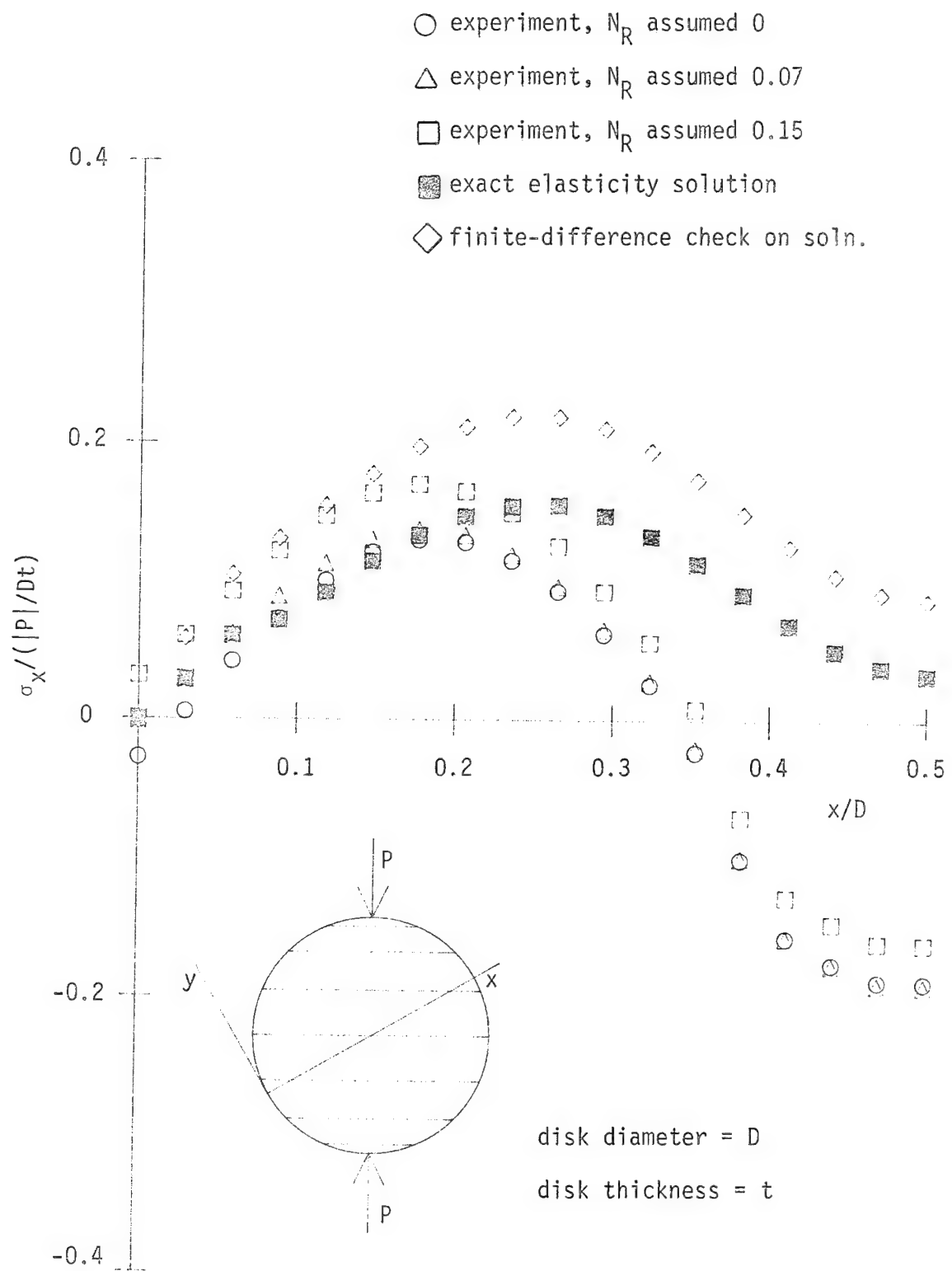
Fig. 103 Comparison of σ_x stresses along 30° diameter, fibers perpendicular to load.
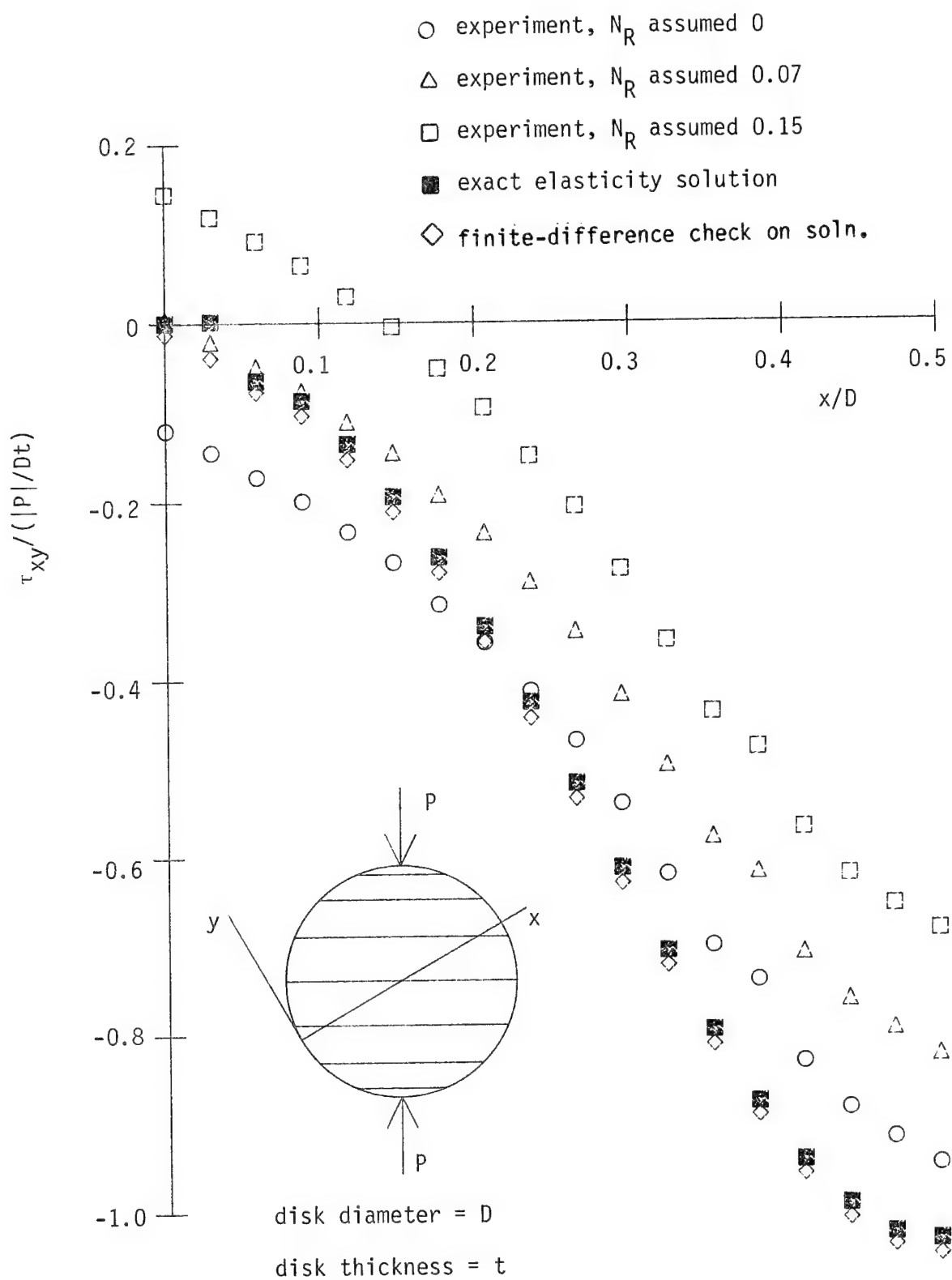
Fig. 104 Comparison of τ_{xy} stresses along 30° diameter, fibers perpendicular to load.

185

The shear stresses in fig. 89 showed a significant sensitivity to the assumed value of N_R. It appeared that if a value of $N_R = 0.02$ or 0.03 had been used, the correlation between theory and experiment for the shear stresses for that particular load and diameter orientation would have been good. The σ_y stresses for this case, fig. 87, would have also correlated well. To keep the scatter of fig. 89 in context, however, the scale of fig. 89 should be compared with the scale of fig. 87.

Fig. 90 shows sensitivity of the major compressive stress component to the assumed value of N_R. Here again a value of $N_R = 0.02 - 0.03$ would have given excellent correlation.

Figure 91 is the first case to show differences between the exact elasticity solution and the finite-difference calculations (solid squares and open diamonds, respectively) when the exact values of N_T and θ_T were used. Due to the magnitude of the stress in Fig. 91 relative to the major stress, fig. 90, there was no concern for the differences.

The case shown in figs. 93-95 deserves mention. Referring to eq. 85e, the value of ϕ for figs. 93-95 is $\phi = 45°$. This means $1/C_5$ is 0, or $C_5 \to \infty$. Also, from eqs. 85a and 85b, $C_1 = -C_2$. This is the special case discussed in eqs. 89a-91. It required a different computer program. The exact solution and the finite-difference calculations, solid squares and open diamonds, were in good agreement for this case. This gave confidence in this special-case computer program. This particular load/fiber orientation resulted in poor correlations between theory and experiment, e.g. fig. 93.

The cases where the load was perpendicular to the fibers, figs. 99-104, offered some unusual comparisons. The exact elasticity solution

186

and the finite-difference calculations using the exact values for N_T and θ_T deviated more in the σ_x stress than they did for any other case studied. Strangely enough, the σ_y and τ_{xy} stresses, figs. 99, 101, 102, and 104 showed good comparison between the two 'exact' cases.

As in the previous section on forward testing, it was of interest to determine how closely the stresses could be computed experimentally in an isotropic disk. Figures 105-107 show the three components of stress, in an isotropic disk, across a diameter perpendicular to the load. The shear stress was computed for the top line of the three-line finite-difference grid. There was no residual birefringence in the material.

Figure 105 shows the major compressive stress, σ_y. Here as in the previous discussions, the solid squares are the exact elasticity solution while the open circles are the results computed from the experimental values of N and θ and the finite-difference scheme. The comparison was good. Exact values of N and θ from the elasticity solution were used to test the finite-difference calculations and the results of that calculation are displayed as open diamonds. It is impossible to see them in fig. 105 since they coincide with the solid squares.

Figure 106 shows the σ_x stress calculations while fig. 107 shows the shear stress calculations. The comparisons between the exact solution and the experimental calculations were good for these stresses. In fact, they were much better than the comparisons for the minor stresses $\left(\sigma_x \text{ and } \tau_{xy}\right)$ in the orthotropic material. Figures 108-110 show the stress comparisons for a diameter which was 30° relative to the diameter perpendicular to the load. The correlation was again good.
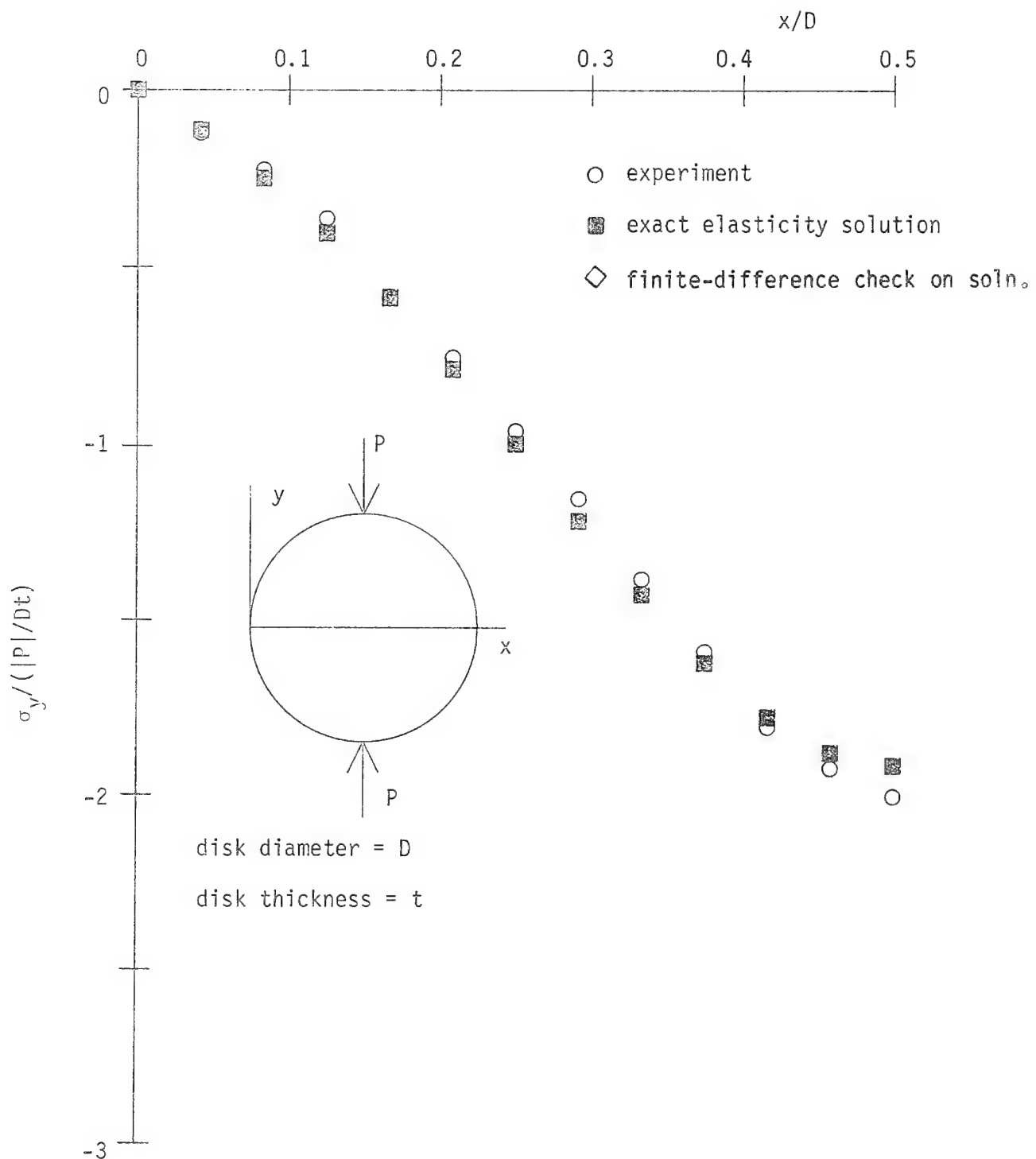
Fig. 105 Comparison of σ_y stresses along diameter perpendicular to load, isotropic disk.

188
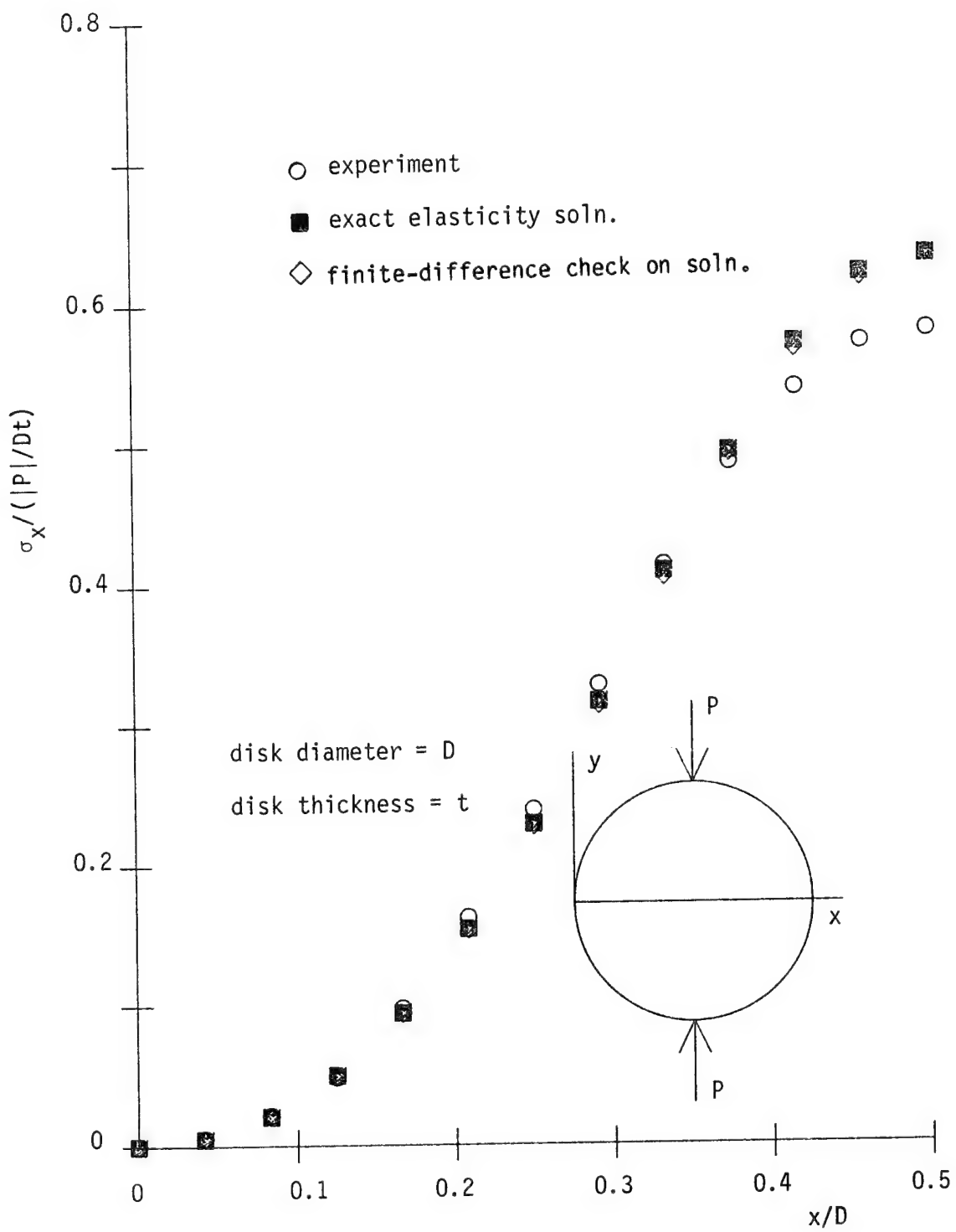
Fig. 106 Comparison of σ_x stresses along diameter perpendicular to load, isotropic disk.

189
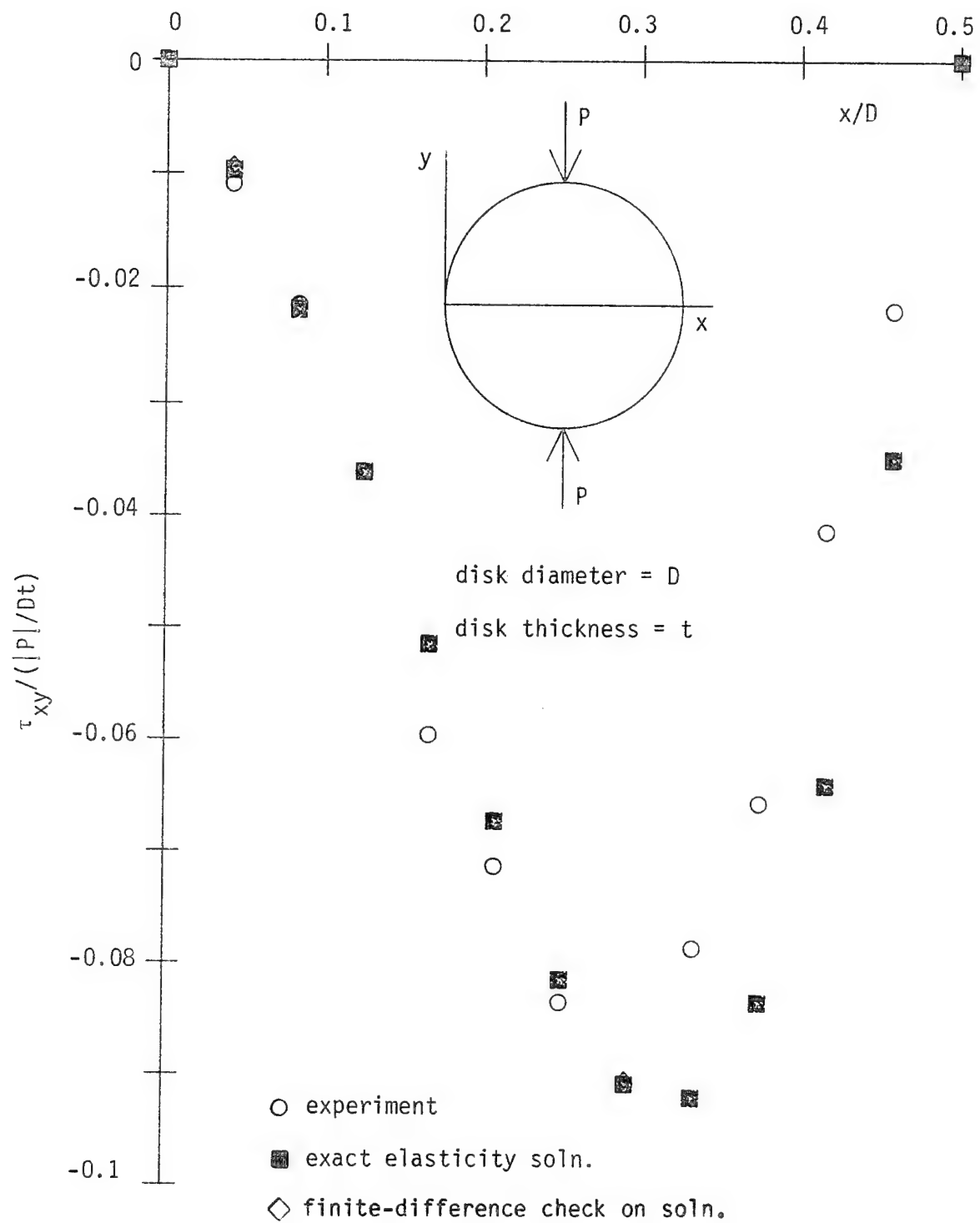
Fig. 107 Comparison of τ_{xy} stresses just off diameter perpendicular to load, isotropic disk.
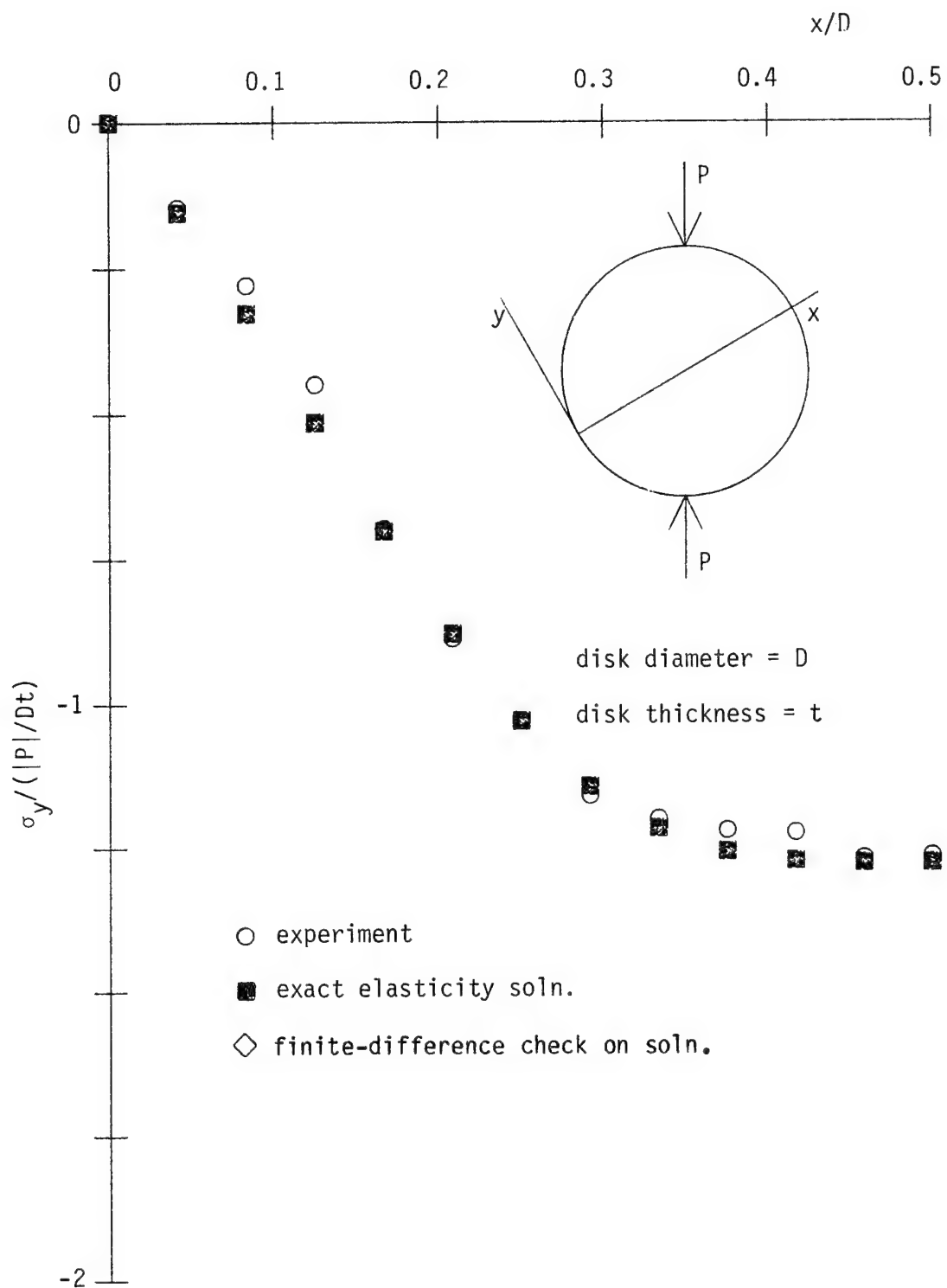
Fig. 108 Comparison of σ_y stresses along 30° diameter, isotropic disk.

191
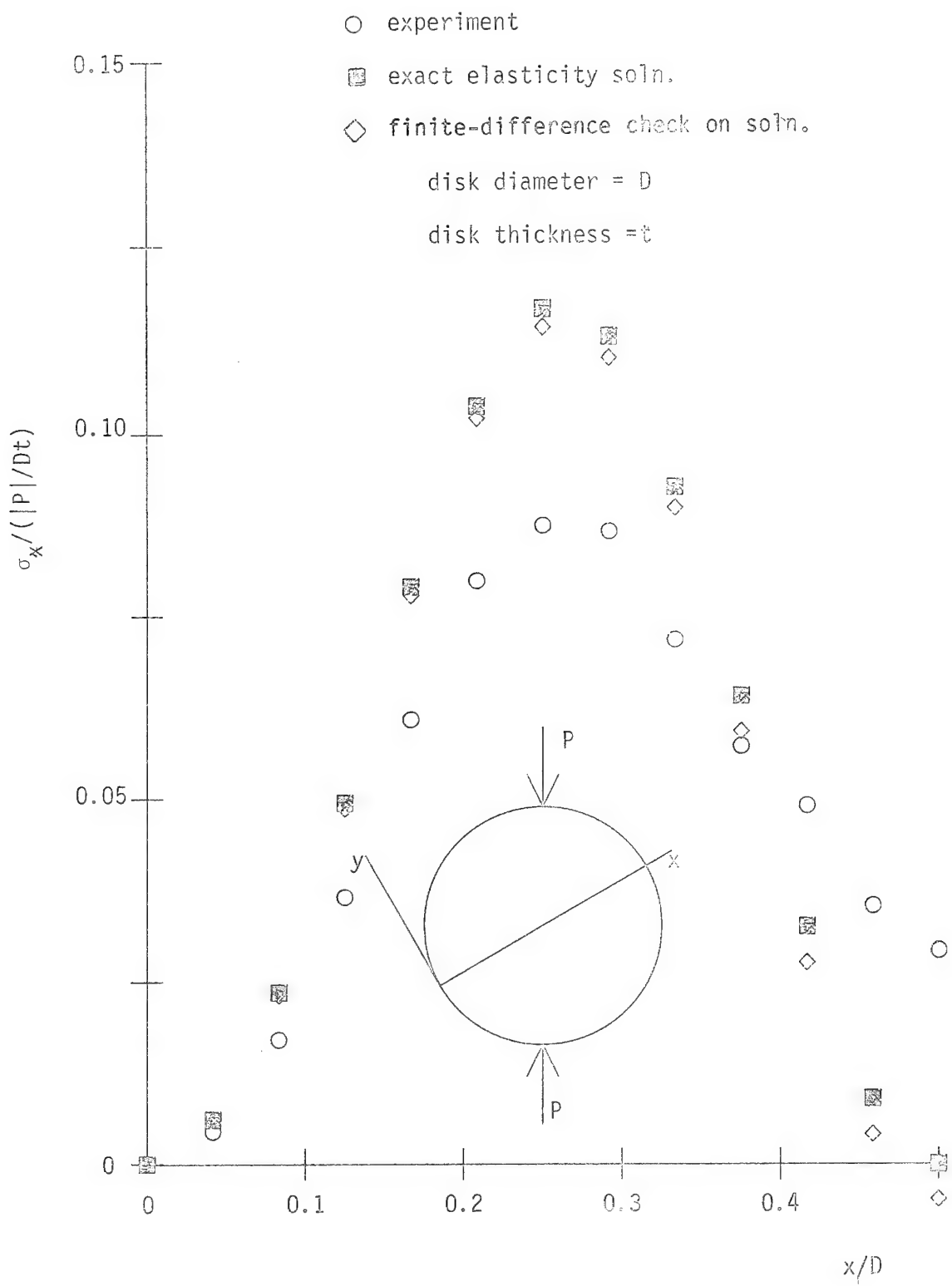
Fig. 109 Comparison of σ_x stresses along 30° diameter, isotropic disk.
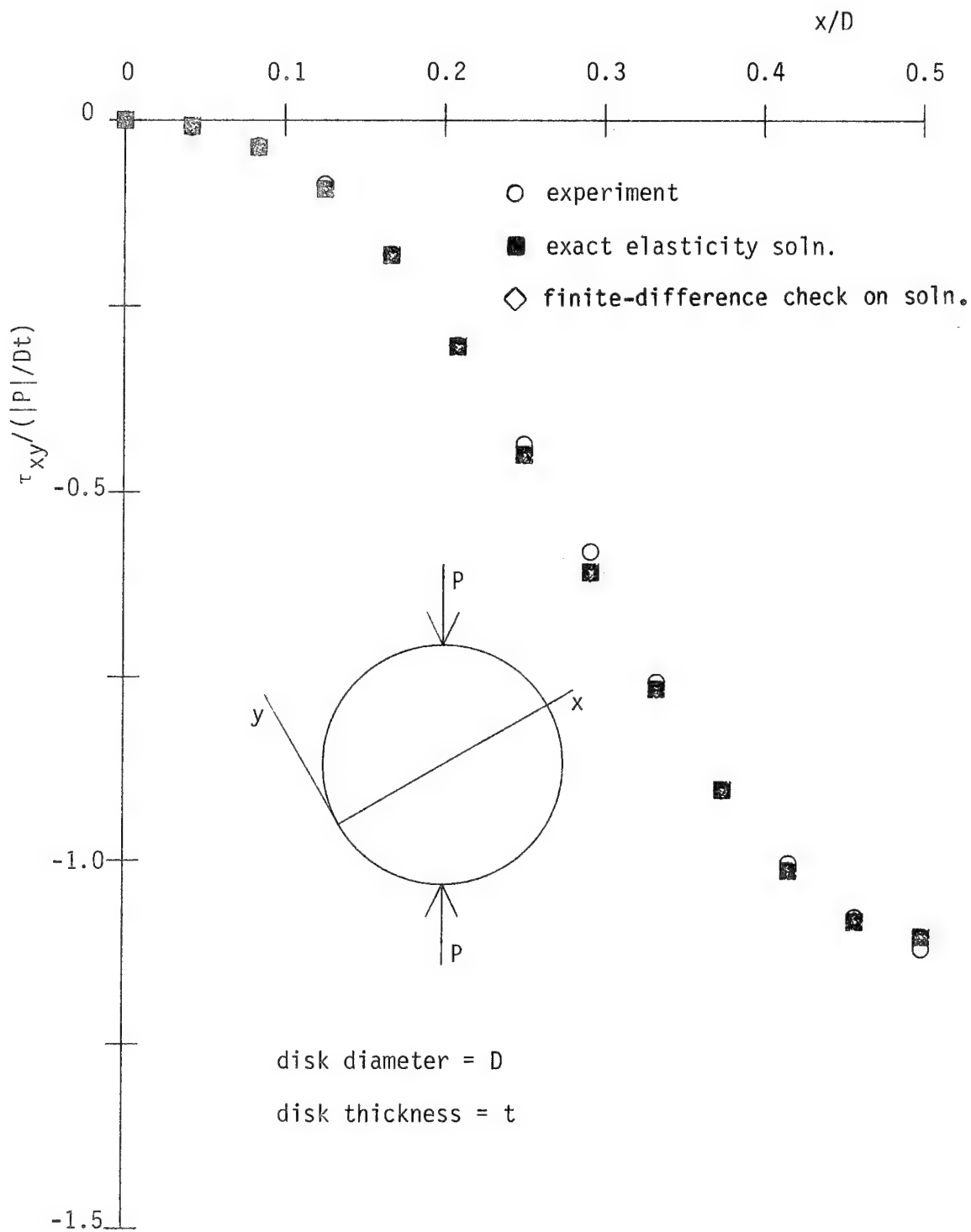
Fig. 110 Comparison of τ_{xy} stresses along 30° diameter, isotropic disk.

193

From the results for the orthotropic and isotropic disks, it is clear, as it was in the section on forward testing, orthotropic photoelasticity does not appear to be as accurate as isotropic photoelasticity. One is faced with the question. Is it the hypotheses and assumptions that are lacking, or is it the practicing of the theory? The lack of good fringe definition could certainly lead to scatter in the stresses predicted from the experimental data. Uncertainty in, or simple miscalculation of, the residual birefringence certainly could also produce the poor results. As has been seen, simply adjusting the level of residual birefringence can lead to excellent correlation between the theoretical elasticity prediction of stresses and the value determined from the experimental photoelastic data. All evidence seemed to indicate the level of residual birefringence, and perhaps a lack of spatial uniformity, were responsible for the lack of correlation that can be achieved with an isotropic disk. To look at the lack of correlation from one other point of view, a numerical study of the effects of inaccuracies in the isocline measurements was conducted. This study, and the motivation for it, are discussed in the next section.

EFFECTS OF ISOCLINE ERRORS
ON STRESS PREDICTIONS

From the figures and discussion of the fringe patterns in the orthotropic disk, e.g. fig. 51, it is clear that fringe definition was a concern in the experiments. The figures of fringe patterns shown previously are illustrations of the isochromatic fringe. The isoclinic fringe have not been illustrated. Several isoclinic fringes, along with their computer-generated predictions, could have been shown in the section on forward testing: global behavior. Since for stress predictions local behavior was more of a concern than global behavior, that exercise was not pursued. However, the importance of the isoclines should not be under-emphasised. In fact, in isotropic photoelasticity, the stress calculations are generally much more sensitive to inaccuracies in the isoclinics than to inaccuracies in the isochromatics. In isotropic photoelasticity, the isoclinic fringes are much harder to discern than the isochromatic fringes. The isoclinics are obscured by the isochromatic fringes and they are not as sharp. In addition, in regions of low stress gradients it is very difficult to see the isoclines. So it was with these experiment with orthotropic materials. The optical isocline was, at times, much more difficult to see than the isochromatics. Dispersion by the fibers, regions over which the isoclines did not change rapidly, and lack of vivid contrast between light and dark regions of the model, all contributed to uncertainties in the isoclinic data. For this reason, numerical studies were conducted to determine the effect of uncertainties in the isocline data on the predictions of σ_x, σ_y, and τ_{xy} for the various fiber and diameter orientations. There were strong

195

indications that some of the discrepancies observed between the exact stress calculations and the computations based on experimental data were due to uncertainties in the residual birefringence level. However, for completeness, the effects of uncertainties in the isocline measurements were studied.

The isocline uncertainty studies were of two types. Both were based on the isoclines predicted by the exact elasticity solution and the stress-optic laws. These were the same data used to generate the open diamonds in figs. 81-104. In the first uncertainty study, the theoretical value of the isocline of each mesh point in the finite-difference scheme was increased by 5°. This adjusted isocline was then used with the exact N_T as 'experimental data' in the finite-difference calculations. All stresses of all eight fiber/diameter orientations were computed using the skewed isocline. These stresses were compared with the stresses from the finite-difference calculations using the correct values of θ_T and, of course, N_T. The results of this study were used to determine how a 5° error in all isoclines affected the predicted stresses. The value of 5° was chosen as a value which could actually occur if several experimental effects were additive. The polariscope being used was a split bench type and the polarizer and analyser were linked together by shafts, universals, and other coupling mechanisms. In addition, these optical elements were rotated by means of gears. It is entirely possible that backlash in the gears and coupling elements could produce a constant bias in the measurements. In addition to the mechanical bias in the polariscope, the alignment of the disks in the polariscope was another source for a constant bias. It is possible that the fiber direction of the disk was not aligned exactly as assumed in the

polariscope. There is a 0° direction in the polariscope but there were no cross-hairs or other alignment aids to insure that the direction of polarization of the optical elements were aligned at a particular angle relative to the disk's fibers. The polariscope was equipped with the standard devices for measuring isocline angle, i.e. a pointer and graduated marks on the circumference of the analyser. The disk could have been rotated inplane by a degree or two relative to the zero degree direction of the polariscope. Related to this, it was evident that within the disk the fibers were not perfectly straight. Thus the fiber/polariscope alignment could have been biased in several ways. No effect was assumed to be large. It was simply assumed all effects added to about 5°.

In the second numerical study, the exact optical isocline at each mesh point was perturbed by adding to it an angle that was generated by a Gaussian random number generator. The mean of these angles added to the exact angles was 0° while the standard deviation was 5°. This random perturbation represented possible experimental error in interpreting the center of the isoclinic fringe. The error was assumed to result from the aforementioned lack of good definition of the isoclinic fringes. All stresses for all 8 fiber/diameter orientations were computed and compared with the finite-difference computations using exact values of θ_T and N_T of each mesh point.

As expected, a myriad of results were generated from the uncertainty studies. The effects of the two types of perturbations varied widely, depending on the fiber and diameter orientation, and the particular stress component. For example, the σ_y stress along the diameter perpendicular to the load, with the fibers aligned with the load, was not af-

197

fected by either type of error. The same was true of the shear stress

for the case with the fibers 30° relative to the load and the diameter

perpendicular to the fibers. On the other hand, there were cases where

one type of error had an effect but the other type did not. For exam-

ple, the σ_x stresses along a diameter perpendicular to the load and with

the load perpendicular to the fibers were more sensitive to random er-

rors than to the constant error. Finally, some stresses were seriously

affected by either disturbance to the isocline. The shear stresses

along a diameter perpendicular to the load and with the fibers 30° rela-

tive to the load were very sensitive to isocline errors.

Tables 4 and 5 rank the various situations as to how they were af-

fected by the errors. The top of the column corresponds to conditions

least affected. There is no significance to the fact that σ_y is the

left column, σ_x the middle column and τ_{xy} is the right column. That is,

it cannot be said that the least affected σ_y stress was less affected

than the least affected σ_x stress. It is possible to say, however, that

for a specific fiber orientation and diameter, the larger of the three

stresses was generally least sensitive to errors. In the tables the

figure number which illustrates the fiber orietation relative to the

load, and the particular diameter, is indicated in parenthesis. Obvi-

ously these figures do not represent the perturbed stress computations.

The major issue, however, was: Could the discrepancies in the

stresses between theory and experiment observed in the various situa-

tions for the actual disk be explained by the presence of either a con-

stant or random error? Figure 111 shows the predicted σ_x stresses along

the diameter perpendicular to the fibers for the case when the fibers

were 30° relative to the load. The figure shows the values predicted

198

Table 4

Ranking of Effects of Constant Isocline Error on Stress Predictions [1]

σ_y		σ_x		τ_{xy}	
fiber/load angle	diameter (fig. no.)	fiber/load angle	diameter	fiber/load angle	diameter
aligned	perp. to load(81)	aligned	perp. to load(82)	30°	perp to fibers(92)
perp.	perp. to load(99)	perp.	perp. to load(100)	aligned	30° (85)
aligned	30° (84)	45°	perp. to fibers(97)	45°	perp. to fibers(98)
perp.	30° (102)	45	perp. to load(94)	aligned	perp. to load(83)
45°	perp. to load(93)	aligned	30° (85)	perp.	30° (104)
30°	perp. to load(87)	30°	perp. to fibers(91)	perp.	perp. to load(102)
30°	perp. to fibers(90)	30°	perp. to load(88)	45°	perp. to load(95)
45°	perp. to fibers(96)	perp.	30° (103)	30°	perp. to load(89)

[1] least affected at top

199

Table 5

Ranking of Effects of Random Isocline
Error on Stress Predictions[1]

σ_y		σ_x		τ_{xy}	
fiber/load angle	diameter (fig. no.)	fiber/load angle	diameter	fiber/load angle	diameter
aligned	perp. to load(81)	45°	perp. to fibers(97)	30°	perp. to fibers(92)
perp.	perp. to load(99)	30°	perp. to fibers(91)	aligned	30° (85)
aligned	30° (84)	aligned	30° (85)	45°	perp. to fibers(98)
45°	perp. to load(93)	30°	perp. to load(88)	aligned	perp. to load(83)
perp.	30° (102)	perp.	30° (103)	perp.	30° (104)
30°	perp. to load(87)	aligned	perp. to load(82)	perp.	perp. to load(102)
30°	perp. to fibers(90)	perp.	perp. to load(100)	30°	perp. to load(89)
45°	perp. to fibers(96)	45°	perp. to load(94)	45°	perp. to load(95)

[1] least affected at top
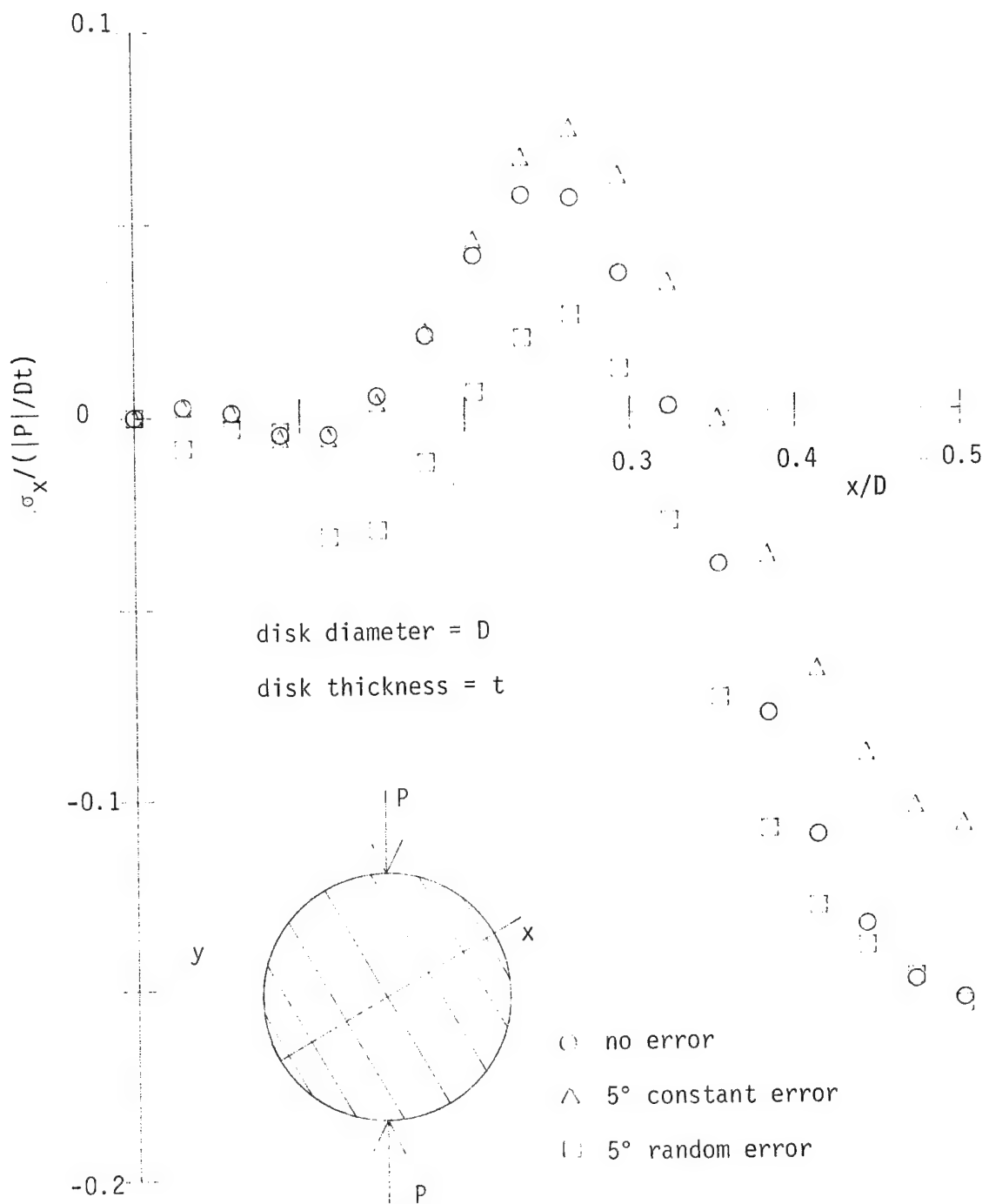
Fig. 111 Effect of isocline errors on predicted σ_x stresses along
diameter perpendicular to fibers, fibers 30° relative to load.

using the exact values of the isocline and predictions based on the two types of disturbances to the isoclines. This figure should be compared to fig. 91. The case of the constant error in fig. 111 looks somewhat like the mismatches in fig. 91. Figure 112 shows the predicted σ_y stresses along a diameter perpendicular to the fibers for the case of the fibers making a 45° degree angle relative to the load. This figure should be compared with fig. 96.

From the figures it is clear a constant error was much more likely than random errors to explain the discrepancies observed between theoretical and experimentally measured stresses. However, there was a significant difference between the discrepancies observed in the actual disk and the discrepancies generated in the numerical error studies. In both fig. 111 and 112 it is seen that the constant isocline errors seemed to affect stresses near the center of the disk more than they affected the stresses near the disk's edge. For example, in fig. 112, the triangles and circles coincide up to about $x/D = 0.15$. In fig. 111 these symbols coincide up to $x/D = 0.2$. After those locations, the two predictions diverge as the center of the disk is approached. In contrast, fig. 96, for example, shows a constant discrepancy along the whole diameter, starting at the edge of the disk. This would seem to indicate a constant error of a type different than a constant isocline error. As was felt all along, and as these isocline error studies confirmed, errors in the level of residual birefringence were more likely to account for discrepancies than other types of errors.

For completeness, similar scatter studies were conducted for the isotropic disk stresses. Recall, the experimentally determined stresses for the isotropic disk were quite close to the predictions of the

202
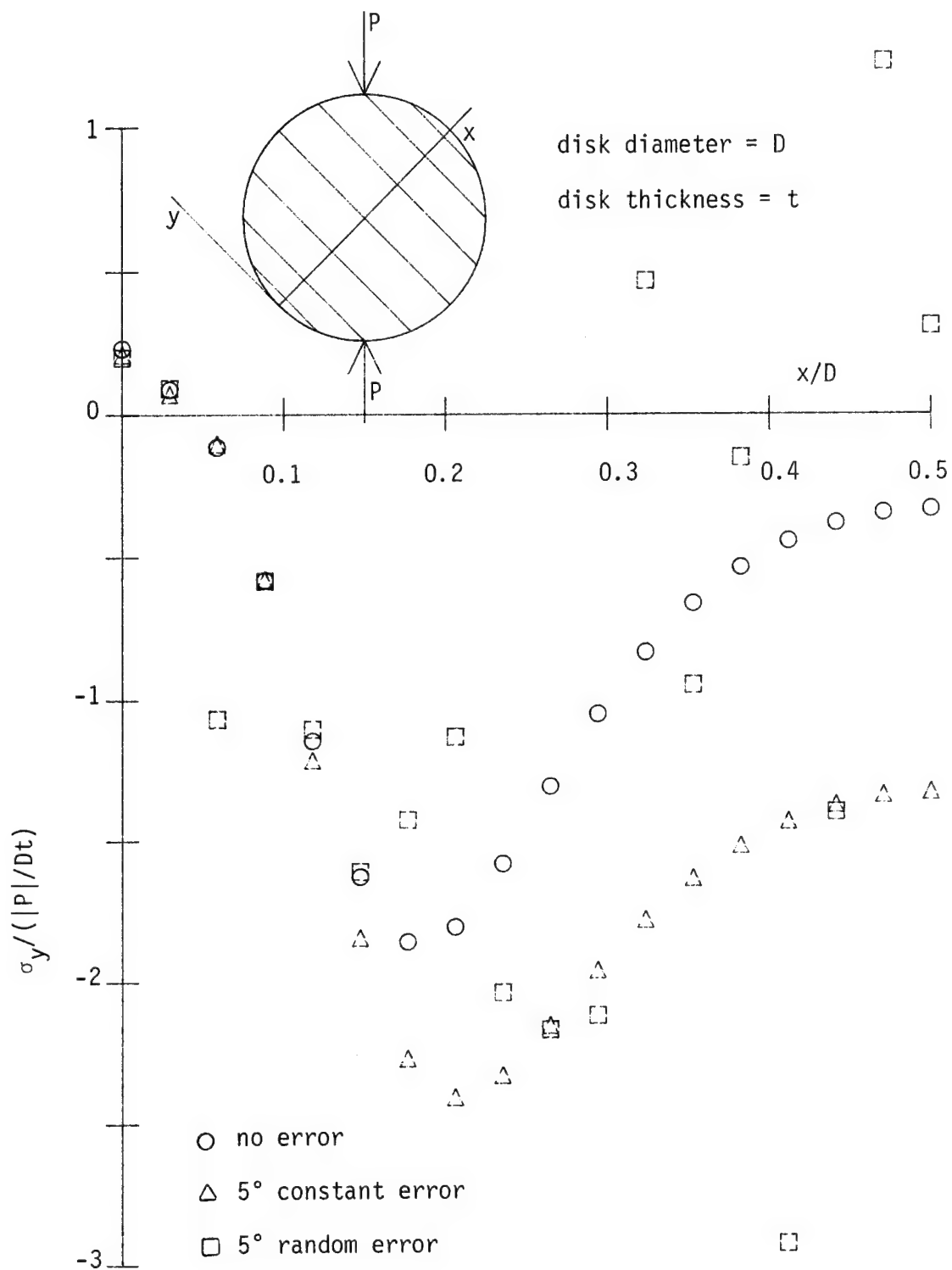
Fig. 112   Effect of isocline errors on predicted σ_y stresses along
diameter perpendicular to fibers, fibers 45° relative to load.

203

elasticity solutions. Figure 109 illustrates the stress which deviated the most from predictions. Figure 113 shows the stresses computed for that same situation but with the two types of errors incorporated into the isocline. As can be seen, both types of errors affect this stress calculation to a significant degree. Comparing figs. 109 and 113, it appears something other than random errors caused deviation in fig. 109. However since neither type of error caused the constant shift along the entire diameter, as for example in fig. 89, the isotropic disk was not studied further.

The results of the error study indicated that while isocline errors can lead to serious errors in the prediction of stresses, such errors were not likely the source of the errors observed in the experiments with the orthotropic disk. The errors observed had very few of the characteristics of random errors and they did not seem to behave exactly like a constant error. These errors were thus discounted as a major source of discrepancy.
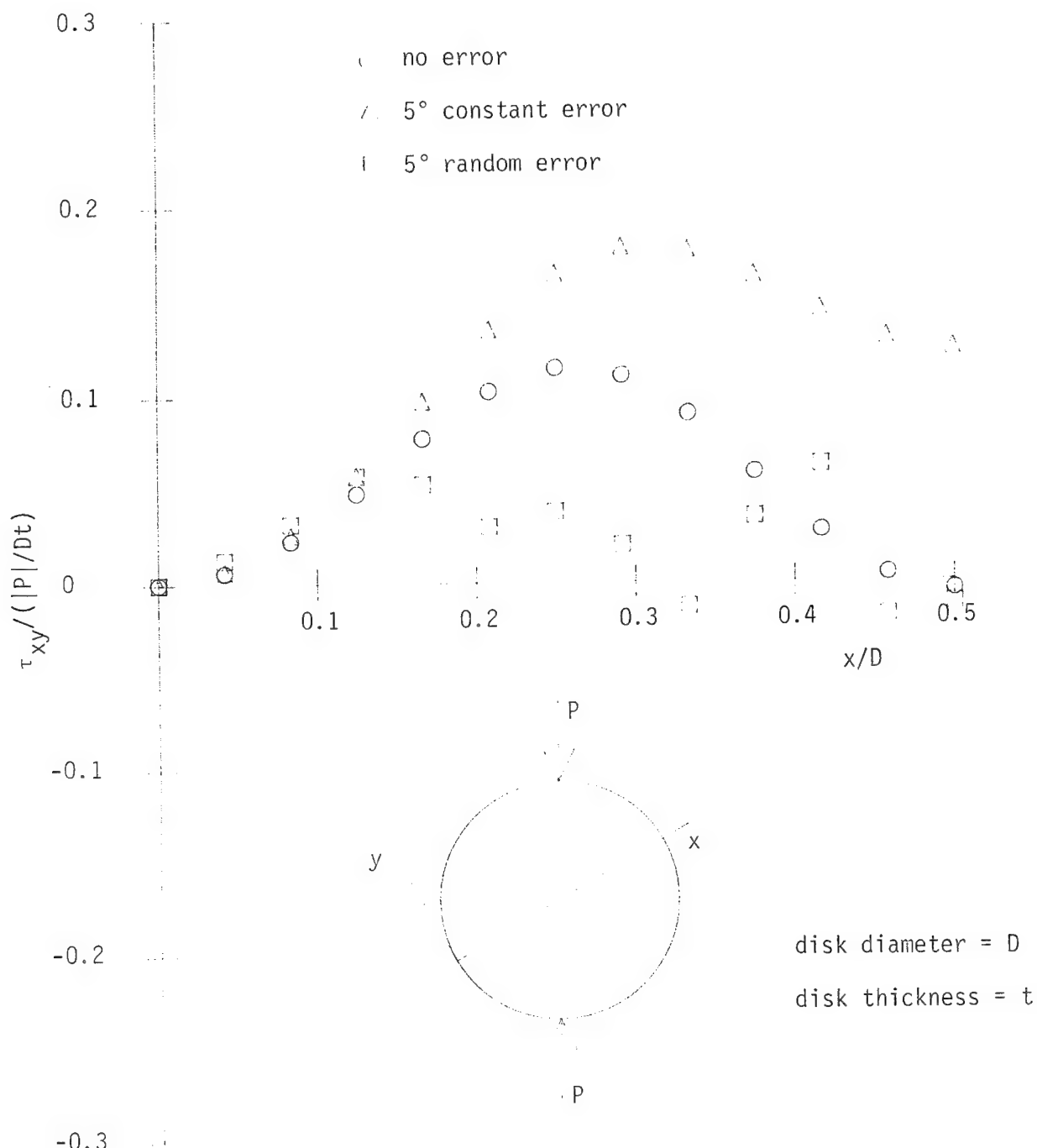
Fig. 113 Effect of isocline errors on predicted τ_{xy} stresses along 30° diameter, isotropic disk.

SUMMARY AND CONCLUDING COMMENTS

A considerable amount of information, both in the form of the derivation of equations and in the form of data, has been presented. In the second section equations governing the photoelastic phenomenon in orthotropic materials were derived. In the third section, calibration of the material was discussed and calibration data were presented. The fourth and fifth sections dealt with testing and checking the orthotropic photoelastic theory in the context of a unidirectional disk in diametral compression. The just-presented section discussed sources of errors in photoelastic materials. As data were presented, they were discussed and put into context with other data. The purpose of this section is to summarize the important results presented.

The theory of orthotropic photoelasticity was developed in the second section so that: (1) the effects of residual birefringence could be accounted for in the photoelastic phenomenon, and (2), the key steps leading to specific operational equations, e.g. stress prediction equations, were shown. The experiments for calibrating the photoelastic material revealed that uniaxial tests are not the best way to calibrate the material. The four-point bend specimen was found to be superior to the uniaxial specimen for calibration purposes. The reasons were as follows:

(1) The stress gradients in the bending specimen will lead to sharper fringes and thus better fringe definition.

(2) A single fixture, specimen, and test can be used to load the material in both tension and compression.

206

(3) The optical neutral axis is a convenient way to assess residual
birefringence.

Unfortunately, uniaxial tests must be conducted for determining elastic
properties and so the four-point bend tests constitute an extra set of
tests.

The comparisons of the computer-generated and the observed fringe
patterns revealed that on-a-whole, the notion of orthotropic photoelas-
ticity, as presented, is valid. As with the uniaxial tests, sharpness
of fringes was shown to be a concern. Also, it was shown that the level
of residual birefringence affected the correlation between the predicted
and observed fringe patterns. By adjusting the assumed level of residu-
al birefringence the predicted and observed fringe pattern could be made
to coincide for a particular case. Unfortunately, the adjustment was a
function of the load orientation relative to the fibers. The computer-
generated fringes also showed that in the presence of residual birefrin-
gence, the sign of the applied load can strongly affect the fringe pat-
tern.

A detailed examination of the predicted and observed photoelastic
behavior was provided by studying the isochromatic and isoclinic fringes
along specific disk diameters. This type of point-by-point analysis was
necessary for accurate determination of the stresses. The fringe pre-
diction study was contrasted by conducting similar studies on isotropic
disks. From the fringe prediction studies, it can be concluded that:

1) The material seemed to exhibit behavior associated with lower rather than higher levels of residual birefringence. Specifically, a value between 0 and 0.07 for N_R would have correlated well with 80% of the cases.

2) Compared to isotropic photoelasticity, orthotropic photoelasticity, as hypothesised here, does not seem as accurate. This may be related to the lack of good fringe resolution or more basically, to the assumptions of the theory itself. Three assumptions which could be suspect are: (a) validity of through-the-thickness averaging, (b) validity of the stress-optic law being orthotropic, and (c), validity of the superposition of residual and mechanically-induced birefringent effects. To challenge these assumptions requires basic research beyond the scope of this study.

The section on stress prediction reinforced the idea that residual birefringence in the material was less than $N_R = 0.15$. Specifically a value between 0.0 and 0.07 appeared to be correct. It is very important to note, however, in no computation nor experimental measurement was there overwhelming support for the assumption $N_R = 0$. Some value of N_R could be chosen so that correlation was good. Unfortunately, the level of N_R needed for good correlation varied from one situation to the other. However, it can be concluded that, in general, stresses can be predicted with confidence using orthotropic photoelastic material. Unfortunately in stress prediction, and in every other phase of the correlation between theory and experiment, when the fibers were perpendicular to the load the correlation between theory and experiment was poor.

208

Finally, studies examining the effects of isocline errors showed that while isocline errors can lead to serious consequences, they were not likely to have caused the observed discrepancies between the experiments and the theoretical predictions.

REFERENCES

1. Dally, J. W. and Riley, W. F., Experimental Stress Analysis, 2nd Edition, New York: McGraw-Hill Book Co., 1978, Ch. 13.

2. Lipson, S. G. and Lipson, H. Optical Physics, Cambridge at the University Press, 1969, Section 5.4.3, p. 120.

3. Bert, C. W., "Theory of photoelasticity for birefringent filamentary composites," Fiber Science and Technology, Vol. 5, 1972, pp. 165-171.

4. Knight, C. E. and Pih, H., "Shear difference method and application in orthotropic photoelasticity," J. of Engineering Materials and Technology, October 1976, pp. 369-374.

5. Doyle, J. F., "Constitutive relations in photomechanics," Int. J. Mech. Sciences, Vol. 22, No. 1, 1980, pp. 1-8.

6. Knight, C. E., Jr., "Orthotropic photoelastic analysis of residual stresses in filament-wound rings," Experimental Mechanics, Vol. 12, Feb. 1971, pp. 107-112.

7. Pipes, R. B. and Dalley, J. W., "On the fiber-reinforced birefringent composite materials," Experimental Mechanics, Vol. 13, August 1973, pp. 348-349.

8. Cernosek, J., "On photoelastic response of composites," Experimental Mechanics, Vol. 15, Sept. 1975, pp. 354-357.

9. Prabhakaran, R., "The interpretation of isocinics in photo-orthotropic-elasticity," Experimental Mechanics, Vol. 16, Jan. 1976, pp. 6-10.

10. Sampson, R. C., "A stress-optic law for photoelastic analysis of orthotropic composites," Experimental Mechanics, Vol. 10, May 1970, pp. 210-215.

11. Daniel, I. M., Niro, T., and Koller, G. M., "Development of orthotropic birefringent materials for photoelastic stress analysis," NASA CR-165709, May 1981.

12. Lekhnitskii, S. G., Anisotropic Plates, translated from 2nd. ed. by S. W. Tsai and T. Cheron, Gordon and Breach, Science Publishers, New York, 1968.

13. Frocht, M. M., Photoelasticity, Vol. 2, John Wiley and Sons, Inc. New York, 1948.

14. Hyer, M. W., "Use of two-dimensional photoelastic models to study stresses in double-lap bolted joints: Load transfer and stresses in the inner lap," VPI & SU College of Engineering Report, VPI-E-80-9, 1980.

Bibliography

1. B. D. Agarwal and S. K. Chaturvedi, "Development and characterization of optically superior photoelastic composite materials," *International Journal of Mechanics Science*, Vol. 20, 1978, pp. 407-414.

2. C. W. Bert, "Theory of photoelasticity for birefringent filamentary composites," *Fiber Science and Technology*, (5) 1972, pp. 165-171.

3. J. Cernosek, "On photoelastic response of composites," *Experimental Mechanics*, Sept. 1976, pp. 354-357.

4. K. Chandrashekhara and K. A. Jacob, "A numerical method of separation of stresses in photo-orthotropic elasticity," *Experimental Mechanics*, Feb. 1978, pp. 61-66.

5. K. Chandrashekhara and K. A. Jacob, "Experimental-numerical hybrid technique for stress analysis of orthotropic composites," *Developments in Composite Materials*, 1, G. S. Holister, ed., Applied Science, Chapter 5, 1977, pp. 67-83.

6. K. Chandrashekhara and A. Jacob, "Photoelastic stress analysis of a composite cylinder subjected to mechanical loading," *AIAA Journal*, Vol. 15, No. 10, Oct. 1977, pp. 1432-1435.

7. K. Chandrashekhara, K. A. Jacob, R. Prabhakaran, "Towards stress freezing in birefringent orthotropic composite materials," *Experimental Mechanics*, August 1977, pp. 317-320.

8. S. K. Chaturvedi, "An approximate theory of photoelasticity for birefringent filamentary composites," *Composites*, July 1981, pp. 173-176.

9. S. K. Chaturvedi, "Isotropic and singular points in photoelasticity of composites," *Composites Technology Review*, Vol. 4, No. 1, 1982, pp. 22-25.

10. S. K. Chaturvedi, "Fundamental concepts of photoelasticity for anisotropic composite materials," *Int. J. of Engineering Science*, Vol. 20, No. 1, 1982, pp. 145-157.

11. J. W. Dally and R. Prabhakaran, "A class of zero-birefringent polymers," *Experimental Mechanics*, Jan. 1971, pp. 26-32.

12. J. W. Dally and R. Prabhakaran, "Photo-orthotropic-elasticity," *Experimental Mechanics*, Aug. 1971, pp. 346-356.

13. J. F. Doyle, "Constitutive relations in photomechanics," *Int. J. Mech. Sci.* Vol. 22, No. 1, 1980, pp. 1-8.

14. C.E. Knight, Jr., "Orthotropic photoelastic analysis of residual stresses in filament-wound rings," Experimental Mechanics, February 1972, pp. 107-112.

15. C. E. Knight, Jr., Orthotropic photoelasticity for fiber-reinforced composite materials, Ph.D. Thesis, U. of Tennessee, 1974, Available University Microfilms, Ann Arbor, MI 48106.

16. S. K. Chaturvedi, "A rational theory of oblique incidence and its extension to stress-separation in birefringent composites," Experimental Mechanics, March 1983, pp. 36-41.

17. C. E. Knight, Jr. and H. Pih, "Shear difference method and application in orthotropic photoelasticity," Journal of Engineering Materials and Technology, Oct. 1976, pp. 369-374.

18. R. H. Marloff and I. M. Daniel, "Three-dimensional photoelastic analysis of a fiber-reinforced composite model," Experimental Mechanics, April 1969, pp. 156-162.

19. H. Pih and C. E. Knight, "Photoelastic analysis of anisotropic fiber reinforced composites," Journal of Composite Materials, Vol. 3, June 1969, pp. 94-107.

20. R. B. Pipes and J. W. Dally, "On the fiber-reinforced birefringent composite materials," Experimental Mechanics, Aug. 1973, pp. 348-360.

21. R. B. Pipes and J. L. Rose, "Strain-optic law for a certain class of birefringent composites," Experimental Mechanics, Sept. 1974, pp. 355-360.

22. R. Prabhakaran, "Determination of principal stresses in birefringent composites by hole-drilling method," Proceedings, 30th Annual Conference, Reinforced Plastics/Compoistes Institute, The Society of the Plastics Industry, Inc. Feb. 16-20, 1981.

23. R. Prabhakaran, "Extension of oblique incidence method to photo-orthotropic-elasticity," Experimental Mechanics, Dec. 1982, p. 462-467.

24. R. Prabhakaran, "On the stress-optic law for orthotropic-model materials in biaxial fields," Experimental Mechanics, Jan. 1975, pp. 29-34.

25. R. Prabhakaran, "Photoelastic analysis of an orthotropic ring under diametral compression," AIAA Journal, Vol. 11, no. 6, June 1973, pp. 777-778.

26. R. Prabhakaran, "Photoelastic investigation of bolted joints in composites," Composites, July 1982, 253-256.

27. R. Prabhakaran, "Strain-optic law for orthotropic model materials," AIAA Journal, Vol. 13, No. 6, June 1975, pp. 723-728.

28. R. Prabakaran and J. W. Dally, "The application of photo-orthotropic elasticity," Journal of Strain Analysis, Vol. 7, No. 4, 1972, pp. 253-260.

29. R. Prabhakaran, "The interpretation of isoclinics in photo-ortho-tropic-elasticity," Experimental Mechanics, Jan. 1976, pp. 6-10.

30. R. C. Sampson, "A stress-optic law for photoelastic analysis of orthotropic composites," Experimental Mechanics, Vol. 10, May 1970, pp. 210-215.

31. D. R. Sutliff and H. Pih, "Three-dimensional scattered-light stress analysis of discontinuous fiber-reinforced composites," Experimental Mechanics, July 1973, pp. 294-298.

32. A. Voloshin, M. Arcan and Z. Hashin, "Interlaminar shear stress distribution in FRM photoelastic coupons," Proceedings, 6th International Conference on Experimental Stress Analysis, München, 18-22 Sept., 1978, pp. 729-736.

33. A. Voloshin, "Stress field evaluation in photoelastic anisotropic materials: experimental numerical technique," J. Composite Materials, Vol. 14, Oct. 1980, pp. 342-350.

APPENDIX A

The form of the dielectric tensor

The dielectric tensor can be expressed as

$$
\left\{
\begin{array}{c}
e_x \\
e_y \\
e_{xy}
\end{array}
\right\}
=
\left\{
\begin{array}{c}
1 + \chi_x \\
1 + \chi_y \\
\chi_{xy}
\end{array}
\right\}
\qquad (A-1)
$$

where χ_x, χ_y, and χ_{xy} are components of the <u>susceptibility tensor</u>. Numerically, the components of the susceptibility tensor are small compared to unity. The quantity e_{ave} is defined as

$$
e_{ave} = \frac{e_x + e_y}{2} \, . \qquad (A-2)
$$

Substituting eq. A-1 it is seen that

$$
e_{ave} = 1 + \frac{\chi_x + \chi_y}{2} \qquad (A-3)
$$

and thus e_{ave} is of order unity.

The quantity Δe is defined as

$$
\Delta e = \sqrt{\left(\frac{e_x - e_y}{2}\right)^2 + e_{xy}^2} \, . \qquad (A-4)
$$

Using eq. A-1, Δe becomes

$$\Delta e = \sqrt{\left(\frac{\chi_x - \chi_y}{2}\right) + \chi_{xy}^2} \; . \tag{A-5}$$

The quantity Δe is small compared to unity and in particular, it is small compared to e_{ave}. Thus the quantity

$$\sqrt{e_{ave} + \Delta e} \tag{A-6}$$

can be approximated, using the binomial expansion, as

$$\sqrt{e_{ave}} \left(1 + \frac{1}{2} \frac{\Delta e}{e_{ave}}\right) \; . \tag{A-7}$$

Similarly,

$$e_{ave} - \Delta e \approx \sqrt{e_{ave}} \left(1 - \frac{1}{2} \frac{\Delta e}{e_{ave}}\right) \; . \tag{A-8}$$

APPENDIX B

Elasticity Solution for Stresses in an Orthotropic Disk

in Diametral Compression

The stresses in an orthotropic disk in diametral compression can be represented by a state of plane stress. If the x-axis is aligned with the stiff (fiber) direction and the y-axis is aligned with the soft (matrix) direction, then the z-axis is perpendicular to the plane of the disk. The nonzero stresses in the disk are σ_x, σ_y, and τ_{xy}. (In the discussion here, x is used to denote fiber direction. In the text this direction has been denoted as 1M. Likewise the y direction here is denoted 2M in the text. Using x and y instead of 1M and 2M is done simply so the subscripts on σ, ε, γ, τ, etc. are more familiar.)

The three-dimension equilibrium equations, in rectangular cartesian coordinates, reduce to

$$\frac{\partial \sigma_x}{\partial x} + \frac{\partial \tau_{xy}}{\partial y} = 0, \tag{B-1}$$

and

$$\frac{\partial \tau_{xy}}{\partial x} + \frac{\partial \sigma_y}{\partial y} = 0. \tag{B-2}$$

Hooke's Law becomes

$$\begin{Bmatrix} \varepsilon_x \\ \varepsilon_y \\ \gamma_{xy} \end{Bmatrix} = \begin{bmatrix} a_{11} & a_{12} & 0 \\ a_{12} & a_{22} & 0 \\ 0 & 0 & a_{66} \end{bmatrix} \begin{Bmatrix} \sigma_x \\ \sigma_y \\ \tau_{xy} \end{Bmatrix} . \tag{B-3}$$

The only nontrivial compatibility equation is

$$\frac{\partial^2 \gamma_{xy}}{\partial x \partial y} = \frac{\partial^2 \varepsilon_x}{\partial y^2} + \frac{\partial^2 \varepsilon_y}{\partial x^2} . \tag{B-4}$$

216

Typically in plane stress problems, a stress function $F(x,y)$ is defined such that

$$\sigma_x \quad = \frac{\partial^2 F}{\partial y^2} \qquad , \qquad\qquad\qquad (B\text{-}5a)$$

$$\sigma_y \quad = \frac{\partial^2 F}{\partial x^2} \qquad , \qquad\qquad\qquad (B\text{-}5b)$$

$$\tau_{xy} = - \frac{\partial^2 F}{\partial x \partial y} \; . \qquad\qquad\qquad (B\text{-}5c)$$

With eq. B-5, equilibrium is automatically satisfied. Using Hooke's Law, eq. B-3, and eq. B-5, the compatibility equation becomes:

$$a_{22} \frac{\partial^4 F}{\partial x^4} + \left(2a_{12} + a_{66}\right) \frac{\partial^4 F}{\partial x^2 \partial y^2} + a_{11} \frac{\partial^4 F}{\partial y^4} = 0 \quad . \qquad (B\text{-}6)$$

Equation B-6 admits a solution of the form

$$F = F(x + \mu y) \; , \qquad\qquad\qquad (B\text{-}7)$$

where μ is a constant.

Substituting eq. B-7 into eq. B-6 results in the so-called characteristic equation,

$$a_{11}\mu^4 + \left(2a_{11} + a_{66}\right)\mu^2 + a_{22} = 0 \quad . \qquad\qquad (B\text{-}8)$$

The solution given by eq. B-7 is only a solution if μ assumes specific values, namely one of the 4 roots of eq. B-8. The roots of eq. B-8 are generally complex, the roots being denoted μ_1, μ_2, μ_3 and μ_4. The complete solution of eq. B-6 is thus

$$F = F_1\left(x + \mu_1 y\right) + F_2\left(x + \mu_2 y\right) + F_3\left(x + \mu_3 y\right) + F_4\left(x + \mu_4 y\right) \; . \qquad (B\text{-}9)$$

217

The roots are in pairs, two roots being complex conjugates of the other two, i.e.

$$\mu_3 = \bar{\mu}_1 \text{ and } \mu_4 = \bar{\mu}_2 \ . \qquad \text{(B-10 a,b)}$$

It is convenient, and the basis of the complex variable approach, to define 4 complex variables z_1, z_2, z_3, and z_4 as follows:

$$z_1 = x + \mu_1 y \ , \quad z_2 = x + \mu_2 y \ , \quad z_3 = x + \mu_3 y \ \text{ and } \ z_4 = x + \mu_4 y \ .$$

$$\text{(B-11 a,b,c,d)}$$

Obviously by eq. B-10,

$$\bar{z}_1 = z_3 \quad \text{and} \quad \bar{z}_2 = z_4 \ . \qquad \text{(B-12 a,b)}$$

By eqs. B-11 and B-12, eq. B-9 can be written as

$$F = F_1(z_1) + F_2(z_2) + F_3(\bar{z}_1) + F_4(\bar{z}_2) \ . \qquad \text{(B-13)}$$

Since the stresses are real, F must be real and so eq. B-13 can be written as

$$F = 2\text{Re}\left[F_1(z_1) + F_2(z_2)\right] \ . \qquad \text{(B-14)}$$

To use eq. B-14 in eq. B-5, the following partial derivatives of F are needed:

$$\frac{\partial F}{\partial x} = \frac{dF_1}{dz_1} + \frac{dF_2}{dz_2} \qquad \text{(B-15a)}$$

$$\frac{\partial F}{\partial y} = \mu_1 \frac{dF_1}{dz_1} + \mu_2 \frac{dF_2}{dz_2} \ . \qquad \text{(B-15b)}$$

218

Usually the derivatives on the right hand sides of eq. B-15 are redefined, i.e.

$$\phi_1(z_1) = -\frac{dF_1(z_1)}{dz_1} \tag{B-16a}$$

$$\phi_2(z_2) = -\frac{dF_2(z_2)}{dz_2} \quad . \tag{B-16b}$$

then

$$\frac{\partial^2 F}{\partial x^2} = \phi_1'(z_1) + \phi_2'(z_2) \tag{B-17a}$$

$$\frac{\partial^2 F}{\partial y^2} = \mu_1^2 \phi_1'(z_1) + \mu_2^2 \phi_2'(z_2) \tag{B-17b}$$

$$\frac{\partial^2 F}{\partial y \partial x} = \mu_1 \phi_1'(z_1) + \mu_2 \phi_2'(z_2) \quad , \tag{B-17c}$$

where

$$\phi_1'(z_1) = -\frac{d\phi_1(z_1)}{dz_1} \tag{B-18a}$$

and

$$\phi_2'(z_2) = -\frac{d\phi_2(z_2)}{dz_2} \quad . \tag{B-18b}$$

With this notation

$$\sigma_x = 2\text{Re}\left[\mu_1^2 \phi_1'(z_1) + \mu_2^2 \phi_2'(z_2)\right] \quad , \tag{B-19a}$$

$$\sigma_y = 2\text{Re}\left[\phi_1'(z_1) + \phi_2'(z_2)\right] \quad , \tag{B-19b}$$

and

$$\tau_{xy} = -2\text{Re}\left[\mu_1 \phi_1'(z_1) + \mu_2 \phi_2'(z_2)\right] \quad . \tag{B-19c}$$

The complex variable approach to these plane stress problems is convenient because (1), since it is assumed F is an analytic function at all but a few points in the domain, the functional form of F is known, and (2), the boundary conditions can be related to F through rather simple integrals. Concerning the latter, let X_n and Y_n represent the x-

and y-direction surface tractions, respectively, on the boundary of the body, in this case the disk.

Assume that on the disk the normal surface traction, σ_r, and the tangential surface traction, $\tau_{r\theta}$, are specified functions of θ. This idea is shown in fig. B-1. The quantities $\sigma_r(\theta)$ and $\tau_{r\theta}(\theta)$ cannot be completely arbitrary in that the disk must be in translational and rotational equilibrium as a rigid body. With X_n denoting the x-component of the surface traction and Y_n denoting the y-component of surface traction, then

$$X_n = X_n(\theta) = \left(\sigma_r(\theta)\cos\theta - \tau_{r\theta}(\theta)\sin(\theta)\right) \qquad \text{(B-20a)}$$

$$Y_n = Y_n(\theta) = \left(\sigma_r(\theta)\sin\theta + \tau_{r\theta}(\theta)\cos\theta\right) \quad . \qquad \text{(B-20b)}$$

The boundary conditions on F become

$$2\text{Re}\left[\phi_1(z_1) + \phi_2(z_2)\right] = -\int_0^\theta Y_n(\theta)R d\theta + c_1 \qquad \text{(B-21a)}$$

$$2\text{Re}\left[\mu_1\phi_1(z_1) + \mu_2\phi_2(z_2)\right] = +\int_0^\theta X_n(\theta)R d\theta + c_2, \qquad \text{(B-21b)}$$

where z_1 and z_2 are evaluated at $z = Re^{i\theta}$, i.e. the boundary of the disk.

Lekhnitskii* states the solutions to $\phi_1(z_1)$ and $\phi_2(z_2)$ for this geometry are:

$$\phi_1(z_1) = A_0 + A_1 z_1 + \sum_{m=2}^\infty A_m P_{1_m}(z_1) \qquad \text{(B-22a)}$$

$$\phi_2(z_2) = B_0 + B_1 z_2 + \sum_{m=2}^\infty B_m P_{2_m}(z_2) \quad . \qquad \text{(B-22b)}$$

---

*Lekhnitskii, S. G., Anisotropic Plates, translated from 2nd ed. by S. W. Tsai and T. Cheron, Gordon and Breach, Science Publishers, New York, 1968, eq. 33.6.
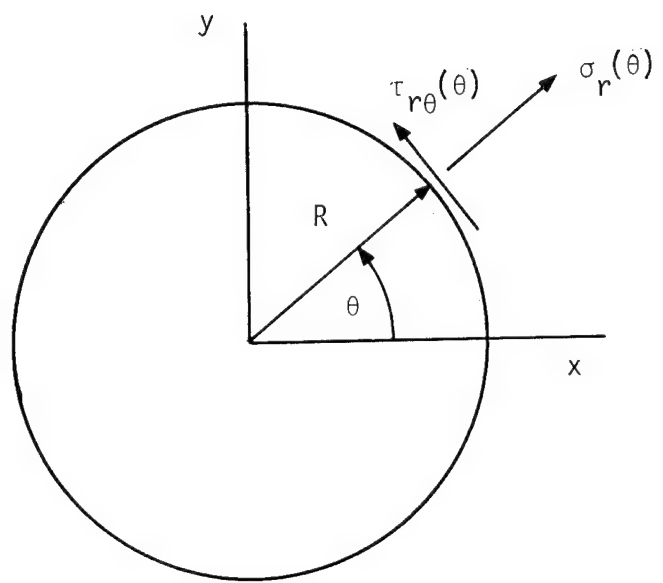
Fig. B-1   Surface tractions on disk boundary.

221

The $P_{1m}(z_1)$ and $P_{2m}(z_2)$ are given by

$$P_{1m}(z_1) = \frac{-1}{R^m(1-i\mu_1)^m}\left\{(z_1 + \sqrt{z_1^2 - R^2(1+\mu_1^2)})^m + (z_1 - \sqrt{z_1^2 - R^2(1+\mu_1^2)})^m\right\}$$

$$(B-23a)$$

$$P_{2m}(z_2) = \frac{-1}{R^m(1-i\mu_2)^m}\left\{(z_2 + \sqrt{z_2^2 - R^2(1+\mu_2^2)})^m + (z_2 - \sqrt{z_2^2 - R^2(1+\mu_2^2)})^m\right\}.$$

$$(B-23b)$$

That these are solutions to $\phi_1(z_1)$ and $\phi_2(z_2)$ is not obvious to even the serious observer of mathematics, let alone the casual observer. These solutions to $\phi_1(z_1)$ and $\phi_2(z_2)$, and other solutions for other domain geometries, is what has made a mark for Letkhnitskii and others working in this field.

Since $\phi_1(z_1)$ and $\phi_2(z_2)$ are expressed in terms of a series, to match the boundary conditions given by eq. B-21, X_n and Y_n of eq. B-20 need to be expressed as a series, specifically a Fourier series in θ. This step is universal in the complex variable approach to elasticity, i.e. the expanding of the known boundary data into a Fourier series.

Assuming $\sigma_r(\theta)$ and $\tau_{r\theta}(\theta)$ are known, the boundary integrals on the right hand side of eq. B-21 can be represented by

$$- \int_0^\theta Y_n(\theta)Rd\theta + c_1 = \alpha_0 + \sum_{m=1}^\infty (\alpha_m\sigma^m + \bar{\alpha}_m\sigma^{-m}) \quad (B-24a)$$

$$\int_0^\theta X_n(\theta)Rd\theta + c_2 = \beta_0 + \sum_{m=1}^\infty (\beta_m\sigma^m + \bar{\beta}_m\sigma^{-m}), \quad (B-24b)$$

where

$$\sigma = e^{i\theta} \ . \tag{B-25}$$

The quantities α_m, $\bar{\alpha}_m$, β_m, $\bar{\beta}_m$ are known coefficients which can be determined by typical Fourier analysis once the functional forms of $X_n(\theta)$ and $Y_n(\theta)$ are specified. Substituting eq. B-24 into the right hand side of eq. B-21, and eqs. B-22 and B-23 into the left-hand side of eq. B-21, and equating coefficients of like powers of σ results in 4 coupled linear algebraic equations for the A_m and B_m of eq. B-22. These equations are:

$$A_m + B_m + \bar{A}_m \bar{t}_1^m + \bar{B}_m \bar{t}_2^m = - \alpha_m$$

$$\mu_1 A_m + \mu_2 B_m + \bar{\mu}_1 \bar{t}_1^m \bar{A}_m + \bar{\mu}_2 \bar{t}_2^m \bar{B}_m = - \beta_m$$

$$t_1^m A_m + t_2^m B_m + \bar{A}_m + \bar{B}_m = - \bar{\alpha}_m \tag{B-26}$$

$$\mu_1 t_1^m A_m + \mu_2 t_2^m B_m + \bar{\mu}_1 \bar{A}_m + \bar{\mu}_2 \bar{B}_m = - \bar{\beta}_m$$

$$m = 2, 3, 4\ldots \quad .$$

The quantities t_1 and t_2 are given by

$$t_1 = \frac{1 + i\mu_1}{1 - i\mu_1} \quad \text{and} \quad t_2 = \frac{1 + i\mu_2}{1 - i\mu_2} \ . \tag{B-27}$$

For the case $m = 1$, matching coefficients in leads to

$$A_1 + B_1 + \bar{A}_1 + \bar{B}_1 = \frac{\alpha_1 + \bar{\alpha}_1}{R} \tag{B-28a}$$

223

$$\mu_1 A_1 + \mu_2 B_1 + \bar{\mu}_1 \bar{A}_1 + \bar{\mu}_2 \bar{B}_2 = \frac{\beta_1 + \bar{\beta}_1}{R} \qquad \text{(B-28b)}$$

$$\mu_1^2 A_1 + \mu_2^2 B_1 + (\bar{\mu}_1)^2 \bar{A}_1 + (\bar{\mu}_2)^2 \bar{B}_1 = \frac{\bar{\beta}_1 - \beta_1}{Ri} \; . \qquad \text{(B-28c)}$$

Equations B28a-c represent 3 equations for 4 unknowns, A_1, $\bar{A}_1$, B_1, and $\bar{B}_1$. An indeterminant solution is not a problem if the situation is examined in detail. Consider only the linear terms in the expressions for $\phi_1(z_1)$ and $\phi_2(z_2)$ in eq. B-22. Substituting only these linear terms into the expressions for stress, eq. B-19 results in

$$\sigma_x = 2\text{Re}\left[\mu_1^2 A_1 + \mu_2^2 B_1\right] \qquad \text{(B-29a)}$$

$$\sigma_y = 2\text{Re}\left[A_1 + B_1\right] \qquad \text{(B-29b)}$$

$$\tau_{xy} = -2\text{Re}\left[\mu_1 A_1 + \mu_2 B_1\right] \; . \qquad \text{(B-29c)}$$

Eliminating the taking of the real part, these three expressions can be written as

$$\sigma_x = \left[\mu_1^2 A_1 + \mu_2^2 B_1 + (\bar{\mu}_1)^2 \bar{A}_1 + (\bar{\mu}_2)^2 \bar{B}_1\right] \qquad \text{(B-30a)}$$

$$\sigma_y = \left[A_1 + \bar{A}_1 + B_1 + \bar{B}_1\right] \qquad \text{(B-30b)}$$

$$\tau_{xy} = -\left[\mu_1 A_1 + \mu_2 B_1 + \bar{\mu}_1 \bar{A}_1 + \bar{\mu}_2 \bar{B}_1\right] \; . \qquad \text{(B-30c)}$$

The right hand side of eqs. B-30a,b,c are related directly to eqs. B-28c,a,b. Thus, the leading terms in the expressions for stress, eq. B-30a,b,c, are

$$\sigma_x = \frac{\bar{\beta}_1 - \beta_1}{Ri} \,, \qquad (B-31a)$$

$$\sigma_y = \frac{\alpha_1 + \bar{\alpha}_1}{R} \,, \qquad (B-31b)$$

$$\tau_{xy} = -\frac{\beta_1 + \bar{\beta}_1}{R} \,. \qquad (B-31c)$$

Since only the derivatives of $\phi_1(z_1)$ and $\phi_2(z_2)$ are required for the computation of stress, A_0 and B_0 in eq. B-22 do not enter into the calculations. Thus eqs. B-31a-c and the solution to Eq. B-26 for A_m and B_m, $m \geqslant 2$, give the necessary constants to completely determine the state of stress in the disk. Evaluating $\phi_1'(z_1)$ and $\phi_2'(z_2)$ at a specific x and y (or r and θ) gives the stresses at a specific location in the disk.

For the diametral concentrated load, the constants α_m and β_m, $m \geqslant 0$, are easily determined. As shown in fig. B-2, consider the concentrated load P at an angle α relative to the x-axis. For this loading

$$X_n(\theta)Rd\theta = \left[P\delta(\theta - \alpha) + P\delta(\theta - \alpha - \pi)\right]\cos\theta Rd\theta \quad (B-32a)$$

$$Y_n(\theta)Rd\theta = \left[P\delta(\theta - \alpha) + P\delta(\theta - \alpha - \pi)\right]\sin\theta Rd\theta, \quad (B-32b)$$

$$0 \leqslant \theta \leqslant 2\pi$$

where $\delta(\ )$ is the Dirac delta and +P represents diametral tension. The integrals on the right hand side of eqs. B-21 are 1/2-cycles of square waves, i.e.
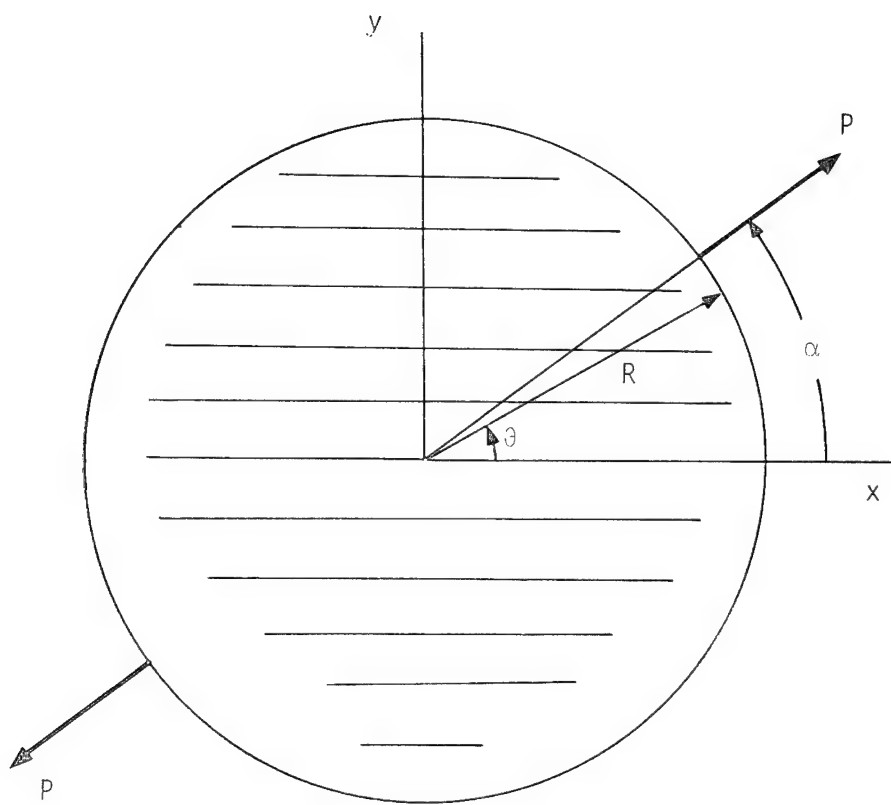
Fig. B-2 Disk with diametral load

$$\int_0^\theta X_n(\theta)Rd\theta = P\left[U(\theta - \alpha)\cos\alpha + U(\theta - \alpha - \pi)\cos(\alpha - \pi)\right]R$$

$$(B-33a)$$

$$\int_0^\theta Y_n(\theta)Rd\theta = P\left[U(\theta - \alpha)\sin\alpha + U(\theta - \alpha - \pi)\sin(\alpha - \pi)\right]R \ ,$$

$$(B-33b)$$

$U(\ )$ denoting the unit step function. Since

$$\cos(\alpha - \pi) = -\cos\alpha \quad \text{and} \qquad\qquad = -\sin\alpha,$$

$$(B-34a,b)$$

eq. B-33 becomes

$$\int_0^\theta X_n(\theta)Rd\theta = P\cos\alpha\left[U(\theta-\alpha) - U(\theta - \alpha - \pi)\right]R \qquad (B-35a)$$

$$\int_0^\theta Y_n(\theta)Rd\theta = P\sin\alpha\left[U(\theta - \alpha) - U(\theta - \alpha - \pi)\right]R \ . \quad (B-35b)$$

These integrals are shown graphically in fig. B-3. Using the usual ideas associated with Fourier analysis, the two integrals can easily be expanded to a Fourier series of the form eq. B-24. The results are:

$$\alpha_0 = -\frac{P\sin\alpha}{2} \quad \text{and} \quad \beta_0 = \frac{P\cos\alpha}{2} \ . \qquad (B-36a,b)$$

For m odd:

$$\alpha_m = \frac{P\sin\alpha}{\pi m}\left\{\sin(m\alpha) + i\cos(m\alpha)\right\} \qquad (B-36c)$$

$$\beta_m = -\frac{P\cos\alpha}{\pi}\left\{\sin(m\alpha) + i\cos(m\alpha)\right\} \ . \qquad (B-36d)$$

for m even:

$$\alpha_m = 0 = \beta_m \ . \qquad\qquad (B-36e,f)$$
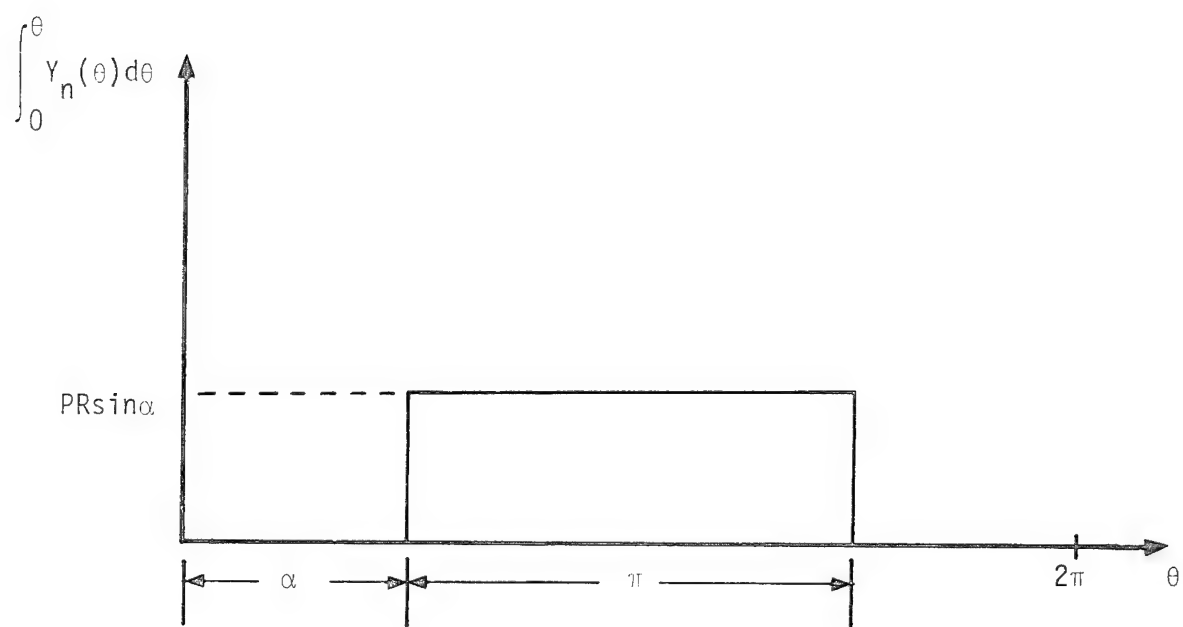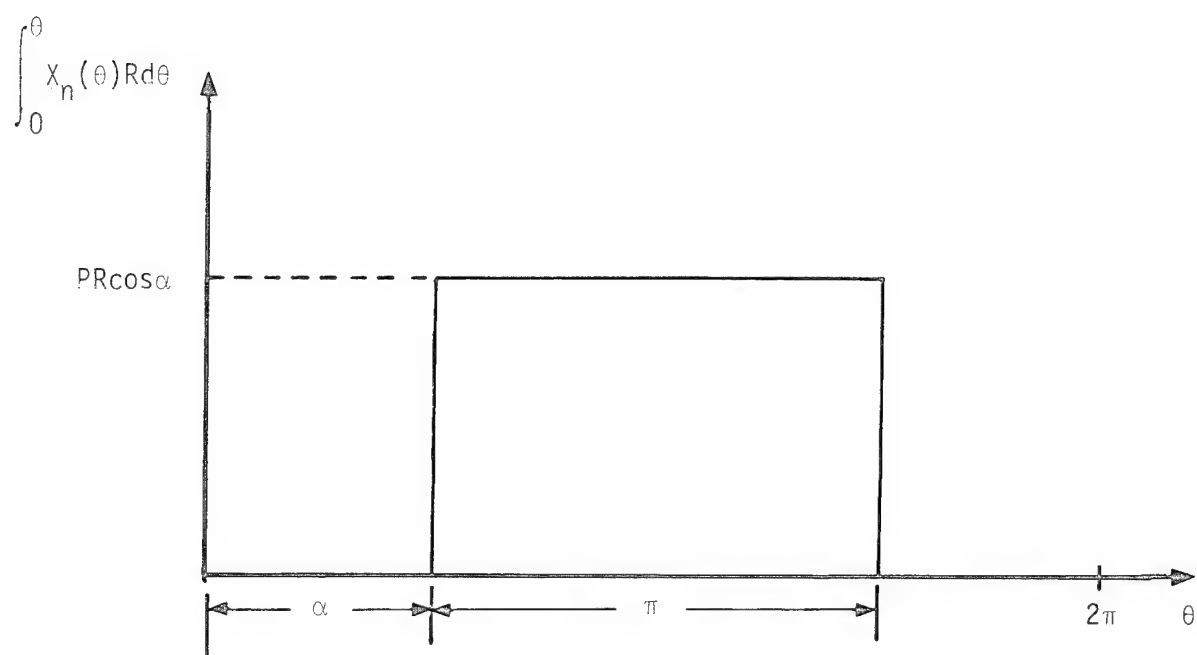
Fig. B-3 Boundary integrals.

228

Obviously only a finite number of terms are actually used in eqs. B-22 and B-24. Concentrated loads pose the most difficult convergence problems for elasticity solutions, particularly if infinite series are truncated. In reality, any finite number of terms results in a convergence problem right at the point of application of the load. So the question is, at points of interest removed from the point of application of the load, what are the convergence characteristics? Numerical studies, based on a FORTRAN progam which coded eqs. B-19, B-22, B-23, B-26, B-27, B-31, and B-36, indicated that toward the center of the disk, 10 terms in the series gave answers nearly identical to the series with 20 terms. Twenty terms gave answers nearly identical to a 40-term series over 85% of the disk. A greater number of terms caused underflow in the computer being used.

As a check, a finite element program, using 216 constant-strain elements in a complete disk, was used to compute the stresses. The element arrangement is shown in Fig. B-4. There was no particular reason for using 216 elements other than the ability to be able to compute stresses at a large number of points. The particular finite element program being used computed stresses at the centroids of the elements and thus many elements were used. To compare the stresses generated by the complex variable solution with the stresses generated by the finite element solution, the following scheme as adopted. For a given load direction relative to the fibers, α, the stresses were compared along the loaded diameter, along a diameter perpendicular to the loaded diameter, along a diameter in the fiber direction, and along a diameter in the matrix direction. Such a comparison would indicate how well the stresses were being computed in a highly loaded region, i.e. moving from

229
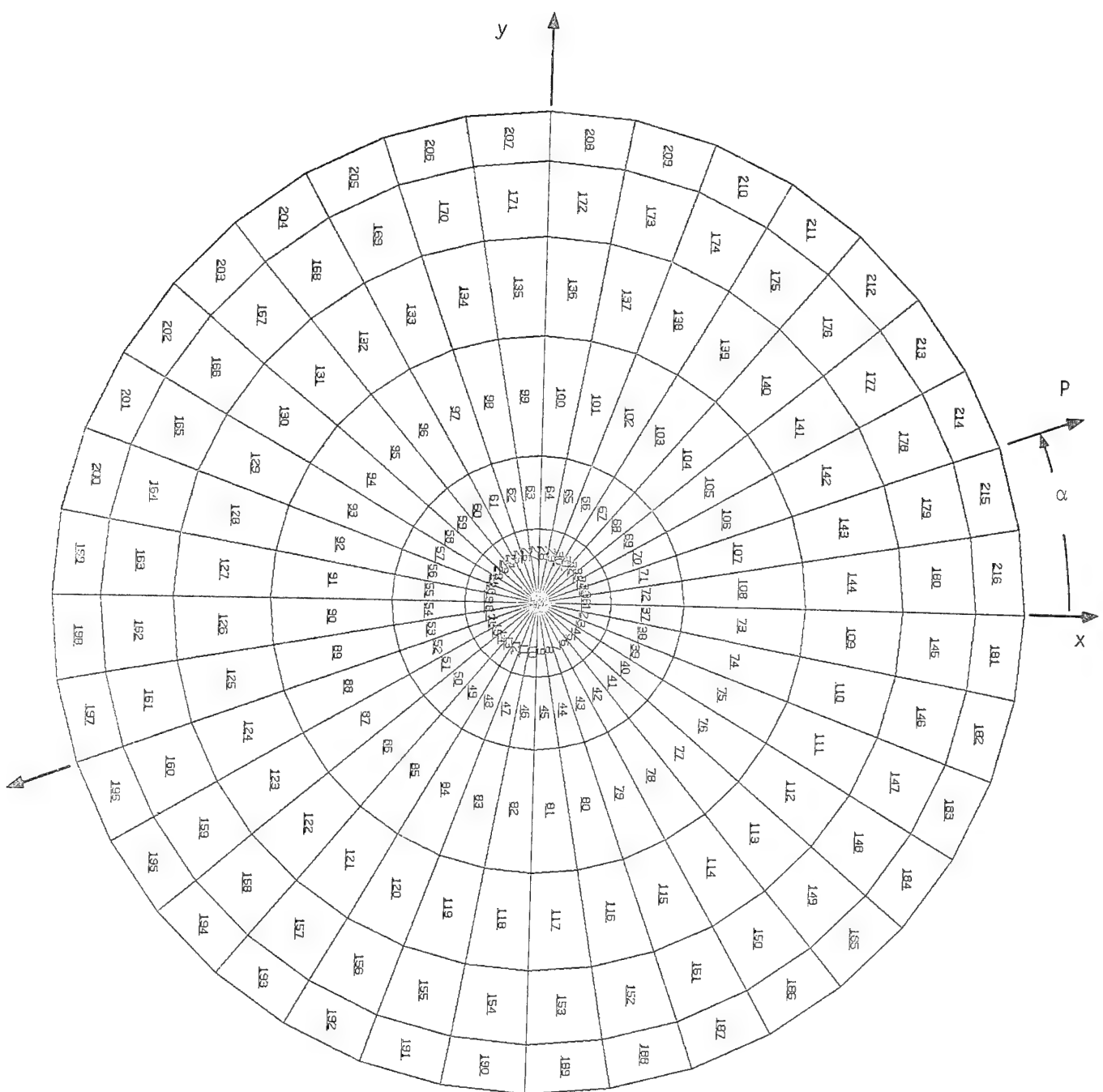
Fig. B-4 Finite element mesh for disk.

the center of the disk toward the point load along a diameter, how well
the stresses were computed in a lightly loaded region, i.e. moving from
the center of the disk toward a free edge along a diameter perpendicular
to the load, and whether the stress diffusion in the stiff and soft dir-
ections was properly represented. The elastic properties of the cases
studied were as follows:

$$E_1 = 28.8 \text{ GPa } (4.18 \times 10^6 \text{ psi})$$
$$E_2 = 9.40 \text{ GPa } (1.36 \times 10^6 \text{ psi})$$
$$G_{12} = 3.17 \text{ GPa } (0.460 \times 10^6 \text{ psi})$$
$$\nu_{12} = 0.3 \; .$$

These values led to values for μ (refer to eq. B-10) of:

$$\mu_1 = 2.83 \text{ i } , \qquad \mu_2 = 0.618 \text{ i } . \qquad \text{(B-37a,b)}$$

In the two computational schemes the disk diameter, D, was 3.00 in.
while its thickness, t, was unity. The comparisons are presented in
nondimensional form, the stresses being divided by P/Dt, where P is the
applied diametral load. The stresses are presented as a function of
their x and y locations. The x and y coordinates are nondimensionalized
by dividing them by the disk radius. With the particular finite ele-
ment, the particular mesh, and the way a point load was applied to the
model, stresses were not computed exactly on the loaded diameter, nor on
the diameter perpendicular to the loaded diameter, etc. For both the
finite element and complex variable solutions, the stresses were compu-
ted at the centroids of the elements and the element centroids were not
exactly on the loaded diameter.

231

Tables B-1 through B-4 indicate the comparison for 4 orientations of the load relative to the fiber direction, i.e. $\alpha = 0°$, $\alpha = 30°$, $\alpha = 60°$, and $\alpha = 90°$. Twenty terms were used in the complex variable solution.

From the tables it is obvious there is good agreement between the finite element solution and the complex variable solution over much of the disk. Which is the 'correct' solution is not clear. The finite element mesh should be finer near the point load to represent the singular behavior of the stresses in that region. The singular solution is 'built-in' to the complex variable solution but it is not clear 20 terms represents this portion of the solution. The problem is not important because in the actual experiment the disk material crazed badly near the point where the load was applied. Fringes could not be observed and compared with theoretical predictions. In addition, the load obviously was introduced over a finite region rather than at a point, as the theory assumes. Thus any fringes in the immediate region of the load would be strongly affected by this lack of idealism. Any comparison between theory and experiment in this region of the disk would be meaningless.

Based on the comparison shown in Tables B-1 through B-4, the complex variable solution was felt to be quite accurate and, compared to finite element solutions, quite quick and inexpensive to run on the computer.

Table B-1

Comparison of Finite Element (FE) and Complex Variable (CV)
Solutions for Disk with Fibers Parallel to Load
($\alpha = 0$, see fig. B-4)

	element no.	$\frac{x}{R}$	$\frac{r}{R}$	$\frac{\sigma_x}{P/Dt}$		$\frac{\sigma_y}{P/Dt}$		$\frac{\tau_{xy}}{P/Dt}$	
				FE	CV	FE	CV	FE	CV
load and fiber dir.	1	0.100	0.007	3.26	3.27	-0.354	-0.358	-0.648×10^3	-0.575×10^{-3}
	72	0.220	0.020	3.38	3.42	-0.374	-0.364	0.282×10^{-2}	0.409×10^{-3}
	108	0.420	0.040	3.91	4.00	-0.376	-0.375	0.236	0.202
	144	0.650	0.053	5.12	5.38	-0.276	-0.337	0.788	0.729
	180	0.820	0.073	6.39	5.46	0.191	0.259	1.60	2.14
	216	0.950	0.080	7.28	1.22	1.72	2.04	2.14	-3.34
perp. to load, matrix dir.	28	0.007	0.100	2.79	2.93	-0.369	-0.317	-0.384×10^{-3}	-0.486×10^{-3}
	64	0.020	0.220	2.05	2.09	-0.197	-0.208	-0.021	-0.021
	100	0.040	0.420	0.882	0.842	-0.048	-0.055	-0.017	-0.021
	136	0.060	0.650	0.198	0.168	0.476×10^{-3}	0.879×10^{-3}	-0.785×10^{-2}	-0.537×10^2
	172	0.073	0.820	-0.279×10^{-1}	-0.250×10^{-1}	0.011	0.010	0.249×10^{-2}	0.300×10^{-2}
	208	0.080	0.950	-0.822×10^{-1}	-0.495×10^{-1}	0.369×10^{-3}	-0.059	0.654×10^{-2}	0.017

233

Table B-2

Comparison of Finite Element (FE) and Complex Variable (CV) Solutions for Disk with Fibers 30° to Load ($\alpha = 30$, see fig. B-4)

	element no.	$\frac{x}{R}$	$\frac{y}{R}$	$\frac{\sigma_x}{P/Dt}$ FE	$\frac{\sigma_x}{P/Dt}$ CV	$\frac{\sigma_y}{P/Dt}$ FE	$\frac{\sigma_y}{P/Dt}$ CV	$\frac{\tau_{xy}}{P/Dt}$ FE	$\frac{\tau_{xy}}{P/Dt}$ CV
load dir.	33	0.080	0.060	0.850	0.887	0.169	0.159	1.17	1.17
	69	0.187	0.127	0.940	1.00	0.167	0.179	1.20	1.20
	105	0.347	0.240	1.39	1.48	0.209	0.236	1.31.	1.33
	141	0.533	0.373	3.40	3.28	0.251	0.313	1.46	1.72
	177	0.673	0.473	10.6	9.08	0.259	0.245	1.29	1.56
	213	0.773	0.540	10.5	8.58	0.63	0.328	1.04	2.08
fiber dir.	36	0.100	0.007	0.856	0.844	0.170	0.169	1.16	1.16
	72	0.220	0.020	0.822	0.802	0.220	0.220	1.17	1.17
	108	0.420	0.040	0.637	0.643	0.461	0.422	1.18	1.17
	144	0.647	0.053	0.267	0.259	0.917	0.891	1.01	0.991
	180	0.820	0.073	-0.050	-0.095	1.06	1.15	0.445	0.433
	216	0.947	0.080	0.016	-0.489	0.672	0.684	0.321×10^{-3}	-0.220
perpendicular to load	24	-0.060	0.080	0.803	0.878	0.132	0.152	1.15	1.14
	60	-0.127	0.187	0.929	0.969	0.113	0.129	1.02	1.03
	96	-0.240	0.347	0.986	1.02	0.105	0.086	0.669	0.719
	132	-0.373	0.533	0.669	0.623	0.062	0.054	0.308	0.280
	168	-0.473	0.673	0.216	0.175	0.014	0.013	0.066	0.048
	204	-0.540	0.773	-0.074	0.041	-0.038	-0.131	-0.057	-0.026
matrix direction	27	-0.007	0.100	0.935	0.921	0.160	0.142	1.17	1.14
	63	-0.020	0.220	1.22	1.25	0.073	0.081	1.04	1.02
	99	-0.040	0.420	1.38	1.54	-0.359×10^{-2}	-0.020	0.614	0.636
	135	-0.053	0.647	0.857	0.781	-0.442×10^{-2}	-0.302×10^{-2}	0.101	0.087
	171	-0.073	0.820	0.101	0.058	0.018	0.025	-0.018	-0.014
	207	-0.080	0.667	-0.198	-0.220	0.892×10^{-2}	0.056	-0.023	-0.063

Table B-3

Comparison of Finite Element (FE) and Complex Variable (CV) Solutions for Disk with Fibers 60° to Load (α = 60, see fig. B-4)

	element no.	x/R	y/R	σ_x P/Dt FE	σ_x P/Dt CV	σ_y P/Dt FE	σ_y P/Dt CV	τ_{xy} P/Dt FE	τ_{xy} P/Dt CV
fiber direction	30	0.040	0.093	-0.161	-0.157	1.02	1.02	1.02	1.02
	66	0.093	0.200	-0.166	-0.133	1.06	1.08	1.15	1.06
	102	0.180	0.387	-0.026	-0.005	1.25	1.28	1.22	1.22
	138	0.273	0.587	0.535	0.515	1.69	1.73	1.73	1.72
	174	0.357	0.747	3.04	2.82	2.12	2.09	2.82	2.95
	210	0.400	0.860	8.68	12.43	2.74	1.09	3.40	2.12
load direction	36	0.100	0.007	-0.165	-0.173	1.04	1.03	1.01	0.991
	72	0.220	0.020	-0.212	-0.204	1.11	1.08	0.913	0.908
	108	0.420	0.040	-0.248	-0.254	1.13	1.16	0.613	0.623
	144	0.647	0.053	-0.180	-0.190	0.913	0.926	0.213	0.225
	180	0.820	0.073	-0.080	-0.046	0.601	0.597	0.030	0.047
	216	0.947	0.080	-0.015	0.278	0.381	0.388	-0.022	0.058
perpendicular to load direction	21	-0.093	0.040	-0.188	-0.162	0.989	1.00	1.00	0.989
	57	-0.200	0.093	-0.162	-0.147	0.964	0.970	0.905	0.908
	93	-0.387	0.180	-0.059	-0.089	0.814	0.826	0.662	0.674
	129	-0.587	0.273	0.002	-0.002	0.574	0.564	0.401	0.402
	165	-0.747	0.347	0.043	0.074	0.352	0.342	0.223	0.224
	201	-0.860	0.400	0.053	-0.103	0.218	0.168	0.119	0.191
matrix direction	27	-0.007	0.100	-0.155	-0.146	1.02	1.00	1.02	1.02
	63	-0.020	0.220	-0.063	-0.069	0.974	0.952	1.05	1.04
	99	-0.040	0.420	0.323	0.246	0.778	0.768	1.11	1.10
	135	-0.053	0.647	1.04	1.08	0.361	0.375	0.956	0.990
	171	-0.073	0.82	1.12	1.31	0.066	0.041	0.321	0.328
	207	-0.08	0.947	0.073	0.051	-0.019	0.003	-0.052	-0.266

235

Table B-4

Comparison of Finite Element (FE) and Complex Variable (CV)
Solutions for Disk with Fibers 90° to Load
($\alpha = 90°$, see fig. B-4)

element no.	$\frac{x}{R}$	$\frac{y}{R}$	$\frac{\sigma_x}{P/Dt}$ FE	$\frac{\sigma_x}{P/Dt}$ CV	$\frac{\sigma_y}{P/Dt}$ FE	$\frac{\sigma_y}{P/Dt}$ CV	$\frac{\tau_{xy}}{P/Dt}$ FE	$\frac{\tau_{xy}}{P/Dt}$ CV
36	0.100	0.007	-0.637	-0.599	1.76	1.76	-0.792×10^{-4}	-0.003
72	0.220	0.020	-0.523	-0.520	1.57	1.58	-0.018	0.016
108	0.420	0.040	-0.312	-0.333	1.11	1.13	-0.033	0.038
144	0.647	0.053	-0.154	-0.149	0.670	0.659	-0.040	0.036
180	0.820	0.073	-0.056	-0.089	0.405	0.408	-0.031	0.031
216	0.947	0.080	-0.010	-0.243	0.271	0.259	-0.024	-0.018
28	0.007	0.100	-0.618	-0.624	1.84	1.84	-0.004	-0.003
64	0.020	0.220	-0.657	-0.638	1.92	1.94	-0.015	-0.023
100	0.040	0.420	-0.708	-0.680	2.28	2.30	-0.118	-0.116
136	0.053	0.647	-0.656	-0.731	3.26	3.35	-0.555	-0.459
172	0.073	0.820	-0.099	-0.185	4.88	4.81	-1.82	-1.91
708	0.080	0.947	4.45	5.00	6.65	3.16	-3.62	-5.73

fiber dir., perp. to load.

matrix dir., parallel to load.

236

Appendix C

Determination of Stresses Using a Finite-Difference
Representation of Equilibrium Equations

In an x-y coordinate system, the plane stress equilibrium equations, in the absence of body forces, are:

$$\frac{\partial \sigma_x}{\partial x} + \frac{\tau_{xy}}{\partial y} = 0, \tag{C-1}$$

$$\frac{\partial \tau_{xy}}{\partial x} + \frac{\partial \sigma_y}{\partial y} = 0. \tag{C-2}$$

The stress-optic law for orthotropic photoelastic materials can be written as

$$\frac{\sigma_x}{C_1} - \frac{\sigma_y}{C_2} + \frac{\tau_{xy}}{C_3} = N_T \cos(2\theta_T) - N_R \cos(2\theta_R), \tag{C-3}$$

$$\frac{\sigma_x - \sigma_y}{C_4} + \frac{\tau_{xy}}{C_5} = \frac{N_T}{2} \sin(2\theta_T) - \frac{N_R}{2} \sin(2\theta_R). \tag{C-4}$$

The constants $C_1 - C_5$ are calibration constants for the material, N_T and θ_T are the total isochromatic fringe number and the optical isocline angle, respectively, and N_R and θ_R are the residual isochromatic fringe number and the residual optical isocline angle. The latter two parameters can be thought of as calibration constants for the material.

Consider a rectangular array of points in an x-y coordinate system as in fig. C-1. For point i, $j + \frac{1}{2}$, point a, the following approximations can be written:
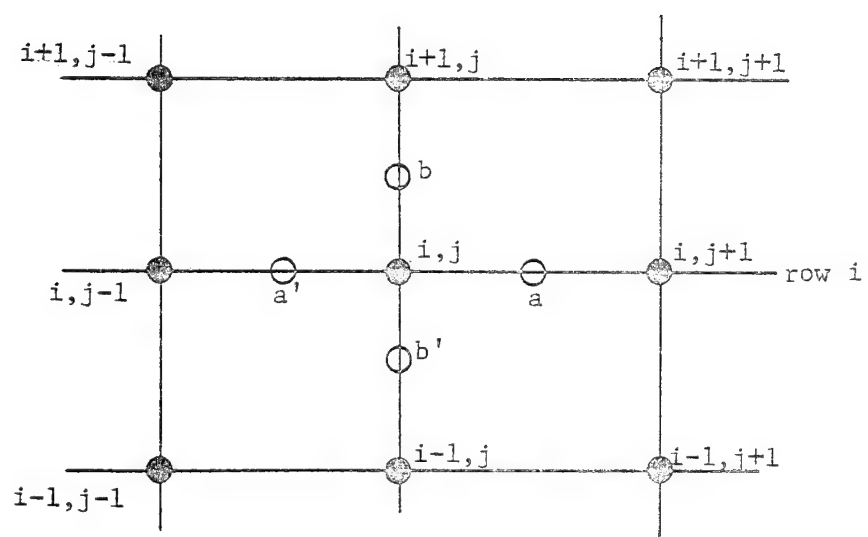
Fig. C-1 Finite-difference mesh.

$$\frac{\partial \sigma_x}{\partial x}\bigg|_{i,j+\frac{1}{2}} = \frac{1}{\Delta x} \left\{ (\sigma_x)_{i,j+1} - (\sigma_x)_{i,j} \right\}; \tag{C-5}$$

$$\frac{\partial \tau_{xy}}{\partial y}\bigg|_{i,j+\frac{1}{2}} = \frac{1}{2} \left\{ \frac{\partial \tau_{xy}}{\partial y}\bigg|_{i,j+1} + \frac{\partial \tau_{xy}}{\partial y}\bigg|_{i,j} \right\}, \tag{C-6}$$

where

$$\frac{\partial \tau_{xy}}{\partial y}\bigg|_{i,j+1} = \frac{1}{2\Delta y} \left\{ (\tau_{xy})_{i+i,j+1} - (\tau_{xy})_{i-1,j+1} \right\} \tag{C-7}$$

and

$$\frac{\partial \tau_{xy}}{\partial y}\bigg|_{i,j} = \frac{1}{2\Delta y} \left\{ (\tau_{xy})_{i+1,j} - (\tau_{xy})_{i-1,j} \right\}. \tag{C-8}$$

Equation C-1 now can be approximated, at point a, as:

$$(\sigma_x)_{i,j+1} - (\sigma_x)_{i,j} + \frac{\Delta x}{4\Delta y} \left\{ (\tau_{xy})_{i+1,j} - (\tau_{xy})_{i-1,j} + \tag{C-9} \right.$$

$$\left. (\tau_{xy})_{i+1,j+1} - (\tau_{xy})_{i-1,j+1} \right\} = 0.$$

Equation C-9 is an approximation to the equilibrium condition in the x direction. It is applied at specific points along the midrow of the three-line mesh, row i. This expression averages shear stresses.

For point $(i + \frac{1}{2}, j)$, point b, the following approximations may be written:

$$\frac{\partial \sigma_y}{\partial y}\bigg|_{i+\frac{1}{2},j} = \frac{1}{\Delta y} \left\{ (\sigma_y)_{i+1,j} - (\sigma_y)_{i,j} \right\}; \tag{C-10}$$

$$\frac{\partial \tau_{xy}}{\partial x}\bigg|_{i+\frac{1}{2},j} = \frac{1}{2} \left\{ \frac{\partial \tau_{xy}}{\partial x}\bigg|_{i+1,j} + \frac{\partial \tau_{xy}}{\partial x}\bigg|_{i,j} \right\}, \tag{C-11}$$

where

$$\frac{\partial \tau_{xy}}{\partial x}\bigg|_{i+1,j} = \frac{1}{2\Delta x} \left\{ (\tau_{xy})_{i+1,j+1} - (\tau_{xy})_{i+1,j-1} \right\} \tag{C-12}$$

and

$$\frac{\partial \tau_{xy}}{\partial x}\bigg|_{i,j} = \frac{1}{2\Delta x} \left\{ (\tau_{xy})_{i,j+1} - (\tau_{xy})_{i,j-1} \right\}. \tag{C-13}$$

Equation C-2 can be approximated at point b as

$$(\sigma_y)_{i+1,j} - (\sigma_y)_{i,j} + \frac{\Delta y}{4\Delta x} \{(\tau_{xy})_{i+1,j+1} - (\tau_{xy})_{i+1,j-1} \qquad (C\text{-}14)$$

$$+ (\tau_{xy})_{i,j+1} - (\tau_{xy})_{i,j-1}\} = 0.$$

Equation C-14 can be applied at discrete points b and b' along the columns of the mesh, columns ...j-2, j-1,...,j+2... The equation also averages shear stresses.

Equations C-3 and C-4 can be written as follows to put them into context:

$$\frac{(\sigma_x)_{i,j}}{C_1} - \frac{(\sigma_y)_{i,j}}{C_2} + \frac{(\tau_{xy})_{i,j}}{C_3} = N_{T_{i,j}} \cos(2\theta_{T_{i,j}}) - N_R \cos(2\theta_R)$$

$$(C\text{-}15)$$

$$\frac{(\sigma_x)_{i,j} - (\sigma_y)_{i,j}}{C_4} + \frac{(\tau_{xy})_{i,j}}{C_5} = \frac{N_{T_{i,j}}}{2} \sin(2\theta_{T_{i,j}}) - \frac{N_R}{2} \sin(2\theta_R).$$

$$(C\text{-}16)$$

(Here N_R and θ_R are assumed to be the same at each mesh point).

Equations C-9, C-14, C-15, and C-16 are the four equations which can be used to compute the stresses σ_x, σ_y, and τ_{xy} at each point i,j. It is obvious that x direction equilibrium is not enforced at the same points as y direction equilibrium and here y direction equilibrium is enforced at twice as many points. There is nothing special about this, it is simply a direct result of the mesh geometry, i.e. long and thin. The photoelastic equations should be applied at every point. The equilibrium equations can be applied so there are exactly as many equations as there are unknown stresses. Alternatively, the equilibrium equations can be applied frequently enough so that there are more equations than there are unknown stresses. Solving an overdetermined set of equations

will give stresses that satisfy all four equations in a least-squares sense.

Finally, of course, there are boundary conditions. At some points one or more stresses may be known, e.q. $(\sigma_x)_{4,5} = 0$. These are simply more equations in the equation count and can be used to give a unique solution or an overdetermined solution.

1. Report No. NASA CR-3773	2. Government Accession No.	3. Recipient's Catalog No.
4. Title and Subtitle AN ASSESSMENT OF THE ACCURACY OF ORTHOTROPIC PHOTOELASTICITY		5. Report Date March 1984
		6. Performing Organization Code
7. Author(s) M. W. Hyer and D. H. Liu		8. Performing Organization Report No.
		10. Work Unit No.
9. Performing Organization Name and Address Department of Engineering Science and Mechanics Virginia Polytechnic Institute and State University Blacksburg, VA 24061		11. Contract or Grant No. NSG-1621
		13. Type of Report and Period Covered Contractor Report (Nov.81–Sept.82)
12. Sponsoring Agency Name and Address National Aeronautics and Space Administration Washington, D.C. 20546		14. Sponsoring Agency Code 505-33-33-07

15. Supplementary Notes

16. Abstract
A study is described which had as its goal the determination of the accuracy of ortho-
tropic photoelasticity. The study consisted of both theoretical and experimental phases.
In the theoretical phase a stress-optic law was developed. The stress-optic law includ-
ed the effects of residual birefringence in the relation between applied stress and the
material's optical response. The experimental phase had several portions. First, it
was shown that four-point bending tests and the concept of an optical neutral axis could
be conveniently used to calibrate the stress-optic behavior of the material. Second,
the actual optical response of an orthotropic disk in diametral compression was compared
with theoretical predictions. Third, the stresses in the disk were determined from the
observed optical response, the stress-optic law, and a finite-difference form of the
plane stress equilibrium equations. It was concluded that orthotropic photoelasticity
is not as accurate as isotropic photoelasticity. This is believed to be due to the lack
of good fringe resolution and the low sensitivity of most orthotropic photoelastic mate-
rials.

17. Key Words (Suggested by Author(s)) Orthotropic photoelasticity Fiber reinforced composites Stress-optic laws, finite-differ. soln. Residual birefringence Complex variables in elasticity	18. Distribution Statement Unclassified – Unlimited Subject Category 39	
19. Security Classif. (of this report) Unclassified	20. Security Classif. (of this page) Unclassified	21. No. of Pages 253	22. Price A12

N-305